



University of
Sheffield

**A study of combustion characteristics of
kerosene-based mixtures**

Si Shi

Supervisors:

Dr Kevin J. Hughes

Prof M. Pourkashanian

A thesis submitted in partial fulfilment of the requirements for the degree of Doctor of
Philosophy

Energy 2050

Department of Mechanical Engineering

July 2023

ACKNOWLEDGEMENT

The author would like to express her sincere gratitude to Dr Kevin Hughes, and also to Dr Ruoyang Yuan, Prof Derek Ingham, and Prof M. Pourkashanian for their dedicated guidance and supports throughout the duration of the PhD work.

The author would also like to thank all her colleagues in Energy 2050, especially the members of the combustion group for their help in the laboratory work. Furthermore, the author is grateful for the technical support from Dmitry Govorukhin, Mohammed Al-Aidroos Chris Todd, Gareth Barker, Matt Kirkland, Oliver Cooper, and others that assist with the equipment optimization and reparation in the laser laboratory. Finally, love and thanks to my friends who always stay with me.

ABSTRACT

In the context of global warming and the increasing demands for the application of sustainable aviation fuels, this work aims to improve the fundamental understanding of kerosene-based fuels through both computational and experimental approaches. Regarding the modelling efforts, the chemical kinetics of mono-methyl alkanes is explored by using 2-methylheptane as the representative. Apart from the core C0-C4 chemistry, reaction classes related to the chemistry at low and intermediate temperatures are examined and optimized. Also, new thermodynamic data related to the 2-methylheptane combustion is calculated. The simulated ignition delay time is validated against experimental results from the literature. Regarding the experimental work, the combustion characteristics of five mixtures are investigated in a flat-flame burner and measurements are conducted at three equivalence ratio conditions for each fuel. Kerosene and two proposed surrogates are the main targets, and the other two gas fuels are utilized as the reference for the quantitative studies. The technique of planar laser-induced fluorescence is employed to capture the profiles of OH and NO in the studied flames. The measured results of the liquid fuels are subsequently quantified to the actual mole fraction of the species and validated against the simulation of the burner-stabilized model in ANSYS Chemkin Pro. Also, coated fine wire type R Pt/Pt-Rh thermocouples and OH LIF thermometry are utilized to measure the temperature data of each flame condition.

CONTENTS

ACKNOWLEDGEMENT.....	I
ABSTRACT.....	II
FIGURES.....	VII
TABLES	XII
NOMENCLATURE	XIV
Acronyms	xiv
Symbol	xv
Chemical compounds.....	xvi
CHAPTER 1.....	1
INTRODUCTION	1
1.1 Background of aviation and global warming	1
1.2 Conventional aviation fuels	3
1.3 Sustainable aviation fuels (SAF).....	4
1.3.1 Fischer-Tropsch fuels	5
1.4 Objectives and novelty.....	7
1.5 Structure of the thesis.....	8
CHAPTER 2.....	10
LITERATURE REVIEW.....	10
2.1 Chemical kinetics	10
2.1.1 Combustion introduction	10

2.1.2 Temperature-dependent reaction	11
2.1.3 Pressure-dependent reaction	12
2.1.4 Reverse reaction	15
2.2 Development of a kinetic mechanism	16
2.2.1 H ₂ and CO oxidation	17
2.2.2 Methane	19
2.2.3 C2 hydrocarbons	20
2.2.4 Autoignition and larger hydrocarbons	23
2.2.5 NO _x	26
2.2.6 Ammonia/methane	28
2.3 ANSYS Chemkin Pro	31
2.3.1 Zero-dimensional closed homogeneous reactor.....	32
2.3.2 Zero-dimensional homogeneous reactors with inflow and outflow	33
2.3.3 One-dimensional laminar flame.....	34
2.4 Proposed surrogates of real fuels	36
2.4.1 Formation of surrogate	36
2.4.2 Kerosene	37
2.4.3 Fischer-Tropsch fuels	39
2.4.4 Previous investigations on branched alkanes	41
2.4.5 Previous investigations on normal alkanes	42
CHAPTER 3.....	45
EXPERIMENT SETUP	45
3.1 Kerosene burner	45
3.1.1 Mass flow controller calibration	47
3.1.2 Optimization of burner performances	49
3.1.3 Flame.....	51
3.2 Laser-induced fluorescence	54
3.2.1 Principals of spectroscopy and specific molecules.....	54
3.2.2 Laser setup	57
3.2.3 Data collection	60
3.3 Temperature measurements.....	64

3.3.1 Thermocouple	65
3.3.2 OH LIF thermometry	69
CHAPTER 4.....	74
KINETIC MODELLING DEVELOPMENT	74
4.1 Initial evaluation for mechanisms that contain 2-methylheptane.....	74
4.2 Initial evaluation for the mechanisms of surrogate blends	78
4.3 Thermodynamic data	82
4.3.1 Corrections – Gauche interactions	85
4.3.2 Corrections – Optical isomers and symmetry	86
4.3.3 Value comparison.....	86
4.4 Development of a sub-mechanism of 2-methylheptane – rate constants	88
4.5 Development of a sub-mechanism of 2-methylheptane – rate rules.....	92
4.5.1 H abstraction: Fuel + OH → R + H ₂ O	93
4.5.2 First and second oxygen addition: R + O ₂ → RO ₂ and QOOH + O ₂ → OOQOOH.....	96
4.5.3 Isomerization: RO ₂ → QOOH	103
4.5.4 Concerted elimination: RO ₂ → alkene + HO ₂	107
4.5.5 QOOH → cyclic ether + OH.....	108
4.5.6 QOOH → alkene + HO ₂	109
4.5.7 Isomerization: OOQOOH → Ketohydroperoxide + OH.....	109
4.5.8 Ketohydroperoxide decomposition	111
4.5.9 Additional optimization.....	112
4.6 Evaluation of the updated mechanism	115
4.7 Summary	121
CHAPTER 5.....	123
EXPERIMENTAL RESULTS AND ANALYSIS	123
5.1 Temperature measurements.....	123
5.1.1 Correction of thermocouple.....	124
5.1.2 Temperature results obtained from OH LIF thermometry.....	130

5.1.3 Comparison and discussion.....	137
5.1.4 Challenges: temperature measurements at the lean conditions.....	140
5.2 PLIF measurements	142
5.2.1 Reference fuels.....	145
5.2.2 OH quantification and validation of the burner-stabilized model	149
5.2.3 NO quantification and validation of the burner-stabilized model	156
5.2.4 Original PLIF signal at the lean condition	164
CHAPTER 6.....	166
CONCLUSIONS AND FUTURE SUGGESTIONS.....	166
6.1 Introduction.....	166
6.2 Kinetic modelling	167
6.3 Experimental studies.....	169
6.4 Suggestions for future work	171
BIBLIOGRAPHY	174
APPENDIX A: NEW GROUP ADDITIVITY VALUE OF STABLE SPECIES AND RADICALS.....	192
APPENDIX B: UPDATED THERMODYNAMIC DATA OF SPECIES RELATED TO 2-METHYLHEPTANE COMBUSTION	193
APPENDIX C: UPDATED RATE RULES OF THE REACTION CLASS RELATED TO 2-METHYLHEPTANE COMBUSTION AT LOW AND INTERMEDIATE REGIONS	203

FIGURES

Figure 1.1 Forecast of the global air passenger travel RPK, pre- and post-pandemic [2].	1
Figure 1.2 Direct CO ₂ emissions from aviation: darker blue indicates international flights and lighter blue indicates domestic flights [4].	3
Figure 1.3 Estimated contributions to achieve the net zero goal in 2050 [6].	5
Figure 2.1 The pressure dependence of rate constant of $\text{CH}_3 + \text{CH}_3 + \text{M} \rightleftharpoons \text{C}_2\text{H}_6 + \text{M}$ at 1000 K.	14
Figure 2.2 Limit of the explosion of a stoichiometric H ₂ /O ₂ mixture [18]: k_2 is the rate constant of reaction 2.4 and k_9 denotes the rate constant of reaction 2.5.	18
Figure 2.3 Ignition delay time of n-pentane/air mixtures at 20 atm [40].	24
Figure 2.4 A schematic of low temperature chain branching of an alkane.	26
Figure 2.5 NO _x emissions of different types of ammonia blend [62].	30
Figure 2.6 Reaction pathway of a stoichiometric 80% NH ₃ /20% CH ₄ mixture at 1000 K and 40 bar [65].	31
Figure 2.7 An example of the simulated ignition delay time: the black line is the temperature profile, and the red line is the OH profile.	33
Figure 2.8 Schematic illustration of a jet-stirred reactor [68].	33
Figure 2.9 Combustion of propane/air at 1 atm and 300 K with the use of flame speed model: (a) Simulated flame speed at the stoichiometric condition; (b) Calculated laminar flame speed as a function of the equivalence ratio.	35
Figure 2.10 Temperature and mole fraction OH and O profiles of H ₂ /O ₂ combustion at 0.4 atm with the use of burner-stabilized model.	35
Figure 2.11 Aromatics volume of JP-8 [13].	37
Figure 3.1 The detailed illustration of the customised kerosene burner [12].	46
Figure 3.2 The detailed illustration of the detailed atomiser of the burner [12].	47
Figure 3.3 Calibration results of the liquid MFC.	48
Figure 3.4 Calibration results of the air MFCs: (a) Primary; (b) Secondary.	49
Figure 3.5 Deformed sintered plate after a period of use.	50
Figure 3.6 Front view of the flame diffuser, dimensions in mm: (a) previous [121]; (b) new.	50
Figure 3.7 Left view of the flame diffuser, dimension in mm: (a) previous; (b) new.	51
Figure 3.8 An example of the premixed laminar flame produced by the kerosene burner.	52
Figure 3.9 Diagram of the energy level of a diatomic molecule. [123].	55

Figure 3.10 Energy level of $A2\Sigma^+\leftarrow X2\Pi$, including absorption (blue), resonance fluorescence (green), fluorescence (black solid), vibrational energy transfer (black dash), rotational energy transfer (double arrow), and quenching (red).....	56
Figure 3.11 An example of the allowed transitions in $A2\Sigma^+\leftarrow X2\Pi$, from $N'' = 13$. [122]	57
Figure 3.12 PLIF equipment setup: (a) general schematic; (b) detailed optical layout, from Sirah dye laser datasheet. [125]	59
Figure 3.13 OH spectrum at 1500 K from both the simulation and observation.	61
Figure 3.14 Design of the temperature measurements by thermocouples [121]......	67
Figure 3.15 Variation of emissivity against temperature, for uncoated and coated wires [138]......	68
Figure 3.16 The simulated spectrum of $R_2(13)$ and $P_1(2)$ at three different temperature conditions.	71
Figure 3.17 The simulated spectrum of $R_2(2)$ and $R_1(12)$ at three different temperature conditions.	72
Figure 3.18 Relationship between the simulated intensity ratio of $R_2(13)/P_1(2)$ and the temperature, from 800 K to 2300 K.	72
Figure 3.19 Relationship between the simulated intensity ratio of $R_2(2)/R_1(12)$ and the temperature, from 800 K to 2300 K.	72
Figure 4.1 Comparisons of the ignition delay time between experimental measurements and kinetic modelling for 2-methylheptane/air combustion at 20 atm: (a) $\varphi = 0.5$; (b) $\varphi = 1$; (c) $\varphi = 1.5$	75
Figure 4.2 Normalised temperature sensitivity of 2-methylheptane/air mixtures at 20 atm: (a) 714 K; (b) 800 K; (c) 1000 K; (d) 1250 K.....	78
Figure 4.3 Simulations (line) of the ignition delay time of a surrogate of Jet A POSF 4658, compared with the experimental results (scatter) at $\varphi = 1$: (a) 8 atm; (b) 20 atm; (c) 40 atm.	79
Figure 4.4 Simulations (line) of the ignition delay time of a surrogate of S-8 4734, compared with the experimental results (scatter): (a) $\varphi = 1$, 20 atm; (b) $\varphi = 1.15$, 7 bar.....	79
Figure 4.5 Simulations (line) of the laminar flame speed of surrogates of real fuels at 1 atm and 470 K, compared with the experimental results (scatter): (a) Jet A1; (b) S-8.....	80
Figure 4.6 Comparisons between the original mechanism and assembled mechanism for the combustion of 2-methylheptane/air, at 20 atm: (a) $\varphi = 0.5$; (b) $\varphi = 1$; (c) $\varphi = 1.5$	82
Figure 4.7 Approximation of the new heat capacity value of 2-methylheptane.....	84
Figure 4.8 Structure of 2-methylheptane with labelled carbon number.	85
Figure 4.9 Mirror images of C2-C3 bond in 2-methylheptane: (a) alkane gauche; (b) RG1; (c) RG2....	85
Figure 4.10 Comparison of the simulated ignition delay time for 2-methylheptane/air at 20 atm and stoichiometric condition, by using the assembled mechanism and different thermodynamic data. ...	87
Figure 4.11 Comparisons of the low-pressure limit for reaction 4.1 between various experimental records (scatter) and three calculated rates (line), reference: blue open square [158].	89

Figure 4.12 Simulated low- and high-pressure limit and fall-off region of reaction 4.1 at three temperature conditions, compared with experimental data at various pressures, reference: square [160], open circle [161], up triangle [157].	90
Figure 4.13 Reaction 4.2 comparison between the experimental records (scatter) and calculated rate constants (line).	91
Figure 4.14 A comparison of k_3 between various experimental records (scatter) and reviews (line).	92
Figure 4.15 Structure of n-heptane.	95
Figure 4.16 Comparison of the rate constant expression of H abstraction by OH: (a) primary carbon site per H atom; (b) secondary carbon site per H atom; (c) tertiary carbon site per H atom.	95
Figure 4.17 Low and high pressure limit and fall off region of $\text{CH}_3 + \text{O}_2 + \text{M} \rightleftharpoons \text{CH}_3\text{O}_2 + \text{M}$, compared with the theoretical pressure dependent value, references: black square [182], blue square [183], red up triangle [186].	98
Figure 4.18 Comparisons of the forward rate constant expression of 1^{st}O_2 addition between theoretical references and experiment values (250-800 K): (a) primary; (b) secondary; (c) tertiary.	100
Figure 4.19 Rate constant expression of $\text{QOOH} + \text{O}_2$ for primary type at low temperature (300-800 K): scatter: EXP value [193]; line: theories.	102
Figure 4.20 Example of isomerization of 1,5s type via transition ring: $\text{C}_8\text{H}_{17}\text{O}_2\text{-6-2} \rightleftharpoons \text{C}_8\text{OOH}_6\text{-2d}$.	103
Figure 4.21 Comparisons of the rate constants between different theories (lines) and experiments (scatter) from 300 K to 1000 K: (a) 1,5p (<i>pp</i>); (b) 1,5s (<i>ps</i>); (c) 1,6s (<i>ps</i>).	106
Figure 4.22 Predictions of the ignition with updated rate rules of the isomerization from different authors, for 2-methylheptane/air mixtures at the stoichiometric and 20 atm conditions.	107
Figure 4.23 Example of a 1,6H type <i>sp</i> isomerization of OOQOOH : $\text{C}_8\text{OOH}_7\text{-OO}_4\text{-2} \rightleftharpoons \text{C}_8\text{KET}_7\text{-4-2} + \text{OH}$: <i>s</i> indicating the position of $-\text{OO}\cdot$ and <i>p</i> indicating the position of the hydroperoxyl group.	109
Figure 4.24 Comparisons of the three types of rate constants between OOQOOH isomer and RO_2 isomer: RO_2 from Sharma et al. [205] and OOQOOH from Sharma et al. [205] and Miyoshi [188].	110
Figure 4.25 Simulations of the updated rules from class one to seven, compared to the original model and experiments: rates of OOQOOH isomerization employed from Miyoshi [188] and Sharma et al. [205].	111
Figure 4.26 Comparisons of the three types of rate constants between the refined OOQOOH isomer and RO_2 isomer.	113
Figure 4.27 Optimized model of the stoichiometric 2-methylheptane/air combustion at 20 atm, compared to the original and cond.0.	114

Figure 4.28 Ignition predictions of the optimized 2-methylheptane model at 20 atm, compared to the original result and experiments: (a) $\varphi = 0.5$; (b) $\varphi = 1$; (c) $\varphi = 1.5$	115
Figure 4.29 Sensitivity analysis of the updated mechanism at the stoichiometric and lean conditions: (a) 670 K; (b) 740 K; (c) 800 K; (d) 870 K; (e) 910 K; (f) 1000 K.....	118
Figure 4.30. Reaction pathway of stoichiometric 2-methylheptane at 20 atm and 800 K: new % is in bold and original % is in brackets.	120
Figure 5.1 Corrected temperature profile of CH ₄ /air flames in three equivalence ratio conditions..	127
Figure 5.2 Corrected temperature profile of CH ₄ /NH ₃ /air flames in three equivalence ratio conditions.....	128
Figure 5.3 Corrected temperature profile of kerosene/air flames in two equivalence ratio conditions.	128
Figure 5.4 Simulated OH mole fraction of the CH ₄ /air at the rich condition, with the temperature profiles calculated by two area boundaries, respectively.	130
Figure 5.5 An example of the temperature profile obtained from OH LIF thermometry with the R ₂ (13)/P ₁ (2) pair, type 1: (a) the raw data of the rich condition of surrogate A; (b) the refined temperature data.....	131
Figure 5.6 An example of the temperature profile obtained from OH LIF thermometry with the R ₂ (13)/P ₁ (2) pair, type 2: (a) the raw data of the stoichiometric condition of kerosene; (b) the refined temperature data.....	132
Figure 5.7 An example of the temperature profile obtained from OH LIF thermometry with the pair of R ₂ (2)/R ₁ (12): (a) the raw data of the rich condition of kerosene; (b) the refined temperature data.	132
Figure 5.8 Comparison of the simulations with different inlet temperature.	136
Figure 5.9 Impacts of the temperature profiles with the example of the kerosene flame at the rich condition: (a) Comparison of the temperature data between the three approaches; (b) Simulated OH mole fraction based on their respective temperature data.	138
Figure 5.10 Impacts of the temperature profiles with the example of the kerosene flame at the stoichiometric condition: (a) Comparison of the temperature data between the three approaches; (b) Simulated OH mole fraction based on their respective temperature data.....	139
Figure 5.11 Impacts of the deficient temperature profiles with the lean condition of the surrogate A flame: (a) Three sets of temperature data; (b) Simulated OH mole fraction based on their respective temperature data.....	141
Figure 5.12 An example of the signal images from the Q ₁ (6) transition, by using the kerosene flame at the stoichiometric condition: (a) raw; (b) background; (c) cuvette.....	142

Figure 5.13 Normed OH intensity with different x-axes.	143
Figure 5.14 Simulated Boltzmann population: (a) OH at $j = 6$; (b) NO at $j = 12 + 20$	144
Figure 5.15 Comparison of the OH profile between the simulations (line) and the PLIF signals (scatter) of the CH ₄ /air flames at rich (black), stoichiometric (red), and lean (blue) conditions.....	146
Figure 5.16 Calculated quenching cross section of $A^2\Sigma + OH$ by three colliders, unit: Å ²	147
Figure 5.17 Comparison of NO profile between the simulations (line) and the PLIF (scatter) of the CH ₄ /NH ₃ /air flames: (a) $\varphi = 1.30$; (b) $\varphi = 1.00$; (c) $\varphi = 0.84$	148
Figure 5.18 Rate of production of the NO: (a) $\varphi = 1.30$; (b) $\varphi = 1.00$; (c) $\varphi = 0.84$	149
Figure 5.19 The OH profile of the kerosene/air flame: (a) $\varphi = 1.30$; (b) $\varphi = 1.00$	152
Figure 5.20 The OH profile of the surrogate A/air flame: (a) $\varphi = 1.30$; (b) $\varphi = 1.00$	153
Figure 5.21 The OH profile of the surrogate B/air flame: (a) $\varphi = 1.30$; (b) $\varphi = 1.00$	154
Figure 5.22 Comparison of the relative OH of the three mixtures at $\varphi = 1.30$: (a) Model; (b) PLIF...	155
Figure 5.23 Rate of Production of the OH in the kerosene flames: (a) $\varphi = 1.30$; (b) $\varphi = 1.00$	156
Figure 5.24 Simulated NO profiles at $\varphi = 1.30$: (a) Model of the three mixtures; (b) Example of the NO ROP.	157
Figure 5.25 NO profiles at $\varphi = 1.00$: (a) Model of the three mixtures; (b) Example of the NO ROP (thermocouple temperature); (c) Example of the NO ROP (OH LIF thermometry temperature).	158
Figure 5.26 PLIF signal with the example of the surrogate A flames: (a) $\varphi = 1.30$; (b) $\varphi = 1.00$	160
Figure 5.27 The NO profile of the kerosene/air flame: (a) $\varphi = 1.30$; (b) $\varphi = 1.00$	162
Figure 5.28 The NO profile of the surrogate A/air flame: (a) $\varphi = 1.30$; (b) $\varphi = 1.00$	163
Figure 5.29 The NO profile of the surrogate B/air flame: (a) $\varphi = 1.30$; (b) $\varphi = 1.00$	164
Figure 5.30 Example of the original PLIF signal at three equivalence ratio conditions: (a) OH; (b) NO.	165

TABLES

Table 1.1 Main characteristics of two conventional jet fuels and two synthetic F-T fuels, sources from: [9, 10, 16, 17].	7
Table 3.1 Flow rates of the liquid fuels and air.	53
Table 3.2 Flow rates ($L \cdot \text{min}^{-1}$) of the gas fuels and air.	53
Table 3.3 An example of equivalence ratio uncertainty.	53
Table 3.4 Laser power and camera gain for the measurements of OH, OH LIF thermometry, and NO.	63
Table 3.5 General laser and camera settings.	63
Table 3.6 Compilation of the approaches used to obtain temperature profile for different flames.	65
Table 3.7 Comparisons of the temperature sensitivity between signal pairs.	71
Table 4.1 Comparison of enthalpy and entropy between the original and modified values.	87
Table 4.2 Rate rules of H abstraction by OH per H atom for each radical.	94
Table 4.3 Comparison of ring strain energy between different authors. (Unit: $\text{kJ} \cdot \text{mol}^{-1}$)	104
Table 4.4 Compilations of updated rate rules with modifications.	122
Table 5.1 Simulated equilibrium temperature (K) of each interested flame.	124
Table 5.2 Temperature profiles of CH_4/air flames by using the thermocouples (type P13R-005).	125
Table 5.3 Temperature profiles of $\text{CH}_4/\text{NH}_3/\text{air}$ flames by using the thermocouples (type P13R-002).	125
Table 5.4 Temperature profiles of kerosene/air flames by using the thermocouples. (Rich condition: type P13R-005, stoichiometric condition: type P13R-003).	126
Table 5.5 Impacts of different flow rate with the reference of the peak temperature.	129
Table 5.6 Temperature profiles of the kerosene flames by using OH LIF thermometry.	133
Table 5.7 Temperature profiles of the surrogate A flames by using OH LIF thermometry, transition: $\text{R}_2(13)/\text{P}_1(2)$.	134
Table 5.8 Temperature profiles of the surrogate B flames by using OH LIF thermometry: the rich condition is from the $\text{R}_2(13)/\text{P}_1(2)$ and the stoichiometric condition is from the $\text{R}_2(2)/\text{R}_1(12)$.	134
Table 5.9 Uncertainty calculation of the $\text{R}_2(13)/\text{P}_1(2)$ pair at 1500 K, note: $\Delta = T_{\text{limit}} - T_{\text{ideal}}$.	135
Table 5.10 Uncertainty calculation of the $\text{R}_2(2)/\text{R}_1(12)$ pair at 1500 K, note: $\Delta = T_{\text{limit}} - T_{\text{ideal}}$.	135
Table 5.11 Comparison of the OH model by using different temperature data at the rich and stoichiometric cases of the kerosene/air flames.	137
Table 5.12 Comparison between the OH model and the OH PLIF of the CH_4/air flames.	146
Table 5.13 Comparison of OH mole fraction between experiments and modelling.	150

Table 5.14 Important parameters of two reference points for quantifying OH.....	151
Table 5.15 Comparison of the NO magnitude at the rich and the stoichiometric condition at the burner distance of 5 mm.	161
Table 5.16 Important parameters of the peak reference point for quantifying NO.	161
Table 5.17 Comparison between the converted NO and the simulated NO at the distance of 5 mm.	162

NOMENCLATURE

Acronyms

ASTM	American Society for Testing and Material
CN	Cetane number
CTL	Coal-to-liquid
DEF STAN	United Kingdom Ministry of Defence
FCU	Frequency conversion unit
F/O	Fuel-oxidizer ratio
F-T	Fischer-Tropsch
GA	Group additivity
GC	Gas chromatography
GHG	Greenhouse gas
GTL	Gas-to-liquid
HAB	Height above burner
HCCI	Homogeneous charge compression-ignition
IATA	International Air Transport Association
ICCD	Intensified charged couple device
IEA	International Energy Agent
IPK	Iso paraffin kerosene
JSR	Jet-stirred reactor
LIF	Laser-induced fluorescence
MFC	Mass flow controller
NNN	Next-nearest neighbour
NTC	Negative temperate coefficient
PLIF	Planar laser-induced fluorescence
PMS	Photoionization mass spectrometer
PSR	Perfectly stirred reactor
RCM	Rapid compression machines
PMT	Photomultipliers

ROP	Rate of production
RPK	Revenue passenger-kilometre
RR	Rate of reaction
SAF	Sustainable aviation fuel
SBO	Surrogate blend optimization
SPK	Synthetic paraffinic kerosene
TSI	Threshold sooting index
UNFCCC	Nations Framework Convention on Climate Change
2 ω HG	Second harmonic module

Symbol

A	Pre-exponential factor (dependent on the reaction order)
bf	Boltzmann distribution
C_p	Heat capacity ($\text{cal} \cdot \text{mol}^{-1} \cdot \text{K}^{-1}$)
d	Bead diameter (m)
E_a	Activation energy ($\text{J} \cdot \text{mol}^{-1}$)
G	Gibbs energy ($\text{cal} \cdot \text{mol}^{-1}$)
h	Planck constant ($\text{J} \cdot \text{s}$)
H	Enthalpy ($\text{kcal} \cdot \text{mol}^{-1}$)
J	Rotational level
K_c	Equilibrium constant in concentration unit
K_p	Equilibrium constant in pressure unit
k_f	Forward rate constant (dependent on the reaction order)
k_r	Reversed rate constant (dependent on the reaction order)
\dot{m}	Mass flow rate ($\text{g} \cdot \text{min}^{-1}$ for the liquid and $\text{L} \cdot \text{min}^{-1}$ for the gas)
M	Third-body collision
MW	Molecular weight ($\text{kg} \cdot \text{mol}^{-1}$)
Δn	Differences of stoichiometric coefficients between the products and reactants
R_u	Universal gas constant ($\text{J} \cdot \text{K}^{-1} \cdot \text{mol}^{-1}$)
S	Entropy ($\text{cal} \cdot \text{mol}^{-1} \cdot \text{K}^{-1}$)

S_L	Laminar burning velocity ($\text{m} \cdot \text{s}^{-1}$)
T_m	Measured temperature (K)
T_c	Corrected temperature (K)
U	Total flow rate ($\text{kg} \cdot \text{m}^{-2} \cdot \text{s}^{-1}$)
ν	Vibrational level
φ	Equivalence ratio (fuel-oxidizer ratio)
ε	Emissivity
σ	Stefan Boltzmann constant ($\text{J} \cdot \text{s}^{-1} \cdot \text{m}^{-2} \cdot \text{K}^{-4}$)
σ_{eff}	Quenching cross section (\AA^2)
σ_{sym}	Total symmetry number in a molecule
λ	Thermal conductivity ($\text{J} \cdot \text{s}^{-1} \cdot \text{m}^{-1} \cdot \text{K}^{-1}$)
η	Dynamic viscosity ($\text{kg} \cdot \text{m}^{-1} \cdot \text{s}^{-1}$)

Chemical compounds

NO_x	Nitrogen oxides
OOQOOH	Hydroperoxyl alkyl peroxy radicals
QOOH	Alkyl hydroperoxyl radicals
RH	Fuel
R	Fuel radicals
RO_2	Alkyl peroxy radicals

CHAPTER 1

INTRODUCTION

1.1 Background of aviation and global warming

Due to globalization and the increase in personal activities, aviation plays a more and more important role in many aspects of modern society. From the market analysis of the International Air Transport Association (IATA) in December 2022 [1], the traffic of passenger air miles has begun to recover considerably after the impacts of the unprecedented COVID-19 in the past two years. Globally, the revenue passenger-kilometre (RPK) in 2022 is 68.5% of the RPK in 2019, which was 41.7% in 2021. Figure 1.1 shows the forecast of global RPK before and after the pandemic from the IATA outlook in June 2022[2]. If the current estimation is correct, the traffic by 2040 will still be around 6% lower than the pre-COVID-19 forecast. Additionally, commercial airlines also indicate positive trends. The revenue is 727 \$ billion in 2022, which is only 13.2% less than the result in 2019, compared to the difference between 2021 and 2019 is 39.6%. The willingness of people to travel and the size of the aviation market are expected to keep growing shortly.

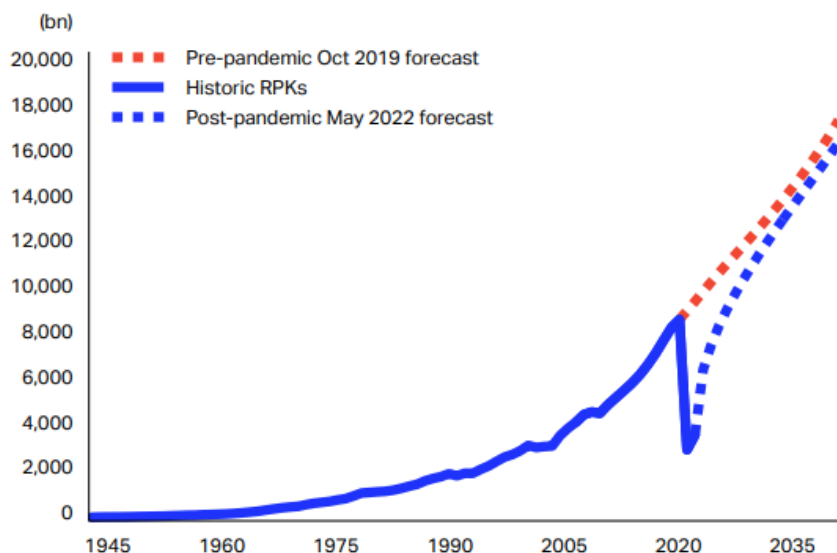


Figure 1.1 Forecast of the global air passenger travel RPK, pre- and post-pandemic [2].

Before the discussions on aviation impact on the environment, global warming is first introduced. The surface temperature of the earth is determined by a balance between the incoming and reflected solar radiation, both directly and indirectly from the emission in

infrared radiation from the heated surfaces. The atmosphere can absorb some of this emitted infrared radiation from the surfaces, leading to additional warming referred to as the greenhouse effect, which is critical to life and daily activities. Some atmospheric components that enhance this greenhouse effect are referred to as greenhouse gas (GHG), for instance, carbon dioxide (CO₂), water vapour (H₂O), methane (CH₄), etc. However, since the Industrial Revolution around the 1750s, due to human activities such as the combustion of fossil fuels, the concentration of these gases has greatly increased which results in the rise of the average surface temperature. This phenomenon is referred to as global warming. Carbon dioxide is the most prominent greenhouse gas, accounting for 74.4% of the total global GHG emissions from a report by Our World in Data in 2020 [3]. Methane is the second largest contributor, which is 17.3%, and the main sources come from livestock, rice cultivation, oxidation of biomass, etc. [3]. Additionally, nitrous oxide (N₂O) and fluorinated gases (F-gases) also have an impact on GHG emissions.

Aviation contributes greatly to climate change, partly due to the current fuels used in aviation are predominantly based on fossil fuels that are heavily responsible for the emission of CO₂. In 2019, global aviation accounted for around 1.9% of the total world carbon dioxide emissions, which is 915 million tonnes. After the sharp plummet in 2020, the emissions from aviation increased back to around 700 million tonnes in 2021 and it is expected to keep growing, as the graph of International Energy Agent (IEA) shows in Figure 1.2 [4]. Concerns have long been raised over the environmental impacts of aircraft emissions and the sustainability of fossil fuels. Furthermore, the rise in the cost of oil, energy supply, and energy security are other driving forces to call for the development of alternative aviation fuels to meet the growth of energy requirements.

To accommodate this challenge, many actions have been taken to reduce emissions, either through policy or technology. The Paris Agreement was formulated by the United Nations Framework Convention on Climate Change (UNFCCC) in 2015, and a total of 195 global parties aim to limit the temperature increase to be smaller than 2 °C above the preindustrial level [5]. IATA stated on October 4th, 2021, that the aviation industry passed a resolution to achieve net-zero carbon emissions by 2050, which is in alignment with the goal of the Paris Agreement. From their calculations, if the current projection stands, about 21.2 gigatons of aviation CO₂ are required to be mitigated to reach net zero between 2021 and 2050 [6]. Substantial efforts

have been made to explore alternative solutions to the conventional aviation industry, including alternative aviation fuels, new aircraft technologies, carbon captures, etc. In addition, regarding the long-lasting effects of the pandemic, Grewe et al. [7] recently evaluated the aviation emissions under several recovery scenarios from COVID-19 up to 2100 and concluded that it is quite likely that the emissions from aviation will fail to achieve the target of the Paris Agreement. In conclusion, although certain milestones have been achieved and further established, it is a major challenge to meet the climate goal of net zero in 2050, and a tremendous amount of work needs to be done by industry, government, the finance sector, the research community, etc.

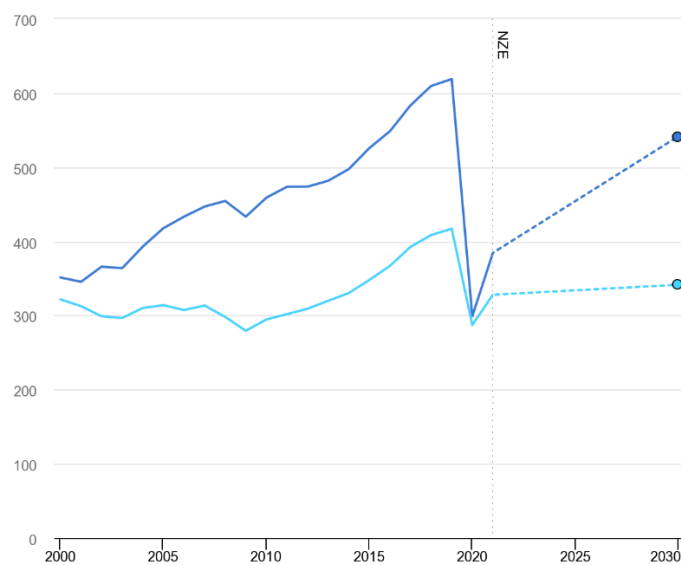


Figure 1.2 Direct CO₂ emissions from aviation: darker blue indicates international flights and lighter blue indicates domestic flights [4].

1.2 Conventional aviation fuels

Aviation fuel is a type of petroleum-based fuel utilized in aircraft, which consists of a mixture of large numbers of hydrocarbons with a carbon chain length of C8-C16 [8], and the one designed for gas-turbine engines is known as jet fuel. In commercial flights, the most common fuels are kerosene-based, referred to as Jet A and Jet A-1, and their only major differences are the freezing point, which is 233 K and 226 K, respectively. Jet A is widely used in the U.S. and Jet A-1 is employed in the rest of the world. Another type of kerosene-based fuel is Jet B, which is much less common in commercial use. It has a lower freezing point than Jet A (213 K) and it has a quite light fuel composition, making it suitable mainly for the military or only in colder regions such as Canada and Alaska. In terms of military demand, JP-8 is

utilized in the United States, which is essentially Jet A-1 with three additional additives to prevent corrosion, static electricity, and system icing [9]. Also, some countries develop their jet fuels, for instance, Russia adopts TS-1 and RT fuels for commercial and military use, respectively.

Some necessary specifications must be met for jet fuels before use in aircraft. The American Society for Testing and Material (ASTM) and the United Kingdom Ministry of Defence (DEF STAN) are two of the main organizations to issue these standards. ASTM D1655 covers the standard specifications for jet fuels, and depending on the views of the investigators, general requirements may be classified differently. From a report on sustainable aviation fuels published by the U.S. Department of Energy [10], basic requirements for jet fuels generally include performance, operability, and other factors. Performance refers to the properties that can greatly encourage financial motivations to consume fuel, such as specific energy, energy density, thermal stability, and soot problems. Operability indicates the safe application of jet fuel under engine conditions, which relates to the physical properties that are highly related to oxidation and include volatility, freezing point, density, viscosity, hydrogen content, etc. Also, properties such as the trace composition are vital, as issues such as corrosion, pump wear, or electrical conductivity may be caused, hence subsequently affecting the functionality of both the fuel and engine.

The detailed contents of jet fuels are complex and vary with different types. Recently, Edwards [11] compiled a list of references on jet fuels and three types of fuels are included: conventional, alternative, and test fuels. The properties and compositions of each category are discussed. From the results of the two-dimensional gas chromatography (GCxGC) measurements, the average Jet A fuel includes 20% of normal alkanes, 30% of branched alkanes, 25% of monocyclic alkanes, 7% bicyclic alkanes, and 19% of aromatics. Each hydrocarbon class has its distinctive characteristics.

1.3 Sustainable aviation fuels (SAF)

Interest in alternative aviation fuels has been increasing rapidly over the years for the reason of reducing carbon dioxide emissions. Along with many considerations, one of the most important factors is the ability of drop-in, meaning that the proposed new fuel can apply directly to the existing engines without altering the fuels and aircraft infrastructure. Sustainable aviation fuel (SAF), sometimes addressed as sustainable alternative fuel, is now a

commonly used term referring to the non-petroleum-based aviation fuels that meet the requirements of drop-in, which makes them more attractive compared to other non-drop-in fuels. From a recent report from the IATA [6], until April 2022 over 450000 commercial flights and 50 airlines are applying SAF, and the estimation milestone shows that to reach the goal of zero carbon in 2050, the contribution of SAF should account for about 65% of the alternative pathways as shown in Figure 1.3, and from the calculations, annually 449 billion litres of SAF fuels should be available.

Detailed specifications have been established and developed, which can be found in ASTM 7566. As of the publication from November 2022, there are currently seven types of annexes that have qualified for this standard. Each SAF candidate is required to be blended with conventional jet fuels up to a maximum 50% before being used. Some of the main challenges for larger SAF applications include the size of the global aviation market is already substantial and keeps growing, also the cost of SAF fuel production is usually higher than conventional fuels [10]. Research and advances in technology are strongly encouraged to help the development of SAF fuels for practical uses.

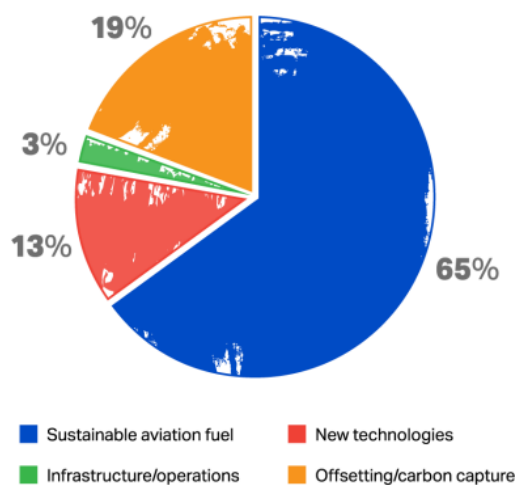


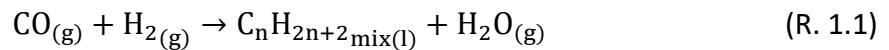
Figure 1.3 Estimated contributions to achieve the net zero goal in 2050 [6].

1.3.1 Fischer-Tropsch fuels

The concept of synthetic paraffinic kerosene (SPK) is first introduced. It is a synthetic hydrocarbon produced from renewable sources by using various technologies, and typical crude materials include syngas, lipids, sugars, and alcohol. The Fischer-Tropsch (F-T) fuel is a type of SPK and has been one of the most promising renewable jet fuels. The blend of F-T SPK

was the first candidate to be approved as a SAF fuel, and later a mixture of F-T SPK and aromatics fuel has also been approved. In addition, both annexes can reach 50% of blending.

This work will solely focus on Fischer-Tropsch fuels. It can be produced from several feedstocks, for example, coal, natural gas, and biomass, although work regarding biomass has been relatively less studied. Initially, the feedstock is gasified to produce a mixture of carbon monoxide and hydrogen gas, commonly referred to as syngas. Then, through a set of reactions, the mixture of syngas will be converted into liquid hydrocarbons [9]. The Fischer-Tropsch process is often referred to as coal-to-liquid (CTL) or gas-to-liquid (GTL) depending on the initial source. The technology was initially developed in the 1920s in Germany, and some of the best well-known plants currently are Sasol IPK in South Africa, Shell GTL in Malaysia, and Syntroleum GTL in Tulsa. A general reaction description is shown as [12]:



The F-T fuels primarily consist of paraffin, which are mixture of iso-alkane and normal alkane [13]. Due to the negligible trace of compounds of aromatics and sulphur, the F-T fuels burn much cleaner compared to kerosene and adapt rather well with the current engines. However, there are some issues when attempting to increase the involvement of F-T fuels in the liquid fuel industry. High production cost is the main concern, as the process requires advanced technology and significant infrastructure investment, which takes about 2-3 years to put into manufacturing and another several years to earn returns on the investment [14]. Also, the availability of reliable feedstock is relatively limited, and the use of coal as the feedstock may lead to considerable greenhouse emissions. Regarding the fuel property, one is that the density of the F-T fuels is relatively lower. From the ASTM D1655 [15], the lowest density requirement at 15 °C for the Jet A application is 775 kg · m⁻³. Furthermore, the lack of aromatics would lead to the shrinkage of seals in normal operation. Thus, to prevent the fuel leakage, a minimum aromatics content in synthetic fuel mixtures is suggested to be 8% [8]. However, in the context of SAF fuels, these drawbacks can be overcome by blending. Additionally, a property comparison between conventional fuels and F-T fuels is shown in Table 1.1.

Table 1.1 Main characteristics of two conventional jet fuels and two synthetic F-T fuels, sources from: [9, 10, 16, 17].

Property	Jet A	JP-8	S-8 4734	Sasol IPK
Flash point (°C)	47	48	49	44
Freezing point (°C)	-49	-49	-59	<-78
Density @ 15 °C (kg · m ⁻³)	806	790	757	762
Viscosity @ -20 °C (cSt)	5.2	4.2	4.6	3.6
Lower calorific value (MJ · kg ⁻¹)	42.8	43	44.1	44
Derived cetane number	47.3 ± 0.67	51	60.4 ± 0.99	30.7 ± 0.32
H/C molar ratio	1.957	2.017	2.152	2.119
Average molecular weight (g · mol ⁻¹)	142	153	168	156

1.4 Objectives and novelty

The primary aim of this work is to investigate the fundamental combustion characteristics of kerosene-based hydrocarbons, and the means of both simulation and experiment are explored.

From the modelling point of view, this work aims to construct and optimize a chemical kinetic mechanism that can be utilized to simulate the oxidation behaviours of a large mono-methyl alkane and ignition delay time from the literature is utilized for the model validation. The main novelty is that chemical mechanisms containing a variety of large hydrocarbons that are suitable to represent the properties of real jet fuels are rather scarce, and the available mechanisms oftentimes require further modifications to improve the model quality. Furthermore, either conventional jet fuels or Fischer-Tropsch fuels comprise a significant proportion of branched alkane, while this hydrocarbon class severely lacks investigations, hence the quality of the jet fuel model is in a way compromised. In general, these knowledge gaps all come down to the improvement of the fundamental understanding of chemical kinetics, particularly around low and intermediate temperatures.

From the experimental point of view, this work aims to measure the OH and NO profiles of the premixed laminar flames of several targeted hydrocarbon fuels, and then quantify the collected signals to the actual mole fraction of the species and validated against the simulation. Also, the temperature data of each flame condition is measured. Regarding the originality of the experimental investigations, despite the great importance, the measured

temperature profile of a premixed laminar flame under atmospheric condition is quite scarce, particularly for large hydrocarbon mixtures. Also, quantifying the species concentration is a great challenge and few investigations have been performed. Therefore, certain degrees of errors are expected, and the precision is highly dependent on the quality of the calibration method.

1.5 Structure of the thesis

The thesis is organized in the following chapters:

Chapter 1: Introduction

This chapter provides the background of general global warming and the important role of the aviation industry. In recent years, an increasing interest has risen regarding the use of sustainable aviation fuels, and the significance to improve fundamental understanding of the oxidation of these large hydrocarbon fuels is addressed. In addition, the objectives and the novelty of this work are discussed.

Chapter 2: Literature review

This chapter first introduces the basic knowledge of chemical kinetics and then elaborates on the development of a detailed kinetic mechanism originating from the oxidation of hydrogen and carbon monoxide. Next, the simulation tool utilized in this work is presented with various model examples. Furthermore, the idea of the surrogate is explained and previous efforts of the proposed surrogates of the real fuels are reviewed.

Chapter 3: Experimental setup

This chapter describes the experimental setup and the concept of the measurements, primarily including the design of the kerosene burner, preparation work before the experiments, the technique of the planar-induced laser fluorescence, and the discussions of the two methods employed to measure temperature profiles.

Chapter 4: Kinetic modelling development

This chapter describes the development of a detailed mechanism for the larger alkane components. Two common approaches are explored extensively to optimize a kinetic package of a type of monomethyl alkane, and the updated simulations are compared with the experimental data from the literature.

Chapter 5: Experimental results and analysis

This chapter provides a comprehensive analysis of the collected data for each mixture condition. Firstly, the temperature results from the employed two approaches are compared, and the uncertainty from either source is discussed. Secondly, the quantitative method is addressed in detail, then the measured OH and NO profiles are examined, and the most ideal results are subsequently converted and further validated against the model. In addition, several assumptions and suggestions are proposed regarding the potential cause of the challenge faced in the experiment.

Chapter 6: Conclusions and future suggestions

This chapter sums up the main activities and the findings of this work and provides several suggestions for future research in aviation combustion.

CHAPTER 2

LITERATURE REVIEW

Chemical kinetics is fundamental to the study of combustion, hence some of the basic concepts and knowledge are initially introduced. The development of a detailed kinetic mechanism is then discussed, commencing from the core chemistry of H₂/CO and C1-C2 hydrocarbons to larger and more complex hydrocarbons. Additionally, the chemistry of nitrogen is addressed along with the newly promising fuel ammonia and its blends. Next, a practical guide of the computational tool employed in this project, ANSYS Chemkin Pro, is presented, including the basic inputs, several modelling programmes related to different types of flame characteristics, and their respective example simulations. Finally, the investigations of the proposed surrogates of kerosene and Fischer-Tropsch fuels, together with individual components of branched alkanes and normal paraffin, are compiled and reviewed.

2.1 Chemical kinetics

The combustion process can be described by a series of elementary reactions, and each reaction is specified by an assigned rate constant obtained from either experiments or theories. Also, the thermodynamic parameters of each species are crucial to determine the reverse rate constant of each elementary reaction.

2.1.1 Combustion introduction

In general, combustion involves reactions between any combustible material and an oxidizer, commonly a fuel and oxygen, to form products. The relative composition of the fuel-oxidizer mixture largely affects the combustion process. This is defined by the equivalence ratio φ , which is a function of the fuel-oxidizer ratio (F/O) as given by [18]:

$$\varphi = \frac{(F/O)}{(F/O)_{st}} \quad (\text{Eq. 2.1})$$

Where $(F/O)_{st}$ represents the fuel-oxidizer ratio at the stoichiometric condition where the reactants are balanced, denoting that the oxidation between the fuel and oxidizer is complete with only carbon dioxide and water left as products. Consider the reaction of methane:



In the balanced reaction, two moles of oxygen are required to combust one mole of methane and $(F/O)_{st}$ in this case is equivalent to 0.5. When $0 < \varphi < 1$, the condition is fuel-lean, meaning that the oxidizer is excess and when $1 < \varphi < \infty$, the condition is fuel-rich which means the fuel is in excess.

2.1.2 Temperature-dependent reaction

The oxidation process occurs at a specific rate which is directly dependent on the concentrations of the reacting species, temperature, and pressure. An elementary reaction is the simplest type of reaction in which the conversion of the reactants to the products takes place in a single step. The understanding of the rate of reaction (RR) is an essential part of chemical kinetics and can further provide accurate predictions of the behaviour of the entire combustion process. Consider a general elementary reaction:



Where A and B represent the reacting species, C and D are the products, and a, b, c, d are the stoichiometric coefficients. The rate of reaction can be expressed as:

$$\text{RR} = \frac{dC_{\text{product}}}{dt} = k[A]^a[B]^b \quad (\text{Eq. 2.2})$$

Where k is referred to as the rate constant, which is usually a function of the temperature and in some cases is pressure-dependent; $[A]$ and $[B]$ are the concentration of reactants; a and b are reaction orders with respect to reactants A and B , and the sum of these exponents is known as the overall reaction order. The reaction rate expression also defines the rate of change with time of the individual chemical species, shown as follows:

$$\text{RR} = \frac{dC}{dt} = \frac{dD}{dt} = -\frac{dA}{dt} = -\frac{dB}{dt} \quad (\text{Eq. 2.3})$$

A temperature-dependent rate constant can be expressed by using the Arrhenius equation:

$$k = A \cdot \exp\left(-\frac{E_a}{R_u T}\right) \quad (\text{Eq. 2.4})$$

Where A is referred to as the pre-exponential factor, or “A-factor”, E_a represents the activation energy, and R_u is the universal gas constant. Alternatively, a modified Arrhenius

expression is commonly utilized to describe the combustion in higher temperature systems, which is displayed as [19]:

$$k = A \cdot \left(\frac{T}{T_{ref}}\right)^n \cdot \exp\left(-\frac{E_a}{R_u T}\right) \quad (\text{Eq. 2.5})$$

Where $\left(\frac{T}{T_{ref}}\right)^n$ is an optional term to account for the observed behaviour over large temperature ranges. It is a dimensionless quantity and the value of T_{ref} is usually 1 K, so the term is oftentimes simplified as T^n .

In some conditions, the rate parameter consists of two parts when there are two different channels leading to the products [20]:

$$k = A_1 \cdot T^{n1} \cdot \exp\left(-\frac{E_{a1}}{R_u T}\right) + A_2 \cdot T^{n2} \cdot \exp\left(-\frac{E_{a2}}{R_u T}\right) \quad (\text{Eq. 2.6})$$

The rate constants can be measured by a variety of laboratory techniques or calculated theoretically. The experiments are usually conducted in a narrow range of temperature and pressure, while the practical environment of combustion is much wider. The Arrhenius expression attained from experimental conditions is usually applied to the entire temperature range. Take methane oxidation for instance, a laminar flame can start from room temperature and reach up to 2000 K [20]. By using this approach, some rate constants may be fitted quite easily even at high temperatures while others can lead to large errors. For each chemical reaction, the expressions of rate constant, also the values of the A-factor, n , and E_a are varied from different investigators.

2.1.3 Pressure-dependent reaction

Importantly, a reaction solely dependent on one reactant concentration is referred to as a first-order reaction. Practically, most simple chemical reactions are initiated by the collisions of two species, hence they are categorized as second-order reactions [21]. As stated in Section 2.1.2, the rate constant k can sometimes be dependent on the pressure, and the unimolecular/recombination reaction is one of these types. Unimolecular reactions occur when a single molecule reorganizes itself to create one or more products, which often appear to be a first-order reaction. It is crucial to define whether a combustion reaction is first or second-order, particularly when the decomposition of large species is involved [22]. Thus, a single rate constant expression under certain pressure and temperature conditions may not

be accurate. Lindemann et al. [23] suggested the use of separable models to characterize the entire process of the unimolecular reaction, and there are three regions in total:

- 1) High pressure limit: the reaction rate is independent of the pressure and characterised by the high-pressure limiting rate constant k_{∞} :

$$k_{\infty} = A_{\infty} T^{n_{\infty}} \exp\left(-\frac{E_{\infty}}{R_u T}\right) \quad (\text{Eq. 2.7})$$

- 2) Low pressure limit: the reaction rate is proportional to the pressure, with the low-pressure limiting rate constant k_0 :

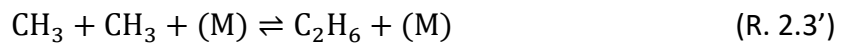
$$k_0 = A_0 T^{n_0} \exp\left(-\frac{E_0}{R_u T}\right) \quad (\text{Eq. 2.8})$$

Noticeably, reactions defined solely in terms of the low-pressure limiting rate constant are written in the Chemkin kinetic mechanism as:



- 3) Fall-off region: the transition from low pressure limit to high pressure limit.

In this case, the reaction in the Chemkin kinetic mechanism is written as:



Where the bracket around the M signifies that both the low- and high-pressure behaviour is accounted for in the overall rate constant expression. At low pressure conditions, a third-body collision, denoted by M, is required to activate the reaction process [24]. Several approaches can be used to estimate the rate constant at this transition region. The first proposed model is from Lindemann [23], and other investigators, such as the Troe method [25], can describe the behaviours of the transition more accurately. The rate constant k at any given pressure condition can be expressed as [20]:

$$k = k_{\infty} \frac{P_r}{1+P_r} F \quad (\text{Eq. 2.9})$$

Where P_r is the reduced pressure, calculated as:

$$P_r = \frac{k_0[\text{M}]}{k_{\infty}} \quad (\text{Eq. 2.10})$$

Where $[M]$ is the concentration of the mixture, and potentially includes the third body efficiencies. Additionally, the third body in some cases can be a specific species such as nitrogen, and then the concentration of $[N_2]$ replaces $[M]$ in the formula [24].

In the empirical fitting approach, the function F and other related constants are given as:

$$\log(F) = \frac{\log(F_c)}{1 + \left[\frac{\log(P_r) + c}{n - 0.14(\log(P_r) + c)} \right]^2} \quad (\text{Eq. 2.11})$$

$$c = -0.4 - 0.67 \log(F_c) \quad (\text{Eq. 2.12})$$

$$n = 0.75 - 1.27 \log(F_c) \quad (\text{Eq. 2.13})$$

$$F_c = (1 - a) \exp\left(-\frac{T}{T^{***}}\right) + a \exp\left(-\frac{T}{T^{**}}\right) + \exp\left(-\frac{T}{T}\right) \quad (\text{Eq. 2.14})$$

Therefore, the parameters of a , T , T^{***} , and T^{**} must be specified, although in ANSYS Chemkin Pro, the term T^{**} is not always used. In the Lindemann case, F is simplified as unity and its limitation is apparent compared to the Troe method. An example of the two fall-off curves of reaction 2.3 at 1000 K is shown in Figure 2.1.

The accurate representation of the fall-off region is of great significance to successfully simulate the combustion processes, especially in the high-pressure range, which is overall less well understood. More research is required both in the modelling and experiments, to accurately determine the rate constant of these pressure-dependent reactions.

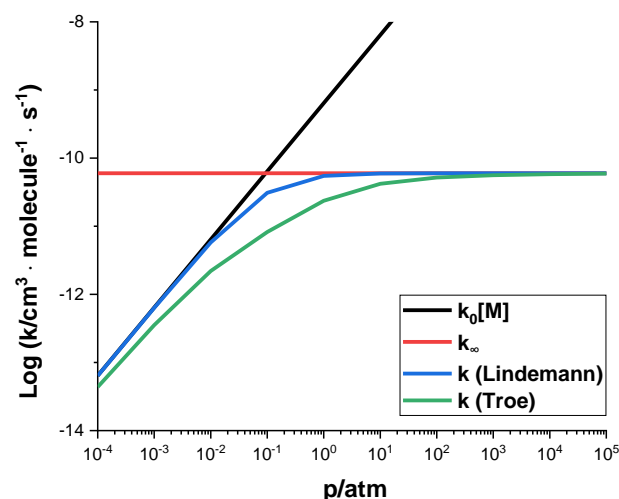
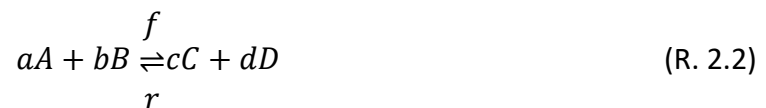


Figure 2.1 The pressure dependence of rate constant of $CH_3 + CH_3 + M \rightleftharpoons C_2H_6 + M$ at 1000 K.

2.1.4 Reverse reaction

All elementary chemical reactions are theoretically reversible [20], meaning that the reactants and products are constantly reacting and being formed with each other. Some reactions are practically irreversible, meaning that the products do not convert back to the reactants at any meaningful rate. Irreversible reactions are denoted by a one-way arrow (\rightarrow) and a bidirectional arrow (\rightleftharpoons) is used to describe a reversible reaction. Consider reaction 2.2 with directions:



The forward reaction rate constant is defined as k_f and the reversed rate constant is defined as k_r , and their relationship can be expressed by the equilibrium constant K_c , usually expressed in concentration unit:

$$K_c = \frac{k_f}{k_r} \quad (\text{Eq. 2.15})$$

In the gas-phase environment, the equilibrium constant K_p in pressure unit is related to the standard Gibbs energy ΔG_T° in the following equation [26]:

$$\Delta G_T^\circ = -R_u T \ln K_p \quad (\text{Eq. 2.16})$$

And the change of free energy is defined as:

$$\Delta G_T^\circ = \Delta H - T \cdot \Delta S \quad (\text{Eq. 2.17})$$

Where ΔH is the enthalpy change and ΔS is the entropy change in the system at standard states.

The relationship between K_p and K_c can be described as:

$$K_p = K_c \cdot (R'T)^{\Delta n} \quad (\text{Eq. 2.18})$$

Where Δn represents the differences in stoichiometric coefficients between the products and reactants. Take reaction 2.2 for instance, Δn is equal to $c + d - a - b$. Importantly, R_u in the reaction 2.16 is the gas constant in the unit of $\text{J} \cdot \text{K}^{-1} \cdot \text{mol}^{-1}$, while R' is the gas constant in the species concentration unit ($1.3626 \times 10^{-22} \text{ cm}^3 \cdot \text{atm} \cdot \text{molecule}^{-1} \cdot \text{K}^{-1}$) [26]. Given the rate constant of the forward reaction rate is known, the rate constant of the reversed reaction can

subsequently be calculated by using equation 2.15-2.18. Thermodynamic properties of the reactants and products are of great importance to the precise prediction of the reversed reaction rate.

2.2 Development of a kinetic mechanism

A kinetic mechanism contains all the elementary reactions required to complete a combustion process, together with the thermodynamic and transport properties of all the species. Mechanisms can be used in numerical applications such as ANSYS Chemkin Pro [27], Cantera [28], Cosilab [29], etc. to predict a certain combustion characteristic, and the simulated results are further validated by a wide range of experimental sources. Shock tubes, rapid compression machines (RCM), jet-stirred reactors, etc, are all common practical tools utilized to perform laboratory measurements. In general, a quality model is dependent on the level of completeness of all the relevant reactions, and the accuracy of all the rate parameters.

A long history can be traced back regarding the advances of kinetic models, from small species (e.g., H₂, CH₄) to larger and more complex components (e.g., jet fuels). GRI-Mech is one of the most comprehensive mechanisms that provides fundamental knowledge of methane combustion including the production of NO, and the current version GRI-Mech 3.0 [30] is validated against a considerably large range of targets. Over the years, more detailed mechanisms of various molecules have been built by different research groups, such as AramcoMech [31], San Diego [32], JetSurf [33], ReSpecTh [34], etc. Each modelling group have their respective interests in fuels and species, while the core chemistry of C0-C4 is quite similar, although users commonly apply different rate constants to the same reaction. Additionally, models of large hydrocarbons are developed on the base of the C0-C4 mechanism.

Elementary reaction data of important small species has been reviewed in detail by many researchers [35–38], and the rate constants are constantly being studied through either measurements or theoretical calculations. Also, the NIST Chemical Kinetics Database [39] is an important source to check any up-to-date sources of basic kinetics.

2.2.1 H₂ and CO oxidation

In addition to being an important fuel, hydrogen and carbon monoxide are also the primary components of syngas. The combustion of H₂ and CO is fundamental to the chemical kinetics of all hydrocarbon fuels, and these two systems are discussed separately.

The oxidation of H₂ requires around 30 elementary reactions to describe its process [40]. After the initiation process, the oxidation is mainly controlled by the competition between chain branching (R. 2.4) and chain propagating (R. 2.5) [40], which can be shown as:



The H₂ system is closely connected to the explosion boundary, and the explosion limit in the space of temperature and pressure is shown in Figure 2.2, along with the relationship of the rate constants between reaction 2.4 and 2.5 at the second limit. In the range of 0.01-0.05 atm, the chain branching rate is massively fast compared to reaction 2.5 and the explosion occurs [18]. When the pressure continues to go higher, reaction 2.5 starts to show more influence and HO₂ is consequently dominating in the intermediate pressure regions. Liang and Law [41] explained that the nonlinear reaction HO₂ + HO₂ ⇌ H₂O₂ + O₂ significantly reduces the impact of HO₂, hence the produced H₂O₂ becomes the most important species at the third explosion limit. Furthermore, hydrogen peroxide will decompose, and this is given as:



Sufficient attempts to optimize the hydrogen mechanism can be found in the literature. Burke et al. [42] updated the kinetic model to improve the differences, particularly at high pressures and suggested the inclusion of the reaction H + HO₂ ⇌ H₂O + O, and later some of the reactions in Burke et al. [42] were updated by Hashemi et al. [43] based on their measurements of flow reactor. Keromnes et al. [44] provided an experimental and modelling study of H₂ and syngas over a wide range of conditions, and H₂ + HO₂ ⇌ H + H₂O₂ and reaction 2.6 are found to be crucial around the intermediate temperature and high-pressure regions. Also, several key reactions such as reaction 2.5 and 2.6 are adjusted. As commented by Curran [40], these studies [42–44] are examples of the manual optimization of the rate constants

through direct or indirect experimental investigations, and most research groups have developed either existing or new mechanisms in a similar by-hand manner. Depending on the individual species system, mathematical or non-mathematical approaches are developed among investigators, but it is preferable to optimize based on the measurements if applicable.

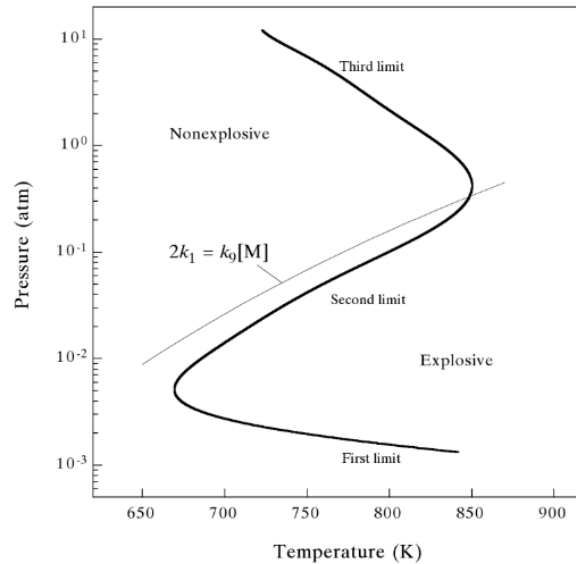


Figure 2.2 Limit of the explosion of a stoichiometric H_2/O_2 mixture [18]: k_1 is the rate constant of reaction 2.4 and k_9 denotes the rate constant of reaction 2.5.

It is possible to form carbon dioxide through the direct reaction between carbon monoxide and oxygen, although this flame is difficult to ignite due to a high activation energy of reaction 2.7:



However, in the presence of even a tiny amount of hydrogen, OH can be formed through several channels, hence the dominant pathway to produce CO_2 becomes [18]:



This reaction produces an H atom, which strengthens the chain branching of H_2 combustion and further enhances the CO combustion.

At higher pressure, another route can also form carbon dioxide:



Syngas has been increasingly attracting interest in recent years, and some mechanisms containing both H_2 and CO have been published and modified. In addition, with the

development of detailed hydrocarbon modelling, reaction 2.4 and reaction 2.8 are generally considered the most essential reactions in a combustion process [18].

2.2.2 Methane

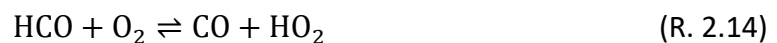
Methane is the simplest form of hydrocarbon. The initiation of oxidation begins with H abstraction and a methyl radical is then produced, and this can be achieved by a variety of small species such as oxygen. At high temperature conditions, the decomposition of methane is more involved in the CH₃ formation route:



The reaction 2.10 is quite slow and the produced methyl radical is more active. Its subsequent interactions with small species are faster and promotes propagation [19]. The reaction between CH₃ and oxygen can go through two routes:



The competition between reaction 2.12a and reaction 2.12b heavily influences the CH₄ ignition [18]. When the ignition is near, the reaction 2.12a becomes more important. The produced CH₃O is quite active and can convert to formaldehyde (CH₂O) primarily through its unimolecular reaction. Consequently, CH₂O can create a highly active formyl radical HCO through the reactions with OH, H, etc., and HCO can be transformed into CO in the following reactions:



The final product CO₂ is converted via CO through multiple channels as explained in Section 2.2.1, and the other H₂O is formed by the oxidized hydrogen atoms [18]. Through this simplified sequence of reactions (R. 2.10-R. 2.14), the combustion process of methane displays a rather hierarchical manner, which is worthy of note for the studies of larger hydrocarbons. Alternatively, methyl radicals can self-react to produce ethane (R. 2.3) or C₂H₅, and these species will go through the ignition themselves.

As Curran [40] commented, the combustion process of CH₄ requires roughly 30 species and 200 elementary reactions. Besides GRI-Mech 3.0, many kinetic mechanisms have been developed and tested against many sets of experimental data, and a compilation of the modelling progress over the past twenty years is available on the ReSpecTh website [34].

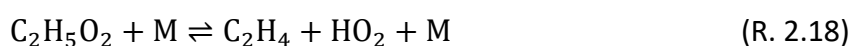
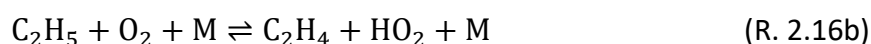
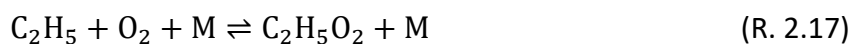
2.2.3 C2 hydrocarbons

Important C2 hydrocarbons ethane, ethylene, and acetylene are discussed in this section. Both C₂H₄ and C₂H₂ are not only fuels but major intermediate species of the combustion of larger hydrocarbons. Similarly, it begins with the formation of ethyl radical by H abstraction from ethane, commonly H, O, or OH. C₂H₅ is quite unstable and can either react with the H atom and oxygen or decompose itself [18]:



Besides ethylene, the reaction between ethyl radicals and oxygen can also lead to the production of acetaldehyde, which is an important species in lower temperature combustion. Subsequently, through H abstraction, the CH₃CO radical is formed and further decomposed to the methyl radical and carbon monoxide.

The system of ethyl and oxygen is the base of ethane oxidation at low temperatures and contributes greatly to the general understanding of hydrocarbon combustion. Substantial efforts from both experimental and computational methods have been made to provide accurate representations of all the channels in this mechanism. One of the discussions focuses on the temperature and pressure dependence of the main channels and their correlated competition. Provided in the pressure-dependent forms, the reactions are as follows:



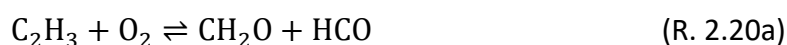
Wagner et al. [45] measured the overall rate constants of the system at multiple temperature conditions from 0.9 torr to 16 torr, also they developed models by using the RRKM theory to explain the experimental observations. Carstensen et al. [46] utilized *ab initio*

calculations to generate both the temperature and pressure dependent parameters of all the related reactions. Their results show that at atmospheric pressure, the rate constant expressions are provided as temperature dependent, and the pressure-dependent expressions are presented from 0.0001 atm to 100 atm with either oxygen or helium as the collider. More recently, Fernandes et al. [47] provided an experimental and kinetic modelling study of reaction 2.17. The experiments were performed at room temperature and between 100 bar and 1000 bar, and the fall-off behaviours can be observed. In the detailed review of Baulch et al. [38], the authors summarized that at low temperature conditions ($< \sim 575$ K), the temperature and pressure dependency of the system is expected and reaction 2.17 is the dominating route. When the temperature goes higher (> 750 K), the pressure dependency becomes insignificant and the reaction 2.16a accounts for the main activities of the mechanism. Furthermore, the knowledge of the reverse channel of $C_2H_5O_2$ is less known. Miller and Klippenstein [48] calculated a series of rate equations for reaction 2.16b-2.18, although both the authors and the review of Baulch et al. [38] considered the rate constant expressions for reaction 2.18 to be less reliable. In addition, to improve the understanding of the general ethyl and O_2 system, experimental work at conditions of $T > 1000$ K is recommended.

The combustion of ethylene and acetylene does not necessarily require H abstraction to start the process. The double bond of C_2H_4 is sensitive to the interactions of O and OH, and the reaction with the O atom is part of the chain-branching process that has multiple products. One example is shown below [18]:



In addition, the oxidation is considerably accelerated due to the produced active radicals. In the fuel rich cases or at high temperature conditions, the reactions of H abstraction become much more significant, leading to the formation of vinyl radicals (C_2H_3). Vinyl radical is also quite active, and one of the prominent reactions is its interaction with oxygen. A set of different products can be formed, and two examples are shown as follows:



From reaction 2.20b, the CH_2CHO radicals play an important role in the combustion of ethylene. At high temperatures, it decomposes rapidly to smaller radicals and around low temperatures, its reaction with oxygen is competing with the unimolecular decomposition route [49].

Another important channel for the vinyl radicals is the production of acetylene:



Reactions between acetylene and small radicals are quite complicated, and like ethylene, this system is integral to the core high temperature mechanisms for larger molecule modelling. Similar to ethylene, H abstraction is not always relevant in the oxidation of C_2H_2 . In the initiation stage, reactions between C_2H_2 and O, OH, and oxygen are some of the major channels, and each class can also lead to multiple product routes. A few examples are displayed:



Detailed studies have been discussed extensively regarding each reaction group and their respective branching ratio of each potential product route at various temperature conditions. Metcalfe et al. [49] provided a comprehensive modelling work of C1-C2 hydrocarbons together with oxygenated fuels. More recently, Slavinskaya et al. [50] investigated the oxidation and pyrolysis of acetylene, and their results indicate that reaction 2.24a, 2.25b, and 2.27 are the prominent influences of the consumption of C_2H_2 at temperature conditions lower than 1300 K. At $T > 1300$ K, reaction 2.25b continues to be a major factor, along with

the reaction 2.24b, 2.25a, 2.26, and a few other routes. Despite the considerable development over the years, numerous problems remain to be addressed. For instance, simulations from several frequently-utilized mechanisms have proved to be quite deficient against one recent ignition dataset of C₂H₂/air mixtures at 10 bar, as commented by Curran [40]. It is suggested that the route of C₂H₂ + HO₂ may be crucial because of the relatively high amounts of HO₂ present in the high-pressure environments.

Ketene is a significant intermediate species, and the ketyenyl radicals HCCO can be directly formed from acetylene oxidation, and it also exists in ethylene combustion. As it is highly active, the HCCO can react with oxygen or H atoms, and some of the key reactions are identified as:



Furthermore, some of the intermediate products such as acetaldehyde (CH₃CHO) and its subsequent radicals formed during the oxidation of C₂ hydrocarbons are important species at lower temperature combustion, and kinetic modelling in terms of these sub-mechanisms has also been researched [49].

2.2.4 Autoignition and larger hydrocarbons

Higher hydrocarbons are usually referred to the components heavier than n-butane. Besides the high temperature combustion, larger hydrocarbons also experience chemistry sequence at low and intermediate temperature regions, which are particularly related to the ignition in practice. For a combustion system, autoignition is defined as the spontaneous ignition of a fuel-oxidizer mixture when no external sources are applied, and a rapid ignition and complete reaction are ideal for the improvement of fuel efficiency [9].

Consider the simulated ignition delay time of n-pentane/air oxidation at 20 atm under three equivalence ratio conditions, as shown in Figure 2.3 [40]. Three discrete temperature regions can be observed. Take the stoichiometric condition for instance, the regions are low (T < 750 K), intermediate (750-1000 K), and high temperature (T > 1000 K). Importantly, the boundary between each temperature region is distinctive and varies with the oxidation of different types of molecules and mixed fuels, and also the general conditions of the system.

During the transition between the low and intermediate regions, a negative temperature coefficient (NTC) regime is formed, in which the general rate of reaction decreases with the increase of the temperature [21]. This phenomenon strongly affects a series of important intermediate species formation and autoignition behaviour.

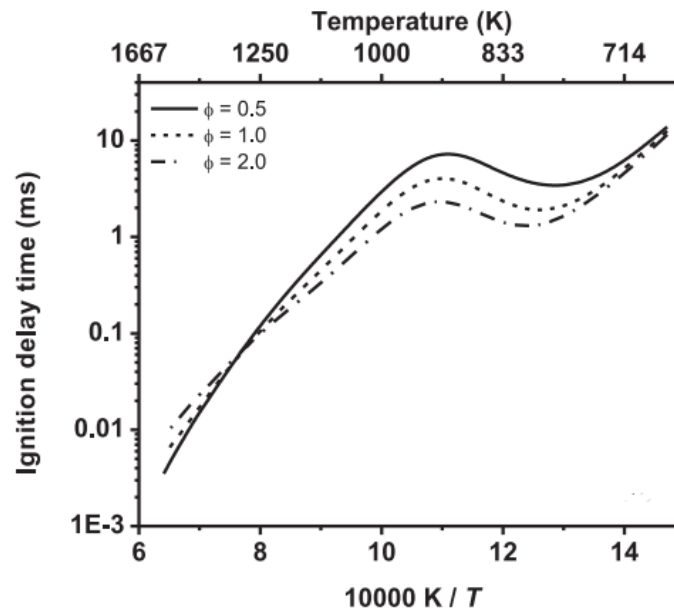
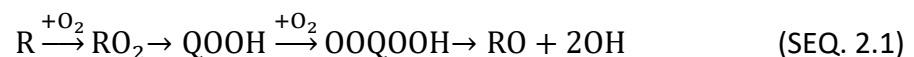


Figure 2.3 Ignition delay time of n-pentane/air mixtures at 20 atm [40].

An example of the schematic pathways of a normal alkane is shown in Figure 2.4. The initial combustion step of a hydrocarbon mainly involves unimolecular decomposition and H abstraction. The targeted fuel is generally termed as RH and the subsequent fuel radical is denoted by the term R, where R will continue to react with oxygen which leads to further processes. The chemistry at low temperatures is quite complicated as the equilibrium of $R + O_2 \rightleftharpoons RO_2$ strongly favours the RO_2 species, and thus addition of oxygen to alkyl radicals is dominating, and isomerization of alkyl peroxy radicals (RO_2) and hydroperoxyl alkyl peroxy radicals ($OOQOOH$) is more favoured. The general chain branching can be described in the following sequence [40]:



When the mixture heats up more and approaches the intermediate region, although decomposition routes of $QOOH$ and $OOQOOH$ become faster, the equilibrium of $R + O_2 \rightleftharpoons RO_2$ shifts to the left and therefore reduces their influence. The impact of alternative decomposition routes through R and RO_2 then becomes more significant, for example, the

concerted elimination ($\text{RO}_2 \rightarrow \text{olefin} + \text{HO}_2$). There is also a build-up of HO_2 which leads to the overall decrease of reactivity, as the formed radical HO_2 is much less reactive than OH , hence explaining the emergence of the NTC region. The HO_2 can react with the fuel leading to H_2O_2 :



This leads to an accumulation of H_2O_2 , which can decompose to two OH radicals (R. 2.6), but at intermediate temperature this is relatively slow, and only becomes important at higher temperature. At high temperatures, the species are decomposed quickly, which eventually results in the termination of chain branching. Final products are produced, for instance, CO and stable small hydrocarbons [18, 21], and kinetic models of H_2/CO and C1-C2 hydrocarbons discussed in previous sections are the essence of the combustion in this temperature region.

Due to the complexity of the detailed chemical kinetics of hydrocarbon combustion and the number of intermediate species involved, accurate and comprehensive reaction mechanisms for many larger hydrocarbons remain to be a challenge. Among all the hydrocarbons, alkanes particularly straight chain, are the simplest and consequently the most studied types. Considerable works have been contributed by various research groups. For instance, the mechanism study of iso-octane and n-heptane from the Curran research group [51, 52] is an important source for many modelling investigators, and a total of 25 reaction classes were developed and individual rate rules at both high and low temperatures were estimated. Westbrook [53] provided a detailed discussion of the kinetic modelling of hydrocarbons under practical environments. More recently, Bugler et al. [54, 55] investigated the ignition of three pentane isomers in shock tubes and rapid compression machines. The kinetics was examined at low temperature chemistry together with the thermochemical properties, and the updated model includes 31 reaction classes. In addition, some recent modelling studies proposed an alternative isomerization route from $\text{OOQOOH} \rightarrow \text{P(OOH)}_2$ that is related to the chemistry of low temperatures [56, 57].

For a targeted hydrocarbon, the determination of the detailed rate rules adopted for each reaction class at low temperature combustion is a great obstacle. Apart from larger normal alkanes, some types of molecules have been even less researched such as mono- and di- methyl branched alkanes with a carbon number of more than eight, and these species commonly lack direct measurements and theoretical calculations are also quite limited. Thus, rate constant results from butane and pentane isomers are oftentimes utilized as prototypes,

or if the mechanism of a larger fuel is available, that is close in carbon number to the interested hydrocarbon, it can also work as the reference. For instance, the iso-octane mechanism developed by Curran et al. [52] was built on their previous n-heptane modelling. Since the structures of these two fuels are quite different, certain rules of optimization must be implemented to improve the overall model quality. In conclusion, the basic understanding of the autoignition behaviours of alkanes is of great significance, particularly at low and intermediate temperature regimes, and it will further upgrade the model accuracy of other types of hydrocarbons.

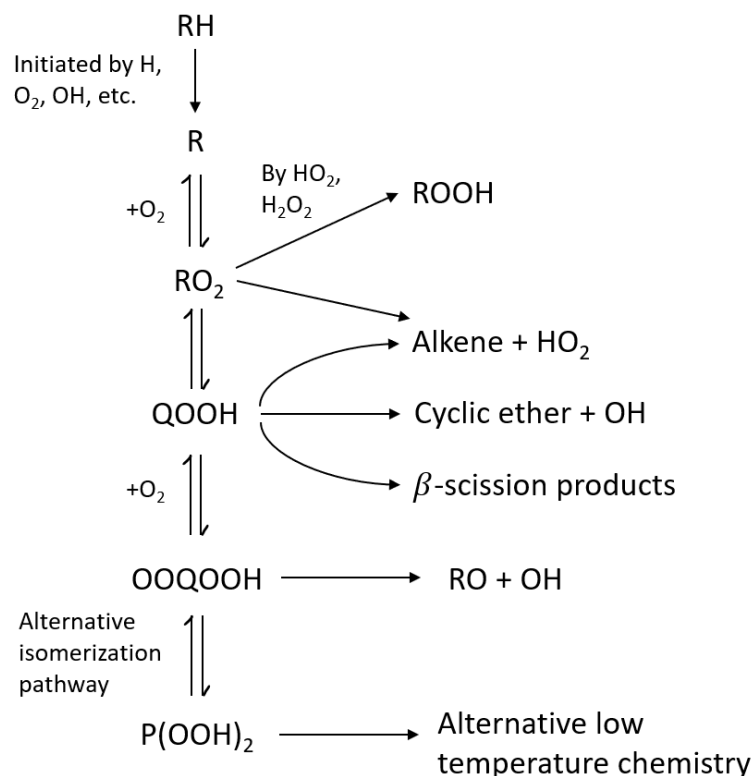


Figure 2.4 A schematic of low temperature chain branching of an alkane.

2.2.5 NO_x

Nitrogen oxides (NO_x) can be formed in the combustion process, which is one of the main environmental concerns derived from fossil fuel oxidation. It mainly consists of nitric oxide (NO) and small amounts of NO₂ and N₂O, and three channels are responsible for its production: thermal NO, prompt NO, and fuel NO. Noticeably, the route of fuel NO indicates the conversion of fuel to N atom through intermediate species such as HCN and ammonia, and eventually produces NO_x [21]. As this usually occurs fuel with high contents of nitrogen, for

example the oxidation of coal, hence it is not relevant in the context of kerosene and surrogates and not discussed further.

The thermal NO only becomes significant in the high temperature region which is commonly regarded as above 1800 K, and sufficient oxygen is required in the environment [18]. The initiation is described as:



Subsequently, the produced N atom quickly reacts with oxygen and OH:

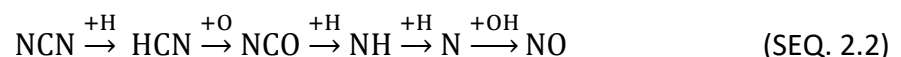


The accuracy of reaction 2.31 is essential and its reverse reaction rate has been measured over a wide range of conditions. Glarborg et al. [58] provided a detailed modelling study of nitrogen combustion, and the updated rate constant of the reverse of reaction 2.31 is obtained from a recent reactor experiment by Abian et al. [59].

Prompt NO is suggested to be the dominant route of turbulent hydrocarbon diffusion flames [60]. The interaction between nitrogen and hydrocarbon radicals commences the process:



Other hydrocarbon radicals can also react with N_2 , while the innate high reaction barriers prevent radicals such as methyl or C_2O from making impactful contributions to this NO system [58]. One of the more competitive routes is the reaction between C and N_2 , and NCN is also one of its products. NCN can eventually convert to NO after going through a series of steps, and its interaction with the H atom is advised to be the most important followed by the reaction with the O atom. The formation sequence can be generally outlined as:



From the modelling point of view, the precise rate parameter of reaction 2.34 is crucial and has been studied both experimentally and theoretically, although the prediction of the CH concentration remains one of the main sources of uncertainty. Also, the discussions of the rate constants of NCN reactions are still ongoing, especially the interactions between NCN

and H atom. In addition, opinions of the NCN thermochemical properties are quite diverse. The difference in the recommended value of the NCN heat formation between authors is over $3 \text{ kcal} \cdot \text{mol}^{-1}$ [58].

The mechanism of the N_2O channel is relatively well understood and is suggested to be more involved in the NO formation at high pressures and lean conditions, which is expressed as:



Alternatively, the reactions between N_2O and the reactive radicals (H, O) can produce nitrogen that competes with the reaction 2.36-2.37. Apart from N_2O , NNH is a minor channel suggested by some investigators. Klippenstein et al. [61] reviewed the previous work regarding the NNH mechanisms and evaluated the heat of formation of NNH. Furthermore, several systems such as reactions between NNH and the O atom were calculated using transition state theory. In the current knowledge, the scale of the impacts on the general NO production through NNH is quite unclear and experimental evidence to support modelling results is greatly insufficient.

2.2.6 Ammonia/methane

Ammonia (NH_3) is a key species in the volatile fuel and nitrogen combustion, and in recent years it has been increasingly attracting the attention as a potential carbon-neutral fuel, either directly or as a hydrogen carrier. Firstly, the oxidation of pure ammonia is briefly introduced. H abstraction is the major channel to consume NH_3 , usually achieved by the reactive radicals (O, H, OH) that subsequently forms the NH_2 radicals. NH_2 can further produce NH radicals through the H abstraction, and two main consumption routes of NH are either reacting with NO or reacting with oxygen to further form NO:



Alternatively, NH_2 may react with even tiny amounts of NO , which have two product routes [58]:



The branching ratio of these two channels largely influences the entire system, as reaction 2.39a indicates chain branching while the other route is terminating. Under fuel lean conditions, NO can be converted to NO_2 which can further interact with the NH_2 radicals. Other competitive channels of NH_2 consumption include the reactions between the reactive radicals (H , O) and NH_2 , and one of the product channels is prominent for the formation of NO at high temperatures:



The main challenges of pure ammonia for the application of internal combustion engines are its low flammability and high ignition temperature [62], and the common solution is to blend ammonia with other fuels such as hydrogen, methane, gasoline, etc. From the report of Erdemir and Dincer [62], the power output of a generator engine was examined on eight types of fuel blends. Their results show the same general trend for all mixtures, that the decrease of the ammonia ratio helps to increase the power output. As this approach may enhance the oxidation process, the addition of the other fuel leads to a growth of CO_2 and NO_x emissions. Figure 2.5 shows an example of the NO_x emissions for different types of fuel mixtures, with the ammonia ratio ranging from 0.2 to 0.8. In general, the decrease in the ammonia proportion leads to an increase in NO emissions. Take the blend of NH_3/H_2 for instance, the emission of NO with the least NH_3 is about 3.5 times greater than the NO emission with the most NH_3 . In short, there are significant problems with the NH_3 combustion in engine conditions, more investigations are required to tackle the issues.

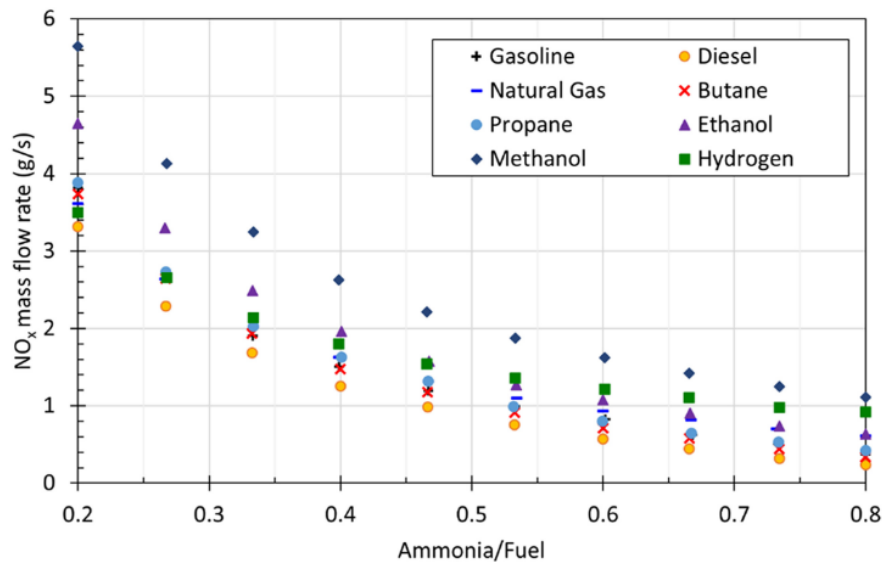


Figure 2.5 NO_x emissions of different types of ammonia blend [62].

In this project, the mixture of NH₃ doped with methane is investigated experimentally, hence the chemical kinetics of this blend is discussed. New reaction pathways will be created by adding another hydrocarbon, and the mole ratio *MR* of ammonia/methane can also influence the concentration of the intermediate and major species. Both methane and especially methyl radicals can react with ammonia radicals. These mechanisms are relatively less known and uncertainties in the models are expected to some extent. An example of the reactions that have been discussed in the literature is the following [58, 63]:



The chemistry of ammonia with other hydrocarbons is a relatively new research topic, nevertheless, a reasonable number of records of both experimental and modelling regarding NH₃/CH₄ can already be found in the literature in recent years. Partly due to the complexity of the mechanism, the ignition of the mixture particularly at elevated pressures remains to be better understood. Over a decade ago, Tian et al. [63] conducted an experimental and modelling study of five premixed flames of different NH₃/CH₄ mole ratios at 4 kPa and stoichiometric conditions. More recently, Okafor et al. [64] measured the laminar flame speed of NH₃/CH₄/air flames at atmospheric pressure and room temperature, and the mole percentage of ammonia varies from 0 to 0.3. Their results indicate that from the sub-mechanism of ammonia, reaction 2.39a, 2.40, and HNO + H ⇌ NO + H₂ are the most

influential reactions on the concentration of the H atom and the OH radical in the mixture flames. More efforts regarding the ignition properties have been made. Shu et al. [65] measured the autoignition of the ammonia/methane mixtures with the use of RCM at 20 bar and 40 bar, and an example of the reaction pathway from their modelling work is displayed in Figure 2.6.

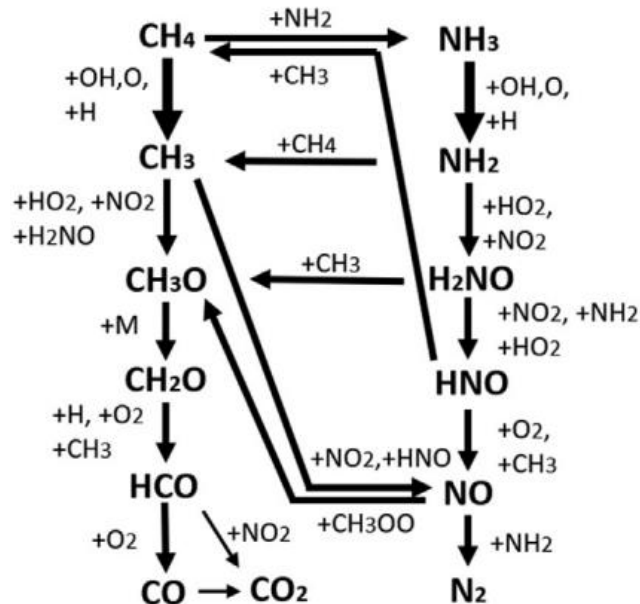


Figure 2.6 Reaction pathway of a stoichiometric 80% NH₃/20% CH₄ mixture at 1000 K and 40 bar [65].

2.3 ANSYS Chemkin Pro

Computational modelling is essential to characterise new fuels before practical application, and significant financial benefits are served if a combustion program including elementary chemistry is effectively developed [9]. The ANSYS Chemkin Pro [27] is a software used to solve complicated chemical kinetics. Created by Kee et al. [66] at the Sandia National Laboratories, the Chemkin Code can model a variety of idealised chemical systems. These include zero-dimensional closed homogeneous reactors used to predict ignition delay time or plug-flow reactor data, zero-dimensional homogeneous reactors with inflow and outflow used to predict jet-stirred reactor data, and one-dimensional models to simulate burning velocity or flame species profile data.

Before the simulation of a given project, a fundamental input that is referred to as the reaction mechanism is required. The package usually consists of a kinetic mechanism file and a thermodynamic data file. In the one-dimensional flame simulation, additional transport

data is needed. The kinetic mechanism file describes all the species involved in oxidation and their related elementary reactions defined by the rate constants. The thermodynamic data file includes all the thermochemical properties of the species in the kinetic file. Transport data is used for the evaluation of the viscosities, thermal conductivities, diffusion coefficients, and thermal diffusion coefficients for the software [24]. For each model, the initial conditions are usually based on laboratory studies and the simulated results should later be validated against the experimental data. In this project, modelling of zero-dimensional closed homogeneous reactor systems and one-dimensional flame systems will be explored, and the example simulation shown in the following sections is based on the tutorial projects from Chemkin.

2.3.1 Zero-dimensional closed homogeneous reactor

As a vital characteristic of flame propagation, autoignition can be influenced by many factors and chemical kinetics plays a key part in it. There are several ways to interpret the ignition delay time both experimentally and computationally, and the results may be significantly different due to the source of the criteria. From the perspective of the model or the laboratory environment, it can be referred to as the time at which the maximum concentration of a specific species is reached, or the time at which the maximum rate of temperature increase takes place [21]. For many practical devices, it is defined as the time interval between the injection of mixtures and the start of the flame [67].

The closed homogeneous reactor is a reasonable representation of the shock tube environment for the study of autoignition, and the necessary inputs for this model include the initial concentration of the fuels and oxidizers, temperature, and pressure. Also, Chemkin allows users to select definitions of the ignition delay time, and it can be determined by either the temperature profile or the concentration of a certain species.

An example of propane autoignition at atmospheric pressure and 1200 K is shown in Figure 2.7. The results of ignition delay time derived from either temperature or OH mole fraction are quite similar. Noticeably, the profile of the OH mole fraction has a small peak at the beginning of the ignition stage, and the second peak is the correct ignition delay time. In this project, the ignition is defined to be the time when the maximum OH mole fraction is reached.

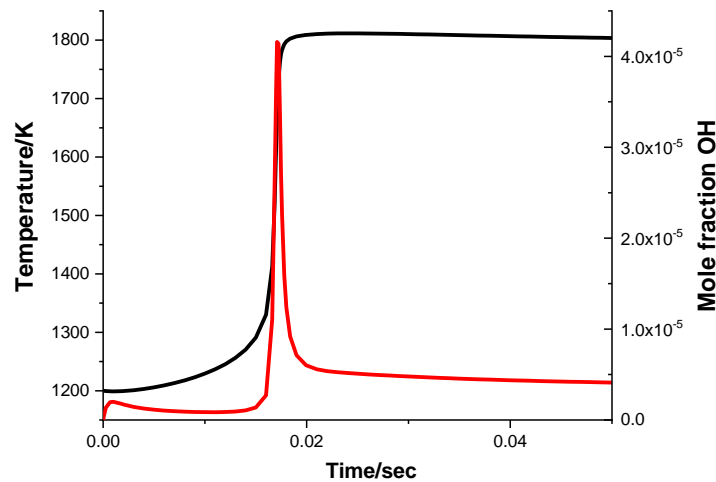


Figure 2.7 An example of the simulated ignition delay time: the black line is the temperature profile, and the red line is the OH profile.

2.3.2 Zero-dimensional homogeneous reactors with inflow and outflow

This computational approach is based on the jet-stirred reactor (JSR) experiments, in which a steady flow of fuel and oxidizer is introduced into the thermally insulated reactor at high velocity through narrow nozzles [68]. These result in a mixing rate that can be considered infinitely fast, and the system can be defined by the chemical reactions. A schematic illustration of the system is shown in Figure 2.8, where \dot{m} is the mass flow rate through the reactor, Y_k is the mass fraction of the k^{th} species, τ is the residence time which relates to the mass flow rate and the reactor volume, and h_k is the specific enthalpy of the k^{th} species. In addition, the superscript (*) denotes the inlet conditions.

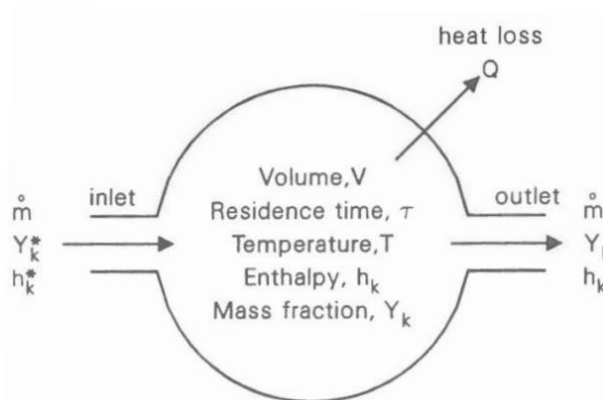


Figure 2.8 Schematic illustration of a jet-stirred reactor [68].

The solution computes the steady-state concentration of each species and the temperature of the mixture. The species concentrations are important to identify and

quantify the major intermediate species and oxidation products, and the results can be utilized to assess the fuel reactivity and determine the potential pathways in the combustion process [9].

2.3.3 One-dimensional laminar flame

This model is useful for both burner-stabilized flame simulations to model flame species profile data, or freely propagating adiabatic flames to model laminar flame speed (burning velocity) S_L . S_L is a fundamental parameter in the combustion of fuel-oxidizer mixtures and flammability limits and is particularly relevant to high temperature oxidation. It is defined as the velocity of the unburned gases moving through a plane combustion wave in the direction perpendicular to the wave surface [18]. Both experimental and modelling reviews suggest that many chemical and physical variables can cause impacts on the flame speed, and it is strongly determined by the temperature, pressure and mixture compositions [21]. Some key input data is required to define the model, including the mixture composition, inlet temperature and pressure, length of the computational domain, key intermediate species concentrations, etc. In the software, laminar flame speed is defined as the velocity at the starting point of the axial velocity profile, and an example of the propane/air mixtures is shown in Figure 2.9 (a). Additionally, Chemkin can solve multiple initial conditions regarding temperature, pressure, or equivalence ratio in a single project, by either setting up a parameter study or using the feature of continuations.

The burner-stabilized flame is helpful to simulate species profiles as a function of the distance above the burner surface. Apart from the initial mixture concentrations and pressure, the inlet mass flow rate must be known. The outcome of this model is largely dependent on the temperature profile, and users can normally provide it as an additional model input through experimental measurements. It could be calculated from the energy conservation equations, but this is not recommended as it would be affected by the heat loss from the flame to the burner and surroundings which is usually unknown. Figure 2.10 displays both the initial temperature input and the predicted mole fraction of OH and O from the hydrogen/oxygen oxidation at 0.4 atm. Any unevenness displayed from the temperature will directly be reflected in the results, as can be observed around the region of 3.75-6.25 cm. An accurate and smooth temperature profile is crucial to analyse the key species after oxidation,

hence it is strongly recommended to apply the temperature input obtained from measurements unless the heat losses of the flame are regarded as negligible [24].

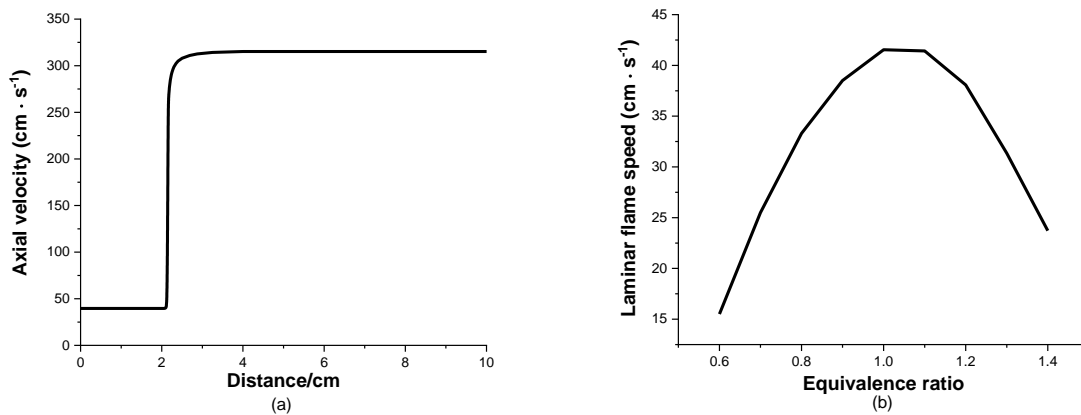


Figure 2.9 Combustion of propane/air at 1 atm and 300 K with the use of flame speed model: (a) Simulated flame speed at the stoichiometric condition; (b) Calculated laminar flame speed as a function of the equivalence ratio.

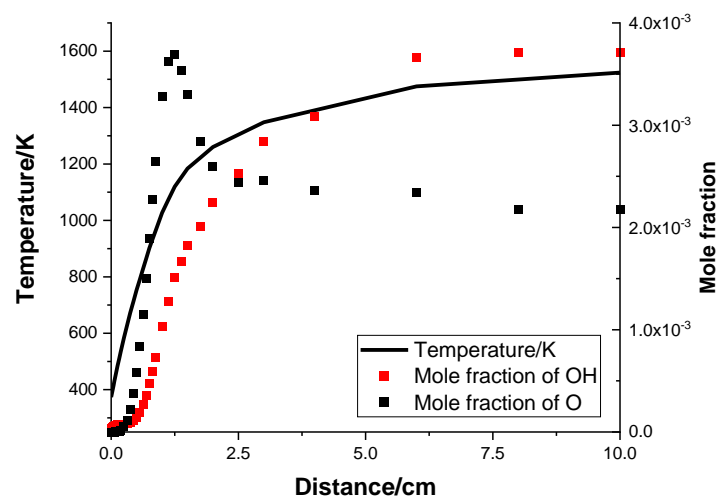


Figure 2.10 Temperature and mole fraction OH and O profiles of H_2/O_2 combustion at 0.4 atm with the use of burner-stabilized model.

The use of the one-dimensional laminar flame model can be prone to many problems, as both types of flames are significantly dependent on the initial conditions and solution procedures, and sometimes may even fail to converge to a meaningful solution. To produce a reasonable solution, users can choose to use less grid points by either reducing the number of grid points or increasing the values of curvature or gradient. Furthermore, the method of continuations is a convenient feature that uses the result calculated from the previous

solution as a starting point to calculate the result for the current condition, and several parameters can be specified depending on the desired outcome [24].

2.4 Proposed surrogates of real fuels

Surrogate components are commonly formulated based on specific criteria of the targeted fuels, and the kinetic mechanisms of these selected components are subsequently developed and validated with experimental data in a wide range of conditions. Ideally, each major molecular class of real fuels should have at least one representative fuel. While only a handful of larger species have been studied extensively, the assembly of mechanisms with different reference compounds and the subsequent model validations are the main obstacle. In addition, the size of the surrogate mechanism often makes the computational process quite time-consuming.

2.4.1 Formation of surrogate

Either kerosene-based jet fuels or alternative fuels are a large mixture of hundreds of hydrocarbons, hence it is extremely difficult to conduct investigations without any simplifications. The widely prevalent solution is the use of a surrogate. It usually consists of several components that can replicate certain combustion characteristics of the targeted fuel. Commonly, fuel surrogates are designed to correspond to physical properties or possess the same chemical-class composition and average molar mass [69], although specific criteria vary among different researchers. From the modelling perspective, candidates with available detailed mechanisms are more favoured, and for experimental investigations, fuel cost is another major factor that may influence the selection of the components [70]. To formulate a surrogate blend for either kerosene or alternative jet fuels, certain properties are initially used as the targets and in many cases are shown as follows [17, 71]:

- 1) Chemical composition.
- 2) Molecular weight (MW): related to diffusive properties of jet fuels.
- 3) H/C molar ratio: related to emulating adiabatic flame temperature.
- 4) Cetane number (CN): related to ignition quality, with the use of cetane reference fuel.
- 5) Threshold sooting index (TSI): related to the formation of soot.

Different investigators use various techniques to determine the components and proportions of surrogate mixtures. Surrogate blend optimization (SBO) is one common

computational tool to optimize the fuel blend based on defined targets [16]. It utilizes global minimization based on a genetic algorithm, then a local optimization will be followed based on Powell's conjugate direction method [24].

2.4.2 Kerosene

The use of surrogate or multiple surrogate components has been an extensively used method for jet fuel modelling, although how to determine the components and their proportion to accurately emulate the real fuel specifications remains a challenge. Researchers often associate the selected surrogates directly with certain properties of the targeted fuel as a starting point [72]. For kerosene modelling, many studies are based on the distribution of the chemical components [73], although some researchers argued that this approach may be impractical because the variations in aviation fuels are substantial. An example of the fraction differences of the aromatics content is illustrated in Figure 2.11, the percentages of aromatics in JP-8 can differ from 11.5% up to 23.5%, which in reality will cause different soot formation [13].

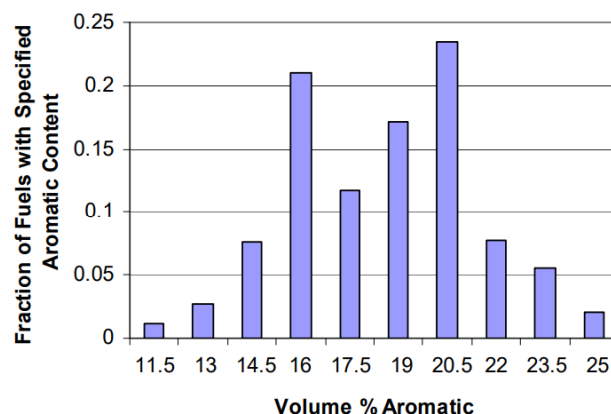


Figure 2.11 Aromatics volume of JP-8 [13].

Dagaut et al. [74, 75] built one of the first n-decane mechanisms and the model can generally reproduce the experimental data of n-decane and kerosene combustion from the JSR. Experiments by Doute et al. [76] with a flat-flame burner later found that the sole n-decane model fails to predict the aromatics concentration and hence a binary- or trinary-component surrogate is suggested to match more of the physical properties of the fuels. Several efforts have been made by adding an aromatic along with n-decane to form a surrogate model that can be evaluated against the premixed flame or counter flow flame experiments [77–79], and the measured results of species concentration show that

components, for instance, toluene, 1,2,4-trimethylbenzene, or propylbenzene can be regarded as an aromatic representative. Despite the efforts, more refined mechanisms were in demand to better capture the behaviour of the non-alkane part in kerosene. As the studies advanced, investigators began to include the class of cycloalkanes in the surrogate. Violi et al. [70] showed that the hydrocarbon class of Jet A contains about 20% of cycloalkanes and suggested including 10 mol% methylcyclohexane as a new reference surrogate for JP-8. Dagaut [80] optimised the cyclohexane and n-propylcyclohexane in a detailed kerosene mechanism, and the simulated species profiles produce a reasonable agreement with the experiments of kerosene conducted in JSR. Dooley et al. [17] outlined a detailed mechanism by incorporating three individual kinetic mechanisms and the surrogate includes 42.67 mol% n-decane, 33.02 mol% iso-octane, and 24.31 mol% toluene, which can be referred to as the 1st generation. Model data is validated against the results from various laboratory tools through a range of temperatures, and an optimal model containing n-dodecane, 1,3,5-trimethylbenzene, and n-propylcyclohexane, referred to as the 2nd generation, was formed afterwards [71]. Malewicki et al. [81] revised the main species in the 2nd generation model and added a few sub-mechanisms to formulate an updated mechanism, and simulated results are validated against the experimental data of ignition delay time in a shock tube and the mole fraction profile in a flow reactor.

In recent years, more reference species are selected to characterize more molecular classes in the fuels. Kim et al. [82] investigated the surrogates for Jet A, IPK, S-8, and the blend of fuels and some physical properties such as density, viscosity, distillation curves and specific heat have been added in the target characteristics since their importance has been recognized [83], and the results are validated against the ignition delay time in a shock tube. Kathrotia et al. [84] provided a semi-detailed mechanism to represent a variety of fuels, and their suggested components for Jet A-1 are composed of 41.1 mol% n-decane, 24.1 mol% 2-methyldecane, 13.6 mol% n-propylcyclohexane, 18.4 mol% n-propylbenzene, and 2.7 mol% decalin. An improved representation of the main molecular classes is essential for the development of fuel surrogates, whilst this leads to a new challenge which is the model validation of individual components, especially for those less well-studied molecules with few experimental sources. From the modelling perspective, apart from the core chemistry of C0-C4, previously many mechanisms have usually contained only a few surrogate components

of their interested fuel, which largely limits the feasibility and makes further validations quite difficult. Investigators have made efforts to compile more detailed mechanisms including a group of larger species that is suitable for the simulation of multiple real fuels. Some surrogate studies [67, 82, 85] are examined by using the mechanisms from the Model Fuels Library, which is encrypted in the ANSYS software containing more than 65 fuel components [86]. Also, an experienced chemical kinetic lab, namely the CRECK Modelling Group, has been developing detailed and semi-detailed mechanisms of pyrolysis, and the oxidation of gases, liquids, and solids for many years. Kinetic packages regarding kerosene surrogates are also part of their research interests [87, 88].

2.4.3 Fischer-Tropsch fuels

Despite the significant compositional difference in fuels, the development of alternative fuels mechanism has been associated closely with the mechanisms of conventional jet fuels. Like kerosene, the chemical composition is a primary approach for developing a detailed alternative fuel mechanism.

S-8 is an F-T fuel derived from natural gas from Syntroleum, and it has been investigated extensively as an example of synthetic paraffinic kerosene. In the beginning, surrogates of F-T fuel were modelled using a mechanism designed explicitly for kerosene [89, 90]. Gokulakrishnan et al. [91] suggested a composition ranging from pure n-decane to a mixture of n-decane and iso-octane, to pure iso-octane. By comparing the experimental results of the ignition delay time, a mixture of approximately 20% n-decane and 80% iso-octane can capture the behaviour of S-8 fuels most reasonably. Also, it is observed that the proportion of iso-octane has little effect on the ignition delay time in the high temperature region. Naik et al. [16] formulated an assembled mechanism of 753 species and 4668 reactions for two surrogates containing iso-octane, n-decane, and n-dodecane, and the interested fuels are S-8 developed by Syntroleum and Shell GTL developed by Royal Dutch Shell plc. Modelling results of both single species and surrogate fuels are validated against published experimental data, which includes the ignition delay time behind a reflected shock, laminar flame speed, and the extinction strain rate from a counterflow flame system. Noticeably, this mechanism restricts the application to only above 1000 K because the engine condition mostly considers only the high temperature kinetics. Another mechanism under similar conditions has been proposed by NASA [92]. Dooley et al. [93] also investigated a simpler blend that consisted of

n-dodecane/iso-octane, with the kinetic mechanism being combined from previous investigations [17, 71, 94]. The formation of this surrogate is guided under specific criteria using the SBO method explained previously. The results are validated against the measurements of ignition delay time in stoichiometric mixtures at 20 atm behind a reflected shock, species concentration in a flow reactor, and extinction rate measured in a non-premixed flame. Noticeably, despite its dominant proportion in F-T fuels, mono- and di- branched alkanes are not employed in surrogate formation. This is majorly due to the concern of experimental cost and consequently the availability of the mechanism for relevant species.

Relatively less research has been carried out in coal-derived and non-petroleum feedstock fuels, and iso paraffin kerosene (IPK) produced by Sasol is one of the fuels that has been studied. Dooley et al. [95] utilized an assembled mechanism for Jet A and several F-T fuels and a four-component mixture for IPK is proposed. Computational results are validated against the experimental data on ignition delay time at 20 atm [96] and laminar flame speed at the condition of 400 K and atmospheric pressure [97]. Ahmed et al. [98] formed a kinetic mechanism of 6228 reactions involving 2006 species for a mixture of n-decane/iso-octane/propylbenzene, and the model is validated against the oxidation species in a JSR over a range of equivalence ratio at 10 atm. From their results, the authors commented that iso-octane is too branched for the iso-paraffin that exists in synthetic fuels. Hence, the candidates for instance methyl-decane are favoured and other work from Edwards et al. [13] suggested the same conclusion. In addition, Huber et al. [99] created a five-component surrogate for synthetic paraffin obtained from biomass, and the results are validated against experimental data on the distillation curve, which is a parameter related to the soot formation. Noticeably, some studies include a trace of aromatics and cyclo-alkane to form the F-T surrogate such as the study of a gas-to-liquid fuel by Dagaut et al. [75]. More recently, Kim and Violi [100] formed an upgraded version of the IPK surrogate by introducing 2,2,4,6,6-pentamethylheptane as a potential surrogate of the next generation fuels, to better represent the ignition quality over the usual iso-octane/iso-cetane.

Importantly, the mechanisms regarding either jet fuels or alternative aviation fuels usually contain thousands of species and reactions, hence they require significant time for the computational resources to handle and often cause numerical difficulties in the solution

process. To overcome this problem, reduced and skeletal mechanisms are necessary for the development of the mechanism and some research groups, such as CRECK modelling, provide these simplified versions. In addition, optimized methods for the jet fuel mechanisms are proposed by some investigators [101, 102].

2.4.4 Previous investigations on branched alkanes

Studies performed on branched alkanes are comparatively limited, in contrast to the model of straight-chain alkanes that has been developed for decades. Early research records have shown that iso-butane has been studied in shock tubes [96, 103]. Westbrook et al. [104] developed a kinetic mechanism for all nine isomers of n-heptane, and their simulated results of the ignition delay time were subsequently validated by experimental results from a rapid compression machine. For larger lightly branched hydrocarbons, Sarathy et al. [105] provided a comprehensive kinetic modelling study for the combustion of 2-methylalkanes from C7 to C20, which also included the kinetics of linear alkanes from C8 to C16. It can moderately predict both alkane classes for the ignition delay time and laminar flame speed, while the disagreement between the modelling and experiments implied improvements were required. A few branched alkanes mechanisms were further built based on this effort of Sarathy et al. [105]. Wang et al. [106] conducted an experimental and modelling study of autoignition for 3-methylheptane in both a shock tube and a rapid compression machine over a wide range of conditions. More recently, Wang et al. [57] discovered a third O₂ reaction path for a mixture of 2-methylhexane/oxygen/argon in a jet-stirred reactor at 1 atm and temperature between 530 K and 740 K.

Researchers also have paid close attention to dimethyl-type alkanes. Sarathy et al. [107] studied the characteristics of 3-methylheptane (3-MHP) and 2,5-dimethylhexane (2,5-DMX) in a counterflow diffusion flame. Liu et al. [108] measured the ignition temperature of a non-premixed flame for several isomers of octane and decane under atmospheric conditions, and the interested fuels include 3-MHP, 2,5-DMX, and 2,7-dimethyloctane (2,7-DMO). Their results indicated that by comparing the ignition temperature of both C8 and C10 isomers, the reactivity of the fuel decreases when the degree of chain branching increases. Similar conclusions were drawn from Li et al. [109] by measuring the ignition delay time of three branched alkanes in a shock tube and Ji et al. [110] by measuring the laminar flame speed of several octane isomers in a counterflow environment. Regarding the ignition delay time of

different hydrocarbons, at the condition of 20 atm, Wang et al. [106] compared their results of 3-MHP with previous experimental data of 2-methylheptane [105, 111] and n-octane [105]. In higher temperatures, the differences in the ignition between isomers are negligible, while in the low and NTC regions, the reactivities vary clearly among fuels. In addition, other investigators have observed indiscernible differences in the reactivity between larger normal alkanes at higher temperatures from both experimental and modelling predictions [112, 113].

Experimental validation is the main obstacle as the available records are quite scarce for branched alkanes, particularly for the carbon atom beyond eight. Besides the apparent lack of validation for the modelling, another inherent problem lies in the approach commonly utilized to compose the mechanism. It is typical to use reaction classes and rate rules that originated from investigations of smaller species or their more common isomers, particularly for the mechanisms of larger hydrocarbons. A few kinetic studies of 2-methylheptane can be traced back to the results of iso-octane and other normal alkanes for instance n-pentane. The former is too branched for mono-methyl alkanes while the latter has no presence of the tertiary C-H bond. Therefore, the plausibility of the rate rules adopted from other types of hydrocarbons may be compromised to some extent. At higher temperatures, this concern is less severe as the intermediates formed and the end products are similar among large hydrocarbons. Moreover, some researchers have suggested the effects of the position of the methyl substitution are significant. Selim et al. [114] investigated 2-methylheptane and 3-methylheptane in a burner-stabilized flat flame under stoichiometric and 20 torr conditions. Major differences were observed in the profile of the intermediate species between the two alkanes, while the comparison of the end-products of the two flames is in good agreement. In conclusion, experimental studies that are exclusively focused on larger branched alkanes are greatly recommended and consequently attribute to the improvements of the kinetic modelling.

2.4.5 Previous investigations on normal alkanes

Detailed chemical reaction mechanisms dedicated to the oxidation of normal paraffin have been developed over many years, from small alkanes to hydrocarbons of high molecular weight. N-decane and n-dodecane are the most common chemicals to represent the class of straight chain alkanes in kerosene-based fuels, and the use of other alkanes such as n-hexadecane or n-tetradecane can also be found. Despite the efforts, n-decane and

n-dodecane are relatively less studied compared to smaller species such as n-heptane, hence the kinetic details are required to improve for higher emulation quality.

Over the years, substantial experimental work of n-alkanes has been performed in a variety of equipment, such as jet-stirred reactors, premixed flames, flow reactors, shock tubes, and rapid compression machines, which are subsequently utilized for kinetic model validations. Pfahl et al. [115] studied the ignition of three fuels mixed with air by using a high-pressure shock tube, and the measurements of n-decane were conducted around 13 bar and 50 bar, in the temperature range of 700-1300 K. Zhukov et al. [116] performed autoignition experiments of n-decane/air mixtures behind reflected shock waves at the pressure of 13 atm and 80 atm and the equivalence ratio of 0.5 and 1. Shen et al. [112] measured the ignition delay time of four normal alkanes with the use of a shock tube, and n-decane and n-dodecane were studied at elevated pressure conditions from 9 atm to 58 atm at $\varphi = 0.25, 0.5, \text{ and } 1$. More recently, Malewicki and Brezinsky [81] conducted an experimental and modelling study on the combustion of n-decane and n-dodecane in a shock tube, from 19 atm to 74 atm at several equivalence ratio conditions. In terms of investigations in premixed flames, Ji et al. [117] measured the laminar flame speed and extinction strain rates of normal alkanes from C5 to C12 over a wide range of conditions. Alekseev et al. [118] measured the laminar burning velocity of n-decane and a mixture of 80% n-decane and 20% benzene at atmospheric pressure and two temperature conditions. Importantly, the available models at earlier times that involved large normal alkanes are commonly assembled with other hydrocarbon classes such as cycloalkanes depending on the proposed fuel surrogates. The JP-8 surrogate from Violi et al. [70] is one example. As the technology and models advance, more recent investigators can concentrate their proposed mechanisms more solely on their targeted alkanes.

Regarding detailed mechanisms dedicated purely or primarily to straight chain alkanes, Westbrook et al. [113] discussed the construction of an exclusive n-alkanes mechanism from C8 to C16 based on the knowledge of n-heptane, including both high and low temperature reaction classes. Apart from the long calculation time due to the mechanism size, this model indicates another habitual challenge for general modelling studies, that is the limitations of more accurate descriptions of intermediate species during the combustion process for these larger hydrocarbons, since many authors constantly draw inspiration from primary reference

fuels. Ranzi et al. [119] investigated extensively the kinetic scheme of oxidation of long-chain n-alkanes based on their previous effort [87]. More recently, Dong et al. [120] formed a detailed kinetic mechanism for various surrogate fuels, including linear alkanes from C8 to C12. In conclusion, several aspects are discussed to further improve the understanding of chemical kinetics for straight-chain alkanes. Firstly, it is recommended to broaden the experimental conditions for the ignition study, especially at higher pressure. Secondly, the use of reaction class is another concern particularly for lower temperature chemistry due to the natural deficiency of mechanism assembly.

CHAPTER 3

EXPERIMENT SETUP

A flat-flame burner was utilized to observe a premixed laminar flame of both liquid and gaseous fuels. Planar laser-induced fluorescence (PLIF) and fine wire type R platinum-platinum/rhodium thermocouples were employed to measure certain combustion characteristics of the targeted flames. The equipment setup and preparation work, principles of the techniques, and concern about errors are provided in the following discussions.

3.1 Kerosene burner

The burner was designed by Patterson et al. [78] to investigate a premixed laminar flame and can operate under a wide range of equivalence ratio conditions. Before the commencement of the experiment, the burner was thoroughly cleaned, and any unfunctional parts were fixed. During the period of operation, regular maintenance was enforced. An illustration of the kerosene burner is shown in Figure 3.1 [12].

For liquid hydrocarbon combustion, fuels were filled into a double-ended sample cylinder provided by Swagelok Manchester and then pressurised with nitrogen gas (99.998%) at 7 bar. Under the influence of the pressure, the fuel is transported to the burner through a PTFE tubing, while the precise liquid flow rate was controlled by a mass flow controller (MFC), which is a Brooks Flomega model 5882. Fuel was premixed with the pressurised primary air inside the atomiser, which broke the liquid into droplets. The gap between the nozzle and inner housing can be altered to achieve an optimal droplet size, as depicted in Figure 3.2 [12]. After the atomisation, the spray of liquid and air was further mixed with a secondary air and was subsequently passed through metal shavings to enhance the mixing. Next, a honeycomb straightener was employed to assist in producing a more uniform flow before leaving the burner. Finally, the mixture of fuel and air escaped through a metal diffuser, where ideally a stabilized and uniform flame was obtained slightly above its surface. During the operation, two separate MFC channels, which are both Brooks Instrument 4800 series, controlled the flow rates of these air supplies, and the equivalence ratio was calculated by their total air flow rate and fuel flow rate. Importantly, when calculating the equivalence ratio, a correction value for the air flow rates is required, as the laboratory environment is not strictly under standard

temperature (25 °C) and pressure (101.325 kPa). Apart from the burner and the fuel cylinder, an electric heater was connected to the pipe wall of the burner, controlled with a CAL 9300 series controller to a given range and monitored with a Type K thermocouple. The reason for the heater application is to prevent the condensation of the liquid fuels and also enhance spray vaporisation. From the experience of Doute et al. [76], it is recommended to heat the entire equipment around the boiling point of the targeted fuels, although the variation of the vaporization temperature makes it less straightforward. For instance, Jet A-1 can range from 156 °C to 293 °C. In this study, the heater is set to operate between 180 °C and 190 °C for the experiments of all liquid fuels. Furthermore, the kerosene burner was placed on an XYZ traverse system controlled by the software Micromech MSS-856-A-000, which can be precise up to 0.1 mm in all three axes.

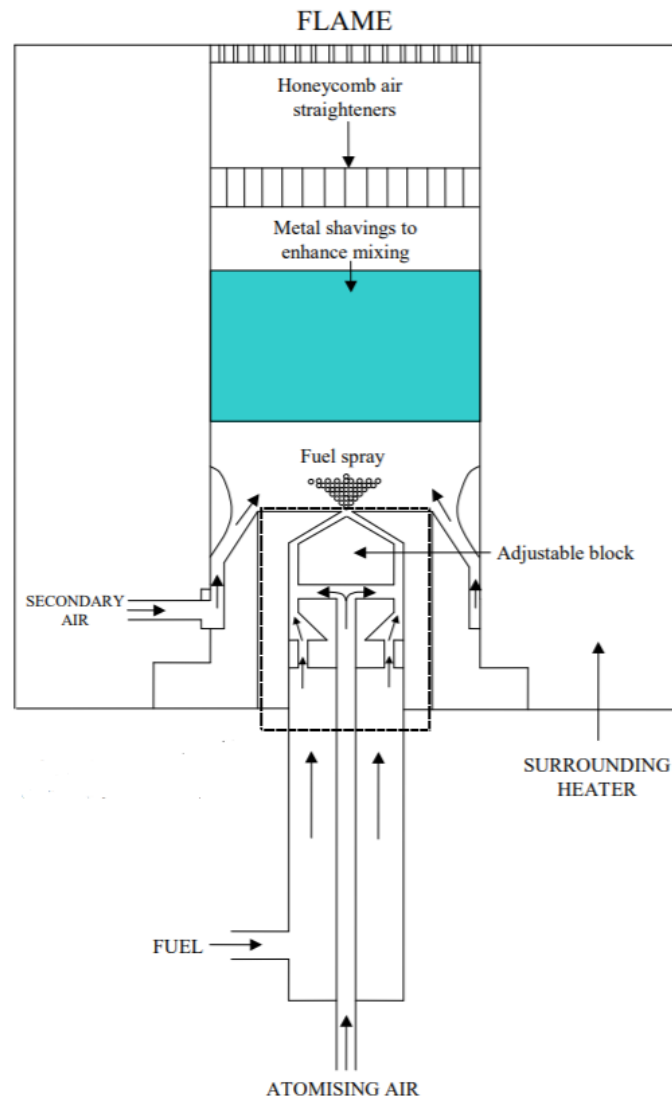


Figure 3.1 The detailed illustration of the customised kerosene burner [12].

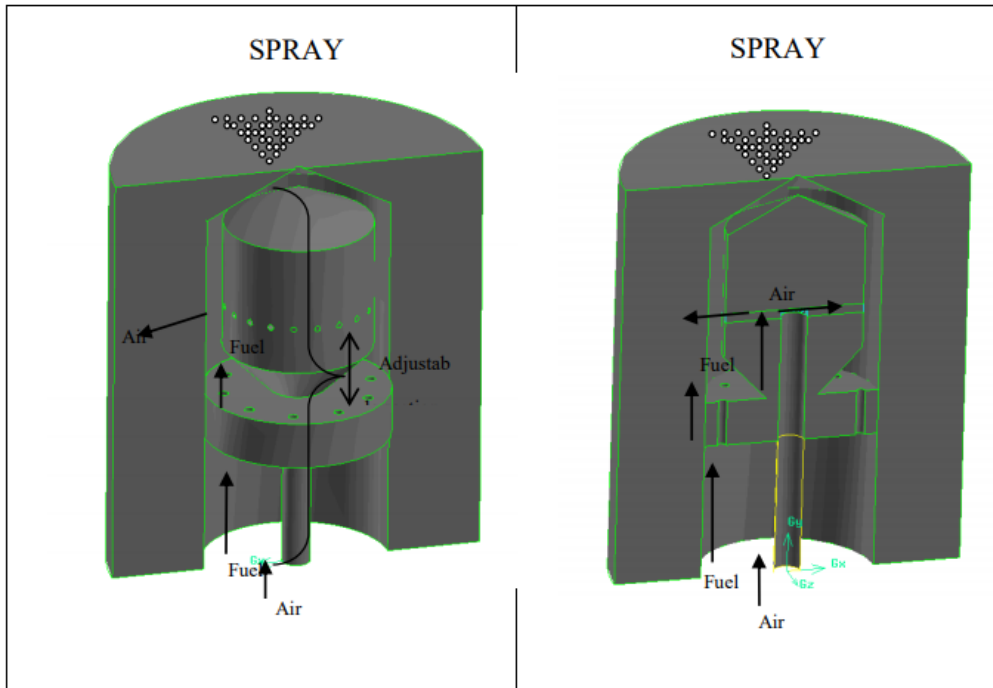


Figure 3.2 The detailed illustration of the detailed atomiser of the burner [12].

Additionally, a pure CH_4 flame and a CH_4/NH_3 flame are used as references to quantitatively determine the mole fraction of OH and NO of the liquid fuel mixtures, respectively. Thus, the heating of the burner and pre-atomization processes are not required. The gases directly passed through the atomizer and mixed with the secondary air channel, and the flame was subsequently formed above the burner. The cylinders of methane and ammonia were both operated at 2 bar, and the MFCs for methane and ammonia are Brooks Instrument 4800 series and Chell CCD100, respectively.

3.1.1 Mass flow controller calibration

The actual flow rates for both liquid fuel and air were measured to ensure accuracy and the processes are discussed separately.

For the liquid fuel calibration, a weighing scale was utilized to determine the actual flow rate. The balance of the scale may require adjustments, and this can be achieved by altering the levelling feet, and then the calibrated air bubble should be in the centre of the level indicator. An empty beaker was placed on the scale and then filled with liquid whose flow rate is controlled by the MFC. The entire process was video recorded by a phone for ten minutes. The calibration was conducted at the driving pressure of nitrogen into the fuel cylinder at 3-7 bar, and three set points of 50%, 60%, and 70% were measured under every

pressure condition. The relationship between the MFC set point and actual liquid flow rate can therefore be determined by the use of the equation of linear curve fitting in the software OriginPro. The result indicates that the stability of the MFC is dependent on pressure, with a higher pressure resulting in a more stable fuel flow. Thus, the nitrogen gas was set to be operated at 7 bar and the relationship is shown in Figure 3.3.

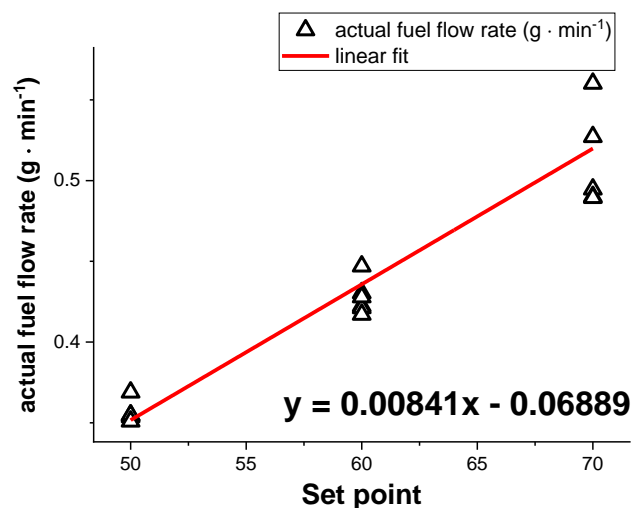


Figure 3.3 Calibration results of the liquid MFC.

For the calibration of gases, a long glass tube and soap solution were used for the measurements. An example is demonstrated in this section with the use of air. Soap was first filled into the rubber pump at the bottom of the glass tube under the air pressure condition of 2-4 bar, the bubble was generated by the pump and travelled inside the tube. To determine the air flow rate, the period for a single complete bubble to travel from point A to point B was recorded by a phone, and the volume of air was then calculated by this distance and cross-section area of the tube. Since residual solutions and irregular bubbles are likely to become blocked along the pathway, hence the measured distance varied from 15 cm to 50 cm. Results of different pressure conditions share almost identical flow rates under the same set point. Similar to the liquid MFC, four set points of $1 \text{ L} \cdot \text{min}^{-1}$, $1.5 \text{ L} \cdot \text{min}^{-1}$, $2 \text{ L} \cdot \text{min}^{-1}$, and $2.5 \text{ L} \cdot \text{min}^{-1}$ were measured and used to calculate the correlation. The calibration results of both air MFCs are shown in Figure 3.4.

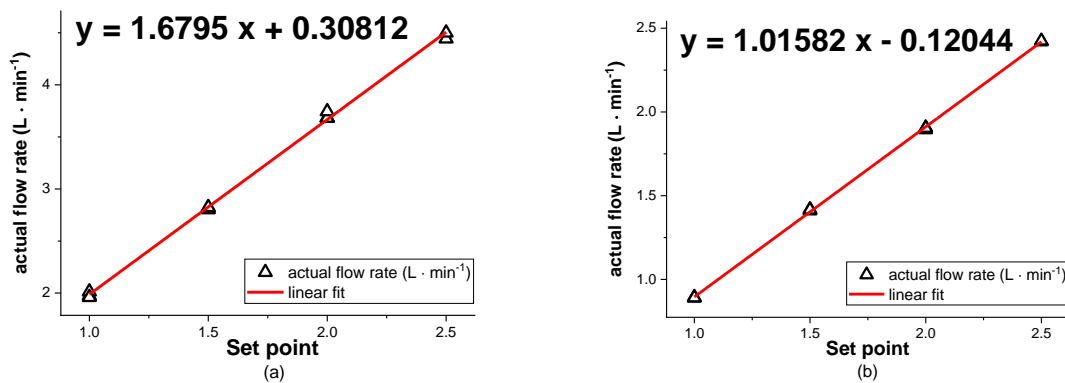


Figure 3.4 Calibration results of the air MFCs: (a) Primary; (b) Secondary.

3.1.2 Optimization of burner performances

The stability of a uniform flame is of great significance for the study of laminar flame structure. For gas fuels, the pure methane flame appears to be exceptionally stable and by introducing ammonia into the mixtures, the stability is relatively reduced. Hence, only a small amount of NH_3 is added for the reference in the quantitative NO investigation. In contrast, the combustion of liquid hydrocarbons is much more difficult to manage, largely because of the process of pre-atomizing. It was quickly perceived after the examination of the atomizer that the spray is highly sensitive to the position of the housing, and to achieve a consistent spray, the nozzle should be closer to the top cap. After a series of testing, it is advised to place the nozzle approximately 5-6 mm above the atomiser bar and the top cap should be tightened in a position where the most consistent spray is obtained. Sealing is another significant factor to help focus the spray only into the exit. Thus, PTFE tape is shrouded on the threads of both the top and bottom nuts, and users are recommended to change the tape periodically for maintenance purposes, especially after the combustion of the gas flame. Additionally, the increase of air pressure feeding the air MFC from 2 bar to 4 bar indicates no apparent correlations to the spray behaviours, so the pressure of 2 bar is set.

Also, prior efforts have investigated several designs of the meshes [121] and general maintenance of the burner [12]. To further optimize the flame behaviour, sintered materials such as steel were initially utilized to forge the diffuser plate, instead of solid metals with drilled holes. The results indicate that the stability is marginally improved but more severely, since sintered metal is much softer, it cannot effectively withstand the high temperature of the flame. Thus, the plate surface is ultimately deformed and fails to produce a uniform flame,

as shown in detail in Figure 3.5. As the temperature of the flame, especially at the centre, can go as high as 2000 K, the endurance and hardness of the material are more impactful factors for long-term use. Hence, solid stainless steel was utilized to be the diffuser material and a few different meshes were subsequently tested, although the effects seem to be rather arbitrary from the observation of the flame, regardless of this, all flames appear to be quite stable. The current plate adopts the design of a 1 mm diameter hole from Auzani [121] with a swirl pattern, as illustrated in Figure 3.6 (b). Furthermore, the previous plate was in the shape of a chamfer while the plate thickness is merely 3 mm. It was observed that such a structure does not place perfectly horizontally on the exhaust tube. Therefore, a step-in diameter was adapted as seen in Figure 3.7 (b), to minimise the potential gaps between the plate and tube. In addition, the aluminium tape used to bind the diffuser and tube should be strictly tightened for the same reason and it is suggested that this should be replaced after a duration of burner operation.



Figure 3.5 Deformed sintered plate after a period of use.

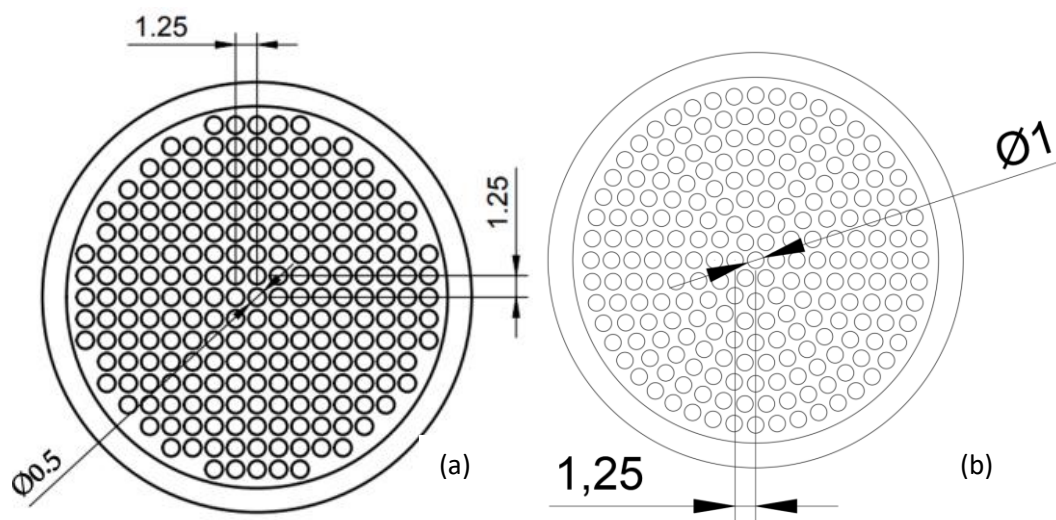


Figure 3.6 Front view of the flame diffuser, dimensions in mm: (a) previous [121]; (b) new.

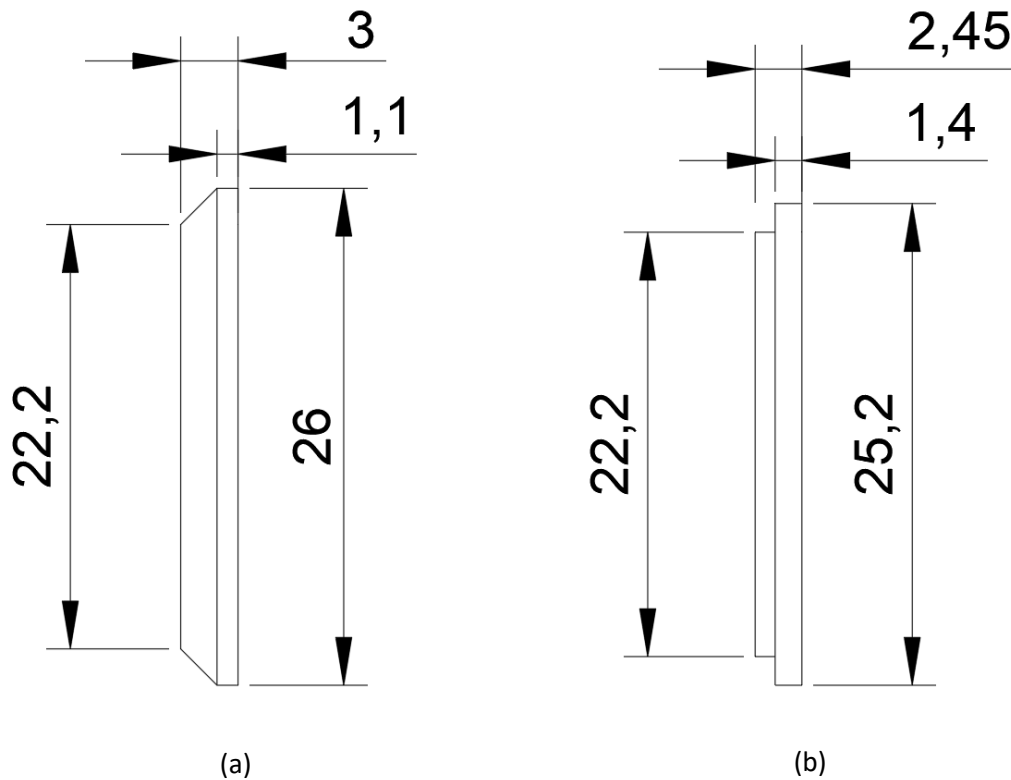


Figure 3.7 Left view of the flame diffuser, dimension in mm: (a) previous; (b) new.

3.1.3 Flame

A total of five different types of flames were studied under lean ($\varphi = 0.84$), stoichiometric ($\varphi = 1.00$), and rich ($\varphi = 1.30$) conditions. Relatively stable flames can be achieved in all three equivalence ratio conditions.

Besides the two reference flames that are gas fuels, the other three types of flames are liquid mixtures, including kerosene and two types of the proposed surrogate. The kerosene is provided by Shell and the detailed composition is not specified because it is commercially sensitive. Surrogate A is a proposed mixture of S-8 4734 fuel from Naik et al. [16], containing 32 mol% of iso-octane, 25 mol% of n-decane, and 43 mol% of n-dodecane. Surrogate B is suggested by this study, which adopts the same hydrocarbon proportions of surrogate A and merely substitutes the component iso-octane for 2-methylheptane. An example of the liquid mixture flame is shown in Figure 3.8. At lean conditions, the flames appear to be in a colour of light blue and only the centre part has a little red at stoichiometric and rich conditions.

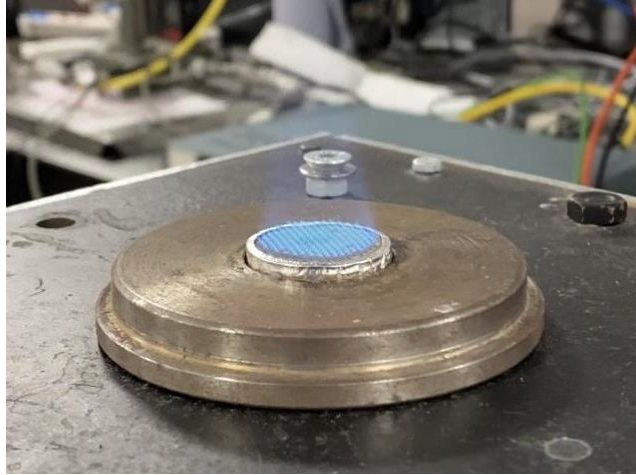


Figure 3.8 An example of the premixed laminar flame produced by the kerosene burner.

Regarding the two gas fuels, methane combustion was stated already in reaction 2.1. For the oxidation of ammonia, the product can be either nitrogen or nitric oxide. The proportion of ammonia addition in the present study is similar to the study of Okafor et al. [64]. From their reaction pathway, nitrogen is regarded as one of the products, hence the chemical reaction is described as:



As discussed in Section 3.1.2, the input of the flow rate of liquid fuels and primary air directly influences the spray formation, thus both values are initially set to be constant and different equivalence ratio conditions are achieved by only altering the flow rate of the secondary air. However, from the observation of the thermocouple measurements, the flames at the stoichiometric and lean conditions seem to be formed slightly under the diffuser plate. The phenomenon is directly reflected in the measured data as the temperature at position 0 mm is already over 1500 K, which is realistically incorrect. Thus, to obtain a more accurate temperature profile, the flow rate of these two cases is relatively increased based on the criteria of their respective rich case. Details of the flow rates of each blend are shown in Table 3.1 and Table 3.2. For further modelling validations, two boundary conditions of the diffuser are set, either the flame only comes from holes ($A_1 = 170.431 \text{ mm}^2$), or the plate is regarded to be solid ($A_2 = 498.759 \text{ mm}^2$). In the practical situation, the covered area should be between these values.

Table 3.1 Flow rates of the liquid fuels and air.

Fuel	Equivalence ratio	Secondary air (L · min ⁻¹)	Primary air (L · min ⁻¹)	Fuel (g · min ⁻¹)	Total flow rate (kg · m ⁻² · s ⁻¹)	
					A ₁	A ₂
Kerosene	0.84	4.075	2.491	0.453	0.831	0.284
	1.00	3.018	2.491	0.453	0.704	0.241
	1.30	1.606	2.324	0.419	0.511	0.175
Surrogate A/B	0.84	4.258	2.491	0.453	0.853	0.291
	1.00	3.171	2.491	0.453	0.723	0.247
	1.30	1.708	2.324	0.419	0.524	0.179

Table 3.2 Flow rates (L · min⁻¹) of the gas fuels and air.

Fuel	Equivalence ratio	Methane	Ammonia	Air	Total flow rate (kg · m ⁻² · s ⁻¹)	
					A ₁	A ₂
CH ₄ /air	0.84	0.360		4.116	0.525	0.179
	1.00	0.360		3.455	0.443	0.151
	1.30	0.360		2.653	0.345	0.118
CH ₄ /NH ₃ /air	0.84	0.338	0.059	4.116	0.519	0.177
	1.00	0.338	0.059	3.455	0.440	0.150
	1.30	0.338	0.059	2.653	0.344	0.117

Importantly, the approach of the fitting curve utilized for the mass flow controller calibration in Section 3.1.1 has certain degrees of error, which directly affects the flame condition and subsequently the measurement accuracy. An example of kerosene flame at stoichiometric condition is used to provide insight into the scale of uncertainty. The upper and lower limits of the equivalence ratio are summarized in Table 3.3, together with their respective adiabatic temperatures predicted by Chemkin. The simulation shows that the error in flow rates may lead to a temperature discrepancy of around 100 K.

Table 3.3 An example of equivalence ratio uncertainty.

	Equivalence ratio	Simulated adiabatic temperature/K
Ideal	1.00	2351.6
Upper limit	1.09	2366.0
Lower limit	0.88	2258.5

3.2 Laser-induced fluorescence

Fluorescence describes the process of a substance absorbing light at a certain wavelength and then emitting the light at the same or a longer wavelength. This phenomenon can be employed to study specific species in combustion, while in practical applications, it can face detection challenges such as the fluorescent light being weak, or the concentration of the targeted species being too low in the flames. The laser is a device that converts input energy into coherent monochromatic light, and since it possesses high power and can be tuned to a precise wavelength, laser-induced fluorescence (LIF) is one of the most widely applied combustion diagnostics in the past decades.

Compared to traditional physical probes, for example, thermocouples, the primary attraction of these laser tools is having no direct influence on the flow behaviours during operations [21]. One major problem is the conversion from the signal to the actual mole fractions of species, and other practical concerns include safety as the laser could damage the users' eyes and skins permanently if it is not properly used, thus laser goggles and lab coats are necessary when conducting an experimental investigation. Planar laser-induced fluorescence (PLIF) is an effective approach that uses optics to expand the beam of the laser to a laser light sheet that passes through the flame, and the fluorescence from the species being studied is collected with a camera. In this project, PLIF was utilized to measure the mole fraction of OH and NO in a few types of flame, and the application of OH LIF thermometry was also explored.

3.2.1 Principals of spectroscopy and specific molecules

A molecule or an atom exists in quantum states, and each state has its distinct energy level and angular momentum [122]. The internal energy of a molecule consists of electronic, vibrational, and rotational energy. A molecule can interact with an incident light photon. Through the absorption of the photon, the quantum state of the molecule is subsequently changed. This process is dependent on the energy of the photon ($h\nu$) matching the energy difference between the two quantum states, described as:

$$\Delta E = E_{\text{upper}} - E_{\text{lower}} = h\nu \quad (\text{Eq. 3.1})$$

Where E_{upper} indicates the photon energy at the excited level, E_{lower} typically indicates the photon energy at the ground level, h is Planck constant ($6.6261 \times 10^{-34} \text{ J} \cdot \text{s}$), and ν is the

frequency. Commonly, the ground electronic state at the lowest energy is denoted as X , and the next excited levels are labelled as A , B , C , etc...

Figure 3.9 depicts the transition between two electronic states of a molecule. The curve reflects the potential energy variation of an electronic state as a function of internuclear separation, and on each electronic state the horizontal lines indicate a set of vibrational levels ($v = 0, 1, \dots$). On each vibrational level, there is another set of rotational levels ($J = 0, 1, \dots$). Importantly, the upper and lower levels are denoted by ' and ', respectively. The population of each energy state, vibrational and rotational, is specified by a Boltzmann distribution, which is dependent on the temperature. The quantized energy states can be interpreted into spectra, and small radicals (e.g., OH, NO, and H₂O) commonly have discrete spectra while larger molecules are usually blended.

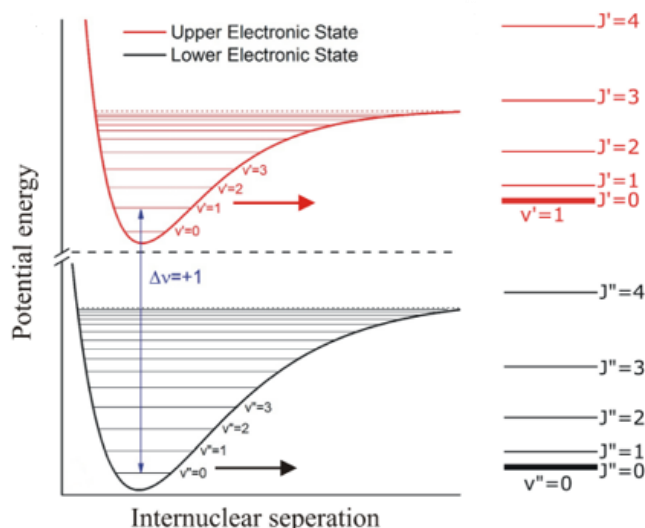


Figure 3.9 Diagram of the energy level of a diatomic molecule. [123]

Although internal transitions are numerous and complicated, when the ground and excited electronic states are fixed, they can be simplified to a two-level model. Laser-induced fluorescence is a useful tool that utilized this concept to investigate elementary combustion kinetics. A molecule or atom is initially excited by a source of energy, in the current case a pulsed laser, to a higher electronic energy level, followed by a spontaneous emission of light from the upper to the ground state that is referred to as fluorescence. Consider a molecule travelling from X ($v'' = 0, J'' = 2$) to A ($v' = 1, J' = 3$). A resonance fluorescence occurs when the molecule returns from the initial excited line to the original ground state, although this is not always the case. In the LIF application, since it is a delayed process, many collisions occur that

can distribute the original excited state to a range of rotational energy levels ($J' = 1, 2, 4$, etc.) in the $v' = 1$ state. Also, it can distribute the excited molecule to a range of vibrational energy levels ($v' = 0, 2, 3$, etc.). Since photon emission is possible from any of these processes, the fluorescence spectrum will be much broader than the designed excited line. However, not all outcomes of collisions are negligible. Molecules can exit to the original electronic state without the release of photons, and this phenomenon is referred to as quenching which is a primary problem for signal quantification. An example diagram of various transitions between energy states is provided in Figure 3.10. To conduct measurements on a specific molecule, the absorption wavelength has to be attainable with the laser and the details of the spectrum must be acknowledged [124].

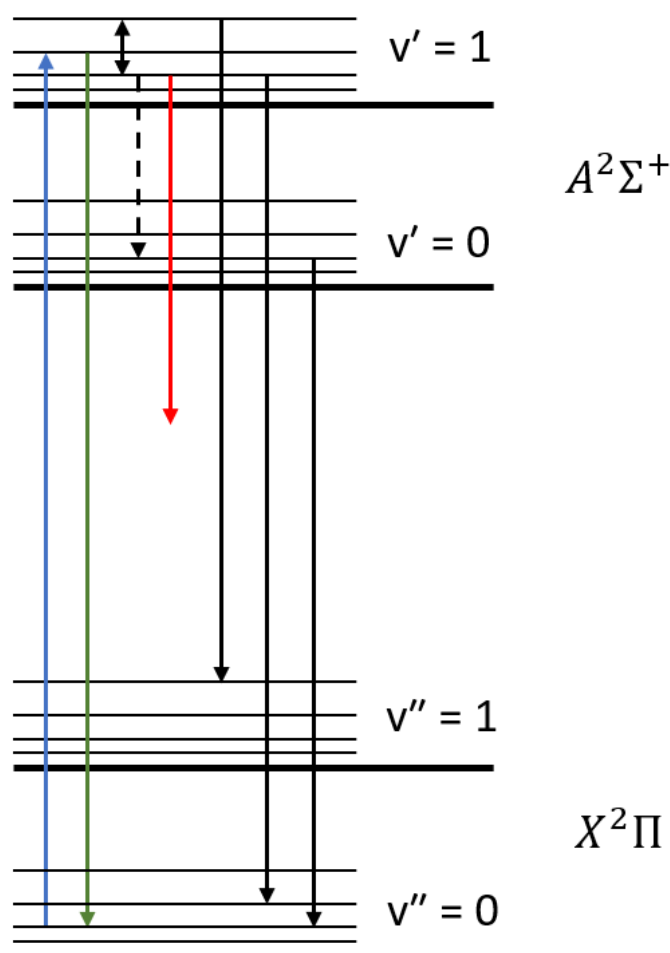


Figure 3.10 Energy level of $A^2\Sigma^+ \leftarrow X^2\Pi$, including absorption (blue), resonance fluorescence (green), fluorescence (black solid), vibrational energy transfer (black dash), rotational energy transfer (double arrow), and quenching (red).

For rovibrational spectra, researchers usually pay attention to $\Delta v = 1$ as it is the strongest. For transitions on the rotational level, the total angular momentum J follows rules that ΔJ can

be equal to -1, 0, and +1, which is termed as the branch P, Q, and R, separately. In practice, weaker transitions such as $\Delta J = \pm 2$ can be observed as well. The NO and OH molecules both contain an unpaired electron, hence it comes with an intrinsic electronic angular momentum of $\frac{1}{2}$. Two primary cases of the Hund's cases are introduced to explain the rotational states with the influences of spin. Hund's case (a) describes the condition that both the orbital angular momentum Λ and electronic angular momentum are not zero, and the spin-orbit coupling is much stronger than the total angular momentum J resulting from the rotational coupling. Hund's case (b) is when $\Lambda = 0$ and electronic angular momentum $\neq 0$, thus the spin-orbit coupling no longer exists, Λ is initially coupled with the angular momentum of the rotating nuclei R to form N , N is then coupled with electronic angular momentum to form J . As spin is either up or down, two spin-split levels can be obtained. The angular momentum energy F is termed as $F_1(J)$ when $J = N + \frac{1}{2}$ and $F_2(J)$ with $J = N - \frac{1}{2}$ [122]. When taking the OH radical for instance, the ground state of X is an intermediate between case (a) and case (b), while the excited level of A is properly described in case (b). As an example of transitions shown in Figure 3.11, branches such as Q_1 and P_1 are placed at state ${}^2\Pi_{3/2}$ ($J = N + \frac{1}{2}$) and R_2 is from state ${}^2\Pi_{1/2}$ ($J = N - \frac{1}{2}$). Regarding the notation of detailed transition, $Q_1(6)$ represents traveling from $N'' = 6, J'' = 6.5$ to $N' = 6, J' = 6.5$, and $R_2(13)$ indicates traveling from $N'' = 13, J'' = 12.5$ to $N' = 14, J' = 13.5$.

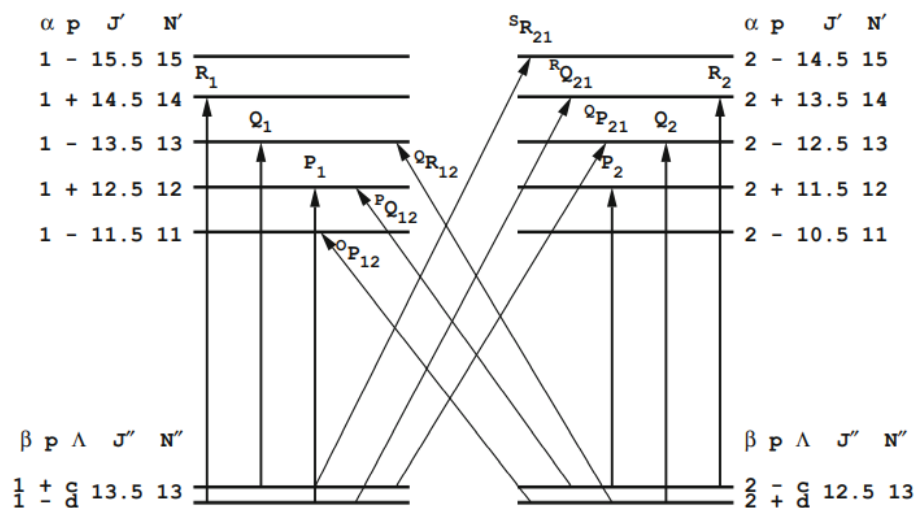


Figure 3.11 An example of the allowed transitions in $A^2\Sigma^+ \leftarrow X^2\Pi$, from $N'' = 13$. [122]

3.2.2 Laser setup

A Nd:YAG laser, Quantel Q-smart 850, was utilized to generate a laser beam at 1064 nm. Initially, depending on the desired wavelength, one or two harmonic modules connected to

the laser head are utilized to manipulate the original frequency. For OH detection, a second harmonic module (2ω HG) was utilized to double the frequency that achieved the green light at 532 nm. For the NO detection, a third harmonic module was added to triple the frequency that leads to ultraviolet light at 355 nm. As the original wavelengths are still present after passing through the HGs, the output is further passed through a dichroic mirror and a dumper to separate the beam and only allow through the desired wavelength. Importantly, when switching to a different wavelength, automatic phase matching is required to re-tune the system. The final output beam (532 nm or 355 nm) then went into the dye laser system, which was a Sirah Cobra-Stretch tunable dye laser in this study. It is based on two dye cells containing dyes as the laser media and the wavelength can be tuned to an aimed outcome by a diffraction grating. Next, the frequency of the refined dye laser beam was further doubled by a BBO crystal to reach the final output at around 283 nm for OH and 226 nm for NO, more compensating optics and a dumper separated these ultraviolet wavelengths from the original dye laser wavelengths and also maintained the positional orientation of the output laser regardless of wavelength. Then the beam passed through light sheet optics to form a laser sheet, which subsequently went through the centre of the flames. In addition, a tripod was positioned at the receiving end as the beam dumper for safety reasons.

The fluorescence signals were captured by an intensified charged couple device (ICCD) camera from LaVision and the software DaVis controls both the Nd:YAG laser and the camera. A specific camera filter for either OH or NO was employed to effectively block out the light noises in the environment and the laser scattering while transmitting the targeted signals at the defined range of wavelength. Also, the intensified delay and gate of the camera should be set properly to achieve the optimum quality of the picture. A higher gain value can improve the intensity of the signal leading to improved accuracy, but as the camera is highly sensitive and to prevent it from overexposure, the image intensity should not surpass 4096. Additionally, Figure 3.12 (a) shows the general setting of the PLIF experiment, and the detailed beam pathway and the key units are shown in Figure 3.12 (b).

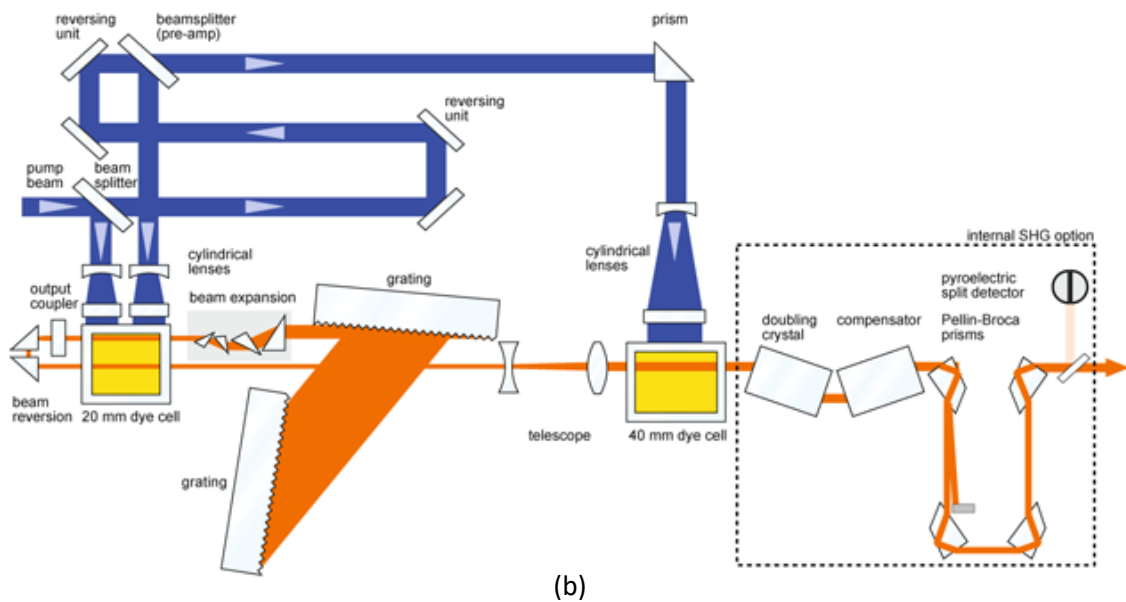
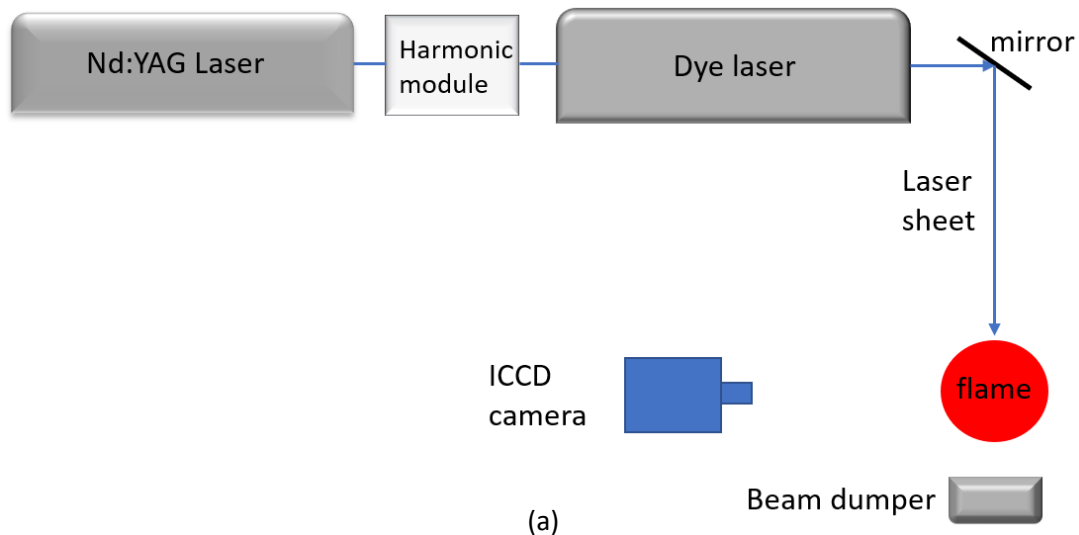


Figure 3.12 PLIF equipment setup: (a) general schematic; (b) detailed optical layout, from Sirah dye laser datasheet. [125]

To optimize the laser power outcome, several preparation steps are essential before taking the measurements. The shape of an ideal beam is commonly an oval-shaped dot, and the properties of the beam can be adjusted either manually or monitored by the computer program Sirah Control. The software covers a variety of tasks, such as setting the precise wavelength and scanning a defined range. To fine calibrate the frequency conversion unit (FCU), a fitting dataset over a wavelength range was generated. The scanned range is 562 nm to 566 nm for OH and 448 nm to 456 nm for NO. At each point, the position of the BBO doubling crystal was altered, and the output was assessed by the reading of a pyroelectric energy sensor from Thorlabs until a maximum value was achieved. Another delicate feature

of the Sirah is the temperature stabilizing of the BBO crystal, which is set to be 50 °C. The quality of the dyes is another important factor related to the laser power. Dyes are usually purchased in powders for storage reasons, and both methanol and ethanol can be utilized as the solvent and no obvious performance differences are observed. The dyes for OH and NO are Rhodamine 6G (559-576 nm) and Coumarin 2 (434-463 nm), respectively, and the concentrations used in the resonator dye cell are $0.09 \text{ g} \cdot \text{L}^{-1}$ for OH and $0.23 \text{ g} \cdot \text{L}^{-1}$ for NO. As recommended by the Sirah manual, solutions in the main amplifier were further diluted by a factor of one-third. From experience, it has been noted that the NO dye degrades much faster compared to the OH dye, thus for a better signal output, it is suggested to change to a fresh solution in two weeks if used daily. After the change of dye, the FCU table should be subsequently renewed. When properly arranged, the power output at 226 nm at optimal is around 3 mJ. Other key maintenance includes changing the filter cartridges in the dye circulator periodically, and the deionizing cartridge and coolant water after about six months.

3.2.3 Data collection

This section describes the procedures and a few necessary precautions during the operation to accurately record the relative mole fraction of OH and NO in the targeted flames. Transitions are from the ground state to the first excited state, which are $A^2\Sigma^+ \leftarrow X^2\Pi (1,0)$ for OH and $A^2\Sigma^+ \leftarrow X^2\Pi (0,0)$ for NO. Selected signals for OH and NO are $Q_1(6)$ and $Q_1(12)/Q_1(20)$, respectively. Also, OH LIF thermometry was investigated with two selected transition pairs, which are $R_2(13)/P_1(2)$ and $R_2(2)/R_1(12)$. Detailed discussion is provided in Section 3.3.2.

The accuracy of the wavelength at a chosen signal is of great importance, particularly for temperature measurements. The spectra can be simulated by the software LIFBASE [126] although in reality, the laser wavelength display does not always correspond precisely. Thus firstly, the calibration of the transition peak was carried out by using the Sirah Control to scan a wide range of wavelengths. The range is 281.8 nm to 283.0 nm for OH and 225.7 nm to 226.4 nm for NO. The process was recorded by a video, and then the signals were observed and selected. For each observed signal, the offset of the simulation and the actual position was calculated. To ensure accuracy, the offset of every obvious transition in the entire range should be matched as shown in Figure 3.13. Importantly, with the current experimental setting, the determination of each wavelength is carried out by visual observation of the

intensity of the PLIF image in the DaVis software and wavelength reading in the Sirah control software. This approach may be adequate for the transitions of $Q_1(6)$ and $Q_1(12)/Q_1(20)$, however, OH LIF thermometry requires a much higher precision of the wavelength peak. Hence, to further improve the accuracy of the judgment, the speed of the flame scan is set to be 0.001 nm per second. Another important factor is the stability of the dye laser transition wavelength, which could be affected by the temperature of the laboratory or any physical disturbance of the laser. However, from the experience, the laboratory environment is relatively stable, and the same wavelength can be applied throughout the process of data collection within the day. But when conducting the PLIF measured on a different day, the signal determined previously may be shifted a little, therefore, it is advised to do a quick flame scan around the region of the targeted transitions before the commencement of the experiments every time. In addition, to minimise the effects of any chemiluminescence or scattered laser light, off-resonance signals were measured close to the observed transition and subtracted from the measurements made on the observed transition.

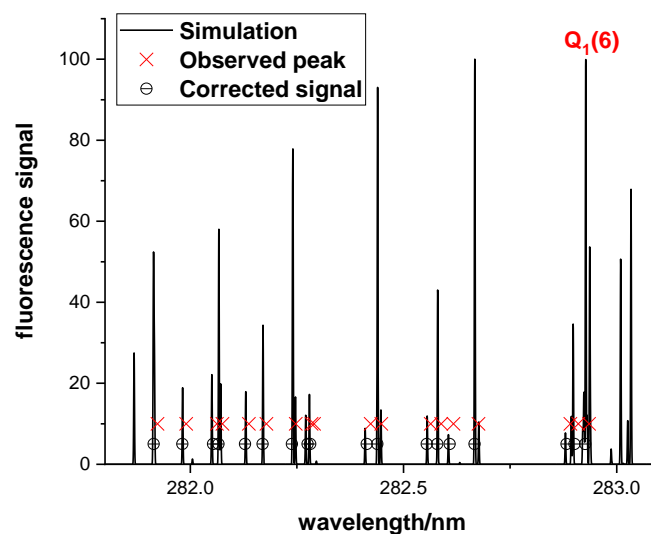


Figure 3.13 OH spectrum at 1500 K from both the simulation and observation.

High intensity of the PLIF image is important to the quality of the species detection, and the output is controlled by adjusting either the laser power or the intensified gain of the ICCD camera. Due to direct contact with the open air, meaningless signals received from the edges and tip of the flames are comparatively stronger than the interested area, which is about 10 mm above the burner at the centre of the diffuser plate. The amount of OH is quite

abundant in these liquid fuels, hence, to maximise the intensity at the targeted area and protect the camera from overexposure, a mask was placed in front of the flame to physically block the irrelevant pixels. The amount of NO, on the other hand, is considerably less. To enhance the laser output, the concentration of the dye in the resonator was refined to $0.23 \text{ g} \cdot \text{L}^{-1}$ rather than the recommended $0.2 \text{ g} \cdot \text{L}^{-1}$ from the manual. Also, a test was conducted from the laser power setting within the DaVis software of 60% to 70% at the beam output of 226 nm, and it is found that the output reaches a maximum value at 65%, hence this energy level is set for all the NO measurements. The camera gain is set to be 80 at maximum, as it is recommended to not stress the device. Additionally, a previous lab user has suggested an adjustment of intensifier gate and delay time for a better quality NO image [121], although no apparent differences were observed from the trial investigations. Detailed settings of the laser and camera are shown in Table 3.4 and Table 3.5, respectively.

The vertical length of the laser sheet is about 20 mm, and its intensity is not uniform, hence, it is advised to first place the burner at a position where the intensity of the beam displays less fluctuations, i.e., approximately in the middle of the beam sheet. Despite the precautions, the laser beam not only passes through the flame, but will also inevitably hit some part of the burner structure. From earlier experimental trials, the observed scattered disturbances near the burner surface were substantial. The precise placement of the ICCD camera can solve the issue as it physically cuts off the signal. In theory, the lens centre should be facing the surface of the burner perfectly horizontally at an angle of 90° , although from experience, it is concluded that better images are attained when the camera is positioned a little below the burner, and the lens must avoid capturing from above. This action, however, causes more difficulty in accurately judging the beginning of a flame on the collected image. Firstly, the camera setup needs to be examined by taking the filter off the lens. The intensifier gate and gain must be set to a specified parameter for the protection of the camera, and also the pathway of the beam must be blocked. Next, the camera focus was adjusted, and the image grid was calibrated in the DaVis software. To determine the location of the rig, a ruler was mounted on the flame diffuser as a relative measure for the image recording. However, this step is prone to errors due to the thickness of the aluminium tape wrapped around the diffuser plate and the limitations in the eye judgement, so a discrepancy of $\pm 0.2 \text{ mm}$ in both the x- and y-axis on the image is expected.

Table 3.4 Laser power and camera gain for the measurements of OH, OH LIF thermometry, and NO.

Transition (simulation)	ER	Liquid fuels		CH ₄		CH ₄ /NH ₃	
		Laser power/%	Intensifier gain/%	Laser power/%	Intensifier gain/%	Laser power/%	Intensifier gain/%
Q ₁ (6): 282.9267	$\varphi = 1.30$	40	70	40	80		
Off:	$\varphi = 1.00$	35	70	40	75		
282.8000	$\varphi = 0.84$	30	70	40	72		
R ₂ (13): 282.5558	$\varphi = 1.30$	40	80				
P ₁ (2): 282.5802	$\varphi = 1.00$	40	78				
Off: 282.5000	$\varphi = 0.84$	40	75				
R ₂ (2): 282.1299	$\varphi = 1.30$	40	78				
R ₁ (12): 281.9819	$\varphi = 1.00$	40	76				
Off: 282.1000	$\varphi = 0.84$	40	72				
Q ₁ (12)/Q ₁ (20): 226.0320	$\varphi = 1.30$	65	80			65	75
Off:	$\varphi = 1.00$	65	80			65	75
226.3100	$\varphi = 0.84$	65	80			65	75

Table 3.5 General laser and camera settings.

Intensifier gate (without filter)/ns	900000
Camera gain (without filter)/%	40
Intensifier gate (with filter)/ns	10000
Intensifier delay/ns	3400
Camera binning	2x2
Camera exposure/ μ s	20000
Q-switch delay max/ μ s	170
Q-switch delay min/ μ s	500
Laser pulse width/ns	5

Besides the recording of raw and background signals, an additional laser sheet correction is required as explained above. Usually conducted before the collection of flame signals, a quartz cuvette filled with deionised water is hit by the beam to manifest the variation in the illumination. Because the bottom of the cuvette has a certain thickness, the burner was moved 4 mm below the original height. In addition, temperature measurements with the use of OH LIF thermometry do not require laser beam calibration due to the nature of the technique that only requires the signal ratio. For each case, 200 frames in 20 s were repetitively recorded, the image was subsequently processed and averaged, and then exported to the software Tecplot 360 for further analysis. Each data set was loaded in zones and can be redefined and calculated. A polyline of 10 mm started from the centre of the burner surface was vertically plotted and 200 points of intensity were extracted. However, the collected signals of OH and NO are just the camera pixel values, or in a way merely the relative mole fraction of the species. Detailed discussions of quantifying the PLIF signals to actual mole fraction are presented in Chapter 5.

3.3 Temperature measurements

The temperature profile of a given flame is of great importance to understand the characteristics of chemical combustion, and many types of techniques are available for research purposes. These approaches can be commonly categorized as invasive and non-invasive, and to select a suitable tool for a targeted application, temperature range, precision, stability, cost, etc., are all required considerations. Knowledge of the measured temperature for the laminar premix flame of large hydrocarbons in general is quite limited, and the experimental conditions are frequently varied among investigators, which makes it even more difficult to compare and validate the results.

Two approaches, thermocouple and OH LIF thermometry, were explored to obtain the temperature profiles of all five fuel mixtures in a flat-flame burner in this project. Given the scale of the study and time limitations, temperature data of the gas fuels are obtained from thermocouples and OH LIF thermometry is primarily utilized to attain the profiles of the liquid fuels. Approaches applied for each case are compiled in Table 3.6.

Table 3.6 Compilation of the approaches used to obtain temperature profile for different flames.

Fuel type	Equivalence ratio	Method of temperature profile	Transition pairs (If applicable)	Thermocouple type (If applicable)
CH ₄	0.84	Thermocouple		P13R-005
	1.00	Thermocouple		P13R-005
	1.30	Thermocouple		P13R-005
CH ₄ /NH ₃	0.84	Thermocouple		P13R-002
	1.00	Thermocouple		P13R-002
	1.30	Thermocouple		P13R-002
Kerosene	0.84	OH LIF thermometry	R ₂ (2)/R ₁ (12)	
	1.00	Thermocouple + OH LIF thermometry	R ₂ (13)/P ₁ (2) + R ₂ (2)/R ₁ (12)	P13R-003
	1.30	Thermocouple + OH LIF thermometry	R ₂ (13)/P ₁ (2) + R ₂ (2)/R ₁ (12)	P13R-005
Surrogate A	0.84	OH LIF thermometry	R ₂ (2)/R ₁ (12)	
	1.00	OH LIF thermometry	R ₂ (13)/P ₁ (2)	
	1.30	OH LIF thermometry	R ₂ (13)/P ₁ (2)	
Surrogate B	0.84	OH LIF thermometry	R ₂ (13)/P ₁ (2)	
	1.00	OH LIF thermometry	R ₂ (2)/R ₁ (12)	
	1.30	OH LIF thermometry	R ₂ (13)/P ₁ (2)	

3.3.1 Thermocouple

Using thermocouples is a common invasive method to measure the temperatures of a flame. It is a sensor device composed of two different metal wires welded together at one end. When the bead is heated or cooled down, a voltage is generated in response to the temperature change in the surrounding environment. The main advantages of this approach are low cost, straightforward to implement, and cover a wide range of temperature conditions. However, major errors can occur that compromise the results. In this project, three sizes of type R Pt/Pt-13%Rh bare wire thermocouples supplied by Omega were employed. They are referred to as P13R-002, P13R-003, and P13R-005 with the initial wire diameters of 50 μm , 75 μm , and 125 μm , separately.

The position of wires can be moved during the heating, which leads to incorrect temperature readings [121]. Therefore, before the measurement, at the Pt-Rh side of the thermocouple, a spring was made in the wire by looping the wire on a thin ceramic tube to

create tension. Another important precaution is the wire coating. The thermocouple was coated with a thin layer of protection to shield the wires from potential catalytic reactions on the surfaces at high temperatures [127] and also to help prevent the platinum from melting as platinum has a melting point of 1700 °C. Earlier investigators commonly utilized the influences of SiO₂. This approach can be problematic as the study found that a little amount of silica can already result in platinum silicide production that embrittles the wires at temperatures higher than 1100 °C [128]. More recently, Kint [129] proposed another coating combination by using Y₂O₃–BeO, although this leads to a new drawback as BeO is a highly poisonous chemical. Nevertheless, the temperature results of adopting this ceramic coat can be found in several fuels combustion, and the operations are conducted around low pressure conditions (< 50 torr) using a type B Pt/6%Rh–Pt/30%Rh wire [130–132]. At atmospheric pressure, however, the use of silica is applied [131, 133]. Also, the smallest diameter of type B from the above references is 100 μm, which is at least twice thicker compared to the usual type R, hence this coating method may not be suitable to be applied on the thinner wires. In all the considerations, the silica method was utilized in this project. The coating was achieved by a gas blow torch supplied by natural gas doped with hexamethyldisiloxane vapour. Once a small flame is generated, it subsequently passed through the bare wire. This process helps to straighten the wires of P13R-002 and P13R-003 as well and especially around the bead area, but it may also break the junction directly if the wire stays in the flame for too long or gets too hot. Thus, it is advised to coat for no more than ten seconds and once a silvery white colour appears on the outer layer, the coating is regarded as finished. The refined thermocouple wire was then mounted with a holder and crossed the flame horizontally, with the bead placed in the centre of the burner. Additionally, soot formations are not considered as a factor for the temperature measurements as no soot was observed from any of the flames or deposited on the thermocouples. The detailed setup is illustrated in Figure 3.14.

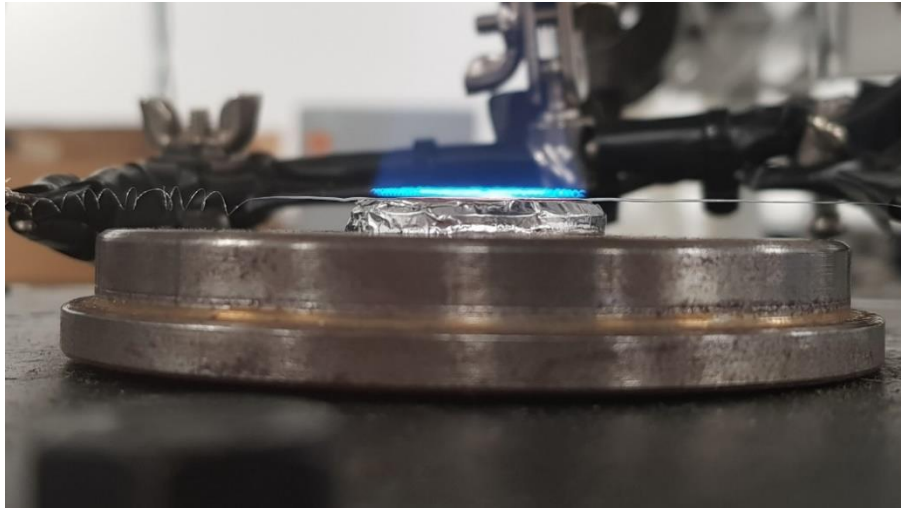


Figure 3.14 Design of the temperature measurements by thermocouples [121].

For each fuel condition, temperatures at a total of 14 positions were measured, from 0 mm to 10 mm vertically above the burner surface. The alteration of height was achieved by the increment feature of the Micromech software to ensure accuracy. All three axes were initially set to the “home” position, and when one direction is moved incrementally, zero value should also be set on the other two axes as a safety precaution. The electric signal of the thermocouples was delivered through a type R compatible extension wire connected to a data logger, namely the Omega Multiscan 1200, which was controlled by the software ChartView. To prolong the use of the thermocouples, the software is set to record the signal at a frequency of 20 Hz for 5 s at each position. The averaged value can then be calculated from the exported data file.

From previous investigators [12, 121] and the literature [76], under atmospheric pressure, the maximum temperature of the kerosene-based flames is estimated to be around 1600-1800 °C or even higher. Since data at this level is currently unavailable, errors are expected to some degree. Radiation and conduction losses from the bead are the main source of measurement error, hence a correction is required. For conduction losses, Bradley and Matthews [127] studied the minimum length of wires to prevent serious cooling effects with Pt/Pt-10%Rh wires ($d = 50.8 \mu\text{m}$), and results show that the conduction can be regarded as negligible when the length of the wires is at the minimum 250 times greater than the diameter. The dimensions of the wires used in this study are all applicable to this standard, and the wires were aligned horizontally, hence the conductive losses are not considered. For the radiation correction, Kaskan [134] provided corrected radiation losses, provided as:

$$\Delta T_{\text{rad}} = \frac{1.25 \varepsilon \sigma T_{\text{tc}}^4 d^{0.75}}{\lambda} \left(\frac{\eta}{U} \right)^{0.25} \quad (\text{Eq. 3.2})$$

Where ε is the emissivity of the coated bead, σ is the Stefan-Boltzmann constant ($5.6704 \times 10^{-8} \text{ J} \cdot \text{s}^{-1} \cdot \text{m}^{-2} \cdot \text{K}^{-4}$), T_{tc} is the raw temperature received from thermocouples (K), d represents the diameter of the bead after coating (m), λ is the thermal conductivity of gas at wire temperature, which is approximately $0.18 \text{ J} \cdot \text{s}^{-1} \cdot \text{m}^{-1} \cdot \text{K}^{-1}$ at 1000 K with little variations, U is the total flow rate ($\text{kg} \cdot \text{m}^{-2} \cdot \text{s}^{-1}$) which is dependent on the fuel and air flow rates and the diffuser area, η is the dynamic viscosity of gases ($\text{kg} \cdot \text{m}^{-1} \cdot \text{s}^{-1}$) assuming air at atmospheric pressure in this case. The formula from Hilsenrath et al. [135] was applied to calculate the specific viscosity at different temperature conditions:

$$\eta \times 10^7 = \frac{AT^{1.5}}{T+B} \quad (\text{Eq. 3.3})$$

Where A is 145.8 and B = 110.4.

The main uncertainties in this traditional method of radiation correction are the values of the coated wire emissivity and the bead diameter after coating. Kaskan [134] assumed a constant value 0.22 ± 0.02 for ε . For uncoated wires, a theoretical expression of the hemispherical emissivity is provided by Davisson and Weeks [136] and this was later validated experimentally by Bradley and Entwistle [137]. The addition of coating, however, may have a considerable impact on the bare wires. Bradley and Entwistle [138] utilized the Pt/Pt-10%Rh infused with SiO_2 to investigate the emittance by numerical solution and further compared the results with the experimental data. The results of ε show a decrease with an increase in temperature, which is opposite to the tendency of uncoated wires as depicted in Figure 3.15.

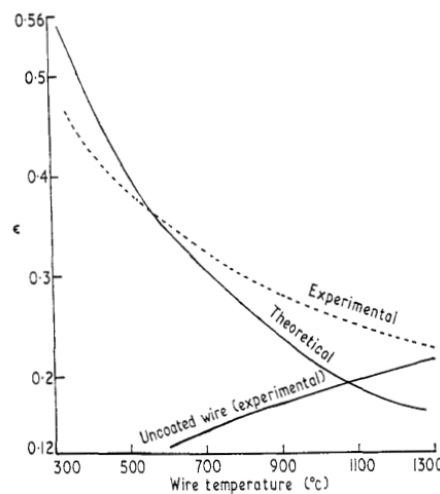


Figure 3.15 Variation of emissivity against temperature, for uncoated and coated wires [138].

At $T > 1000\text{ }^{\circ}\text{C}$, the theoretical value of the coated wires begins to converge more to the value of the uncoated wires, and at 1280 K, the uncoated result is approximately 30% greater than the coated result in theory while it is rather close to the experimental value. To simplify the calculation, ε is set to be as a constant 0.2 independent of the temperature as Kaskan [134] suggested. Deciding the bead diameter is another challenge, as its size is mostly an estimation. When welded properly, the diameter of the bare junction should be less than twice the wire diameter [134], however, exposure to non-catalytic coating will further increase the diameter of the bead. The cross section of wires can be examined by a microscope, although it is reported that locating the bead is rather difficult once the wire was placed under the lenses [121]. Records have shown that previous authors have regarded the bead to be 2.5 times greater than the wire [121, 133], and in this study, the same rule is applied to all three types of thermocouples. The refined diameters of P13R-002, P13R-003, and P13R-005 are $125\text{ }\mu\text{m}$, $187.5\text{ }\mu\text{m}$, and $313\text{ }\mu\text{m}$, separately. In addition, according to the black body radiation, the colour of the object at 1500 K is red-orange while it turns to be yellow-orange around 2000 K. From the observation of the flame, the wire appeared to be colour of red. This information is utilized as the reference in case the temperatures after the correction result in an unreasonably high level.

One major obstacle in obtaining a successful temperature measurement is the innate fragility of the wires. It was suggested that the thicker wires may endure the heat longer [121], although from experience, reasons for wire breaking appear to be quite arbitrary and type P13R-002 is capable of withstanding high temperature flames for a long time. The wire placement is another issue, as it is a rather delicate job to locate the wire perfectly horizontally and, in the meantime, not over-stretch it. Moreover, due to its greater thickness, type P13R-005 is quite unaffected by the length of the coating, but it is oftentimes unnaturally bent, which may lead to additional uncertainties.

3.3.2 OH LIF thermometry

The principle of LIF thermometry is to reflect the population distribution of two or multiple electronic states concerning temperature variation. Either molecules or atoms can be employed as the fluorescence markers. The evident advantage of this technique is that no physical contacts need to be imposed on the investigated object, although there are certain limitations. For molecules, the measured temperature is rather restricted to a certain level,

for instance, a high temperature for OH, along with other obstacles such as the quenching effects, background emissions, and complicated setup. The use of atoms is another less common method. Although atom tracers typically possess much higher transition strengths than molecules, it is technically difficult to properly plant the metal seed into the flame. Previous attempts of using OH LIF thermometry [139, 140] and NO LIF thermometry [141, 142] to study flame structures can be found in the literature. Instead of the conventional two-line approach, multi-line that attains the shape of a range of the spectrum is frequently utilized for NO LIF because the interference from the neighbour lines is quite significant when individual NO transitions are studied. The signal distribution of the OH spectrum is comparatively less crowded, and the high concentration of OH in the hydrocarbon combustion makes the measurement more favourable. Therefore, this work utilized the method of the two-line molecule fluorescence of OH.

In a more ideal situation, two dye lasers with a very short delay time between each will be tuned to their respective transitions, and two ICCD cameras will be recording the two wavelengths virtually simultaneously. As only one system is available in the current laboratory, two signals and an off-resonance measurement were recorded in sequence, which consequently demands higher stability of the flame. To improve the accuracy of the results, the number of images is reduced to 100 frames in 10 s for each recording. Thus, the total process of each equivalence ratio condition of the fuel can be completed in 50 s. The selection of the transitions is essential, and the ratio of the pair is required to demonstrate high temperature sensitivity, particularly above 1500 K. Firstly, transitions that are overlapped must be avoided. Also, branches with quite low-level intensity in general are not recommended, while stronger transitions do not necessarily bring about quality results. From the examination of the $Q_1(8)/P_1(4)$ pair for instance, the initial efforts failed to produce reasonable thermometry results, and this may largely be because the ratio of transitions is not sensitive enough towards the temperature. Some transitions have been proposed and discussed by previous investigators. Devillers et al. [139] examined the performance of a few couples in OH lines for CH_4 /air flames in engines. Kostka et al. [140] concluded that the line pair of $Q_1(14)/Q_1(5)$ results in the most precise data for the H_2 /air combustion. Theoretical analysis of these selected signals was produced by the LIFBASE simulation and compiled in Table 3.7.

Table 3.7 Comparisons of the temperature sensitivity between signal pairs.

Transition pairs	(T = 2000 K) / (T = 1000 K)	(T = 2000 K) / (T = 1500 K)	Intensity of the weaker signal at 1000 K
Q ₁ (14)/Q ₁ (5)	10.4	2.19	2.16
R ₂ (13)/P ₁ (2)	10.5	2.17	3.42
R ₂ (2)/R ₁ (12)	6.76	1.89	5.50
P ₁ (7)/Q ₂ (11)	3.80	1.56	20.3
Q ₁ (8)/P ₁ (4)	2.00	1.26	83.0

Results of both Q₁(14)/Q₁(5) and R₂(13)/P₁(2) similarly indicate a higher level of temperature sensitivity than others, while other pairs, such as P₁(7)/Q₂(11), demonstrate a reasonable balance between the sensitivity and signal strengths. After a couple of trial tests, R₂(13)/P₁(2) was eventually chosen, as temperature sensitivity is the most important parameter. Also, the weaker signal of Q₁(14)/Q₁(5) has a marginally lower intensity than R₂(13)/P₁(2), and the two lines are quite far apart, which takes a longer time to switch between wavelengths. In addition, relatively reasonable temperature graphs were obtained from the transition pair R₂(2)/R₁(12) that was employed previously [121], and discussions of these temperature graphs will be given in Section 5.1.2. Figure 3.16 and Figure 3.17 show the simulated spectrum of these two pairs in three temperature conditions, and the resolution is set to be 0.03 corresponding to the practical observations.

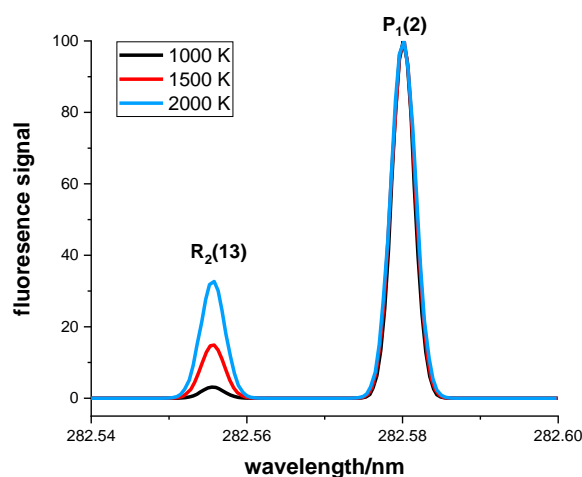


Figure 3.16 The simulated spectrum of R₂(13) and P₁(2) at three different temperature conditions.

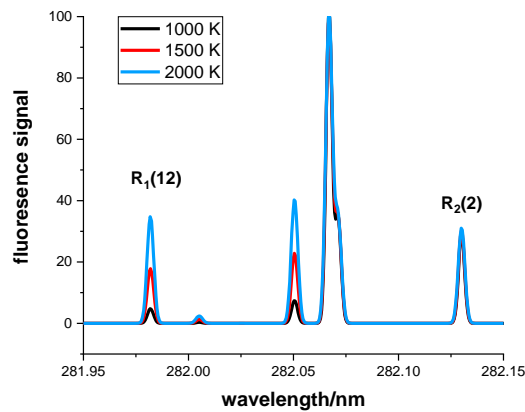


Figure 3.17 The simulated spectrum of $R_2(2)$ and $R_1(12)$ at three different temperature conditions.

The fitting curves of $R_2(13)/P_1(2)$ and $R_2(2)/R_1(12)$ were consequently generated with the use of the software OriginPro, as shown in Figure 3.18 and Figure 3.19, respectively.

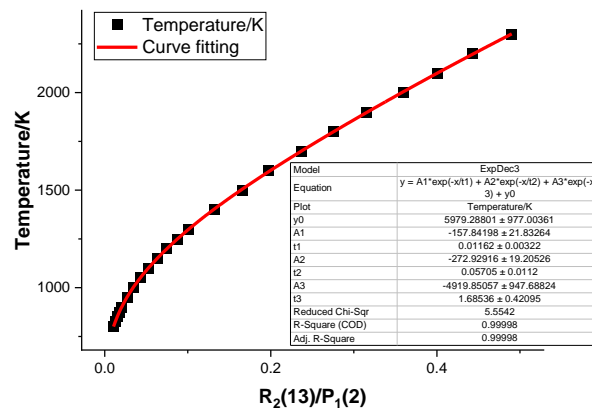


Figure 3.18 Relationship between the simulated intensity ratio of $R_2(13)/P_1(2)$ and the temperature, from 800 K to 2300 K.

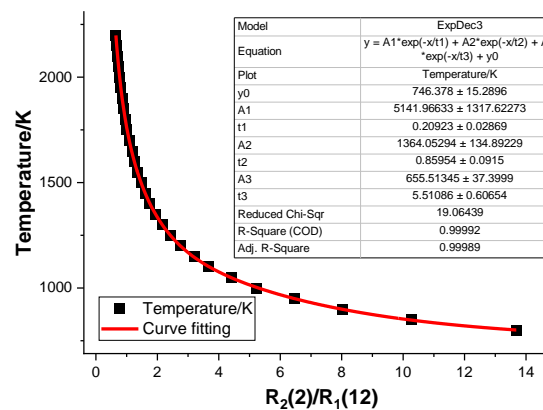


Figure 3.19 Relationship between the simulated intensity ratio of $R_2(2)/R_1(12)$ and the temperature, from 800 K to 2300 K.

The fitting function is arbitrary, chosen because it was found from trial and error to provide an accurate representation of the data. In practice, this method is rather difficult to employ, and the results are oftentimes merely meaningless noise. One innate source of error is the assumption that the targeted flame remains identical during the separate signal recordings, and the judgement of the wavelength peak of each transition directly influences the quality of the LIF outcome. Since the intensity of $R_2(13)$ is quite low, it is also a challenge to produce a more intense image. Regarding the data processing afterwards, compared to the use of thermocouple wires, one advantage of the OH LIF thermometry is that no additional corrections are required, because the quenching effects of two lines are identical.

CHAPTER 4

KINETIC MODELLING DEVELOPMENT

Detailed kinetic mechanisms of hydrocarbon fuels have been developed for decades to improve the ignition performances of combustion technologies, and the demand for much better modelling understanding keeps increasing with the increase in advanced engine concepts, such as homogeneous charge compression-ignition (HCCI). Branched alkanes can be found in petroleum jet fuels, diesel fuels, and also Fischer-Tropsch fuels. A detailed chemical classification of S-8 from Naik et al. [16] indicates that 73.2% of hydrocarbons are branched alkanes with 78% of which fall into the category of single methyl. Previous F-T fuel surrogates commonly utilized highly branched hydrocarbons such as iso-octane to represent the branched alkanes [16, 82, 93, 95]. Also, several F-T studies have previously suggested the involvement of monomethyl alkanes as part of the surrogate [98].

This chapter aims to explore the plausibility of a quality kinetic model for both large normal alkanes and monomethyl alkanes with the use of the software ANSYS Chemkin Pro. Apart from iso-octane, the modelling of branched alkanes is much less studied compared to straight chain alkanes, and their mechanisms usually are individual packages, meaning that the chemical kinetics of other larger hydrocarbon fuels are not included. In this study, 2-methylheptane is utilized to represent the monomethyl alkanes. Firstly, mechanisms with 2-methylheptane kinetics will be examined and selected, then combined into a detailed mechanism containing components of kerosene surrogates. Secondly, further optimizations of the combustion of 2-methylheptane in this new mechanism will be investigated by employing two approaches. In addition, new thermodynamic data of the species related to the combustion of 2-methylheptane will be calculated with the use of updated group additivity values.

4.1 Initial evaluation for mechanisms that contain 2-methylheptane

Experimental studies on the ignition delay time for 2-methylheptane were previously carried out with the use of a shock tube over a wide range of temperature conditions. The measured ignition delay time selected for model validation is from Sarathy et al. [105], at 20 atm and three equivalence ratio conditions. In the simulations using ANSYS Chemkin Pro,

a closed homogeneous batch reactor using the model type of “constrain volume and solve energy equation” was utilized to mimic the environment of the shock tube. Previous autoignition studies of hydrocarbons have based the model in either the “constrain volume” or “constrain pressure” environment, although the discrepancies between these two assumptions are rather trivial with differences not being significant until large changes in temperature or numbers of molecules in the system occur, which is only the case close to the point of ignition. In the current project, the “constrain volume” system was employed to be consistent with the reference mechanism developed by Wang et al. [106], which was utilized as the fundamental base of the modelling study of 2-methylheptane. For a given equivalence ratio condition, the model pressure was set to be the same as the experiment and the range of the simulated temperature was set to be 650-1350 K. In each temperature condition, the predicted ignition delay time was obtained when the peak OH concentration was achieved, as explained in Section 2.3.1.

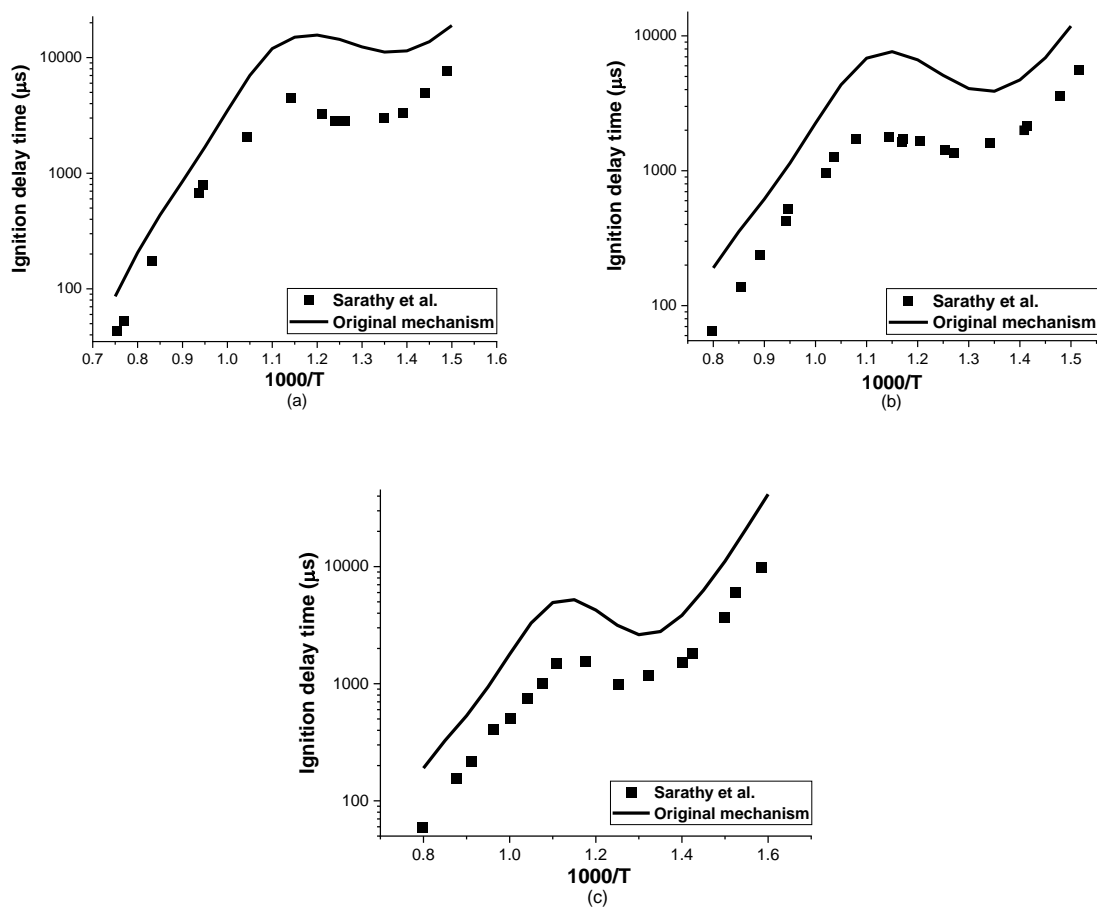
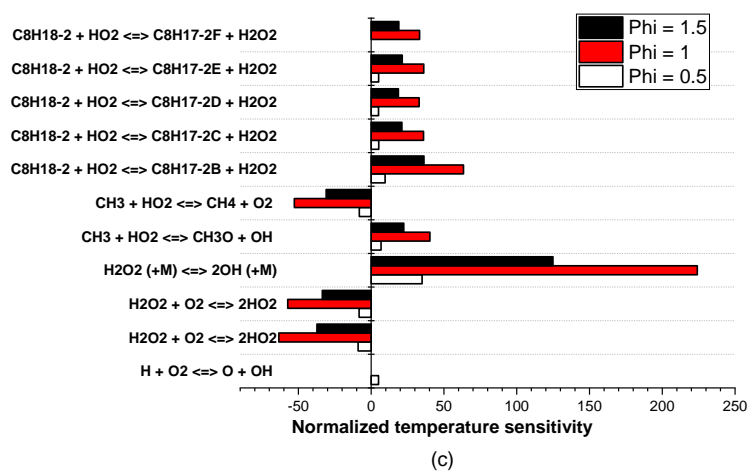
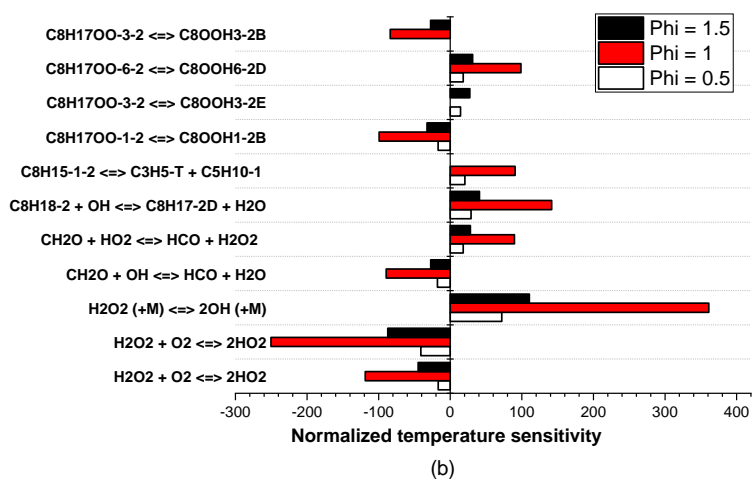
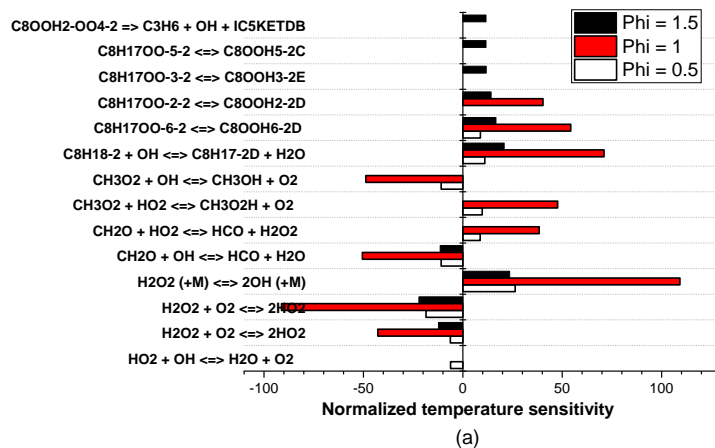


Figure 4.1 Comparisons of the ignition delay time between experimental measurements and kinetic modelling for 2-methylheptane/air combustion at 20 atm: (a) $\phi = 0.5$; (b) $\phi = 1$; (c) $\phi = 1.5$.

Comparisons between experimental data and modelling results are given in Figure 4.1. Three distinct temperature regimes can be observed for 2-methylheptane at all three conditions, and the length of the transitional NTC period of the computational results is in good agreement with experimental data. In addition, it can be observed that the predicted results of the rich condition have the fastest ignition delay time at low temperatures, while the lean condition is the slowest. This result aligned with the comments from Curran [40], as more fuel radicals are being consumed in the rich case that subsequently accelerates the chain branching process. However, the differences between the two approaches are great throughout the entire temperature region, although the gap at the higher temperatures (> 1000 K) is relatively less significant compared to the rest of the regime. In conclusion, mechanism modifications are required to improve the simulation process unless more updated experimental results prove the current sources are defective.

Identifying the dominant reactions in a combustion process is the first step to optimise the performance of a kinetic mechanism. Hence, a temperature A-factor sensitivity analysis for 2-methylheptane at all three equivalence ratios was employed at various temperatures. From the simulated results, the intermediate regimes of 2-methylheptane are approximately 770-870 K for the stoichiometric and lean condition and 800-870 K for the rich condition. Hence, to gain a full picture of the entire temperature regime, results of 714 K, 800 K, 1000 K, and 1250 K were chosen and displayed in Figure 4.2. For a highlighted reaction, if its sensitivity is positive, it indicates that an increase of that rate constant will enhance the reactivity of the combustion process for that temperature condition. Conversely, a negative sensitivity indicates that an increase of that rate constant will reduce the combustion reactivity for that temperature condition. From the sensitivity, the important reactions at all three equivalence ratios are roughly the same with varied scales of importance, except at 714 K when the situation is more complicated. It can be observed from the first three temperature conditions that $\text{H}_2\text{O}_2 + \text{M} \rightleftharpoons 2\text{OH} + \text{M}$ is the most sensitive reaction in the regions where the temperatures are lower than 1000 K, and this is followed by $\text{H}_2\text{O}_2 + \text{O}_2 \rightleftharpoons 2\text{HO}_2$. Furthermore, the result at 1000 K underlines the importance of the H abstraction of the fuel by HO_2 at intermediate and high temperatures combustion. When the temperature rises to a higher level (> 1200 K), the ignition was primarily affected by the C0-C4 chemistry, with $\text{H} + \text{O}_2 \rightleftharpoons \text{O} + \text{OH}$ being the most significant reaction. These analyses corresponded well with

previous theoretical and modelling studies, although the precise temperature boundaries in each domain deviate from different targeted fuels. Additionally, a couple of isomerisation reactions between the RO₂ and QOOH were noticeably prominent at 714 K and 800 K.



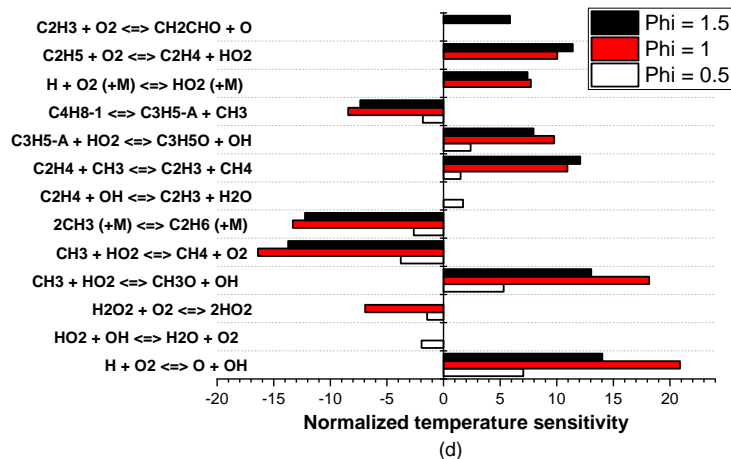


Figure 4.2 Normalised temperature sensitivity of 2-methylheptane/air mixtures at 20 atm: (a) 714 K; (b) 800 K; (c) 1000 K; (d) 1250 K.

The sensitivity results at all three temperature regions in general align well with the discussions of autoignition and the base mechanisms of larger hydrocarbons in Section 2.2.4. The modifications of the kinetic mechanism in the following sections will be based on the sensitivity analysis and the chemistry of chain branching and termination.

4.2 Initial evaluation for the mechanisms of surrogate blends

Due to the size of the detailed mechanism of the CRECK Modelling group, a skeletal mechanism of kerosene surrogates (231 species and 5591 reactions) [88, 143, 144] containing high and low temperature kinetics, along with a newly published C3MechV3.3 mechanism (2857 species and 16522 reactions) of Dong et al. [120] from the NUIG group were selected to examine the quality of the prediction of the surrogate blends of the real fuels. Proposed mixtures from Dooley et al. [17] were utilized to represent Jet A, and the surrogate blends from Naik et al. [16] were used to represent S-8. Computational results were subsequently validated against ignition measurements [96, 145] and the laminar flame speed [146] of real Jet A-1 and S-8 fuel, respectively. The model of premixed laminar-flame speed calculations was utilized to mimic the environment for the laminar flame speed. After the validations, a sub-mechanism related to 2-methylheptane combustion will be assembled to the core of the selected mechanism, and also the key reactions of C0-C4 will be examined.

Computational results of a stoichiometric mixture of Jet A at three pressure conditions were validated against experimental data as shown in Figure 4.3.

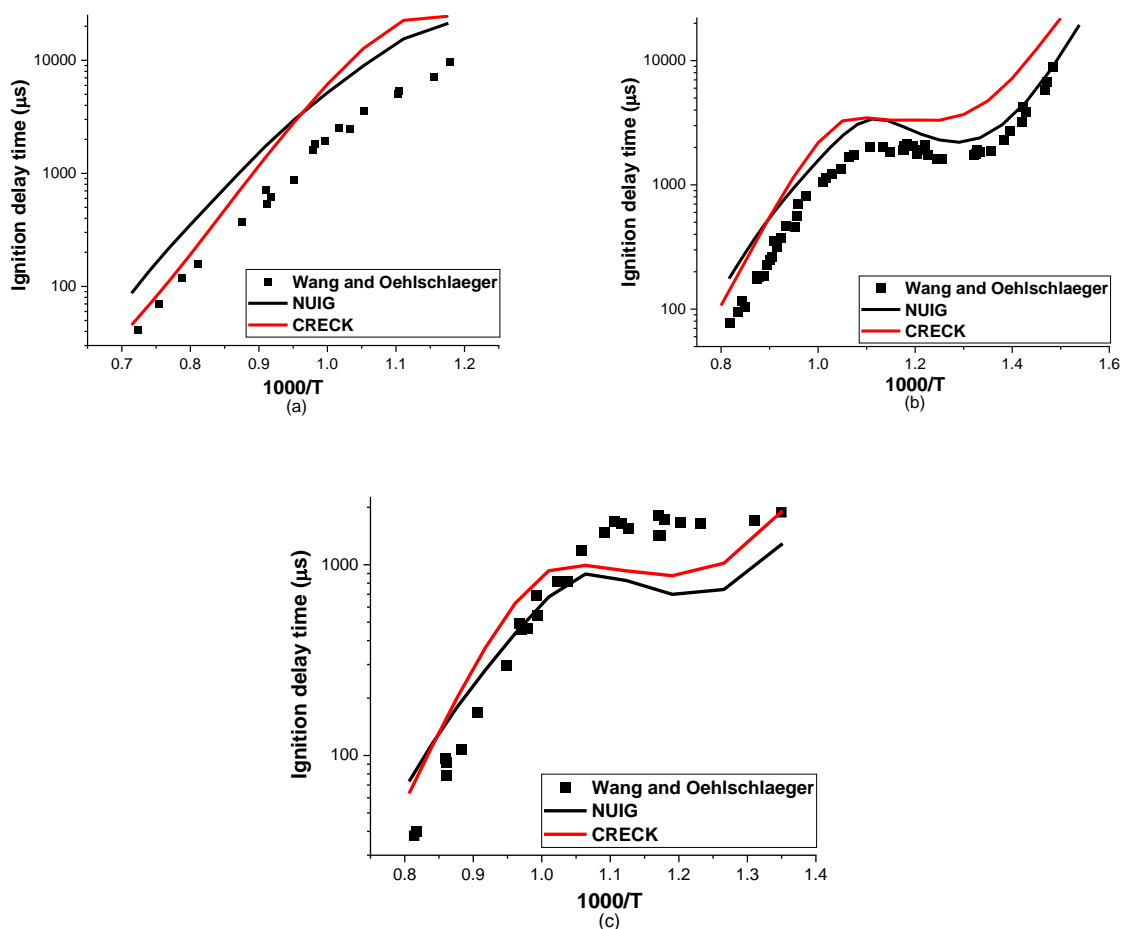


Figure 4.3 Simulations (line) of the ignition delay time of a surrogate of Jet A POSF 4658, compared with the experimental results (scatter) at $\phi = 1$: (a) 8 atm; (b) 20 atm; (c) 40 atm.

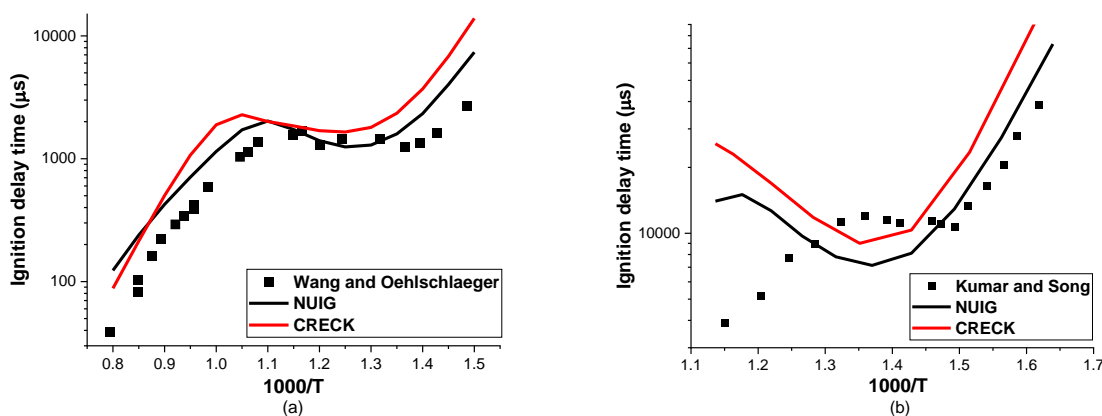


Figure 4.4 Simulations (line) of the ignition delay time of a surrogate of S-8 4734, compared with the experimental results (scatter): (a) $\phi = 1$, 20 atm; (b) $\phi = 1.15$, 7 bar.

At 40 atm, both mechanisms largely underpredict reactivities at low and intermediate temperatures while to some extent overpredict in the high temperature region, indicating a lack of understanding of the kinetics at high pressure conditions. Trends at lower pressure

appear to be more agreeable. At 8 atm, simulations from NUIG generally overpredict the ignition by a factor of two to three for the temperature conditions of 850-1400 K. Simulations from CRECK on the other hand, show a greater discrepancy with the experimental data at $T < 1000$ K while at higher temperatures, particularly above 1250 K, it agrees very well with the measurements. At 20 atm, predictions of ignition delay time from NUIG correspond quite reasonably, especially at low temperatures, and the period of NTC (around 770-900 K) matches excellently with the experimental results. Similar conclusions can be drawn for the surrogate mixture of S-8 fuel at the same pressure condition as depicted in Figure 4.4 (a).

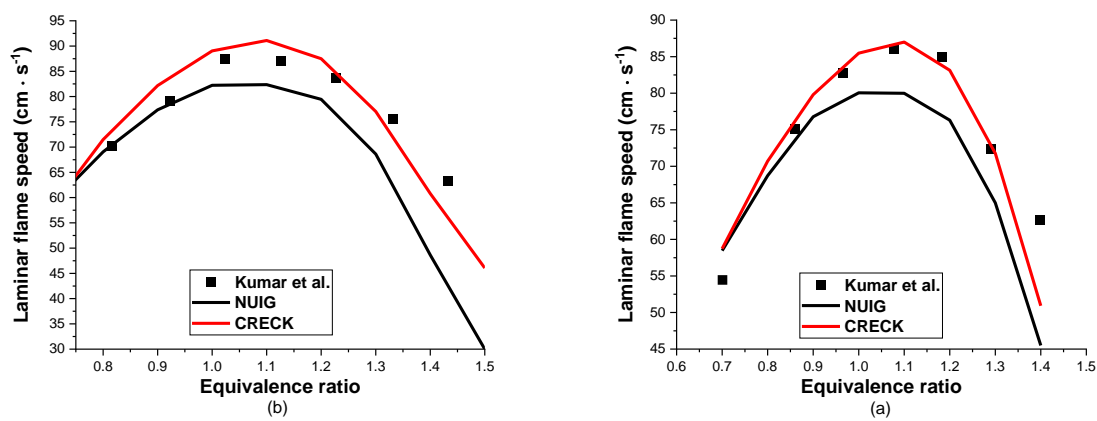


Figure 4.5 Simulations (line) of the laminar flame speed of surrogates of real fuels at 1 atm and 470 K, compared with the experimental results (scatter): (a) Jet A1; (b) S-8.

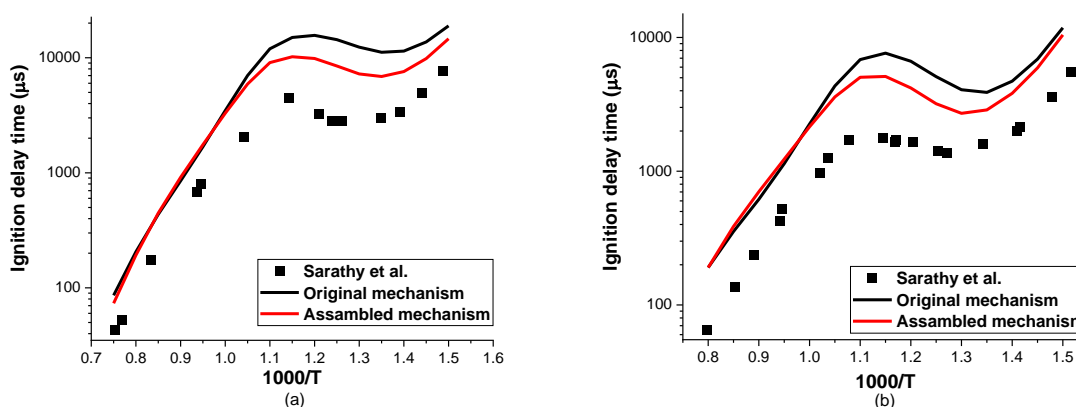
Both ignition delay time results of 7 bar at $\phi = 1.15$, however, show an opposite trend once the temperature increases above 700 K, suggesting an intrinsic disagreement of the kinetics at lower pressure. Results of the laminar flame speed at 1 atm and 470 K are shown in Figure 4.5. Both surrogate modelling values indicate that CRECK predicts reasonably well with the measurements while NUIG simulates reasonably well only at the flame lean conditions while underestimates by about 15-20% at stoichiometric and rich conditions. In summary, both mechanisms can estimate the combustion process reasonably in one model type while it requires optimizations for another characteristic.

To improve the mechanism of 2-methylheptane, the ignition delay time from the literature and species mole fraction from PLIF in this study were employed for validation. Ideally, modifications should be addressed for all the reactor models concerned, while obstacles are noted in both interested mechanisms due to the size or their different methods of assembly. CRECK provides their chemical kinetics in a lumped manner, meaning similar species of one

group are treated as a single representative. Moreover, the complicated breakdown of large hydrocarbons is also combined in a single reaction, which causes extra difficulty in the simulation of the ignition delay time. Outside the rate constants of the C0-C4 kinetics, therefore, it is impossible to traditionally refine the rate rules of each reaction class for bigger hydrocarbons without the discussion of the CRECK research group. As for NUIG, mainly because of its great size, the process of 1D premixed laminar flame simulation is extremely time-consuming. After judging the pros and cons, the sub-mechanism of the 2-methylheptane kinetics was decided to compile with the C3MechV3.3. One modification was made in regard to the decomposition of a large carbonylhydroperoxide IC5KETDB (SMILES representation: =O=CCC(C)(C)OO, a representative of the OOQOOH class of compound). As this reaction was originally highlighted in the low temperature combustion, hence the rate constant was updated to that value from the original mechanism of Wang et al. [106]. The rate constant expression of IC5KETDB \rightleftharpoons CH3COCH3 + CH2CHO + OH is stated as:

$$k = 10^{-1.93} \times \exp(-19628/T) \text{ cm}^3 \cdot \text{molecule}^{-1} \cdot \text{s}^{-1}$$

Simulated results with the use of the assembled mechanism for 2-methylheptane/air combustion at all three equivalence ratio conditions are shown in Figure 4.6, compared with the original predictions and measurements. The graph shapes are mostly identical, although the transition of intermediate to high temperature region is increased by about 40 K in the case of $\varphi = 1.5$. Marginal improvements were shown at temperatures below 700 K and in the NTC region 750-950 K, and the modelling shows that reactivities are increased by 35% at the lean and stoichiometric conditions and by 30% at the rich condition. In addition, the kinetics at high temperature remains unchanged.



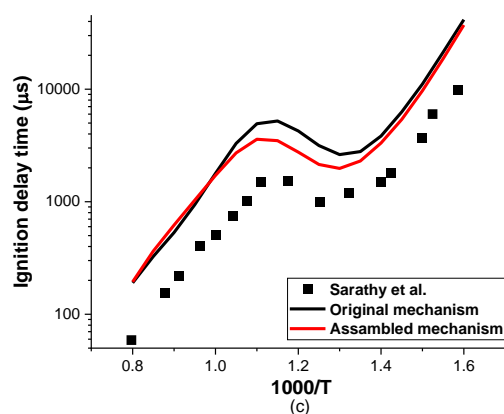


Figure 4.6 Comparisons between the original mechanism and assembled mechanism for the combustion of 2-methylheptane/air, at 20 atm: (a) $\phi = 0.5$; (b) $\phi = 1$; (c) $\phi = 1.5$.

4.3 Thermodynamic data

As briefly discussed in Section 2.1.4, thermochemistry is of great importance to accurately describe the combustion process of fuels, because it is useful to evaluate equilibrium constants and hence the reverse rate constant of an elementary chemical reaction can be obtained, which consequently improves the quality of chemical kinetics.

Benson and co-workers [147] proposed an empirical approach to estimate the thermodynamic properties of species within uncertainties. The molecule is first divided into polyvalent atoms and for each atom, a specific value is assigned. Thus, the total function of the molecule is the accumulation of one or a few atoms. Properties of interest include heat capacity C_p , enthalpy H , and entropy S , and the accuracy of results is largely dependent on the sources of data. Enthalpy is typically measured by experiments, while entropy is commonly calculated with the use of statistical thermodynamics. Heat capacity can be measured experimentally for stable species, while it is difficult for free radicals. Hence, discrepancies are inevitable between sources, and it has been commented that studies of entropy and heat capacity are comparatively fewer than enthalpy [148]. Validated thermodynamic results are frequently found in the demands among radicals, especially for larger hydrocarbons, notwithstanding the significant efforts of the combustion community. This is partly due to the experimental obstacle to determining the accurate thermodynamic properties of radicals, hence the application of group additivity is effectively hindered. Previously, a detailed compilation of group values over a wide range of species was reported by Benson [26], at standard conditions of 1 atm and 25 °C. Recently, a few studies have provided new insights

into the database by employing theoretical approaches. Goldsmith et al. [149] examined the properties of 219 molecules relevant to combustion by using the *ab initio* method, including many small radicals. Burke et al. [148] reviewed the literature and updated the group value of the thermochemical properties for a variety of C1-C4 species. Some modelling studies have since then made efforts to update the thermodynamic data with the new group values from Burke et al. [148]. Bulger et al. [54] studied the oxidation of three pentane isomers in a rapid compression machine, and their results indicate that by replacing the old thermochemical value with an updated source, a significant improvement is observed between the experiments and simulations at lower temperatures. A similar conclusion can be drawn by Mohamed et al. [56] in a modelling study of 2-methylhexane.

The program THERM developed by Ritter [150] utilized the method of group additivity (GA) from Benson et al. [147] to calculate thermochemical data of gas phase radicals and molecules, and this has been largely employed by researchers to generate large amounts of data. Results are presented in the NASA polynomial form, and detailed thermochemical properties can be calculated by the following equations:

$$\frac{C_p}{R} = a_1 + a_2 T + a_3 T^2 + a_4 T^3 + a_5 T^4 \quad (\text{Eq. 4.1})$$

$$\frac{H^\circ}{R_u T} = a_1 + \frac{a_2}{2} T + \frac{a_3}{3} T^2 + \frac{a_4}{4} T^3 + \frac{a_5}{5} T^4 + \frac{a_6}{T} \quad (\text{Eq. 4.2})$$

$$\frac{S^\circ}{R} = a_1 \ln T + a_2 T + \frac{a_3}{2} T^2 + \frac{a_4}{3} T^3 + \frac{a_5}{4} T^4 + a_7 \quad (\text{Eq. 4.3})$$

Where a_1 , a_2 , a_3 , a_4 , a_5 , a_6 , and a_7 denote numerical coefficients, T is temperature, and R_u is the universal gas constant. Each data file includes a total of 14 coefficients to fit a wide range of temperatures, commonly from 300 K to 5000 K. A breakpoint temperature (T_{bk}) is defined to ensure the temperature from low to high can function with continuity [151]. The first set of seven constants covers the temperature higher than this value and the second set of seven constants belongs to the temperature condition lower than T_{bk} [150].

This study utilized the concept of THERM. The thermodynamic properties at low temperatures were calculated with the use of the modified value of the group additivity from Burke et al. [148], and a few corrections on the enthalpy and entropy were also explained in the following sections. Noticeably, as Burke et al. [148] commented, C/C2/H/OO, OO/C/H, and ALPEROX that are related to the structures of RO₂, QOOH, and OOQOOH radicals are

among the groups of undergoing the largest change of value. The data in the GA is applicable from 300 K to 1000 K, and the coefficient for high temperature was generated by the fitting graph approximation. An example is displayed in Figure 4.7.

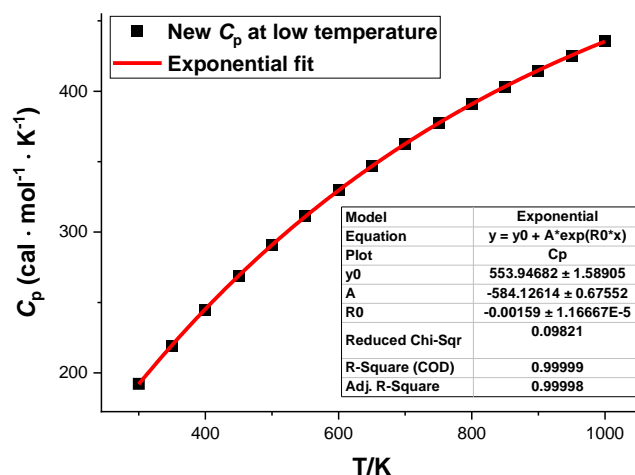


Figure 4.7 Approximation of the new heat capacity value of 2-methylheptane.

To estimate the enthalpy of the free radicals, consider the H atom abstraction of the fuel:



The bond dissociation energy of the forward reaction, or in other term the bond dissociation enthalpy, is defined as $DH^\circ(\text{R}-\text{H})$:

$$DH^\circ(\text{R}-\text{H}) = H^\circ(\text{R}') + H^\circ(\text{H}') - H^\circ(\text{RH}) \quad (\text{Eq. 4.4})$$

The enthalpy of radicals can then be calculated, and the bond dissociation energy for the H atom is estimated to be $52.1 \text{ kcal} \cdot \text{mol}^{-1}$ [26]. A similar ideology of a parent molecule is used to determine the entropy and heat capacity, which can be calculated in the following equations:

$$S^\circ(\text{R}') = S^\circ(\text{RH}) + \Delta S_{298}^\circ \quad (\text{Eq. 4.5})$$

$$C_p(\text{T})(\text{R}') = C_p(\text{T})(\text{RH}) + \Delta C_p(\text{T}) \quad (\text{Eq. 4.6})$$

Where the values of ΔS_{298}° and $\Delta C_p(\text{T})$ are estimated from RH, accounting for the discrepancies in vibrational frequencies and rotational barriers of internal rotors [152]. Also, the correction due to electron spin for the entropy is required. Factors of symmetry and chirality are excluded from the estimation of ΔS_{298}° which requires further adjustments.

4.3.1 Corrections – Gauche interactions

For larger and branched hydrocarbons, gauche interaction can occur between the hydrogen atoms when their attached carbon atoms form a dihedral angle of 60° . Similar to alkanes, this also happens for radicals with two common types, RG1 and RG2. To explain the term more clearly, each carbon position of 2-methylheptane was labelled as shown in Figure 4.8. Consider the second and third carbon, Figure 4.9 depicts the potential interactions for each case. The reaction increases the heat formation of the molecule, for instance, every gauche accounts for about $0.8 \text{ kcal} \cdot \text{mol}^{-1}$ for alkanes [26], thus a correction of the enthalpy is needed.

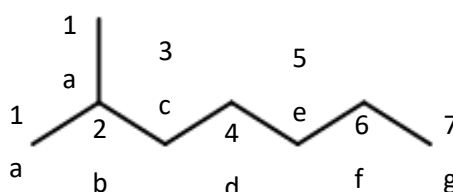


Figure 4.8 Structure of 2-methylheptane with labelled carbon number.

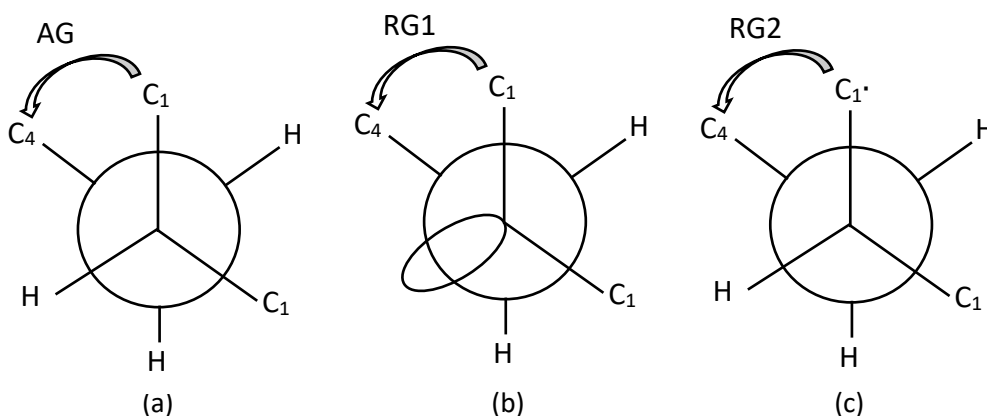


Figure 4.9 Mirror images of C2-C3 bond in 2-methylheptane: (a) alkane gauche; (b) RG1; (c) RG2.

While the Benson group only briefly mentioned this phenomenon and did not discern the differences between radicals and alkanes, later researchers have addressed the condition of the hydrocarbon radicals more attentively, although the results are not quite consistent. Marsi et al. [153] used the *ab initio* theory to investigate the geometries and enthalpies of 4 alkanes and 31 alkyl radicals at standard states, and the estimated group values were $-0.2 \text{ kcal} \cdot \text{mol}^{-1}$ for RG1 and zero for RG2. Sabbe et al. [154] calculated the standard enthalpy of a set of hydrocarbons and hydrocarbon radicals by CBS-QB3 theory, and corrections made

for RG1 and for RG2 are $0.43 \text{ kcal} \cdot \text{mol}^{-1}$ and $0.17 \text{ kcal} \cdot \text{mol}^{-1}$, respectively. In this project, gauche interaction for RG1 employed values from Sabbe et al. [154] and was set to be zero for RG2. Additionally, alkyl peroxy and alkyl hydroperoxy radicals are expected to have no gauche interactions present. Take fuel radical $(\text{CH}_3)_2\text{CHCH}(\cdot)(\text{CH}_2)_3\text{CH}_3$ at position c as an example:

The molecule is formed by the following groups:

$$3[\text{C/C/H3}] + 4[\text{C/C2/H2}] + [\text{C/C3/H}] + [\text{S}] - \Delta H^\circ(\text{H}\cdot) = -6.2$$

Gauche interaction for RG1 = 0.43

$$\text{Hence, } H^\circ = -6.2 + 0.43 = -5.77 \text{ kcal} \cdot \text{mol}^{-1}.$$

4.3.2 Corrections – Optical isomers and symmetry

Optical isomers share mirrored structures but are non-superimposable on each other, which can be described as chiral. A carbon atom attached to four different groups is referred to as chiral carbon, and a correction of $R\ln 2$ must be added to the total entropy since it introduces disorder to the species [56, 147]. On the contrary, symmetry structure reduces the disorder, hence the contribution to entropy is calculated by subtracting $R\ln \sigma_{\text{sym}}$, where σ_{sym} is the symmetry number in a molecule. Symmetry can be internal or external, and the total number is calculated as $\sigma_{\text{sym}} = \sigma_{\text{in}} \times \sigma_{\text{ex}}$. In the current species of interest, only external types are found. An example for alkyl peroxy radical is shown as follows:

S° for $(\text{CH}_3)_2\text{CHCH}_2\text{CH}(\text{OO}\cdot)(\text{CH}_2)_2\text{CH}_3$

The molecule is formed by the following groups:

$$3[\text{C/C/H3}] + 3[\text{C/C2/H2}] + [\text{C/C3/H}] + [\text{C/C2/H/OO}] + [\text{ALPEROX}] + [\text{OO/C/H}] = 131.09$$

Symmetry: three methyl- groups. Hence, $-R\ln \sigma_{\text{sym}} = -R\ln 27 = -6.55$

Optical isomer: $R\ln 2 = 1.38$

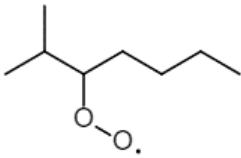
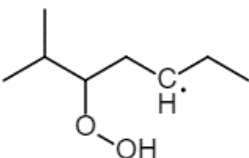
$$S^\circ = 131.09 - 6.55 + 1.38 = 125.92 \text{ cal} \cdot \text{mol}^{-1} \cdot \text{K}^{-1}.$$

4.3.3 Value comparison

An example of the modified thermodynamic properties for RO_2 and QOOH is shown in Table 4.1, compared with original values. Reverse reaction rate constants were calculated by use of the forward reaction rate constant from Wang et al. [106]. The increase of enthalpy and entropy leads to the balance shift of the reaction, hence the new reaction rates of $\text{QOOH} \rightarrow \text{RO}_2$ are approximately twenty times faster at room temperature and six times faster

at 800 K. Figure 4.10 demonstrates the simulations of the assembled mechanism with original and new thermochemistry data.

Table 4.1 Comparison of enthalpy and entropy between the original and modified values.

		H° (kcal · mol ⁻¹)	S° (cal · mol ⁻¹ · K ⁻¹)	ΔG (kcal · mol ⁻¹)	k_r (cm ³ · molecule ⁻¹ · s ⁻¹)
C8H17OO-3-2 	original	-43.38	124.92		
	new	-40.83	125.92		
	Δ	+2.55	+1.00		
C8OOH3-2e 	original	-30.53	130.17		
	new	-26.26	130.66		
	Δ	+4.27	+0.49		
C8H17OO-3-2 → C8OOH3-2e	original Δ	12.85	5.25	11.29	7.93×10^{-21}
	At 298.15 K new Δ	14.57	4.74	13.16	1.90×10^{-19}
C8H17OO-3-2 → C8OOH3-2e	original Δ	13.28	6.20	8.32	2.07×10^{-17}
	At 800 K new Δ	14.04	3.63	11.14	1.19×10^{-16}

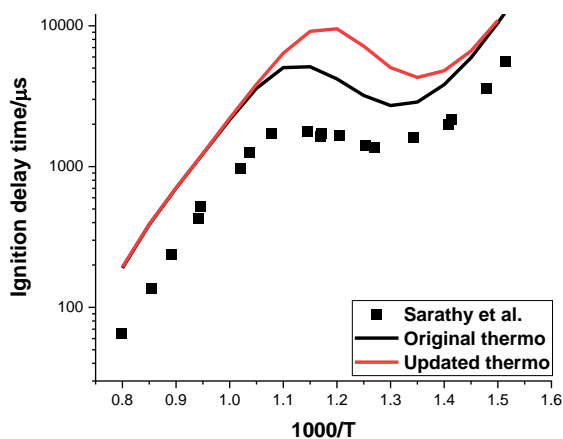


Figure 4.10 Comparison of the simulated ignition delay time for 2-methylheptane/air at 20 atm and stoichiometric condition, by using the assembled mechanism and different thermodynamic data.

The reactivity is mainly reduced around the NTC region, as the transition of intermediate to high temperature region is decreased by 40 K. In the stoichiometric case, ignition delay

time is slowed down most significantly at 770-870 K, by a factor of 1.5 to 2. The kinetics at high temperature and low temperature (< 700 K) on the other hand remain unaffected. This trend is consistent with the results of Mohamed et al. [56]. The compilation of the group additivity values and the full set of updated new thermodynamic data in NASA polynomial form are listed in Appendix A and Appendix B, respectively.

4.4 Development of a sub-mechanism of 2-methylheptane – rate constants

Refining the kinetic data of the important reactions is the most common approach to upgrading a mechanism, and the rate constant of a singular reaction can be determined by various methods, from quantum theory to experimental investigation. Baulch et al. [37] compiled a comprehensive review of 196 fundamental reactions, and Baulch et al. [38] later extended and updated the previous work. Also, a few more updated studies concentrated on the rate constant of small radical reactions and presented new perspectives with the assistance of advanced laboratory techniques [40]. Importantly, the chemistry of C0-C4 is the base of all large hydrocarbon combustion, thus, to not disturb the general environment in the NUIG mechanism, the rate constant expressions of the following reactions are recommended to remain unchanged for 2-methylheptane kinetics unless large disagreements are observed. Based on the sensitivity in Figure 4.2, details of the following five reactions are discussed, and their significance varies in three temperature regimes:



The decomposition of hydrogen peroxide is a pressure-dependent reaction. It is the most significant reaction for the autoignition of larger hydrocarbon in the intermediate region, which is around 750 K to 1000 K in the case of 2-methylheptane. Earlier experimental studies were mostly conducted around atmospheric pressure [155, 156]. In recent times, Hong et al. [157–159] contributed greatly to the understanding of fundamental kinetics with the use of a

shock tube in the temperature range of 930-1290 K. In an argon bath gas, measurements were performed at lower pressure conditions, between 1-2 atm [157, 159] and near 3.5 atm [158]. Kappel et al. [160] measured the reaction rate behind reflected shock waves at 1 bar, 4 bar, and 15 bar, from 954 K to 1289 K. Sajid et al. [161] also performed the experiment behind a reflected shock wave in a mixture of diluted H₂O₂ and Argon between 930-1235 K, and at a pressure of 1 atm, 2 atm, and 10 atm. Arrhenius expressions for both low and high pressure subsequently are derived from the respective experimental data of these investigators. Figure 4.11 shows several calculated rates from the low-pressure limit, compared with experimental sources that were conducted below 2 atm. As indicated from the graph, both expressions of rate constant from Hong et al. [157] and the NUIG mechanism agreed with the measurements quite reasonably while the result of Baulch et al. [37] overpredicted by approximately a factor of 2 in the high temperature region.

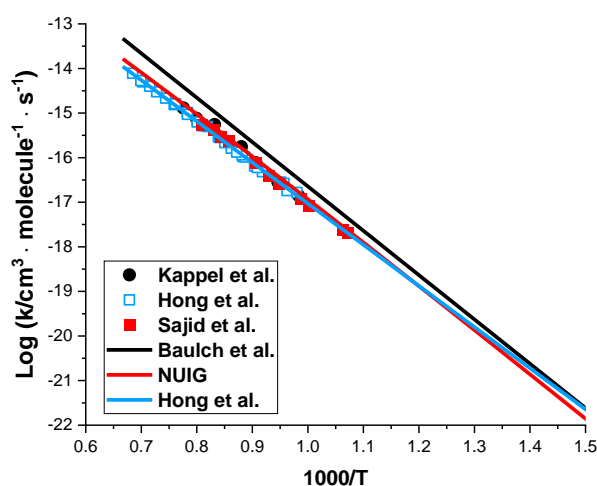


Figure 4.11 Comparisons of the low-pressure limit for reaction 4.1 between various experimental records (scatter) and three calculated rates (line), reference: blue open square [158].

There are no measurements at the pressure condition of 100 atm or above for validation. Commonly, the high-pressure limit is estimated by the extrapolation of the fall-off curve. However, only the rate constants that are near the low-pressure limit are usually available and the transition behaviours from 1 atm to 10 atm are not necessarily apparent, hence uncertainties are expected for both the intermediate region and the fitted high pressure rate [160, 161]. The Troe approach [155] is frequently used to calculate the fall-off range. In addition, at three temperature conditions, low- and high-pressure limit, and fall-off region

were calculated with the use of the expressions from NUIG, as displayed in Figure 4.12. At around 10 atm, all three temperatures begin to experience fall-off, and each curve corresponds well with their respective experimental results. To improve the kinetic models, more measurements at high pressure and also at temperature conditions below 900 K are highly recommended.

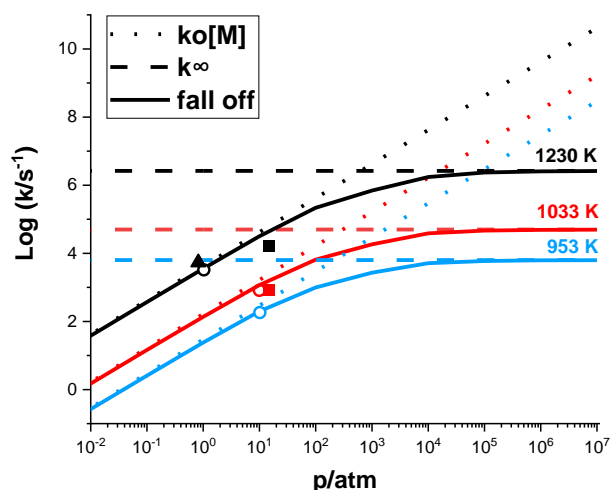


Figure 4.12 Simulated low- and high-pressure limit and fall-off region of reaction 4.1 at three temperature conditions, compared with experimental data at various pressures, reference: square [160], open circle [161], up triangle [157].

Examination of reaction 4.2 was carried out similarly, and the comparison between reviews and a selection of experimental measurements [159, 160, 162–164] is shown in Figure 4.13. One unique characteristic of this reaction rate is that the apparent discontinuity can be observed between the low and high temperature regions. This phenomenon may be related to the pressure dependency of k_2 at lower temperatures (< 500 K), which no longer becomes a factor once the temperature increases [165]. Thus, a single Arrhenius expression, such as the review of Baulch et al. [37], fails to capture the entire rate constant variation or is only reasonable over a certain temperature range. The original mechanism from Wang et al. [106] derived the rate value from Kappel et al. [160] that concentrated on hydrogen peroxide and its subsequent reactions. Their results are in good agreement with the measurements by Hong et al. [159] at 1072–1283 K. From the graph, the originally calculated rates also correspond reasonably well with some experimental data in the low temperature conditions. Other double-part references also showed good agreement with some of the experimental

results at temperatures below 500 K. However, when the temperature increases to around 1000 K, the predictions of Baulch et al. [38] start to deviate.

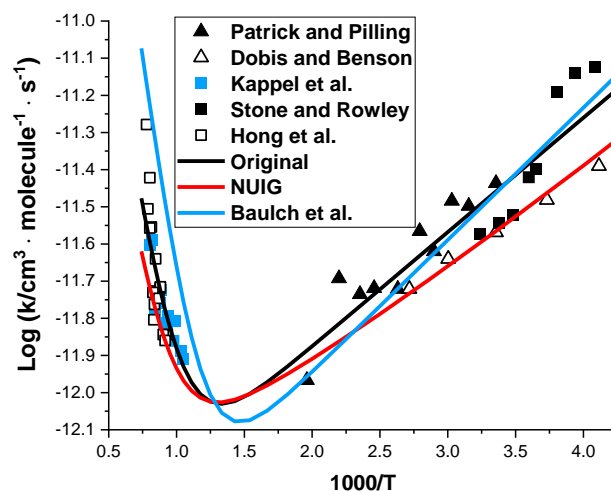


Figure 4.13 Reaction 4.2 comparison between the experimental records (scatter) and calculated rate constants (line).

As the most significant reaction for hydrocarbon combustion in the high temperature range, the reaction rate constant of $\text{H} + \text{O}_2 \rightleftharpoons \text{O} + \text{OH}$ is substantially investigated with both experiments and theories. For instance, Hong et al. [166] measured the rate constant by using a shock tube over the temperature range of 1100–1530 K and provided a refined rate equation, which has been adopted in modelling groups such as CRECK and NUI Galway. Figure 4.14 shows a comparison between the experimental studies [166–169] and a few rate constant expressions from 900 K to 3000 K. Throughout the total temperature range, the original value from Wang et al. [106] is about 10% quicker than the result of Hong et al. [166] and is in reasonable agreement with various sources of measurements. The preferred expression from the review of Baulch et al. [37] on the other hand, began to deviate more visibly from the other two sources around 1500 K. Interactions between CH_3 and HO_2 are other important reactions, which lead to two pathways that are dominating and competing. The production of CH_3O and OH improves the reactivity while the forming of CH_4 and O_2 terminates the reaction chain, as the sensitivity in Figure 4.2 (d) and a new study of ignition behaviours of C1–C3 blends from Martinez et al. [170] indicate. The original mechanism employed the theoretical rates from Jasper et al. [171] for both channels while NUIG utilized the rate

constant expression from Zhu and Lin [172] for reaction 4.5, which enhanced the termination process for about 50-60% compared to the results of Jasper et al. [171] at 1000-1500 K.

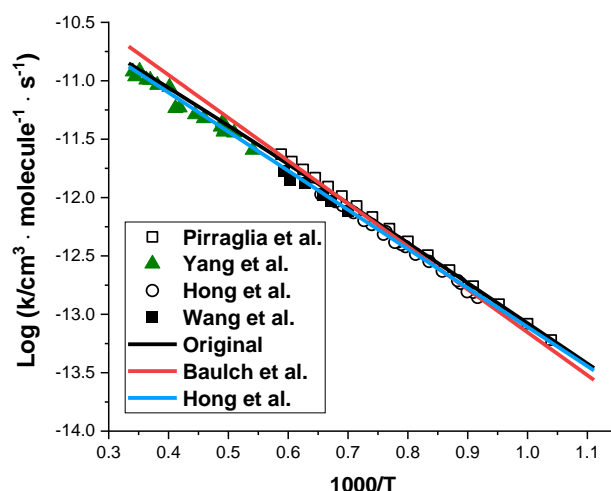


Figure 4.14 A comparison of k_3 between various experimental records (scatter) and reviews (line).

In conclusion, rate constants calculated by the C3MECHV3.3 mechanism show good quality in the simulation of the key aspects in the combustion environment, although minor adjustments can be argued. The rate constant expressions of all five investigated reactions are suggested to remain unchanged and details are stated below:

For the pressure dependent reaction 4.1:

$$k_0 = 10^{0.6} \times T^{-2.3} \times \exp(-24531) \text{ s}^{-1}$$

$$k_\infty = 10^{12.3} \times T^{0.9} \times \exp(-24533.97/T) \text{ s}^{-1}$$

For the other temperature dependent reactions:

$$k_2 = 10^{-9.77} \times \exp(-5556/T) + 10^{-12.49} \times \exp(709/T) \text{ cm}^3 \cdot \text{molecule}^{-1} \cdot \text{s}^{-1}$$

$$k_3 = 10^{-9.76} \times \exp(-7693/T) \text{ cm}^3 \cdot \text{molecule}^{-1} \cdot \text{s}^{-1}$$

$$k_4 = 10^{-5.93} \times T^{0.269} \times \exp(346/T) \text{ cm}^3 \cdot \text{molecule}^{-1} \cdot \text{s}^{-1}$$

$$k_5 = 10^{-20.52} \times T^{2.83} \times \exp(1877/T) \text{ cm}^3 \cdot \text{molecule}^{-1} \cdot \text{s}^{-1}$$

4.5 Development of a sub-mechanism of 2-methylheptane – rate rules

For mechanisms of more complex species, with considerable numbers of intermediate species and reactions, it is unrealistic to completely describe all the involved reactions based

on experimental or theoretical expressions of the actual rate constants, as in the vast majority of cases there are no actual measurements or theoretical studies available. Thus, the rate rule designed for specific reaction classes is another useful tool, particularly for the larger hydrocarbon. In the subsequent sections, nine reaction classes that are significant to the chemistry of low and intermediate temperatures from the original mechanism were examined with more updated rate rules in the literature.

The balance of the chain branching is the prime priority, hence the most prominent rate rules in each class do not necessarily end up being the best option, and the compatibility of the mechanism also needs to be considered. To avoid confusion, all modelling tests were performed with the new thermodynamic data from Section 4.3. Updated rate rules will be applied to the assembled mechanism in sequence. For instance, during the discussion of the third reaction class, the updated rules of the previous two reaction classes will be employed as well as the current one. Additionally, the reaction classes with multiple sources of rate rules such as $\text{RO}_2 \rightarrow \text{QOOH}$, and the undetermined classes, such as the second oxygen addition, will be initially analysed in their respective sections and concluded later at the end of the chapter. A compilation of new rate rules of all reaction classes is presented in Appendix C.

4.5.1 H abstraction: Fuel + OH \rightarrow R + H₂O

By interacting with small radicals such as OH, HO₂, or CH₃, hydrocarbon fuels break down into fuel radicals which then quickly decompose or further react with other species. Due to the single methyl- on the straight chain, distinctive 2-methylheptane radicals can be formed on primary (1°), secondary (2°), and tertiary (3°) sites. Abstraction by OH is of great importance during the entire combustion process, and sensitivity (Figure 4.2 (b)) shows that the 2° type at position *d* (Figure 4.8) is highlighted in the low temperature region under 800 K.

Earlier mechanism studies of gasoline surrogates [51, 94] were inspired by the experiments of propane or *i*-butane [173]. Partly due to the simple structures of the chemicals, the authors did not differentiate the types of abstraction specifically in the kinetic modelling, meaning that the chosen rate rule of all radicals on 1° or 2° was set to be the same. Cohen [174] proposed that these three types of bonds should be divided into smaller classes because the activation energy may be dependent on the next-nearest neighbour (NNN) carbons. For example, the primary site in this approach can be defined as P₁ or P₂, where the subscript

indicates the number of carbons attached to the NNN carbons. A few direct experimental measurements have brought more insights in recent years. Sivaramakrishnan and Michael [175] measured the rate constants of OH abstraction for five C5-C8 liquid fuels behind the reflected shock tube, at a wider range of temperatures from 789 K to 1308 K. Badra et al. [176] also investigated this reaction class for seven larger alkanes behind the reflected shock waves, from 880 K to 1440 K. This work adopted the rate rules from both studies and the updated Arrhenius expressions are compiled in Table 4.2.

Table 4.2 Rate rules of H abstraction by OH per H atom for each radical.

Radical	C-H type	A ($\text{cm}^3 \cdot \text{molecule}^{-1} \cdot \text{s}^{-1}$)	n	E_a ($\text{cal} \cdot \text{mol}^{-1}$)
C8H18-2a	P_2 [175]	6.50×10^{-13}	2.08	375.5
C8H18-2b	T_{100} [176]	2.00×10^{-5}	0	2261
C8H18-2c	S_{21} [176]	3.15×10^{-6}	0	1578
C8H18-2d	$S_{11'}$ [175]	3.27×10^{-7}	0.32	846
C8H18-2e	S_{11} [175]	3.33×10^{-12}	1.81	-1015
C8H18-2f	S_{01} [175]	4.11×10^{-9}	0.94	504.7
C8H18-2g	P_1 [175]	5.30×10^{-12}	1.81	868.3

Noticeably, the influences of the in-plane and out-of-plane abstraction on the 1° and 2° sites were previously discussed [175, 177], and n-heptane was utilized to investigate this unique phenomenon on the secondary sites. The molecule structure is depicted in Figure 4.15. The H atoms of S_{11} at position d ($S_{11'}$) all neighbour with the S_{11} H atoms as well, while the H atoms of S_{11} at position c (S_{11}) and e (S_{11}) neighbour with the S_{01} H atoms on one side and S_{11} H atoms on the other. These two kinds of S_{11} have a $0.4 \text{ kcal} \cdot \text{mol}^{-1}$ discrepancy in the barrier heights based on *ab initio* calculations, and the rate constant expressions were later measured experimentally. Rate constants of OH + 2-methylheptane were measured by Badra et al. [176], and the investigators adopted the $S_{11'}$ model of Sivaramakrishnan and Michael [175] to determine the radical at position d . This may lead to arguments as H atoms on this S_{11} neighbour with the S_{21} H atoms and S_{11} H atom. Because no other experimental records regarding this 2° type are available presently, this study will also use the $S_{11'}$ expression on the radical d . Figure 4.16 compares the rate rules of various sources for all three abstraction types.

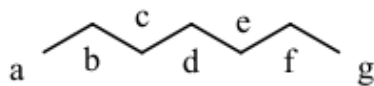


Figure 4.15 Structure of n-heptane.

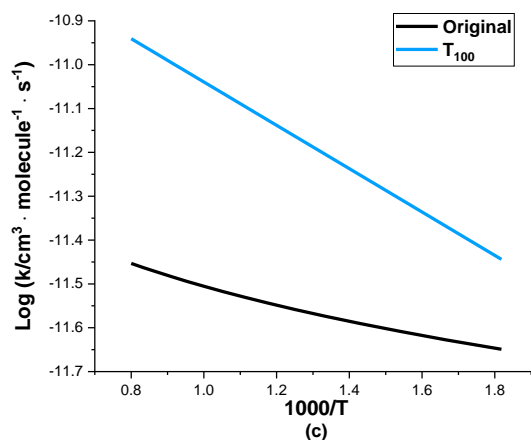
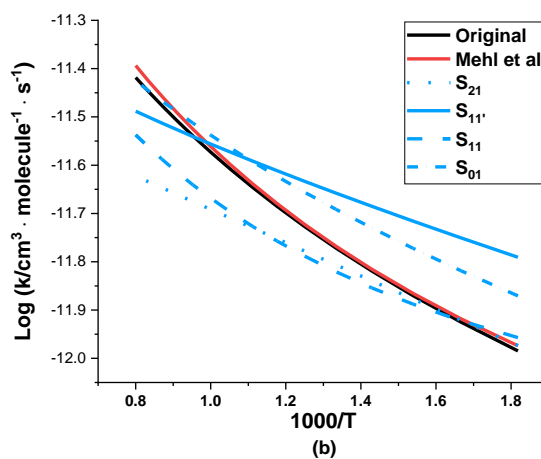
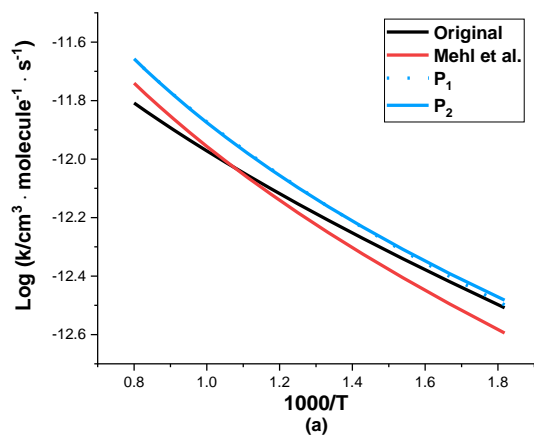


Figure 4.16 Comparison of the rate constant expression of H abstraction by OH: (a) primary carbon site per H atom; (b) secondary carbon site per H atom; (c) tertiary carbon site per H atom.

For the primary site, the rates of P_1 and P_2 show little differences throughout the temperature regions, and in general are faster than the original value, particularly at temperatures above 1000 K by approximately 30%. Conditions are more complicated for secondary carbon sites. Abstraction rates at position d and f are enhanced at lower temperatures to some extent (< 1000 K), while the other two become relatively slower. The new tertiary rate is greatly increased compared to the original value. By applying these new rules, only little modelling improvements have been shown only around the intermediate temperature. More experimental data, especially on the larger branched alkanes, to distinguish the abstraction types for future research is highly recommended.

Additionally, reactions between the fuel and HO_2 radical on tertiary and secondary carbon are emphasized at intermediate and high temperatures in the initial sensitivity analysis, suggesting more consumption of HO_2 is positive to the combustion process. This may partly be due to the decomposition of H_2O_2 (R. 2.6) that is produced from HO_2 (R. 2.30) being more significant at higher temperatures, as discussed in Section 2.2.4. Similar to the OH radical, larger hydrocarbons commonly utilize the reference of n-butane, and no up-to-date sources are available. From the normal alkane models of C3MECHV3.3, the A-factor of the reactions on secondary carbon is increased by a factor of 1.5, compared to the initial model of Curran et al. [52], and the trial test shows that this modification improves the ignition by 10-15% at 950-1050 K. Mohamed et al. [56] also provided the upper and lower limits for the A-factor of all three reaction types of HO_2 abstraction. To better understand the scale of the impacts on the mechanism, the adjustments of the H abstraction by HO_2 will be addressed at the end of the chapter and the modifications from the C3MECHV3.3 are temporarily used as a reference for the analysis of other reaction classes. Furthermore, rules of other molecules such as H, O, O_2 , and CH_3O_2 all have other suggested values from different investigators [56, 120], but as they are less important radical groups for H abstraction, the original values from Curran et al. [52] are kept unchanged.

4.5.2 First and second oxygen addition: $\text{R} + \text{O}_2 \rightarrow \text{RO}_2$ and $\text{QOOH} + \text{O}_2 \rightarrow \text{OOQOOH}$

Reactions between fuel radicals and oxygen play an important chemistry role at lower temperature oxidation, mainly because at low temperatures the equilibrium is very much in favour of the adducts, which in turn provide routes to branching reactions at low temperature. From the detailed review of Baulch et al. [37] and Atkinson et al. [36], chemical reactions such

as $\text{H} + \text{O}_2$ and $\text{CH}_3 + \text{O}_2$ are considered sensitive to pressure variations. As discussed briefly in Section 2.2.3, a few experimental or theoretical studies of the interaction between ethyl radicals and oxygen (R. 2.17) [45–47] also demonstrate the rate constant of this reaction to be influenced by the pressure. It is rather uncertain, however, to what extent is the pressure dependent of the first oxygen addition for larger alkyl radicals. Few experimental records are available for validations with pentyl being the largest radicals investigated, and conditions for temperature are usually below the commencement of combustion and for pressure, they varied among investigators. Lenhardt et al. [178] measured reaction rates of four butyl radicals and oxygen with a photoionization mass spectrometer (PMS) at room temperature and 1–4 torr, and no obvious pressure dependency is observed. Their results have been commonly adopted for propyl and larger alkyl radicals in modelling.

For propyl radicals, Slagle et al. [179] measured rate constants on primary carbon from 0.4 torr to 6.8 torr, and Ruiz and Bayes [180] studied both *n*-propyl and *i*-propyl at room temperature and from 1 torr to 4 torr. Neither result of the reaction rate demonstrates a strong inclination towards pressure change, and as Ruiz and Bayes [180] suggested, these reactions may already be near or at the limit of high pressure at these very low pressure conditions. Reviews of Atkinson et al. [35, 36, 181] have classified the reaction of both propyl radicals with oxygen as pressure dependent with these listed two sources as the high pressure coefficient, and they also commented that the negative temperature slope observed by Slagle et al. [179] from 297 K to 635 K may be an attribution to the fall-off effects. Several theoretical works have estimated the high-pressure limit of propyl and oxygen with a master equation method. Goldsmith et al. [182] studied the impact of $\text{QOOH} + \text{O}_2$ and subsequent chain branching kinetics at low temperatures by using propyl + O_2 as a model. Rate constant expressions for each reaction class were provided at 0.01 atm, 0.1 atm, 1 atm, 10 atm, and 100 atm, separately. Huang et al. [183] examined the *ab initio* equation for the propyl system and then validated it against the measured OH signal with LIF at various temperatures. The modified Arrhenius parameter was re-calculated at 10 torr, 100 torr, 760 torr, and 7600 torr.

The review of Atkinson et al. [35] has classified the reactions of 1- C_4H_9 and 2- C_4H_9 with O_2 to be pressure related as well but commented on a potential of large errors due to Lenhardt et al. [178] being the only experimental resource available at the time. Dilger et al. [184] investigated this class with muonium-substituted *t*-butyl radicals at 1.5 bar and from 241 K to

462 K, and they discovered that the rate constant of RO_2 production is rather weakly dependent on the change of pressure and decreases when temperature increases, which is aligned with propyl results. Moreover, Xi et al. [185] investigated the temperature with neopentyl radicals at 3 torr, and the rate at 374 K is approximately half of the rate at 266 K. More recently, Eskola et al. [186] conducted both experimental and theoretical studies of n-butyl radicals on primary and secondary carbon by using PMS techniques, and the radical concentrations at a condition range of 200 K to 500 K and 0.4-5.6 torr were observed. The predicted rate constants were given at thirteen pressure conditions from 0.01 atm to 100 atm.

To determine how the rate changes with pressure for larger radicals, a plot of $\text{CH}_3 + \text{O}_2 + \text{M} \rightleftharpoons \text{CH}_3\text{O}_2 + \text{M}$ at 800 K was made by using the rates from Baulch et al. [38], as shown in Figure 4.17. Both the low and high pressure utilized the preferred value, and the fall-off region was calculated by the Troe method [187]. Reaction rates from 0.01 atm to 100 atm at the same temperature were next obtained by theoretical studies of Goldsmith et al. [182] (n-propyl), Huang et al. [183] (n-propyl) and Eskola et al. [186] (n-butyl).

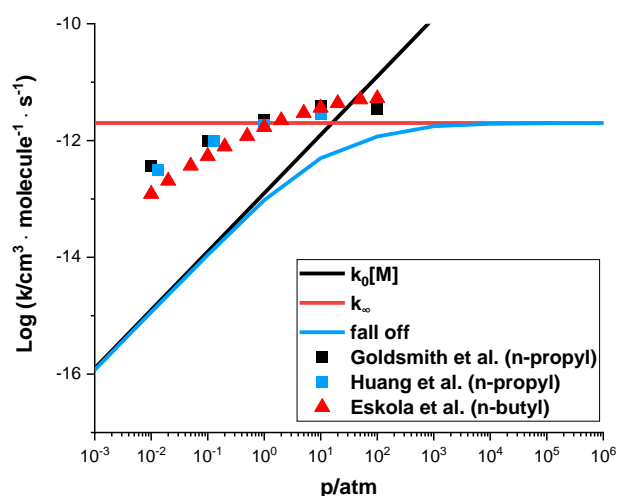


Figure 4.17 Low and high pressure limit and fall off region of $\text{CH}_3 + \text{O}_2 + \text{M} \rightleftharpoons \text{CH}_3\text{O}_2 + \text{M}$, compared with the theoretical pressure dependent value, references: black square [182], blue square [183], red up triangle [186].

Compared to the lower pressure trend of the $\text{CH}_3 + \text{O}_2$, rates from theories display some fall-off behaviours but the variations are generally quite unobvious. Take the results of Eskola et al. [186] for instance, from 0.01 atm to 0.1 atm the rate increases by a factor of 4.5, and changes from the other two references are even smaller. It can be deduced that for the first oxygen addition of alkyl radicals, the reactions are to some degree pressure dependent

although at atmospheric pressure and above, the rates are closer to the high-pressure limit, and may fluctuate less for radicals bigger than propyl and butyl. As Goldsmith et al. [182] concluded, n-propyl is the smallest prototype of the larger alkyl radicals to experience low temperature combustion, hence in this study the reaction of $R + O_2 \rightarrow RO_2$ is not considered to be pressure dependent.

To further optimize the rate rules of this class, some theoretical studies with temperature dependency were examined. Miyoshi [188] systematically investigated the unimolecular reactions of RO_2 , $QOOH$, and $OOQOOH$ with the CBS-QB3 quantum method. Villano et al. [189] used C2-C6 normal alkanes to estimate three classes of rate rules related to RO_2 at high pressure by employing the CBS-QB3 theory. A couple of computational studies were carried out by the Bozzelli group to estimate the thermodynamic properties and chemical kinetics of the iso-octane radicals and oxygen. Auzmendi-Murua and Bozzelli [190] studied the secondary type, and Snitsiriwat and Bozzelli [191] investigated the tertiary carbon site. The theoretical value from these references for the primary, secondary, and tertiary were calculated at low and intermediate temperatures and then further compared with experimental data, and details are shown in Figure 4.18. Given Villano et al. [189] only provided expressions of rate constant in the direction of $RO_2 \rightarrow R + O_2$, reverse rates were obtained by using updated thermodynamic data from Section 4.3. Additionally, the rate constant expressions of Goldsmith et al. [182] and Eskola et al. [186] at each pressure condition were also calculated concerning the temperature change, and some conditions demonstrate a reasonable shape and level compared to their respective carbon types, such as Goldsmith et al. [182] at 1 atm for the primary (Figure 4.18 (a)) and Eskola et al. [186] at 0.1 atm for the secondary (Figure 4.18 (b)). The experimental data utilized for comparisons were from Lenhardt et al. [178], Ruiz and Bayes [180], Slagle et al. [179], Xi et al. [185], Eskola et al. [186], and Dilger et al. [184], labelled from one to six, respectively.

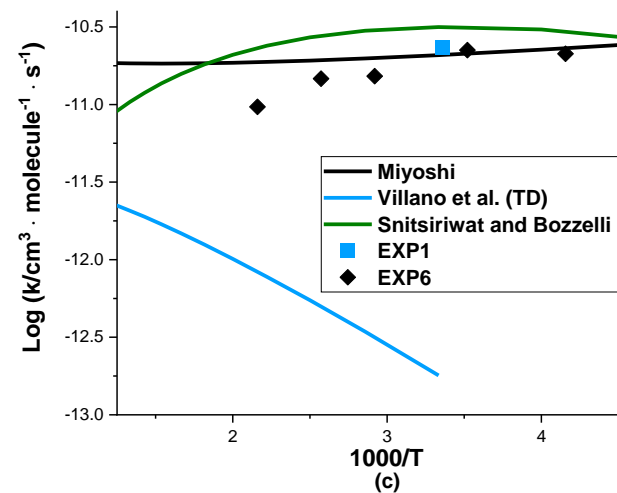
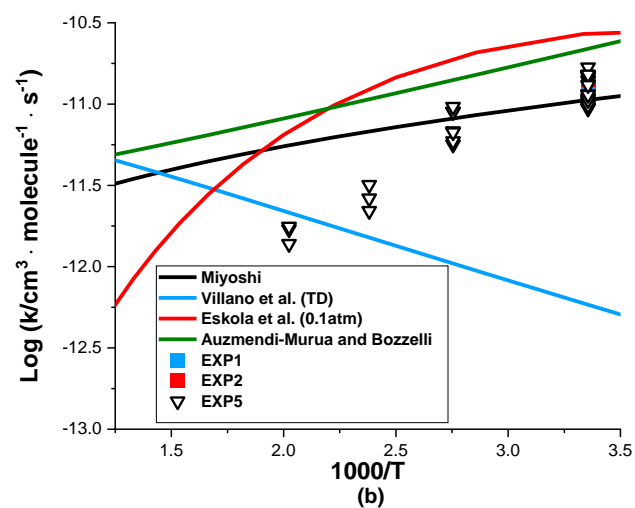
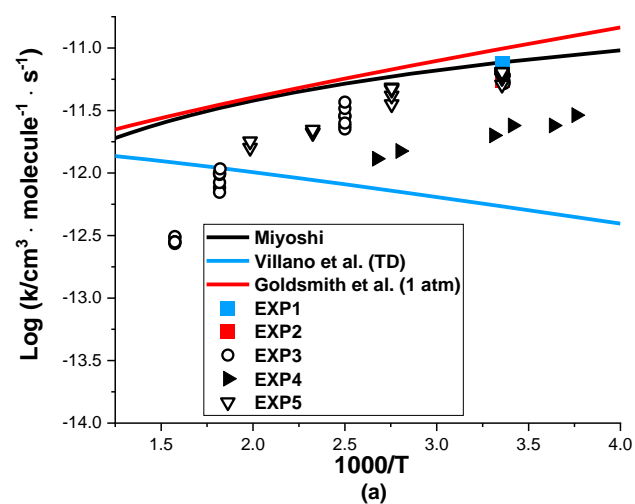


Figure 4.18 Comparisons of the forward rate constant expression of 1st O₂ addition between theoretical references and experiment values (250-800 K): (a) primary; (b) secondary; (c) tertiary.

The rate temperature dependence of Villano et al. [189] for all three carbon types is opposite to other sources, and does not correlate with the measurements well, either. Both simulated rates from the Bozzelli group show a reasonable agreement with experiments in terms of the trend, although it generally overpredicts by some margin. For primary carbon, the result of Miyoshi [188] is in excellent agreement with the experimental data at room temperature and fits the general rate trend, although it displays less temperature dependency when the temperature rises above 500 K. At 635 K, the calculated rate is about ten times greater than the average value from Slagle et al. [179] at the same condition. Similar observations can be drawn from the result of Miyoshi [188] for secondary carbon, as the estimated number is greater than the laboratory value from Eskola et al. [186] by a factor of four at 494 K. The simulation of Miyoshi [188] for tertiary carbon corresponds well with the current experimental data. Hence, the computational rate rules of all three carbon types from Miyoshi [188] will be applied to the reaction class of $R + O_2 \rightarrow RO_2$ for propyl and larger alkyl radicals.

The second oxygen addition for alkanes has not been addressed much due to the difficulty of measuring it experimentally in a clean and thus simple to interpret system. Therefore, previous modelling studies have frequently followed the identical rate rules of the first O_2 addition. The group of Bozzelli have contributed largely to the knowledge of the oxidation of alkyl hydroperoxyl radicals with oxygen, by performing computational calculations to estimate both the kinetic and thermochemistry parameters with the fundamental models ranging from ethyl to pentyl. For instance, Sun and Bozzelli [192] studied the system of hydroperoxyl neopentyl radicals, and the parameter obtained is both dependent on the pressure and temperature. As mentioned above, Goldsmith et al. [182] also determined the class of $QOOH + O_2$ to be pressure-dependent with high-level *ab initio* calculations. It is observed that for the secondary carbon type, their result for the first addition is faster than the second addition by a factor of 2 approximately. Mohamed et al. [56] adopted this rule in the group of second oxygen addition for their modelling work of 2-methylhexane oxidation. Zador et al. [193] is the first study to measure both the decomposition of $(CH_3)_2C(OOH)CH_2\cdot$ and its reaction with oxygen in two approaches at room temperature. Infrared absorption was conducted between 8 torr and 90 torr and multiplexed photoionization mass

spectrometry was performed at 4 torr, and the data was subsequently compared with a theoretical characterised by VRC-TST.

Comparisons between theoretical and experimental values are shown in Figure 4.19. From the initial examination of Sun and Bozzelli [192], in the lower temperature region, differences between the calculated rate constants at each pressure range are not evident, thus here the result at 0.0001 atm was displayed. Also, the rules of $R + O_2 \rightarrow RO_2$ from Miyoshi [188] and Villano et al. [189] were divided by two as Goldsmith et al. [182] suggested. Results from Goldsmith et al. [182] and Villano et al. [189] do not correspond well with experiments at room temperature, while predictions from both Sun and Bozzelli [192] and Miyoshi [188] are in excellent agreement. The temperature dependence of these two sources, however, do not match well at all. As the secondary O_2 addition is based on analogy with the first addition, the trend of Miyoshi [188] seems to be a more reasonable fit in the current state of knowledge. From the modelling perspective, by applying the same rules for first and second oxygen addition from Miyoshi [188], little differences are shown compared to the original rate rule values. Furthermore, examination shows that to halve the reaction rate for the class of $QOOH + O_2$, reactivities of combustion are relatively reduced at low and intermediate temperatures. Take the stoichiometric condition of 2-methylheptane for example, an increase of ignition delay time by 50-60% between 800 K and 900 K is estimated. In the discussion of the following parts, the same rate rules for both classes of O_2 addition are applied until further explanations.

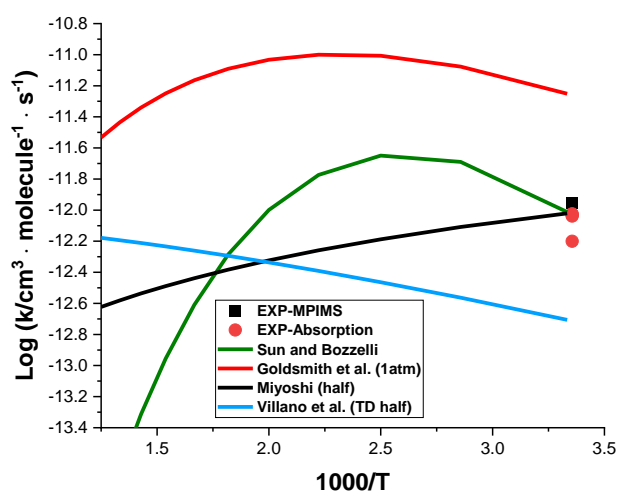


Figure 4.19 Rate constant expression of $QOOH + O_2$ for primary type at low temperature (300-800 K): scatter: EXP value [193]; line: theories.

4.5.3 Isomerization: $RO_2 \rightarrow QOOH$

Isomerization of alkyl peroxy is another significant channel in the low temperature combustion. An alkyl peroxy radical can generate several types of alkyl hydroperoxy radicals depending on the H abstraction. Transition state ring size varies from size four to eight, transferring on one of the three types of carbon. An example of the transition is depicted in Figure 4.20. A six-member ring is formed and by extracting one hydrogen atom on a secondary carbon, one potential alkyl hydroperoxy radical is then produced.

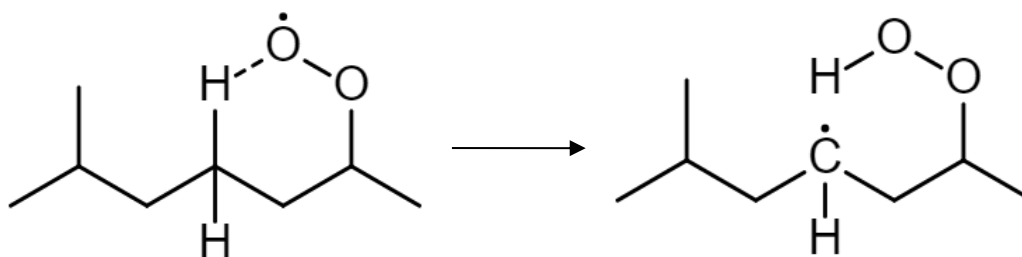


Figure 4.20 Example of isomerization of 1,5s type via transition ring: $C_8H_{17}O_2-6-2 \rightleftharpoons C_8OOH_6-2d$.

A few experimental records can be found by using neopentane in earlier investigations. Baldwin et al. [194] studied the reactions in an environment of hydrogen and oxygen from 653 K to 793 K, and by measuring the product ratios, the kinetic parameter for the 1,5p isomerization was determined. Hughes et al. [195] generated neopentyl radicals by laser flash photolysis, and in the presence of varying quantities of oxygen, measured the production of OH by laser induced fluorescence, and thus was able to calculate a rate constant for the 1,5p isomerisation at 700 K, and at 660-750 K in a similar study [196]. Their results for the 1,5p H atom transfer are in general smaller than the rates of Baldwin et al. [197] by a factor of 10 to 15. More recently, Nozriere and Vereecken [198] directly observed five larger alkyl peroxy radicals and their subsequent OOQOOH radicals by chemical ionization mass spectrometry at 298 K and 0.9 atm. As more than one OOQOOH component can be detected, especially for larger hydrocarbons, the proportion for each transition type was determined by a theoretical method. Coefficients of 1,5s and 1,6p were obtained from 1-butyl, 1,5s and 1,6s from 1-pentyl, 1,5s 1,6s, and 1,7s from 1-hexyl.

Estimating the rate rule of a single transition type is usually served as a basis for general modelling purposes, and a set of expressions for different transition ring sizes and C-H bonds can be subsequently generated. The pre-exponential factor per H atom is decreased by a factor of 8 every time the ring size increases by one atom due to the loss of internal rotation,

as Baldwin et al. [197] discussed based on the transition state theory, and this analysis is commonly adopted among researchers such as Curran et al. [52] in their modelling study of iso-octane. The determination of activation energy (E_a) for each transition condition on the other hand, is more complicated. Bozzelli and Pitz [199] investigated the rate constants of several hydroperoxyl-propyl channels with the use of thermodynamic parameters, QRRK analysis, and transition state structure. Their estimation of E_a is an accumulation of ring strain, abstraction energy depending on the carbon bond, and enthalpy of reaction. For the same member ring, a tertiary bond has the lowest energy barrier while a primary type is the most difficult to be abstracted. When the ring size increases, the activation energy decreases which can mostly be attributed to the ring strain energy, although the value chosen among investigators shows a great discrepancy as presented in Table 4.3. Curran et al. [51] suggested the ring-strain energy should be lower than the preferences of Baldwin et al. [194] for better prediction of the heterocyclic concentration. In theory, E_a can be calculated by the Evans-Polanyi relationship ($E_a = E + nRT$) [200], although several works [201, 202] suggested that the curve of Blowers-Masel [203] showed promising agreement in a few reactions.

Table 4.3 Comparison of ring strain energy between different authors. (Unit: $\text{kJ} \cdot \text{mol}^{-1}$)

	5 Ring	6 Ring	7 Ring	8 Ring
Hughes et al. [204]	69.0	38.2	19.3	6.9
Curran et al. [51]	36.0	11.7	0.0	11.7
Bozzelli and Pitz [199]	25.1	0.4	25.1	

Records of this class by theoretical approaches are much more common, although many authors only provided insights into limited types of transition. Due to the single methyl- on the straight chain which creates a tertiary bond, the hydroperoxyl radicals ranging from five to eight ring size on primary, secondary, and tertiary carbon can be formed for 2-methylheptane. In more recent years, detailed compilations of rate rules can be found in the studies of Miyoshi [188] and Villano et al. [189] for isomerization of alkyl peroxy, and their results have been commonly utilized by modelling researchers. Noticeably, the isomers produced from the four-member ring are unstable and quickly lead to the formation of a carbonyl and OH radical, as discussed by Villano et al. [189]. Thus, this reaction group is not considered here. Sharma et al. [205] also studied the intramolecular hydrogen migration in RO_2 and QOOH radicals by using the CBS-QB3 and B3LYP/CBSB7 methods, and rate constants

and thermochemical properties for a series of reactions and molecules were calculated. Noticeably, both Miyoshi [188] and Sharma et al. [205] further differentiated specific types for each transition ring based on the position of peroxy radicals and where the abstraction takes place. Take reaction $\text{CH}_3(\text{CH}_2)_2\text{CH}_2\text{OO}\cdot \rightleftharpoons \text{CH}_3\text{CH}_2\text{CH}(\cdot)\text{CH}_2\text{CH}_2\text{OOH}$ for instance. The $-\text{OO}\cdot$ is initially connected with a primary carbon and then abstracts a H atom from a secondary carbon, hence this type of 1,5s can be referred to as *ps*. Additionally, rate rules from Sharma et al. [205] cannot apply for every reaction type of 2-methylheptane, therefore, for those without direct parameters, their nearest analogy was adopted with the A-factor value being halved, as an-hexane modelling study from Zhang et al. [206] suggested. Consider reaction $\text{C}_8\text{H}_{17}\text{OO}-2-2 \rightleftharpoons \text{C}_8\text{OOH}_2-2\text{d}$. The transition is a 1,5-H type *ts*, so 1,5-H type *ss* was used as a reference.

Based on the reaction types of available experimental sources, rate rules of a few transition member rings were selected and calculated at the low temperature region and comparison is depicted in Figure 4.21. Also, isomerization reactions of 1,5s type are highlighted in low temperature environment as the sensitivity in Figure 4.2 (a) indicates. Reactivities of all three references are largely increased compared with the original data. Simulated results of 1,5s and 1,6s from Miyoshi [188] agree well with the experimental data of Noziere and Vereecken [198] at room temperature. Around low and intermediate temperatures, the rate constant of Miyoshi [188] appears to be the fastest among the three theoretical sources, for instance, type 1,6s is greater than its original value by approximately a factor of 28. Results from both Villano et al. [189] and Sharma et al. [205] show a relatively less increase in rate, as 1,6s is only about a factor of 10 than that of the original value. Also, both predictions of 1,5p at 650-750 K correspond reasonably with the neopentyl studies from Baldwin et al. [194]. A modelling test for 2-methylheptane/air at the stoichiometric condition was subsequently carried out. Figure 4.22 shows that certain effects can be observed under 900 K for all three sources, with the result of Sharma et al. [205] being the most substantial, followed by Villano et al. [189], and Miyoshi [188] displaying the least improvements. General shapes are all similar and predictions around the NTC region agree well with the experimental data.

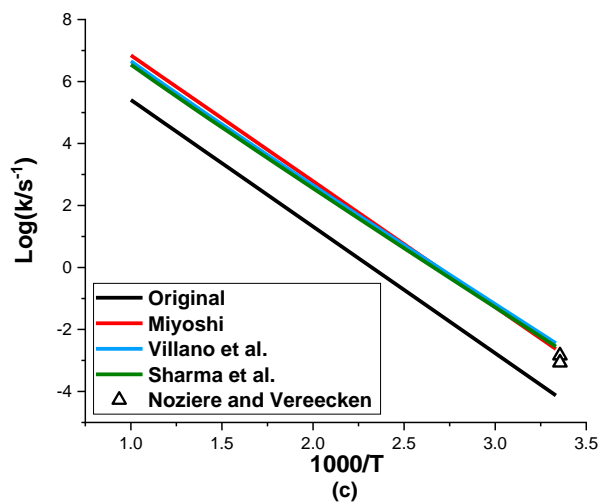
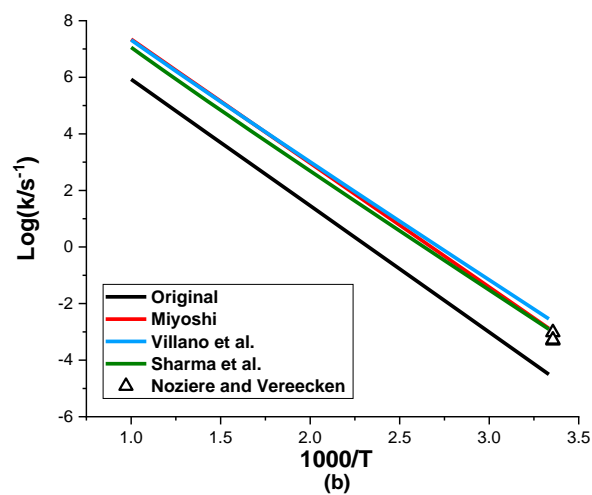
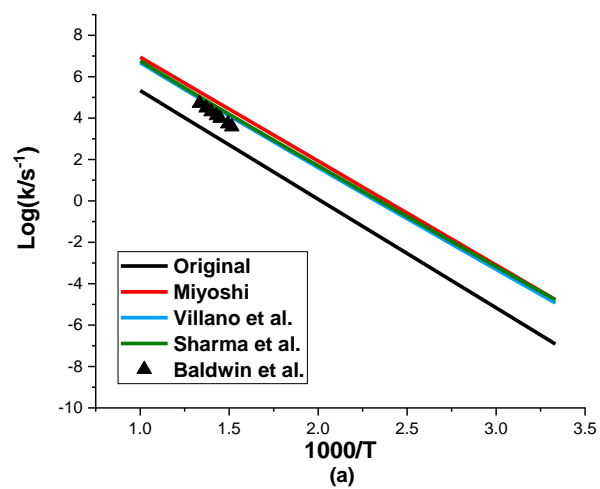


Figure 4.21 Comparisons of the rate constants between different theories (lines) and experiments (scatter) from 300 K to 1000 K: (a) 1,5p (*pp*); (b) 1,5s (*ps*); (c) 1,6s (*ps*).

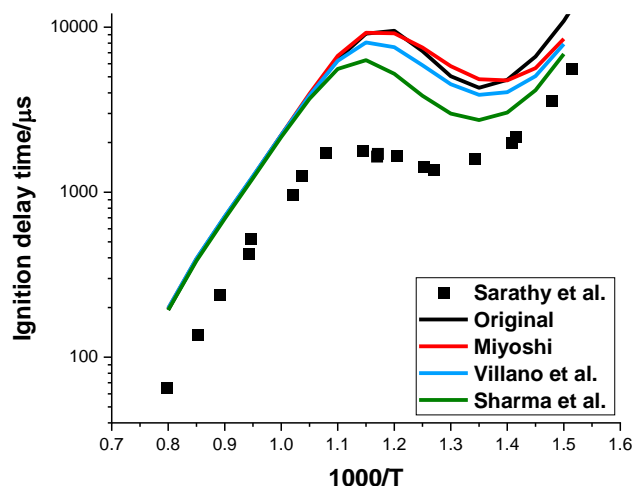


Figure 4.22 Predictions of the ignition with updated rate rules of the isomerization from different authors, for 2-methylheptane/air mixtures at the stoichiometric and 20 atm conditions.

The rate rules provided from either experiments or theories are not strictly unchanged in the model applications. Depending on the targeted fuels, the hydrocarbon that the rate constant expressions were attained from may not be the most suitable prototype, hence adjustments are necessary. Curran et al. [52] discussed in their study of iso-octane that by applying the identical rate rules for n-heptane [51], reactivities at the NTC region were greatly overpredicted, hence the A-factor was correspondingly divided by 30 to match the quality of the iso-octane model. Similarly, Mehl et al. [94] commented in their model of gasoline surrogates that, by further reducing the value of the activation energy by $400 \text{ cal} \cdot \text{mol}^{-1}$ from the recommendations of Curran et al. [52], the activities at low temperatures are favourably enhanced. To better interpret the effect of these additional alterations, discussion will be resumed at the end of the chapter and the rate rules from Sharma et al. [205] will be temporarily used as references for the upcoming analysis.

4.5.4 Concerted elimination: $\text{RO}_2 \rightarrow \text{alkene} + \text{HO}_2$

The production of HO_2 becomes more active around the NTC region, although no related reactions were highlighted in the initial sensitivity analysis. Both Villano et al. [189] and Miyoshi [188] estimated the group values with differentiation of the specific peroxide group and extracted carbon positions, and Bugler et al. [54] provided a single expression based on both references with upper and lower limits. Villano et al. [189] noted that the reactions leading to the production of highly substituted alkenes are about two to three times faster

than those produce by less substituted olefins. Given the structure of 2-methylheptane, rules for less substituted olefins were therefore employed. From the observation of the modelling test, at the stoichiometric condition, the predicted results from Villano et al. [189] and Bulger et al. [54] were reasonably similar, which reduced the reactivities by 25-30% between 800-900 K compared to the original data. Around the same temperature range, the predictions from Miyoshi [188] on the other hand enhanced the elimination process by a factor of 2. As Mohamed et al. [56] commented, the rate of this reaction class is mainly determined by the type of olefin that is formed. To simplify the model, the rules from Bugler et al. [54] were utilized in this work and the rate constant expression per H atom is given as:

$$k = 10^{9.46} \times T^{0.93} \times \exp(-14997.5/T) \text{ s}^{-1}$$

4.5.5 QOOH → cyclic ether + OH

This group describes one of the most important channels of QOOH decomposition in the low to intermediate temperature range. By breaking the bond of O-O, a cyclic ether is consequently formed, and the rate constants are estimated based on the ring size [51]. Villano et al. [207] modified the rate constants of four types of QOOH isomers from the CBS-QBS calculations and observed that the exothermicity of the reaction may be related to the positions of QOOH radical and hydroperoxyl group. For each ring size, the activation energy is estimated in a linear fitting corresponding to the enthalpy of the reaction at 298 K, over a range of 500-1000 K. Since new thermochemistry was generated in this project, this method was adopted and the activation energy for each specific reaction was calculated. Uncertainties of *ab initio* calculations are estimated to be a factor of 2 for the pre-exponential factor and $\pm 1 \text{ kcal} \cdot \text{mol}^{-1}$ in barrier height. By applying the new rate rules, the modelling test shows a decline of reactivities by approximately 20% at 750-800 K, and results of other temperature conditions remain almost intact. Moreover, Zhang et al. [206] suggested to halve all the Arrhenius factors in their n-hexane model with the reference of Villano et al. [207], to better fit with their measurements in JSR. By using the ratio of uncertainty, the reactivities at 750-800 K were increased by 15% compared to the result obtained without corrections. This work adopted the same concept with a ratio of 0.5 applied to the A-factor for all reactions in this group.

4.5.6 QOOH → alkene + HO₂

Similar to the discussions in Section 4.5.4, Bugler et al. [54] provided the recommended rate rules established from the computational studies of Villano et al. [207] and Miyoshi [188] and were employed for this reaction class. The general rate constant expression is given as:

$$k = 10^{10.26} \times T^{0.79} \times \exp(-7599.4/T) \text{ s}^{-1}$$

Additionally, the QOOH formed from a six-member ring can go through β -scission. Mohamed et al. [56] updated the rate constant of this route, which is about forty times faster than the original value from Curran et al. [52]. From the simulation perspective, this boost shows rather negligible effects, implying that this channel is less significant during the combustion process. Thus, the rate constant expression remains unchanged.

4.5.7 Isomerization: OOQOOH → Ketohydroperoxide + OH

The production of ketohydroperoxide and OH through isomerization of OOQOOH is essential to chain branching at low temperature conditions. An example of a seven-member ring (1,6-H) formation is depicted in Figure 4.23.

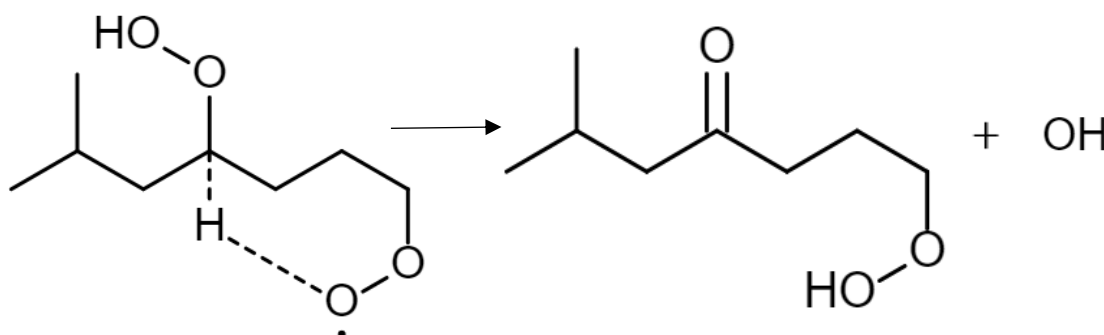


Figure 4.23 Example of a 1,6H type *sp* isomerization of OOQOOH: C8OOH7-OO4-2 \rightleftharpoons C8KET7-4-2 + OH: *s* indicating the position of -OO· and *p* indicating the position of the hydroperoxyl group.

Previously, investigators have commonly employed the rate rules from Curran et al. [51] for this pathway, which treated it as the analogy of RO₂ isomerization with a reduction of 3 kcal · mol⁻¹ for the activation energy because the additional hydroperoxyl attached to the carbon consequently should make the H atom abstraction easier. From the initial sensitivity analysis, only one reaction of the 1,5-H type *ps* is highlighted in the rich case at 670 K, indicating a lack of activity in this class. Both Sharma et al. [205] and Miyoshi [188] calculated the coefficients of the high-pressure limit for this class. More recently, Mohamed et al. [208] studied the effects of hydrogen bonding on several reaction routes emphasized at

intermediate temperature, and provided modified parameters for a group of butane OOQOOH radicals from ring size five to seven.

Similar to their expressions of RO₂ isomerization, Sharma et al. [205] were not particularly concerned with the conditions for the tertiary carbon bond and presented only two types of rate constants for the 1,7-H isomerization. Hence, the rate constants of these reactions were generated based on their RO₂ analogy as Curran et al. [51] suggested. For the transition types whose rate constants are available for both isomerization classes, the calculated values of a few examples were compared and displayed in Figure 4.24.

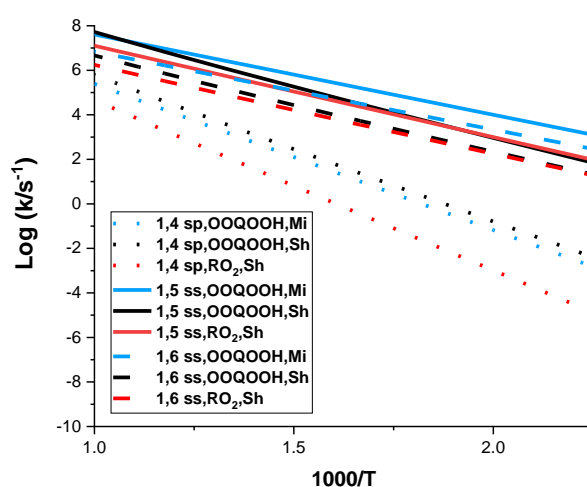


Figure 4.24 Comparisons of the three types of rate constants between OOQOOH isomer and RO₂ isomer: RO₂ from Sharma et al. [205] and OOQOOH from Sharma et al. [205] and Miyoshi [188].

From the discussions in Section 4.5.3, the rates of Sharma et al. [205] in general are the fastest among the three references, thus it is utilized to represent the class of RO₂ isomer. At 500-800 K, for the 1,5-H ss and 1,6-H ss, rates of OOQOOH isomerization from Sharma et al. [205] are in reasonable agreement with their respective RO₂ isomerization. As for the 1,4-H sp, the results of OOQOOH are 40 to 50 times faster than their RO₂ rates. On the other hand, the rates of Miyoshi [188] are generally greater than the rates of RO₂ isomerization by an order of magnitude or more. Importantly, the -OOH group that is attached to a tertiary carbon is quite important as the sensitivity indicated, while its transition does not follow the same rule as the other OOQOOH radicals because this structure is quite unstable and the hydroperoxyl will quickly break and form a carbonyl. Consider the reaction $C8OOH2-OO4-2 \rightleftharpoons C_3H_6 + OH + IC5KETDB$ as an example. The -OO· connected to the fourth carbon abstracts the H atom on the sixth carbon and forms a six-member ring of type ss.

Hence, the isomerization of this OOQOOH follows the rules of RO₂ isomerization, and in the current condition, the rules of Sharma et al. [205] will be employed for these reactions.

Updated rate rules were examined with the use of the stoichiometric case and the results are shown in Figure 4.25. Compared with experimental data, both references show that the reactivities at low and intermediate temperatures are largely increased and to some extent underpredict the ignition. The ignition delay time of Miyoshi [188] is about 20% quicker than that predicted by Sharma et al. [205] at $T < 900$ K. In addition, rate rules from Mohamed et al. [208] were applied to a few reactions and then combined into other reactions with the rates of Sharma et al. [205], and only marginal differences were observed. The main issue of the current model is the intermediate range, as the ending of the NTC region of Sharma et al. [205] and Miyoshi [188] has been increased by 40 K and 80 K, respectively, thus indicating an imbalance of chemistry between low and intermediate temperatures. As Figure 4.24 suggested, an over-increase of ignition at low temperature conditions may conversely suppress the activities around the NTC region. Thus, isomerization rates of both RO₂ and OOQOOH will be further discussed in Section 4.5.9.

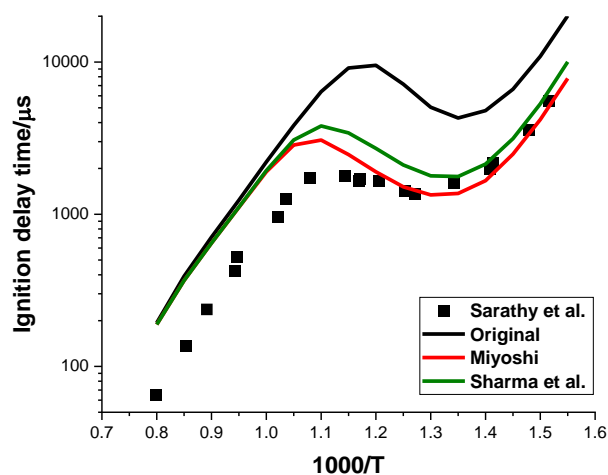


Figure 4.25 Simulations of the updated rules from class one to seven, compared to the original model and experiments: rates of OOQOOH isomerization employed from Miyoshi [188] and Sharma et al. [205].

4.5.8 Ketohydroperoxide decomposition

Production of one or multiple carbonyl radicals and OH through ketohydroperoxide are also significant for low temperature combustion. According to the modelling of Curran et al. [51], a single rate parameter is given for all related reactions although each type of

ketohydroperoxide may have different thermochemistry properties, and the activation energy is set to be 43 kcal · mol⁻¹. Sarathy et al. [105] utilized the activation energy of 39 kcal · mol⁻¹ from the modification of Mehl et al. [94] to better predict the 2-methylheptane model. Limited investigations can be found regarding this pathway. Jalan et al. [209] employed a propane model to study the new reaction pathway of γ -ketohydroperoxide with theoretical approaches. For larger hydrocarbons, however, the carbonyl will quickly break down into smaller oxygenated species. Zhang et al. [206] describe the decomposition process of their n-hexane simulation in two separate parts with an intermediate C6 carbonyl radical, and the activation energy chosen for the first part is close to the suggested value from Jalan et al. [209]. This approach may not be suitable for the current case, also to simplify the mechanism, the original reactions and rates hence remain unchanged. The expression is given as follows:

$$k = 10^{16} \times \exp(-19627.58/T) \text{ s}^{-1}$$

4.5.9 Additional optimization

Experiments of 2-methylheptane/air ignition with the use of a shock tube at 20 atm show that the intermediate regions start roughly from 800 K to 880 K at all three equivalence ratio conditions. As pointed out in Section 4.1, despite the relatively large discrepancies in ignition delay time, the temperature ranges of the original modelling correspond well to the measurements. The current NTC regions of the modified model are all extended by 40-80 K depending on the sources of RO₂ and OOQOOH isomerization, and little improvements are shown once the temperature rises higher than about 1000 K. Thus, the aim of these additional changes in the rate rules is to refine the shape of the computational graphs and in particular the combustion chemistry at temperature regions from 850 K to 1000 K, while keeping the differences in the ignition delay time between experiments and simulations at a reasonable level.

The first attempt is to refine the reaction rates of the second oxygen addition by multiplying by 0.5 all the A factors of the first oxygen addition. Also, since multiple sources of isomerization of RO₂ and OOQOOH are available, different combinations of these two reaction groups were examined. Test modelling shows that the updated rules of QOOH + O₂ in general correspond better with experiments, but the ending of the NTC range is still increased by 40 K at best. The subsequent step is to adapt chemical reactivities at low and

intermediate temperatures. From the observations, results with the use of RO₂ rules from Villano et al. [189] and Sharma et al. [205] are quite similar and the prediction from the latter at low temperatures was marginally better, hence the results of Sharma et al. [205] were selected. Manipulations are focused on the OOQOOH radicals as their subsequent reactions strongly enhance the chain branching activity at lower temperatures. The rules of Miyoshi [188] were selected to represent the isomerization of OOQOOH because the differences between OOQOOH rules from Miyoshi [188] and RO₂ rules from Sharma et al. [205] are quite consistent with each transition type around the targeted temperature regions. From the examination, the activation energy of all the reactions of OOQOOH isomerization is suggested to increase by 3 kcal · mol⁻¹ than the original value so that the modelling of the NTC range can fit better with the experimental data. Modified rate constants of the OOQOOH isomerization were subsequently calculated and compared with the RO₂ rates of the same reaction type, as presented in Figure 4.26.

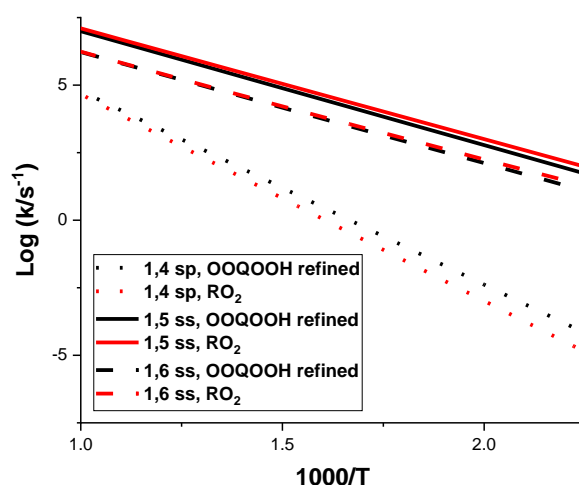


Figure 4.26 Comparisons of the three types of rate constants between the refined OOQOOH isomer and RO₂ isomer.

At 500-800 K, the rates of alkyl peroxy are slightly quicker than OOQOOH for 1,5-H ss and 1,6-H ss, and for 1,4-H sp, rates of OOQOOH are now 2.5 times faster than RO₂, which was previously about 25 times faster. The current model corresponds decently with the theory of Curran et al. [51] of the analogy between these two reaction groups, and the modified rate rules are applied for examinations. Compared to the results before this adjustment (Cond.0 in Figure 4.27), the new modelling shows that the reactivity at 800-870 K was the most

affected, which was reduced by approximately 50%. The influence on the low temperature chemistry at 650-750 K is relatively less, as the ignition delay time is greater than the initial value by 35%.

Next, it is indicated from the initial sensitivity analysis that H abstraction from fuel by HO₂ is the most prominent class at higher temperature combustion. To further increase the model reactivity at 850-1000 K, the upper limit of this class from Mohamed et al. [56] was employed, meaning that the original pre-exponential factor is increased by a factor of 4 for all three carbon types. Certain levels of errors are expected, as the reaction group between the fuel and HO₂ lacks either experimental or theoretical validations. Since this class elevates the ignition process more at $T > 900$ K than $T < 900$ K, the increase of E_a for OOQOOH isomerization is consequently adapted to 2.8 kcal · mol⁻¹ to less suppress the reactivity around the low and NTC region (e.g., 19100 cal · mol⁻¹ → 21800 cal · mol⁻¹). By employing these new adjustments, the optimized simulation is shown in Figure 4.27. Compared to the earlier modification, which only increases the A-factor by a factor of 1.5 in the secondary carbon reactions, the chemistry at 870-950 K is the most influenced with the ignition delay time reduced approximately by 80%. Improvements at high temperatures can also be observed, from 1000 K to 1100 K the reactivities are promoted by 60%. In addition, no obvious differences in the simulation are shown at $T < 800$ K. With these optimization approaches, the current model can reasonably predict the ignition delay time in terms of both the graph shape and result level.

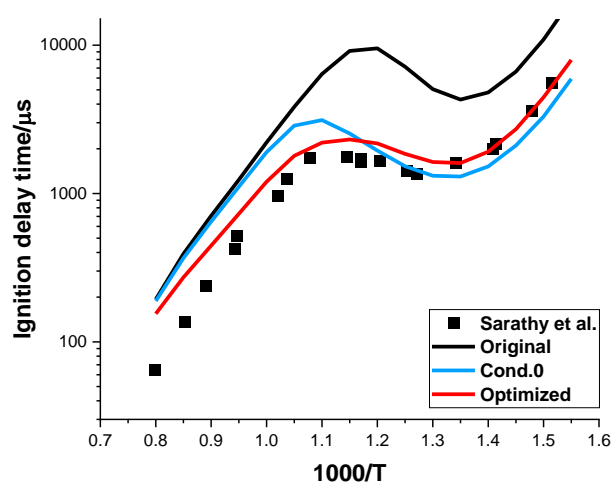


Figure 4.27 Optimized model of the stoichiometric 2-methylheptane/air combustion at 20 atm, compared to the original and cond.0.

4.6 Evaluation of the updated mechanism

Figure 4.28 shows the results of the optimized 2-methylheptane model at lean, stoichiometric, and rich conditions at 20 atm.

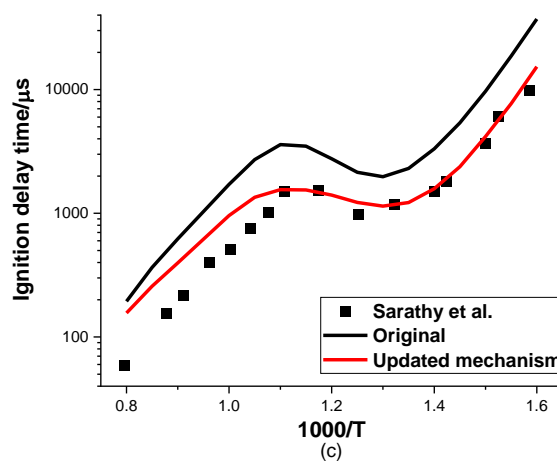
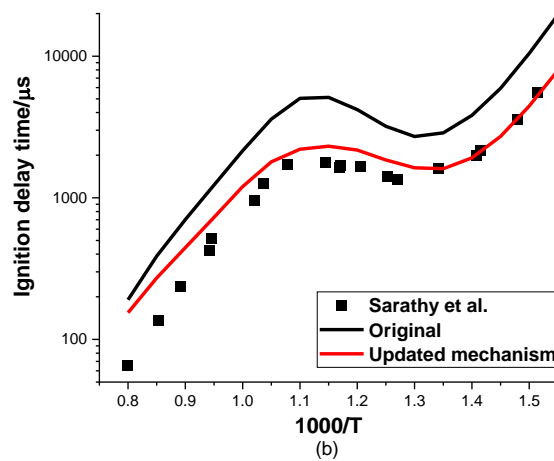
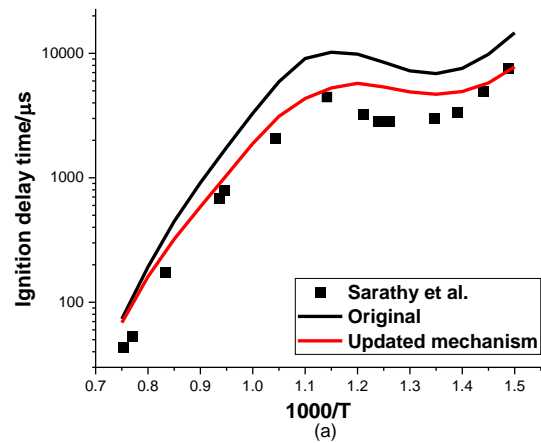
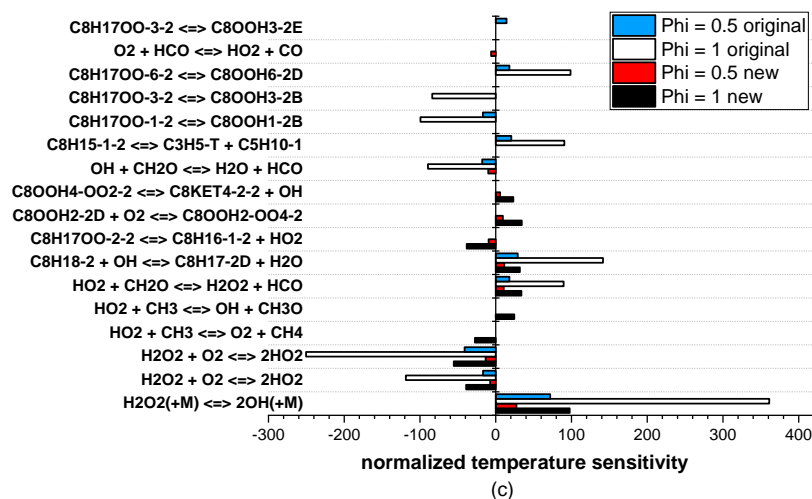
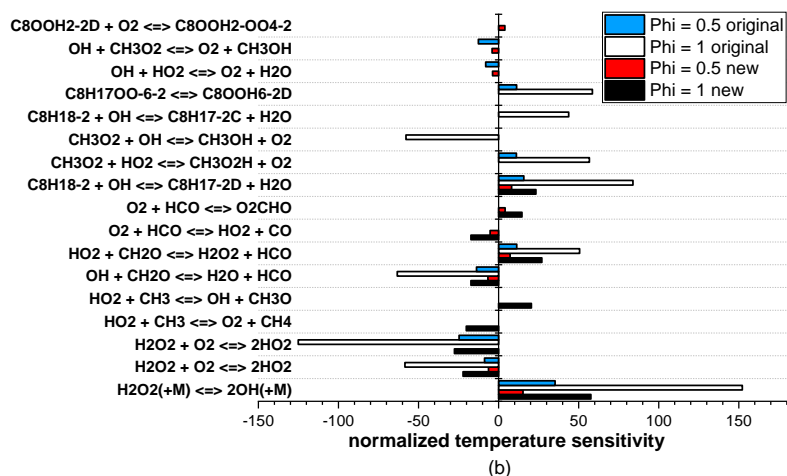
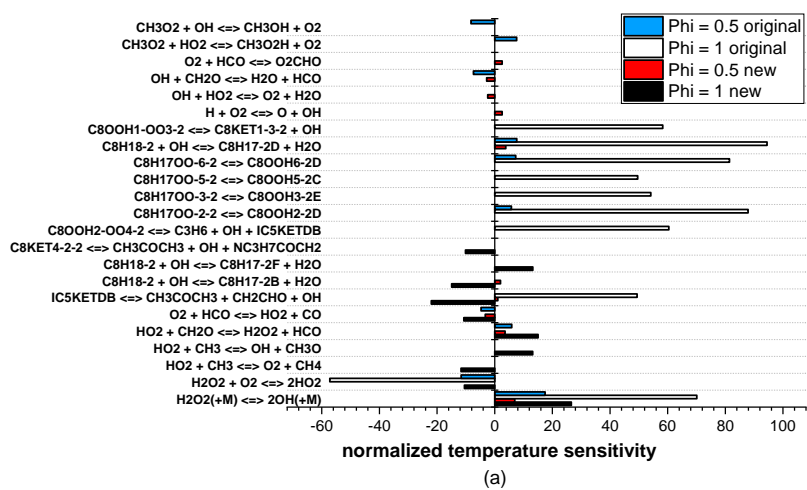


Figure 4.28 Ignition predictions of the optimized 2-methylheptane model at 20 atm, compared to the original result and experiments: (a) $\phi = 0.5$; (b) $\phi = 1$; (c) $\phi = 1.5$.

In the stoichiometric and rich cases, current simulations correspond excellently with the experimental results. Compared with the original results by using the NUIG core mechanism and original thermochemical properties, the computational combustion process shows the most improvements at the temperature ranges of 870-1000 K and 650-700 K, which is approximately faster by 55% for the stoichiometric condition and at the rich case, the ignition is enhanced by a factor of 1.3. Also, upgrades are observed in the regions of low to intermediate temperatures (700-870 K) and higher temperatures (1000-1100 K), which is about 40% when $\varphi = 1$ and 75-90% when $\varphi = 1.5$. The lean case demonstrates the least differences. In the NTC range, the ignition is improved by 50%, however, the transition from NTC to higher temperature is decreased by 40 K, which becomes 830 K now.

A new sensitivity analysis is subsequently conducted at six temperature conditions. Since the result of the rich case is comparatively better, only the stoichiometric and lean cases are shown in Figure 4.29, together with their respective original sensitivity results. The chemistry at low temperatures ($650 \text{ K} < T < 750 \text{ K}$) has been greatly changed and noticeably, no reactions of RO_2 isomerization are detected while a group of them was highlighted in the original analysis. On the other hand, reactions between the fuel and OH radical becomes more significant, although the effects on different fuel radicals appear to be inconsistent. At 670 K, abstraction on the tertiary bond shows a negative trend while it is positive for the radical on the primary carbon g . At 740 K and 800 K, the abstraction on the secondary carbon d also indicates a positive sensitivity. This may be due to the more substantial increase of the reaction on the tertiary carbon compared to the other two carbon types as displayed in Figure 4.16, which reversely discourages the chemical reactivity. Noticeably, small radical reactions are much more involved in this temperature range while previously only the decomposition of hydrogen peroxide and $2\text{HO}_2 \rightleftharpoons \text{H}_2\text{O}_2 + \text{O}_2$ are dominant influences. For instance, $\text{HO}_2 + \text{CH}_2\text{O} \rightleftharpoons \text{H}_2\text{O}_2 + \text{HCO}$ becomes quite important in both the stoichiometric and lean conditions. At the intermediate region, $\text{H}_2\text{O}_2 + \text{M} \rightleftharpoons 2\text{OH} + \text{M}$ remains the most significant reaction which promotes the enhancement of the combustion process, followed by $2\text{HO}_2 \rightleftharpoons \text{H}_2\text{O}_2 + \text{O}_2$ which reduces the reactivity. Also, other combustion aspects at this region are relatively modified, concerted elimination, second O_2 addition, and isomerization of OOQOOH are all highlighted while the original sensitivity mainly contains the class of RO_2 isomerization. The H abstraction by HO_2 begins to demonstrate the importance around the

end of the NTC region (870 K) and from $T > 900$ K, the sensitivity of the current mechanism is quite similar to the original results.



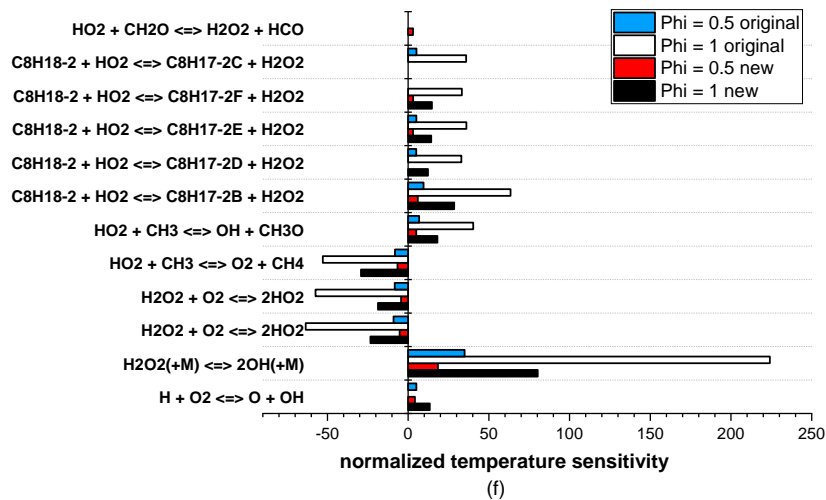
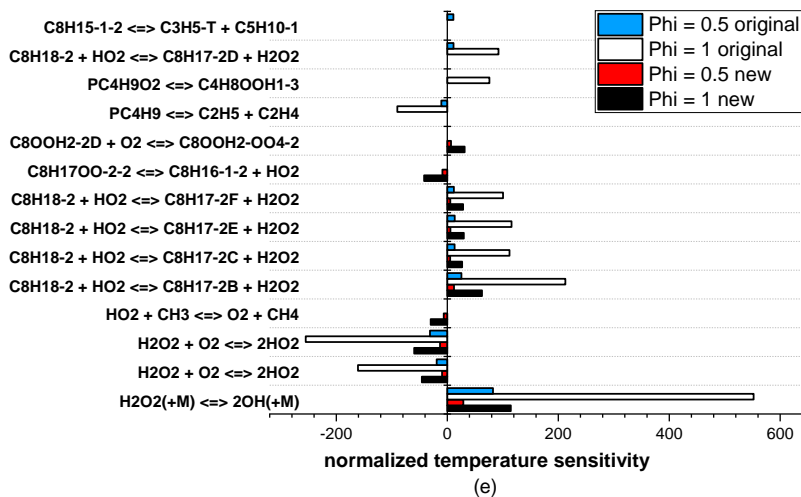
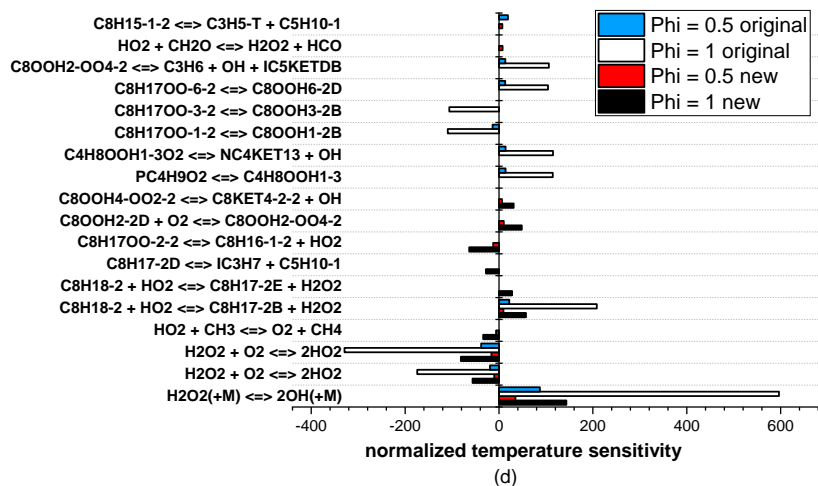


Figure 4.29 Sensitivity analysis of the updated mechanism at the stoichiometric and lean conditions: (a) 670 K; (b) 740 K; (c) 800 K; (d) 870 K; (e) 910 K; (f) 1000 K

The reaction pathway is also plotted and analysed with the use of Chemkin. An example at 800 K and the stoichiometric condition is shown in Figure 4.30, compared with the original results. Among the seven total fuel radicals, the one where the H abstraction takes place on the tertiary carbon undergoes the most change, from the least branching ratio (12.1%) to the most (23.7%). The radical abstracted on the first carbon was previously the most prominent branch, which was 17.1% and now it is around 16.2%. The ratios of the radicals abstracted on the secondary carbon were all identically 15.5% before and now they vary from 11% to 16%, which in general does not show substantial differences. For the corresponding RO₂ of each fuel radical, concerted elimination is relatively less important for the -OO· positioned at the primary and secondary carbons but increased by 10% for -OO· at the tertiary carbon. After the isomerization, the formed QOOH radicals can go through three channels, and these are second oxygen addition, cyclic ether formation, and production of olefin. Among all the QOOH radicals that can be produced from a given RO₂, the QOOH that can experience all three routes are usually less likely to be formed. A few examples were chosen to show the subsequent chain branching processes. For C8OOH1-2b and C8OOH4-2c, the route of cyclic ether is largely increased while the second oxygen addition is much less significant, and the proportion of alkene production is also comparatively reduced. For C8OOH2-2e that does not produce olefins, the second O₂ addition becomes more important which improves by 25%, and the ratio of cyclic ether formation is consequently decreased. These results show the scale of the impacts of these updated rate rules and how one reaction class may affect the entire chain branching sequences.

The main concern of the present model is the considerably increasing impacts of the fuel radical on the tertiary carbon, which is mainly related to the new rules in the H abstraction by OH. Therefore, more research is recommended to validate the current source. Also, the H abstraction by HO₂ is prone to uncertainty as few up-to-date investigations are available, and this model utilized the upper limit value from a previous computational study of 2-methylhexane. Furthermore, the simulation at high temperatures ($T > 1100$ K) shows negligible improvements, although this part of the kinetics is rather dependent on the performance of the C0-C4 chemistry.

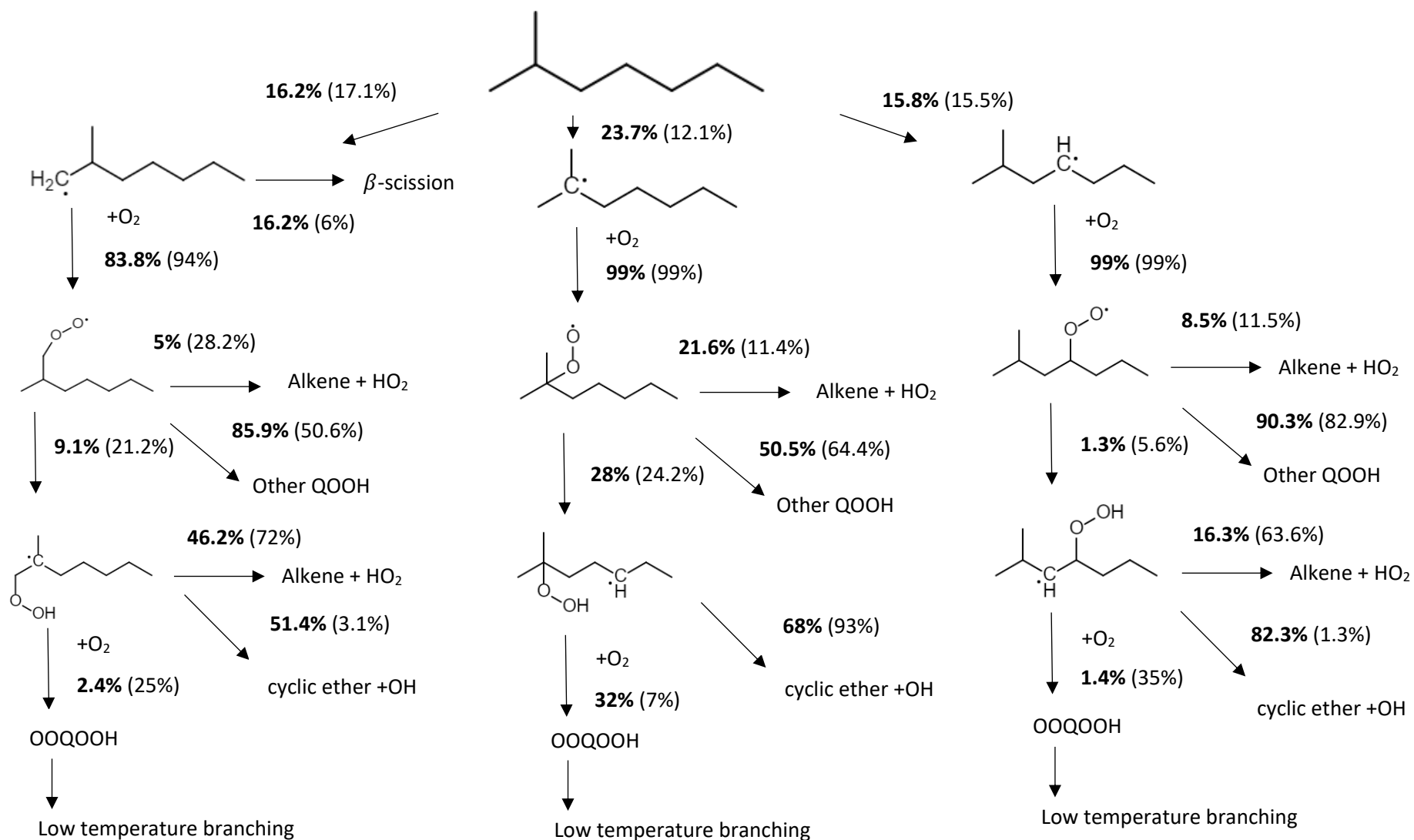


Figure 4.30. Reaction pathway of stoichiometric 2-methylheptane at 20 atm and 800 K: new % is in bold and original % is in brackets.

4.7 Summary

In this chapter, the mechanism optimization of 2-methylheptane mixtures is explored in detail using a closed homogeneous batch reactor of ANSYS Chemkin Pro and the predicted results are validated against the ignition delay time from shock tube experiments. The mechanism from Wang et al. [106] was chosen to run the initial simulations, which were operated at 650-1350 K and 20 atm for three equivalence ratio conditions, followed by the sensitivity analysis at various temperatures. Next, simulations of kerosene and S-8 fuel surrogates were performed to examine the quality of two detailed mechanisms from the NUIG and CRECK research groups, and modelling results were validated against experimental data of ignition delay time and laminar flame speed. The C3MECHV3.3 mechanism [120] from NUIG was chosen, hence the reaction classes related to the low temperature combustion of Wang et al. [106] were subsequently incorporated with their core chemistry. Further manipulation of the kinetics and thermodynamic properties is based on this combined mechanism.

New thermodynamic data related to the 2-methylheptane combustion was first calculated based on the group additivity method, and new group values were adopted from Burke et al. [148] with additional corrections. By using the updated thermochemical data, the new model shows that the reactivities around the NTC region are reduced by a factor of two. Next, five individual reactions selected from the sensitivity results were inspected, and the results indicate that the kinetics quality of C0-C4 in C3MECHV3.3 is reasonably good, hence the rate constants are suggested to remain unchanged.

The most significant section in this chapter is the investigation of updated rate rules of ten reaction classes that are key to the chain branching process around the low and intermediate temperature conditions. A compilation is shown in Table 4.4 and some refinements regarding their corresponding group is also added. Optimized simulations show great improvements at $T < 1100$ K compared to the previous models, especially the modelling of the stoichiometric and rich cases, which correspond excellently in the low and intermediate temperature ranges. The prediction of the lean condition is relatively less influenced and some upgrades at the NTC region are suggested. Sensitivity and reaction pathway analysis were subsequently conducted and discussed in detail, to show the scale of the impacts of these optimization approaches and certain issues and uncertainties in the current kinetic model.

Table 4.4 Compilations of updated rate rules with modifications.

Reaction class	References of rate rules	Comments (if applicable)
H abstraction by OH	[175, 176]	
R + O ₂ → RO ₂ and second O ₂ addition	[188]	Rules of second O ₂ addition are half as the first O ₂ addition.
RO ₂ → QOOH	[205]	For reactions without given rate rules, using nearest analogy and A × 0.5. Example: C8H17OO-3-2 → C8OOH3-2f, 1,6-H ss Utilized rules of 1,6-H ps
Concerted elimination	[54]	
Cyclic ether form	[207]	All A factor × 0.5.
QOOH → olefin + HO ₂	[54]	
Isomerization of OOQOOH	[188]	All E _a + 2.8 kcal · mol ⁻¹ Reactions with -OOH on the tertiary carbon follow the rules of RO ₂ isomerization
Ketohydroperoxide decomposition	[105]	Original value unchanged
H abstraction by HO ₂	[56]	Errors are expected

CHAPTER 5

EXPERIMENTAL RESULTS AND ANALYSIS

In this chapter, temperature measurements by using both the thermocouples and OH LIF thermometry are initially presented and discussed. Next, detailed quantifying of the OH and NO PLIF for the three liquid fuels is provided. Regarding the model validations, the detailed mechanism containing 537 species and 18250 reactions from CRECK modelling [119, 144, 210] is utilized for the liquid fuels, because the C3MechV3.3 mechanism has significant difficulties in simulating 1-D premix model, as explained in Section 4.2. As for the references fuels, GRI-Mech 3.0 mechanism [30] will be employed to model the CH₄/air flame and Okafor et al. [64] will be utilized to simulate the CH₄/NH₃/air flame. In addition, the height above burner is abbreviated as “HAB” in the following descriptions.

5.1 Temperature measurements

Before the discussions of the measured temperatures in the targeted flames, the adiabatic temperature of each flame condition was initially estimated, to provide a general indication of the maximum temperature that can be achieved in the targeted flames.

The calculations were carried out by using the model of the chemical and phase equilibrium calculations from Chemkin, and this model only requires the thermodynamic data of all the relevant species. The problem type employed is constant pressure enthalpy, and the initial reactants, temperature, and pressure are required to set up the model. From experience, it is found that the room temperature of the laboratory is quite stable and is commonly between 20-21 °C, hence the inlet temperature is set to 293 K and the initial pressure is set to 1 atm for the conditions of the gas fuels. As for the liquid fuels, the initial temperature is the temperature of the heated burner, which is 453 K as explained in Section 3.1. The compilation of the predicted results is presented in Table 5.1. It can be observed that for each fuel, the flame at the stoichiometric condition has the highest value, and the temperature of the rich condition is slightly higher than the lean condition. Also, the temperatures of the liquid fuels appear to be at a higher level than the two gaseous fuels, and the flame temperatures of CH₄/NH₃/air are at a lower level than the pure methane flames.

Table 5.1 Simulated equilibrium temperature (K) of each interested flame.

Flame	Equivalence ratio		
	1.30	1.00	0.84
CH ₄ /air	2054.5	2222.1	2050.7
CH ₄ /NH ₃ /air	2040.8	2211.5	2038.0
Kerosene	2256.1	2351.6	2212.4
Surrogate A	2242.4	2344.2	2203.9
Surrogate B	2243.1	2344.6	2204.4

Importantly, the adiabatic flame temperature is the maximum temperature of a specific fuel mixture oxidizing in a system without heat losses [24], while in the practical environments, the flame will exchange heat with the surroundings, hence the actual temperature is likely to be lower than the adiabatic value. However, the degree to which the measured temperature deviates from the ideal condition is largely unknown and also may differ depending on the specific experimental setup. For example, Doute et al. [76] measured the kerosene/air at 1 atm with the use of a flat-flame burner, and their results show that for the flame condition of equivalence ratio of 1.7, the temperature measured by thermocouples reaches the maximum value around 1770 K at the distance of 2-2.5 mm above the burner surface. By using the same equilibrium model from Chemkin and applying the inlet temperature of 473 K, the calculated adiabatic temperature is 1981.5 K, which is about 12% higher than the measured result. In conclusion, some level of discrepancy is expected, and the simulated temperatures are utilized as a reference to show that the obtained temperature data from the following experiments is realistically possible.

5.1.1 Correction of thermocouple

As stated in Section 3.3.1, the corrected temperatures (T_c) are calculated by using equation 3.2, and the temperature results of the CH₄/air, CH₄/NH₃/air, and kerosene flames are presented in Table 5.2, Table 5.3, and Table 5.4, respectively.

Table 5.2 Temperature profiles of CH₄/air flames by using the thermocouples (type P13R-005).

HAB/mm	$\varphi = 1.30$		$\varphi = 1.00$		$\varphi = 0.84$	
	T _m /K	T _c /K	T _m /K	T _c /K	T _m /K	T _c /K
0.0	899.0	915.3	1359.6	1444.7	1353.2	1433.2
0.2	1246.7	1310.0	1485.6	1608.5	1429.8	1530.4
0.4	1460.1	1582.0	1556.0	1704.9	1476.0	1590.7
0.6	1557.3	1716.4	1686.1	1893.7	1556.4	1699.4
0.8	1622.1	1810.5	1737.4	1972.5	1659.6	1846.1
1.0	1667.6	1878.8	<u>1751.6</u>	1994.8	1709.5	1920.2
1.2	1699.1	1927.4	1748.8	1990.3	1735.5	1959.8
1.4	1720.8	1961.4	1739.8	1976.2	<u>1742.6</u>	1970.7
1.7	<u>1732.7</u>	1980.2	1732.1	1964.2	1740.1	1966.8
2.0	1730.5	1976.7	1726.1	1954.9	1739.3	1965.7
2.5	1720.3	1960.6	1713.3	1935.2	1735.2	1959.3
3.0	1711.4	1946.5	1710.7	1931.2	1732.2	1954.8
5.0	1696.9	1923.9	1698.3	1912.3	1721.2	1938.0
10.0	1690.6	1914.2	1684.6	1891.4	1701.6	1908.3

Table 5.3 Temperature profiles of CH₄/NH₃/air flames by using the thermocouples (type P13R-002).

HAB/mm	$\varphi = 1.30$		$\varphi = 1.00$		$\varphi = 0.84$	
	T _m /K	T _c /K	T _m /K	T _c /K	T _m /K	T _c /K
0.0	1227.6	1257.5	1425.5	1477.7	1344.1	1383.4
0.2	1469.9	1533.0	1583.4	1664.1	1460.9	1516.4
0.4	1621.3	1715.9	1674.5	1776.2	1678.1	1776.5
0.6	1717.7	1837.9	1818.3	1961.4	1817.3	1954.3
0.8	1790.3	1933.0	1882.3	2047.3	1868.9	2022.6
1.0	1831.1	1987.6	<u>1894.3</u>	2063.7	<u>1877.4</u>	2034.0
1.2	1851.7	2015.6	1878.7	2042.5	1860.6	2011.5
1.4	<u>1858.3</u>	2024.8	1862.3	2020.2	1846.6	1992.8
1.7	1853.4	2018.1	1852.4	2006.9	1828.9	1969.4
2.0	1841.5	2001.8	1839.5	1989.6	1815.2	1951.5
2.5	1831.8	1988.7	1820.1	1963.7	1801.9	1934.0
3.0	1820.7	1973.6	1812.8	1954.1	1791.9	1921.1
5.0	1796.3	1962.1	1795.1	1930.7	1768.6	1890.9
10.0	1785.2	1940.9	1772.3	1900.9	1739.5	1853.7

Table 5.4 Temperature profiles of kerosene/air flames by using the thermocouples. (Rich condition: type P13R-005, stoichiometric condition: type P13R-003)

HAB/mm	$\varphi = 1.30$		$\varphi = 1.00$	
	Tm/K	Tc/K	Tm/K	Tc/K
0.0	1251.0	1309.2	1372.6	1427.4
0.2	1449.9	1557.1	1508.3	1589.3
0.4	1606.5	1770.5	1667.5	1790.3
0.6	1697.4	1903.3	1780.8	1941.9
0.8	1760.7	2000.3	1865.9	2061.4
1.0	1773.2	2020.0	<u>1880.4</u>	2082.2
1.2	<u>1778.2</u>	2027.8	1872.4	2070.8
1.4	1772.3	2018.4	1864.8	2059.9
1.7	1763.9	2005.3	1859.4	2052.2
2.0	1757.6	1995.4	1853.0	2043.0
2.5	1746.2	1977.7	1841.2	2026.3
3.0	1739.7	1967.7	1837.0	2020.2
5.0	1726.0	1946.7	1812.3	1985.6
10.0	1711.3	1924.2	1808.8	1980.7

For each fuel, the highest level of maximum temperature is achieved at the stoichiometric condition, and the peak temperature of the lean and rich conditions are rather close, which is consistent with the observations of the equilibrium temperatures. In terms of the absolute values, although the peak temperatures of each equivalence ratio condition of the fuels are all lower than their respective adiabatic temperature, the flames of CH₄/NH₃/air appear to be relatively hot, with all three conditions having a maximum temperature of over 2000 K. At a given flame condition, the peak of the CH₄/NH₃ blend is consistently about 50-60 K greater than the peak of the pure methane, while the thermodynamic theory in Table 5.1 demonstrates an opposite trend, suggesting that either one or both measurements of the flames has significant uncertainty. Although the two fuels are not measured by the same thickness of thermocouples, for the sake of consistency, the same method of radiation correction was applied. However, in practice, the impacts of the coating on the emissivity of the bead and the bead diameter may not be directly comparable on different wires. Also, depending on how the coating is being made, if part of the bare wires emerges in the flame, the measurements will be affected to some extent. Nevertheless, the measured temperatures

of the ammonia/methane mixtures are considered a little too high and certain errors are expected, particularly in the subsequent quantifying of the NO PLIF results. In addition, regarding the general shape, rich conditions of all three types of fuels produce the most reasonable profiles and the peak positions are reached at 1.7 mm, 1.4 mm, and 1.2 mm for methane, methane/ammonia blend, and kerosene, respectively.

Apart from the maximum values, another concern of error is the profiles of the stoichiometric and lean conditions, as the initial temperatures are all at a relatively high level and the propagating of the temperature at the region of 0-1 mm is less smooth compared to the rich conditions. Figure 5.1-5.3 demonstrate the temperature variation along the increase in height in detail. The phenomenon can be traced back to the determination of the position of the burner surface, and the potential cause of the high initial temperature may be due to the flame formed is a little below the diffuser plate. Also, for the flame conditions where type P13R-005 was employed, since the wire is generally thicker, even if the flames are produced above the plate, it is still difficult to manage a reasonable temperature reading at the position 0 mm. Therefore, it is sensible to assume that the temperatures obtained at 0 mm at the stoichiometric and lean conditions have an offset of +0.1 mm to +0.3 mm, which consequently affects the entire shape of the profiles.

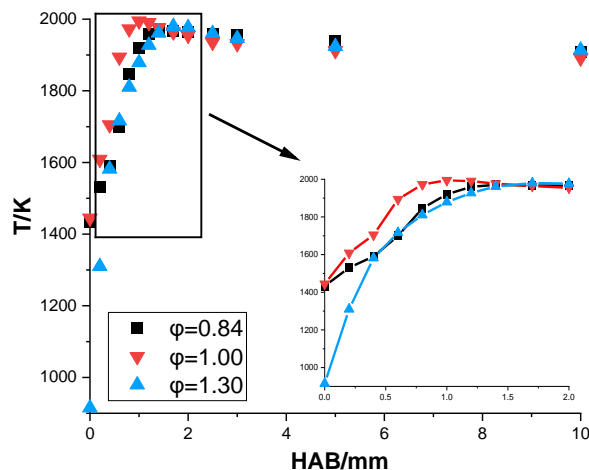


Figure 5.1 Corrected temperature profile of CH₄/air flames in three equivalence ratio conditions.

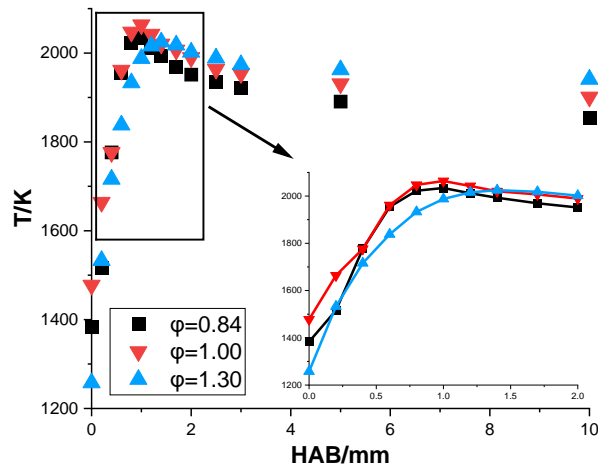


Figure 5.2 Corrected temperature profile of CH₄/NH₃/air flames in three equivalence ratio conditions.

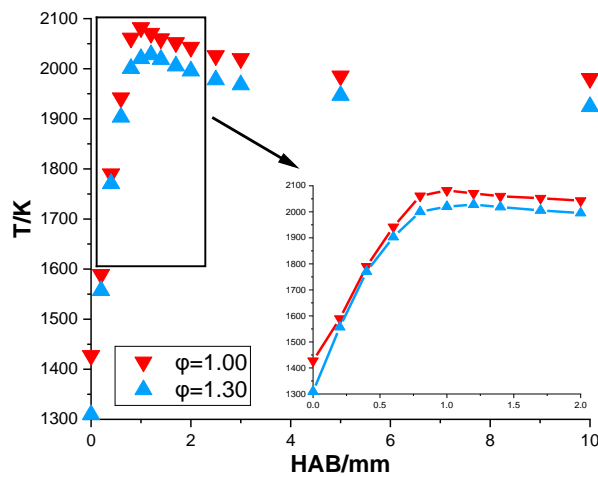


Figure 5.3 Corrected temperature profile of kerosene/air flames in two equivalence ratio conditions.

As explained in Section 3.1.3, a higher total flow rate for the stoichiometric and particularly lean conditions is helpful to push the flame out of the rig. While it may work more agreeably for the gas fuels, practical observations show that it is already difficult to attain reasonable temperature data with the current flow rates of the liquid fuels listed in Table 3.1, let alone the lean condition. Further increasing the flow rate can be a solution, while it will also largely increase the risks of breaking the thermocouple straight away with the stronger flow, as the trial tests showed. In conclusion, finding the delicate balance between the durability of a specific thickness of thermocouple wire and the total flow rate employed is crucial to measure the temperature data at the stoichiometric and lean conditions. Due to time limitations, for

the liquid fuels, only the kerosene flames at the rich and stoichiometric conditions have been obtained. The general shape, temperature propagation, and the corrected values of the thermocouple data are utilized as a reference to compare and determine the quality of the temperature data measured by OH LIF thermometry in the subsequent section.

Additionally, the corrected temperatures compiled in Table 5.2-5.4 were calculated based on the assumption of the fuel from the whole plate (A_2). Theoretically, another boundary condition of area A_1 can be utilized for temperature correction. Table 5.5 compiles and compares the peak temperature of each equivalence ratio condition of the fuels, with the use of two total flow rates listed in Table 3.1 and Table 3.2. Results show that wire type P13R-005 leads to the largest discrepancy, which is about 55 K, and type P13R-002 has about 40 K difference between two boundary flow rates. Realistically, the temperature should be somewhere in between these two values. The impacts of these two profiles are directly reflected in the model predictions, and an example of the simulated OH mole fraction of the pure methane flames at the rich condition is displayed in Figure 5.4. The OH mole fraction reached the maximum at 1.2 mm and 1.35 mm for A_1 and A_2 , respectively. The general shapes are also quite similar, as the proportion of the remaining product is 17.2% for A_1 and 22.8% for A_2 . The only major difference is the absolute value, with the maximum temperature of the A_1 being approximately 2-3 times greater than the peak of the A_2 .

Table 5.5 Impacts of different flow rate with the reference of the peak temperature.

Fuel	Equivalence ratio	T_{A_1}/K	T_{A_2}/K	Δ/K
CH ₄ /air	1.30	1921.9	1980.2	58.3
	1.00	1937.5	1994.8	57.3
	0.84	1917.0	1970.7	53.7
CH ₄ /NH ₃ /air	1.30	1985.6	2024.8	39.2
	1.00	2023.8	2063.7	39.9
	0.84	1997.2	2034.0	36.8
Kerosene	1.30	1969.0	2027.8	58.8
	1.00	2034.7	2082.2	47.5

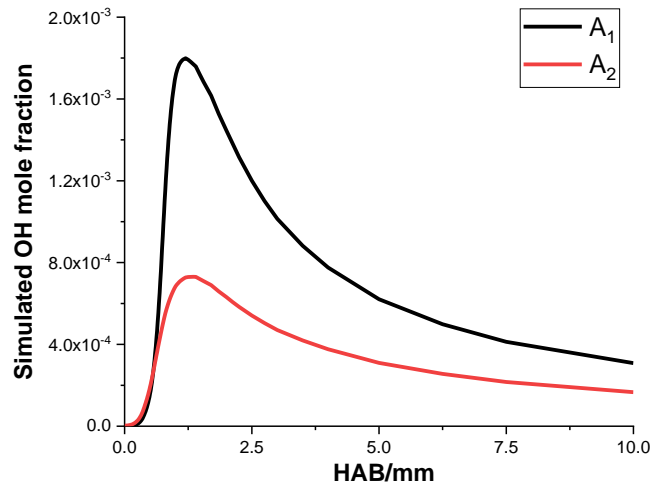


Figure 5.4 Simulated OH mole fraction of the CH₄/air at the rich condition, with the temperature profiles calculated by two area boundaries, respectively.

5.1.2 Temperature results obtained from OH LIF thermometry

Temperature data obtained from OH LIF thermometry for liquid fuels are discussed as follows. Firstly, experiments show that it is quite difficult to record a reasonable profile, and the collected data on the lean conditions of the targeted flames is primarily regarded as deficient, and the discussion of this challenge and suggestions for future research will be provided in Section 5.1.4. Therefore, only the temperature results at the stoichiometric and rich conditions are included in the subsequent analysis.

After obtaining the ratio of the two selected signals from the PLIF recording, the temperature can be calculated by using the equations in Figure 3.18 and Figure 3.19. It is difficult to determine whether a measured profile is sensible because the knowledge of the flame temperature is quite limited, and the signal interferences picked up from either the surroundings or the regions around the burner surface are inevitable. From the previous literature [12, 76], at the atmospheric pressure, a common temperature profile of a flat-flame burner keeps increasing until it reaches the maximum value around the distance of 2-3 mm above the burner surface, and then it decreases and stabilizes at a consistent level. Therefore, the general shape of the measured data should largely correspond to this description. Additionally, a clear peak value must be observed, and it must not exceed the simulated equilibrium temperature in their respective condition stated in Table 5.1.

The temperature profiles measured by the two transition pairs are not similar and shall be discussed separately. For the transition pair of $R_2(13)/P_1(2)$, there are two types of graphs that both correspond well to the general shapes of temperature results from the literature. However, the detailed aspects are quite different and data refinements are required accordingly to ensure a smooth and consistent graph. The first type of graph is commonly for the rich condition and Figure 5.5 shows an example of both the raw data and the temperature points selected based on their original measurements. The result demonstrates a reasonable trend at the height of approximately 0-7 mm above the burner surface. When the distance further increases and the flame mixture is more exposed to the open air, the temperatures start to increase, as shown by the red part in Figure 5.5 (a). This upward tendency offers little meaningful insights since the combustion is coming to an end in this region, thus an arbitrary temperature has been set at the distance of 10 mm to indicate the termination of the process and the value is set to be relatively lower than the previous data point.

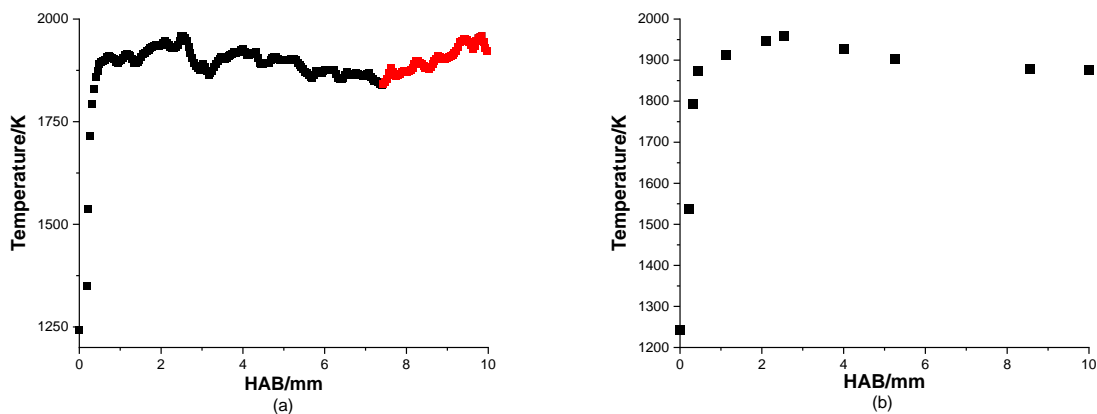


Figure 5.5 An example of the temperature profile obtained from OH LIF thermometry with the $R_2(13)/P_1(2)$ pair, type 1: (a) the raw data of the rich condition of surrogate A; (b) the refined temperature data.

The second type of profile is commonly for the stoichiometric and lean conditions and an example is demonstrated in Figure 5.6. In general, it shows a quite rational trend that corresponds well with the literature, while there is a small peak in the region near the burner surface, as the red part in Figure 5.6 (a) highlighted. As this observation does not fit the description of the general graph shape from the literature, this peak region is regarded as being affected by the signal noises and therefore will not be taken into consideration when selecting the data points of the temperature.

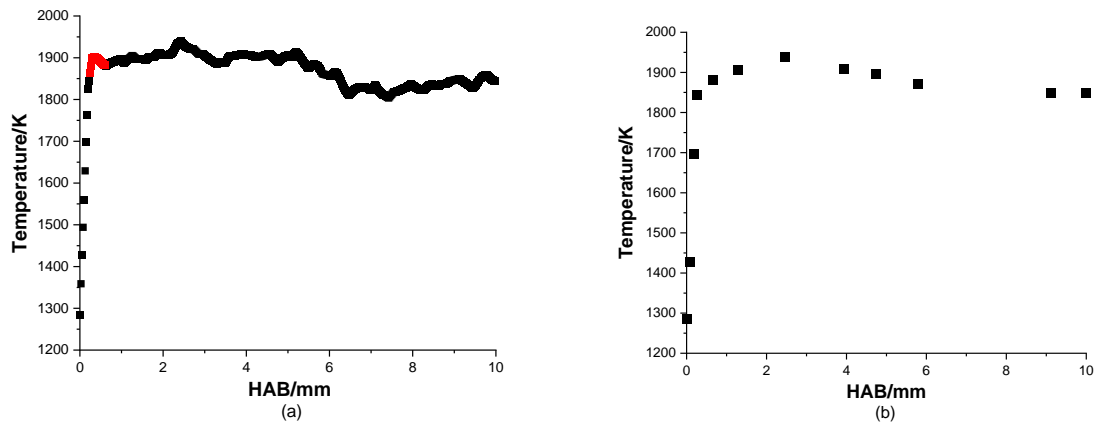


Figure 5.6 An example of the temperature profile obtained from OH LIF thermometry with the $R_2(13)/P_1(2)$ pair, type 2: (a) the raw data of the stoichiometric condition of kerosene; (b) the refined temperature data.

For the transition pair of $R_2(2)/R_1(12)$, typically measured result is shown in Figure 5.7. Similar to the type 1 of the $R_2(13)/P_1(2)$ pair, the graph indicates a decent temperature progress with the change of the distance above the burner, until it approaches the end of the process the temperature starts to increase. Hence, an arbitrary value is also given at the distance of 10 mm based on the smoothness of the general graph. Importantly, unlike the thermocouple measurements where the temperature value at the end of the combustion region is relatively certain, the data at this area obtained from OH LIF thermometry is merely an estimation. Therefore, the approximation may influence the shape of the simulated OH mole fraction to some degree and a certain level of error is expected.

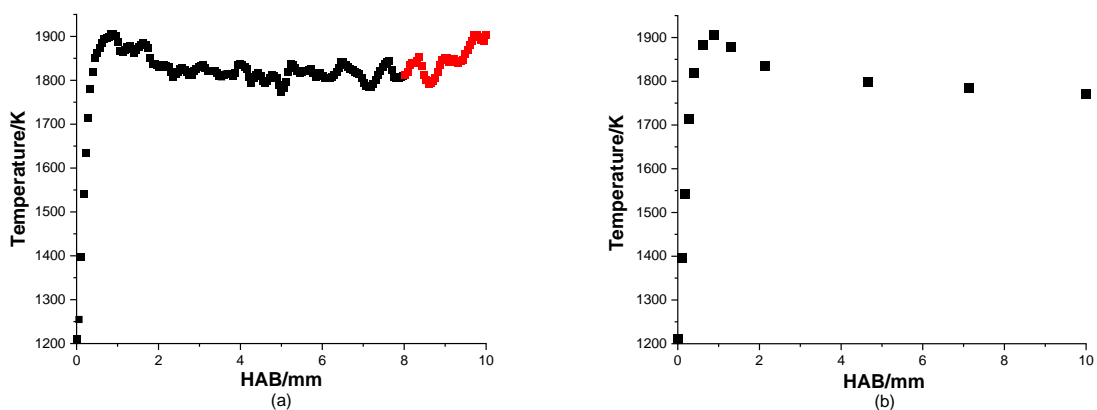


Figure 5.7 An example of the temperature profile obtained from OH LIF thermometry with the pair of $R_2(2)/R_1(12)$: (a) the raw data of the rich condition of kerosene; (b) the refined temperature data.

The detailed compilations of the temperature data of kerosene, surrogate A, and surrogate B are displayed in Table 5.6, Table 5.7, and Table 5.8, separately. Firstly, by comparing the

stoichiometric and rich case of the kerosene flames, it can be observed that the results from the pair of $R_2(13)/P_1(2)$ have a higher level of maximum temperature than the result from the pair of $R_2(2)/R_1(12)$, with the difference being about 150 K for the rich condition. Regarding the propagation of the temperature, around near the burner surface, the temperatures from the $R_2(13)/P_1(2)$ pair appear to be already at a quite high level. Take the rich condition of kerosene for instance, the flame starts around 1200 K from both transition pairs, and the temperature is already 1850 K at 0.11 mm from the result of the $R_2(13)/P_1(2)$ pair, while the value from the $R_2(2)/R_1(12)$ pair at the same distance is only 1400 K. At the region of 0-0.5 mm, the steadier temperature growth measured by the $R_2(2)/R_1(12)$ pair on the other hand, is quite agreeable with the profiles measured by the thermocouples. In terms of the position where the peak temperature is achieved, for the $R_2(13)/P_1(2)$ pair it is reached around 1.8-2.5 mm above the burner surface, which correspond reasonably with the results from the literature. For the $R_2(2)/R_1(12)$ pair, the position is around 1-1.3 mm, which is in decent agreement with the thermocouple measurements from Section 5.1.1.

Table 5.6 Temperature profiles of the kerosene flames by using OH LIF thermometry.

$\varphi = 1.30$				$\varphi = 1.00$			
$R_2(2)/R_1(12)$		$R_2(13)/P_1(2)$		$R_2(2)/R_1(12)$		$R_2(13)/P_1(2)$	
HAB/mm	T/K	HAB/mm	T/K	HAB/mm	T/K	HAB/mm	T/K
0.0	1201.8	0.0	1215.4	0.0	1453.0	0.0	1286.4
0.11	1396.9	0.04	1451.7	0.06	1511.5	0.08	1428.7
0.17	1541.9	0.11	1855.7	0.17	1646.1	0.18	1697.2
0.28	1713.7	0.55	1991.1	0.28	1744.0	0.25	1843.9
0.39	1819.7	1.57	2037.0	0.45	1836.7	0.65	1881.0
0.62	1884.0	2.10	<u>2061.5</u>	0.67	1880.6	1.28	1905.4
0.90	<u>1913.3</u>	3.56	2039.2	1.07	<u>1922.3</u>	2.46	<u>1939.6</u>
1.29	1878.8	5.67	2028.2	1.74	1898.4	3.94	1909.0
2.14	1834.6	7.55	2002.9	2.98	1869.8	4.74	1895.2
4.67	1797.7	8.27	1992.8	4.10	1851.1	5.79	1872.0
7.13	1784.6	10.0	1990.0	6.23	1838.0	10.0	1850.0
10.0	1770.0			10.0	1820.0		

Table 5.7 Temperature profiles of the surrogate A flames by using OH LIF thermometry, transition: $R_2(13)/P_1(2)$.

$\varphi = 1.30$		$\varphi = 1.00$	
HAB/mm	T/K	HAB/mm	T/K
0.0	1241.6	0.0	1368.2
0.22	1538.3	0.09	1505.2
0.31	1793.2	0.18	1746.7
0.45	1874.4	0.49	1886.0
1.11	1912.2	1.20	1934.1
2.09	1946.7	1.92	<u>1951.8</u>
2.54	<u>1959.3</u>	2.89	1935.6
4.01	1926.7	4.05	1918.8
5.25	1903.4	5.34	1899.2
8.55	1878.9	6.28	1880.7
10.0	1875.0	9.93	1858.5
		10.0	1858.0

Table 5.8 Temperature profiles of the surrogate B flames by using OH LIF thermometry: the rich condition is from the $R_2(13)/P_1(2)$ and the stoichiometric condition is from the $R_2(2)/R_1(12)$.

$\varphi = 1.30$		$\varphi = 1.00$	
HAB/mm	T/K	HAB/mm	T/K
0.0	1211.1	0.0	1056.7
0.06	1479.5	0.11	1331.7
0.23	1752.5	0.23	1627.1
0.45	1841.9	0.34	1727.5
1.01	1907.9	0.56	1827.6
1.74	<u>1953.3</u>	0.79	1854.9
2.76	1922.7	1.35	<u>1869.1</u>
4.59	1892.9	1.97	1846.0
7.12	1871.5	3.20	1831.8
10.0	1860.0	4.66	1808.2
		6.96	1794.4
		10.0	1785.0

Importantly, as discussed in Section 3.3.2, the determination of wavelength peak directly influences the temperature output and from experience, the visual observation of a given

transition can result in an uncertainty of ± 0.001 nm, particularly for weaker signals. Table 5.9 and Table 5.10 compile the temperature differences between actual and ideal conditions for the two transition pairs, respectively. For the pair of $R_2(13)/P_1(2)$, the recording of $R_2(13)$ is more prone to errors, as $P_1(2)$ has relatively strong intensity and shows little temperature variation (Figure 3.15). If the actual wavelength of $R_2(13)$ is away from the peak by 0.001 nm, the modified ratio may lead to a temperature value that is approximately 130 K smaller than the ideal result. For the pair of $R_2(2)/R_1(12)$, the intensities of both signals are similar although $R_2(2)$ is slightly less intense (Figure 3.16). If the actual wavelength of $R_2(2)$ is away from the peak by 0.001 nm, the modified ratio can result in a temperature value that is about 160 K greater than the ideal result. The calculations only provide an insight into the uncertainty scale, as in practice, both transitions of a given pair may be away from the peak wavelength by different margins.

Table 5.9 Uncertainty calculation of the $R_2(13)/P_1(2)$ pair at 1500 K, note: $\Delta = T_{\text{limit}} - T_{\text{ideal}}$.

	Simulated wavelength of $R_2(13)/\text{nm}$	Simulated intensity of $R_2(13)$	$R_2(13)/P_1(2)$ ratio	Temperature/K	Δ/K
Ideal	282.5558	14.88	0.149	1455.0	
Lower limit	282.5548	12.89	0.129	1393.3	-61.7
Upper limit	282.5568	10.95	0.110	1329.0	-126.0

Table 5.10 Uncertainty calculation of the $R_2(2)/R_1(12)$ pair at 1500 K, note: $\Delta = T_{\text{limit}} - T_{\text{ideal}}$.

	Simulated wavelength of $R_2(2)/\text{nm}$	Simulated intensity of $R_2(2)$	$R_2(2)/R_1(12)$ ratio	Temperature/K	Δ/K
Ideal	282.1299	30.27	1.454	1506.0	
Lower limit	282.1289	23.76	1.142	1662.6	+156.6
Upper limit	282.1309	24.55	1.180	1639.7	+133.7

The main concern of reliability and accuracy regarding the temperature data derived from this approach is the maximum value achieved among the equivalence ratio conditions for each liquid mixture. Both the adiabatic temperature model and the thermocouple results suggest that for a certain fuel, the stoichiometric condition flame has the highest peak temperature and the maximum temperatures achieved at the equivalence ratio of 1.3 should be relatively lower. However, the peak derived from the OH LIF thermometry appears to be

rather random, and from the results of the $R_2(13)/P_1(2)$ pair, the rich condition of all three mixtures has a higher value than the stoichiometric case. For kerosene flames, the peak value of the rich condition is about 120 K higher than the stoichiometric case, while for the surrogate A flames, the gap of the maximum temperatures between the rich and the stoichiometric conditions are quite close, which is only about 10 K. As for the surrogate B flames, the available temperature data of the rich and stoichiometric conditions is not attained by the identical transition pair, hence is not directly compared. Nevertheless, the temperature measured by the $R_2(2)/R_1(12)$ pair appears to be at a lower level compared to the result of the $R_2(13)/P_1(2)$ pair.

Additionally, in some cases where the temperature at the position 0 mm is at a relatively high level, further manipulation is suggested for the quality of the modelling. Figure 5.8 displays an example of the predicted OH mole fraction by using the result of surrogate A at the stoichiometric condition, whose original temperature is 1368 K at position 0 mm. The black block shows that a certain level of OH has already formed at the burner surface, which is realistically incorrect. Therefore, an arbitrary temperature of 1100 K is provided at position 0 mm and the rest of the temperature data remains unchanged, and the simulation is shown in the red line of Figure 5.8. After this change in the data, the simulated OH mole fraction appears to be at the appropriate level at the burner surface, and the peak value and the general graph shape are not altered.

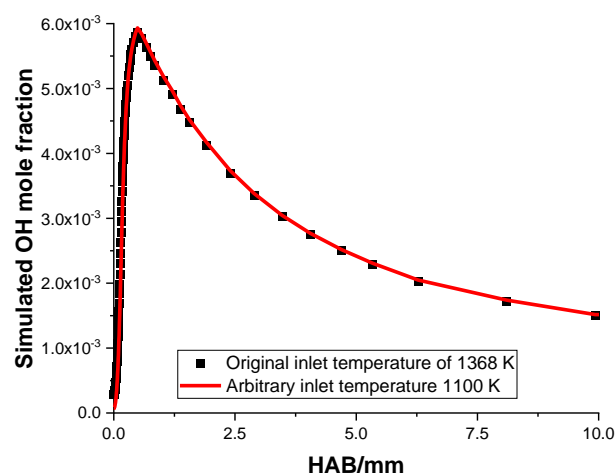


Figure 5.8 Comparison of the simulations with different inlet temperature.

5.1.3 Comparison and discussion

This section aims to compare the temperature profiles from different approaches and demonstrate their subsequent impacts on the simulated OH profiles. Three criteria of the simulations are addressed to determine the quality of the temperature profiles, that are the position where the peak is reached, the maximum mole fraction of the OH, and the profile shape. The percentage of the remaining product is an indication of the graph shape, calculated by the OH mole fraction at the end divided by the maximum OH mole fraction. In addition, a compilation of the model comparisons is shown in Table 5.11.

Table 5.11 Comparison of the OH model by using different temperature data at the rich and stoichiometric cases of the kerosene/air flames.

Temperature approach	Peak position/mm		Peak concentration		%Remaining product	
	$\varphi = 1.30$	$\varphi = 1.00$	$\varphi = 1.30$	$\varphi = 1.00$	$\varphi = 1.30$	$\varphi = 1.00$
Thermocouple	0.80	0.80	2.08×10^{-3}	6.48×10^{-3}	12.4	32.6
OH LIF thermometry: R ₂ (13)/P ₁ (2)	0.52	0.43	2.26×10^{-3}	5.69×10^{-3}	12.9	25.3
OH LIF thermometry: R ₂ (2)/R ₁ (12)	0.62	0.51	1.67×10^{-3}	5.43×10^{-3}	7.21	24.8

Simulations of the rich condition of the kerosene flame are shown in Figure 5.9. The difference in the maximum temperature between the thermocouples and OH LIF thermometry of the R₂(13)/P₁(2) pair is around 35 K, and consequently, the predicted results show that the peak mole fractions from these two methods are rather close with the difference being within 10%, and also the general shapes correspond well. The main discrepancy is the position of the peak, which has about 0.3 mm offset between the two methods. As explained in Section 5.1.2, this is primarily due to the fast temperature propagation at the region of 0-0.5 mm from the R₂(13)/P₁(2) data. As for the result of the R₂(2)/R₁(12) pair, the simulated OH at maximum is about 35% lower than the peak from R₂(13)/P₁(2), and the shape of the remaining product has approximately 5% differences compared to the simulations of the other two temperature data. From the OH PLIF measurements, the proportion of the remaining product of the kerosene/air flame at the rich condition is typically around 25-30% and the position where the peak is achieved is about

0.8-1 mm. Therefore, the result from the thermocouple wires appears to be the most appropriate temperature representation of the kerosene flame at the equivalence ratio of 1.3.

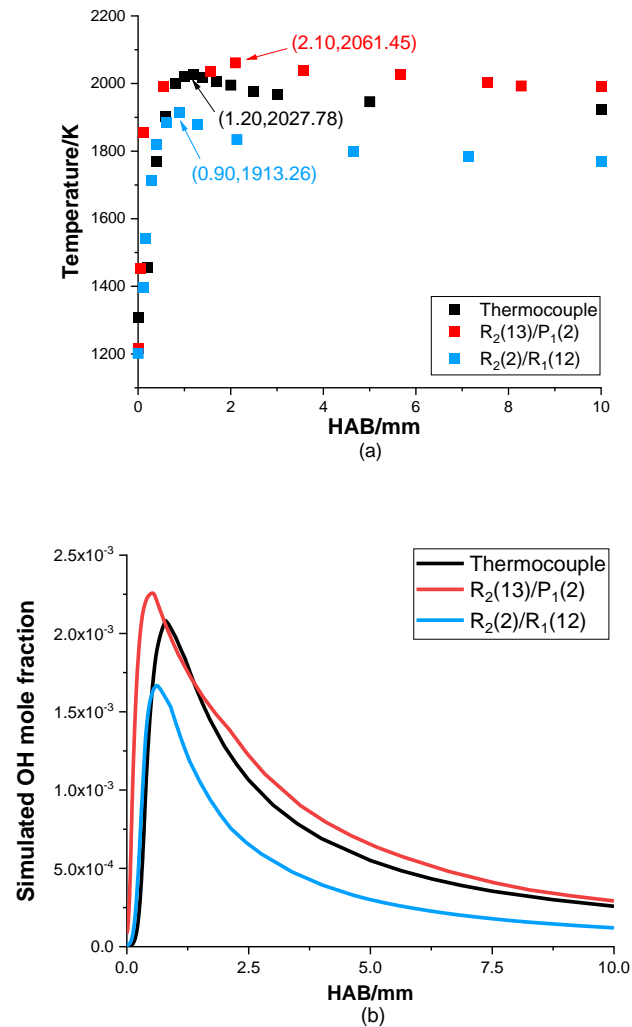


Figure 5.9 Impacts of the temperature profiles with the example of the kerosene flame at the rich condition: (a) Comparison of the temperature data between the three approaches; (b) Simulated OH mole fraction based on their respective temperature data.

Simulations of the stoichiometric condition of the kerosene flame are shown in Figure 5.10. The temperature results of the two transition pairs are rather similar. However, the maximum temperature from the thermocouple is about 150 K greater than the data from the OH LIF thermometry of the R₂(13)/P₁(2). Apart from the apparent differences in the maximum predicted OH mole fraction, this also leads to a discrepancy of 8% regarding the modelling shape. In addition, like the rich condition, the position of the peak from thermocouples has about 0.3-0.4 mm deviation compared to the results of OH LIF thermometry. From the OH

PLIF measurements, the proportion of the remaining product of the kerosene/air flame at this condition is typically between 36-45% and the peak position is reached around 0.9-1.1 mm. Hence, it is sensible to assume that the thermocouple measurement provides a more accurate insight into the temperature in the targeted flame.

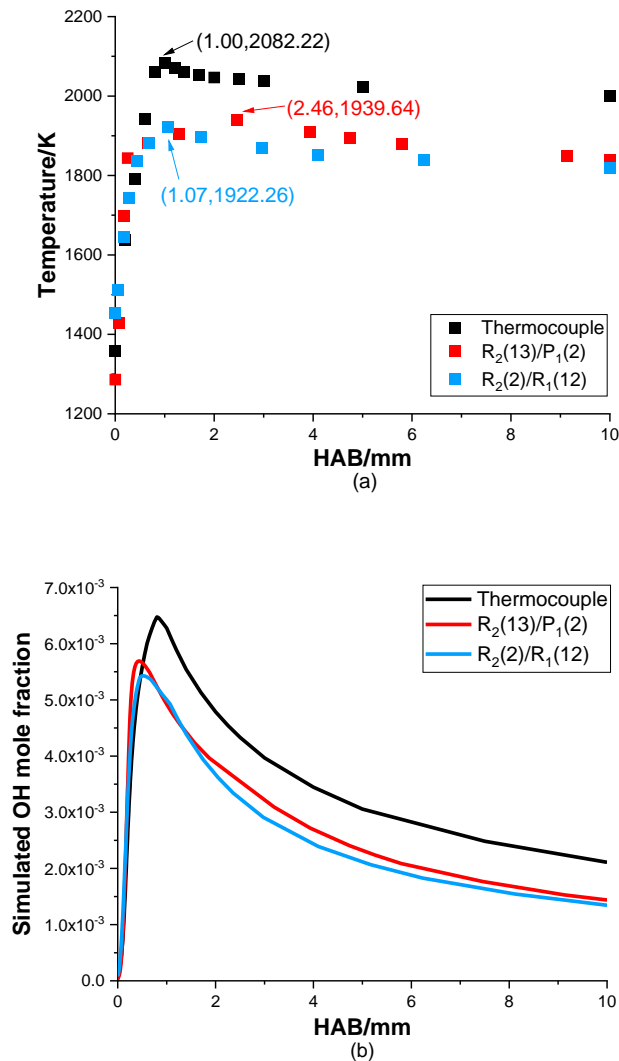


Figure 5.10 Impacts of the temperature profiles with the example of the kerosene flame at the stoichiometric condition: (a) Comparison of the temperature data between the three approaches; (b) Simulated OH mole fraction based on their respective temperature data.

Importantly, although the results of the thermocouple in both cases of the kerosene flames produce a more agreeable model of the OH, it cannot be concluded that the temperature data is precise, and the use of the thermocouple is a better approach for obtaining the temperature profiles from a flat-flame burner. As discussed in Section 5.1.1 and 5.1.2, both methods entail inherent issues and consequently, results may be compromised to some

extent. Also, due to the difficulties of the operation, the credibility of the temperature result of a given condition, either by thermocouple or OH LIF thermometry, is primarily dependent on a single set of experimental data, and the previous comparisons suggest that the key aspects of the temperature profile obtained from different methods do not particularly align with each other and few clear patterns can be found.

In conclusion, some aspects of the temperature data measured by either method are sensible, while certain degrees of errors are expected. The maximum value directly indicates the peak value of the OH mole fraction, and the temperature growth at the region of 0-1 mm largely influences the position where the peak is achieved. In addition, the shape of the profile is an accumulated result of these various factors. Regarding the quality of the two transition pairs, both have some aspects of inadequacy. Judged by the modelling output and the comparison with the thermocouple results, the data of the $R_2(13)/P_1(2)$ pair is regarded to be more reasonable. Since no thermocouple experiments are conducted for the two surrogate mixtures, the accuracy of the temperature data derived by the OH LIF thermometry partly relies on the references of the kerosene/air flames.

5.1.4 Challenges: temperature measurements at the lean conditions

Despite being the most stable flame among the three equivalence ratio conditions, the temperature result of the lean case is the hardest to manage. Partly due to the same concern as the thermocouple wires, it is more difficult to detect the beginning of the flame with the current level of total flow rates, which subsequently affects the general shape of the profile.

Figure 5.11 demonstrates three temperature profiles obtained by OH LIF thermometry of the lean case of the surrogate A and their respective OH modelling. The general shape of type 2 corresponds well with the other $R_2(13)/P_1(2)$ data listed in Table 5.6-5.8, however, the result shows a peak temperature value of 2300 K, which is theoretically impossible as it surpasses the adiabatic temperature. On the other hand, the measurement from the $R_2(2)/R_1(12)$ pair has a sensible maximum temperature, while the inlet temperature appears to be too high. Additionally, type 1 seems to be the most reasonable in terms of the general shape and the level of both inlet and maximum temperature, although compared to the other $R_2(13)/P_1(2)$ results, the temperature propagation at the region of 0-1 mm appears to be much steadier.

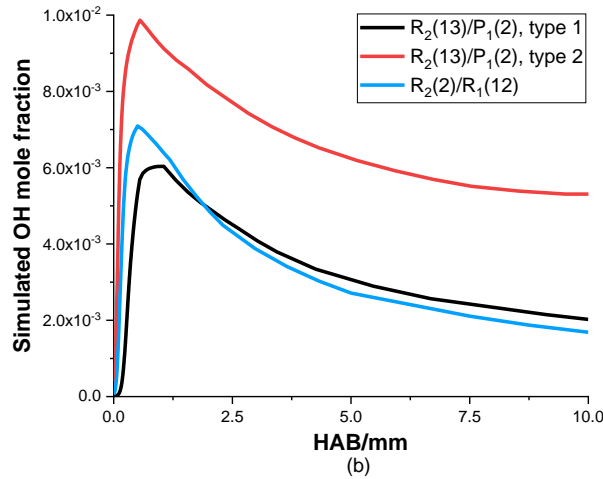
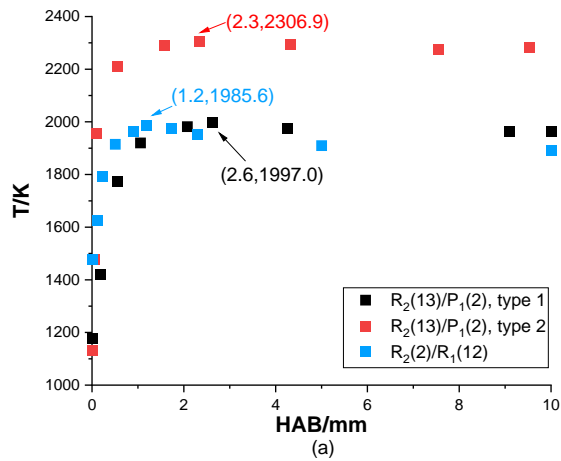


Figure 5.11 Impacts of the deficient temperature profiles with the lean condition of the surrogate A flame: (a) Three sets of temperature data; (b) Simulated OH mole fraction based on their respective temperature data.

The OH simulations based on these profiles show that the remaining product is 33.5%, 53.8%, and 23.8% for the type 1, type 2, and $R_2(2)/R_1(12)$, respectively. The considerable discrepancy among temperature sources makes it difficult to determine the general shape at this flame condition. From the measurements of the OH PLIF, the proportion of the remaining product of all three flames at the lean condition is typically between 55-65%, which is rather agreeable with the modelling of type 2 of the $R_2(13)/P_1(2)$. Despite the considerations of the experimental errors and the lack of general knowledge of the OH mole fraction consumption at a fuel-lean condition of a kerosene-based mixture, the differences between the PLIF and the simulations from the other two profiles is quite substantial, thus it is reasonable to consider the temperature data derived from the type 1 and the $R_2(2)/R_1(12)$ as flawed.

Furthermore, the peak temperature of type 1 of the $R_2(13)/P_1(2)$ is about 10 K higher than the $R_2(2)/R_1(12)$, however, the maximum simulated OH mole fraction of type 1 is about 20% lower than the result from the $R_2(2)/R_1(12)$, indicating either one or both temperature sets is deficient.

5.2 PLIF measurements

The PLIF data collection and calculation were previously discussed in Section 3.2.3, and an example of the OH raw signal, the background noise, and the cuvette is shown in Figure 5.12.

It is first observed that the intensity of the raw signal seems to be the strongest in the centre and does not appear to be that consistent across the x-direction of the diffuser plate, and this phenomenon may be due to the design of the new diffuser plate. Figure 3.6 (b) shows that the pattern of the holes in the new plate is the most condensed around the centre, compared to the old design in Figure 3.6 (a), which is relatively unchanging across the entire surface. To further confirm the uniformity of the flame, the corrected signals at different x-positions are plotted and demonstrated in Figure 5.13. Since the width of the metal bar described in Section 3.2.3 is a little over 6 mm, the range on either symmetrical side of the flame is set to be 0-3 mm, where 0 mm indicates the centre of the diffuser. Line number one in Figure 5.12 (a) indicates the centre of the burner and the distance between each vertical polyline is 1 mm. The results show little variations in the x-position, as the difference of the peak position is within 0.1 mm and the largest OH shape discrepancy between condition 1 and condition 4 is around 4%. Hence, the studied laminar flames can be regarded as uniform and suitable to apply for the model of burner-stabilized flame in the subsequent validations.

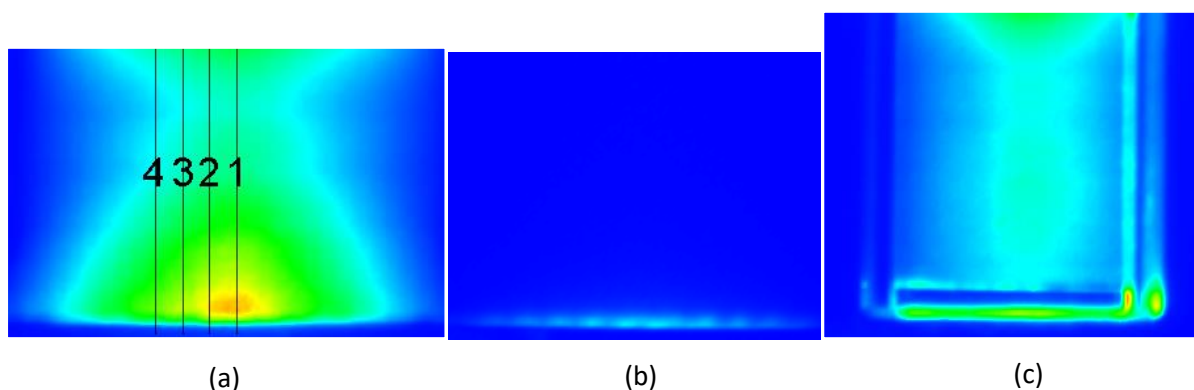


Figure 5.12 An example of the signal images from the $Q_1(6)$ transition, by using the kerosene flame at the stoichiometric condition: (a) raw; (b) background; (c) cuvette.

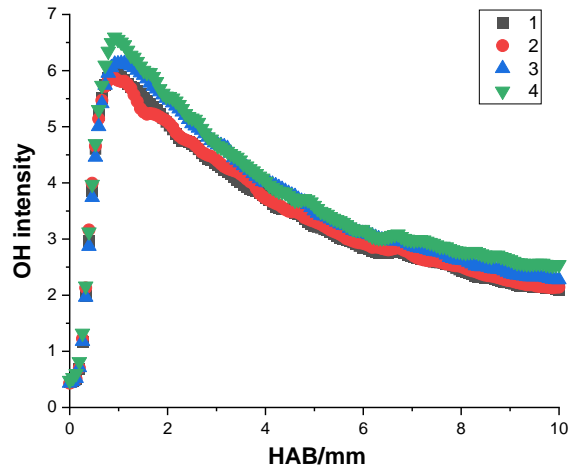


Figure 5.13 Normed OH intensity with different x-axes.

The PLIF results presented in the following discussion, referred to as the “original PLIF signal”, have already corrected the effects of the background fluorescence and the laser sheet intensity. To convert the PLIF intensity to the absolute mole fraction of either OH or NO, a certain calibration method is required, and the accuracy of the radical concentration results is largely determined by it. Studies of quantitative PLIF data of the key radicals in a flame are relatively scarce and lack validations, hence certain levels of errors are expected. This work adopted the methodology of OH measurements from Hughes et al. [211], and the same concept will also be employed for the NO validation.

It is both extremely difficult and error-prone to calibrate the image of PLIF directly, as the fluorescence intensity is dependent on several parameters, such as laser intensity, laser sheet volume in the observation region, quantum efficiency of the camera and intensifier system, etc. However, the problem can be simplified when two LIF signals are captured with the use of the same detection equipment operating under identical conditions and the relationship can be described as [211]:

$$\text{LIF} \propto \frac{N}{Q} \quad (\text{Eq. 5.1})$$

Where N represents the population of the probed energy level and Q represents the total quenching rate. The population can be calculated by the multiplication of the total OH mole fraction and the Boltzmann distribution (bf) of the targeted levels in the rotational state, which is rotational level 6 for OH, and the sum of rotational level 12 and 20 for NO,

respectively. LIFBASE can simulate the population distribution at the desired level, and both fitting curves as a function of temperature are shown in Figure 5.14.

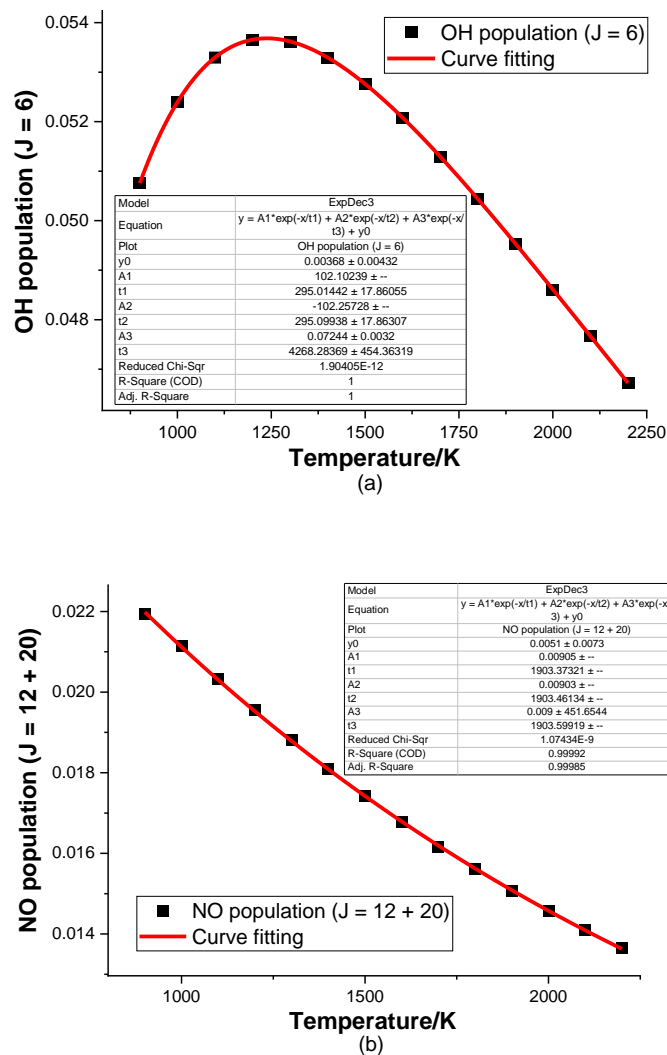


Figure 5.14 Simulated Boltzmann population: (a) OH at $j = 6$; (b) NO at $j = 12 + 20$.

For the total quenching rate, it can be calculated as:

$$Q = \sum_i \sigma_i N_i V_i \quad (\text{Eq. 5.2})$$

Where σ_i , N_i , and V_i indicate the quenching cross section, concentration, and velocity of the species i , respectively. Based on the thermodynamic and kinetic theory, equation 5.1 can be rewritten as [211]:

$$\text{LIF} \propto \frac{[\text{OH}] b_f \sqrt{m} \sqrt{T}}{\sigma P} \quad (\text{Eq. 5.3})$$

Where m represents the molecular weight, T is the temperature, and P is the pressure of the experimental environment. Regarding the quenching rates, Tamura et al. [212] measured the quenching rates of three species at the A-states in the laminar methane flames, and the data is subsequently compared with the models of quenching coefficient and the compositions of the flame. The expression of the cross section σ_{eff} (unit: \AA^2) is dependent on the types of the collider. For practical reasons and also the availability of data, only the major four species present in the combusted fuel, that are N_2 , O_2 , CO_2 , and H_2O , are considered. In the case of the OH, a simple two-parameter equation is utilized to describe the quenching cross section, and as for NO, different expressions are provided based on the colliders.

Thus, by using equation 5.3, the concentration of the liquid fuels can be described as:

$$[\text{OH}]_L = \frac{LIF_L[\text{OH}]_{ref}bf_{ref}\sqrt{m_{ref}}\sqrt{T_{ref}}\sigma_L P_L}{LIF_{ref}bf_L\sqrt{m_L}\sqrt{T_L}\sigma_{ref}P_{ref}} \quad (\text{Eq. 5.4})$$

Instead of correcting the whole PLIF graphs, a reference point is required for each parameter of both the liquid and gas fuels. It can be either the maximum or the end point ($HAB = 10 \text{ mm}$), and the specific values of the temperature, predicted OH mole fraction of the reference fuel, and the two original PLIF signals are subsequently assigned according to the selected source. Both the Boltzmann fraction and the quenching cross section can be obtained by their respective equations concerning the temperature. The molecular weight can be calculated with the use of the Chemkin models. In addition, the experiments of liquid and gas fuels are conducted in the same environment, therefore the pressure conditions are both 1 atm.

5.2.1 Reference fuels

Importantly, the results of the simulations and the experiments from the gas fuels directly affect the quality of the quantitative OH and NO determinations of the liquid fuels, and the examinations are discussed separately as follows.

Figure 5.15 demonstrates both the OH model and the original PLIF signals of the CH_4 /air flames at three equivalence ratio conditions. The position of the peak and the percentage of the remaining product are compared and subsequently compiled in Table 5.12. Results at the rich condition show that the positions of the maximum OH match excellently between the model and PLIF, and the difference of the OH graph shapes is within 5%. Also, the PLIF signals of the stoichiometric and lean conditions appear to be quite agreeable with the models.

However, one major uncertainty is the level of relative OH. The model suggests the highest level of OH is reached at the stoichiometric condition, which is directly reflected in the measured temperature profiles. On the other hand, PLIF data shows that the pure methane flame at the lean condition has the most amount of OH.

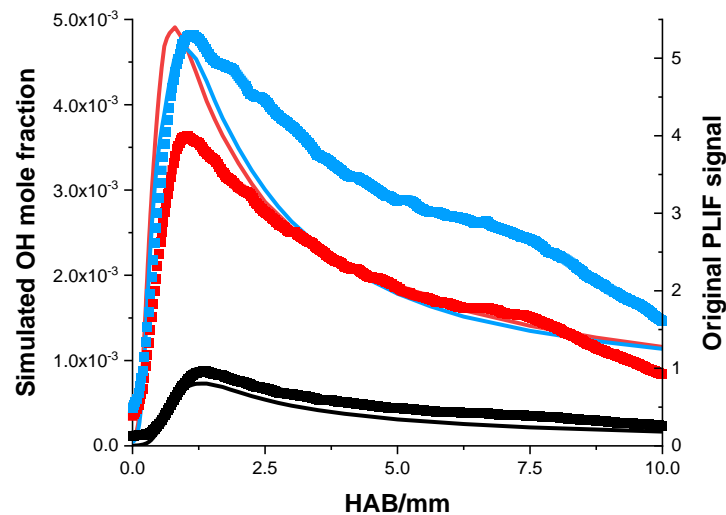


Figure 5.15 Comparison of the OH profile between the simulations (line) and the PLIF signals (scatter) of the CH₄/air flames at rich (black), stoichiometric (red), and lean (blue) conditions.

Table 5.12 Comparison between the OH model and the OH PLIF of the CH₄/air flames.

Method	Peak position/mm			%Remaining product		
	$\varphi = 1.30$	$\varphi = 1.00$	$\varphi = 0.84$	$\varphi = 1.30$	$\varphi = 1.00$	$\varphi = 0.84$
Model	1.35	0.80	1.00	22.8	23.6	24.4
PLIF	1.36	1.05	1.14	26.8	22.9	30.2

Since the LIF signals are not yet corrected and are also difficult to manage with a single recording, the pixel values cannot be directly compared. Some assumptions can be given regarding the phenomenon. Firstly, the quenching cross section only considered the major species in the flames and does not include the hydrocarbon collider. In practical situations, the fuel is burnt out at the lean condition, while at the stoichiometric and particularly rich condition, a certain amount of fuel is likely to exist in the mixtures, approaching the end of the combustion. Hence, the OH fluorescence quenching induced by methane is an impactful factor, resulting in a greater correction for the signal at the stoichiometric and rich conditions. Furthermore, hydrocarbons commonly have considerably larger quenching cross section, and an example of calculations is shown in Figure 5.16 with the use of the expressions from

Tamura et al. [212]. At 1500-2000 K, the quenching caused by methane is about twenty times greater than the effect of nitrogen. Additionally, Smith and Crosley [213] measured the quenching of OH by a series of species, and their results show that the cross section by methane is 14.9 \AA^2 at 1150 K and the cross section by n-butane is 71.2 \AA^2 at 1200 K. This implies that the scope of the quenching effects by larger hydrocarbons is much greater in the kerosene and surrogate flames at the stoichiometric and rich conditions.

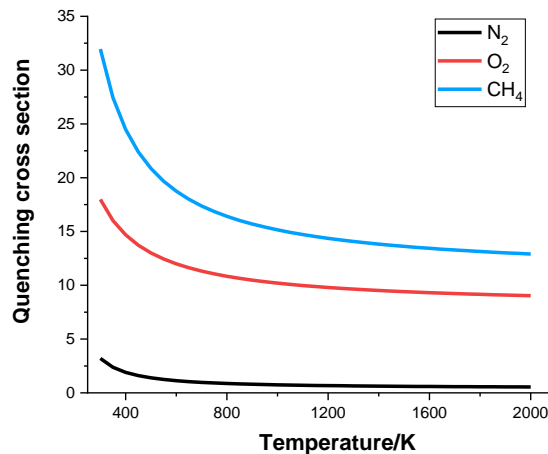


Figure 5.16 Calculated quenching cross section of $A^2\Sigma^+$ OH by three colliders, unit: \AA^2 .

For the quantifying of NO, one innate problem lies in the reliability of the NH_3/CH_4 blend modelling, as the available mechanisms are not widely validated like the GRI-Mech 3.0 for methane combustion. Initially, the mechanisms of Tian et al. [63], Okafor et al. [64], and Lamoureux et al. [214] were examined against the experimental data from the literature, and the work from Okafor et al. [64] were selected to simulate the laminar flames in this study.

The general shapes of the NO PLIF at all three equivalence ratio conditions are quite similar. Starting from the burner surface, the concentration of NO increases and reaches a maximum value, then relatively drops down by approximately 20-30% to a rather consistent level. Also, the positions of the peak value are around 1.5-1.6 mm for all three cases. Figure 5.17 demonstrates both the NO model and the original PLIF signals of the $\text{CH}_4/\text{NH}_3/\text{air}$ combustion. At the rich condition, the trend of the model corresponds sensibly with the PLIF. Regarding the position of the peak, the result of PLIF has an offset of 0.7 mm against the simulated data. The models at the stoichiometric and lean conditions, however, largely do not agree with the measurements. The NO in both models quickly reaches the peak, but instead of gradually decreasing to a lower level, it stays constant.

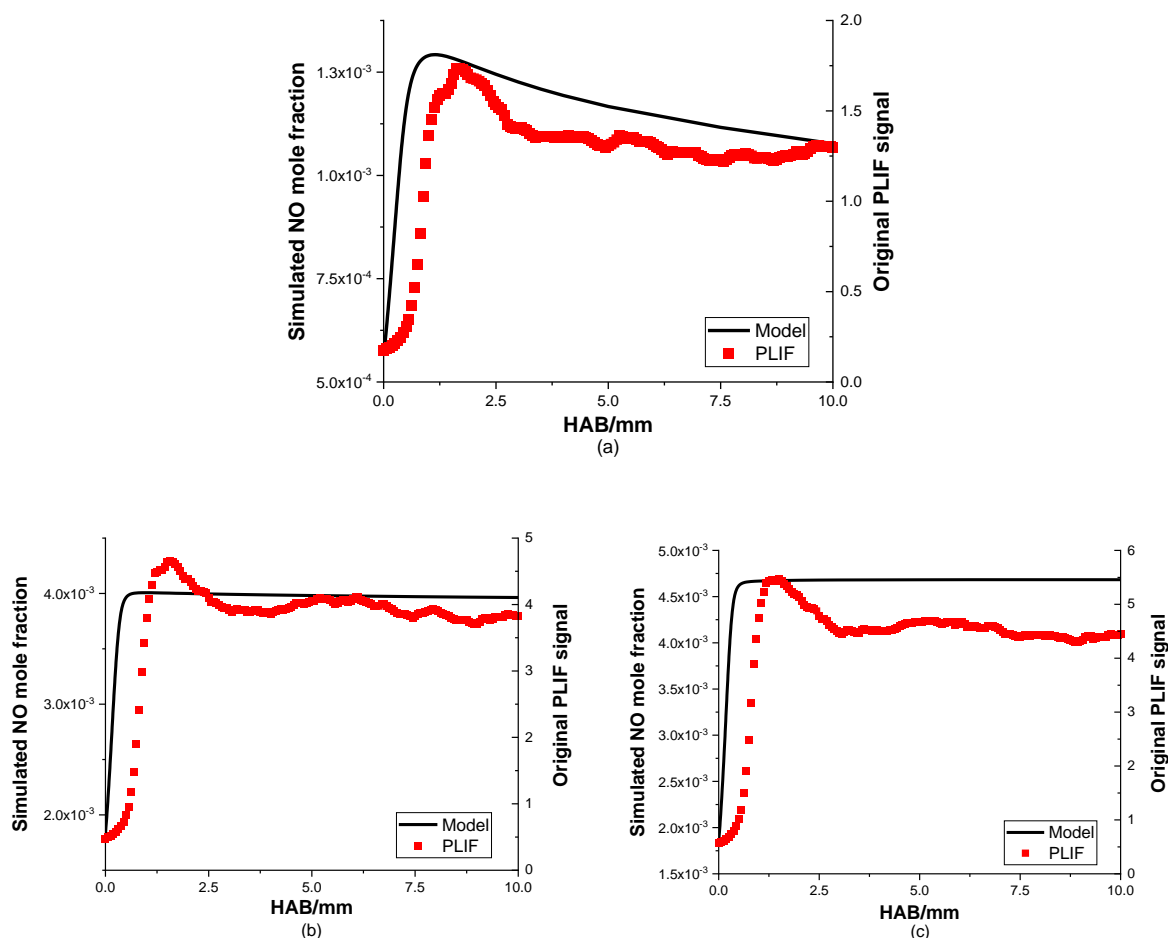


Figure 5.17 Comparison of NO profile between the simulations (line) and the PLIF (scatter) of the $\text{CH}_4/\text{NH}_3/\text{air}$ flames: (a) $\varphi = 1.30$; (b) $\varphi = 1.00$; (c) $\varphi = 0.84$.

The NO rate of production (ROP) is subsequently examined and shown in Figure 5.18. In all three equivalence ratio conditions, $\text{HNO} + \text{H} \rightleftharpoons \text{NO} + \text{H}_2$ is responsible for the primary production of the NO and $\text{NH} + \text{NO} \rightleftharpoons \text{N}_2\text{O} + \text{H}$ is responsible for the main consumption of the NO. Furthermore, the oxidation appears to be coming to an end around 2 mm above the burner surface for the rich condition, and for the stoichiometric and lean case, the processes terminate even faster as little activity can be observed beyond the distance of 1 mm. Due to the scale of the study, the optimization of the CH_4/NH_3 mechanisms is not carried out and errors for the quantifying NO are anticipated to some extent.

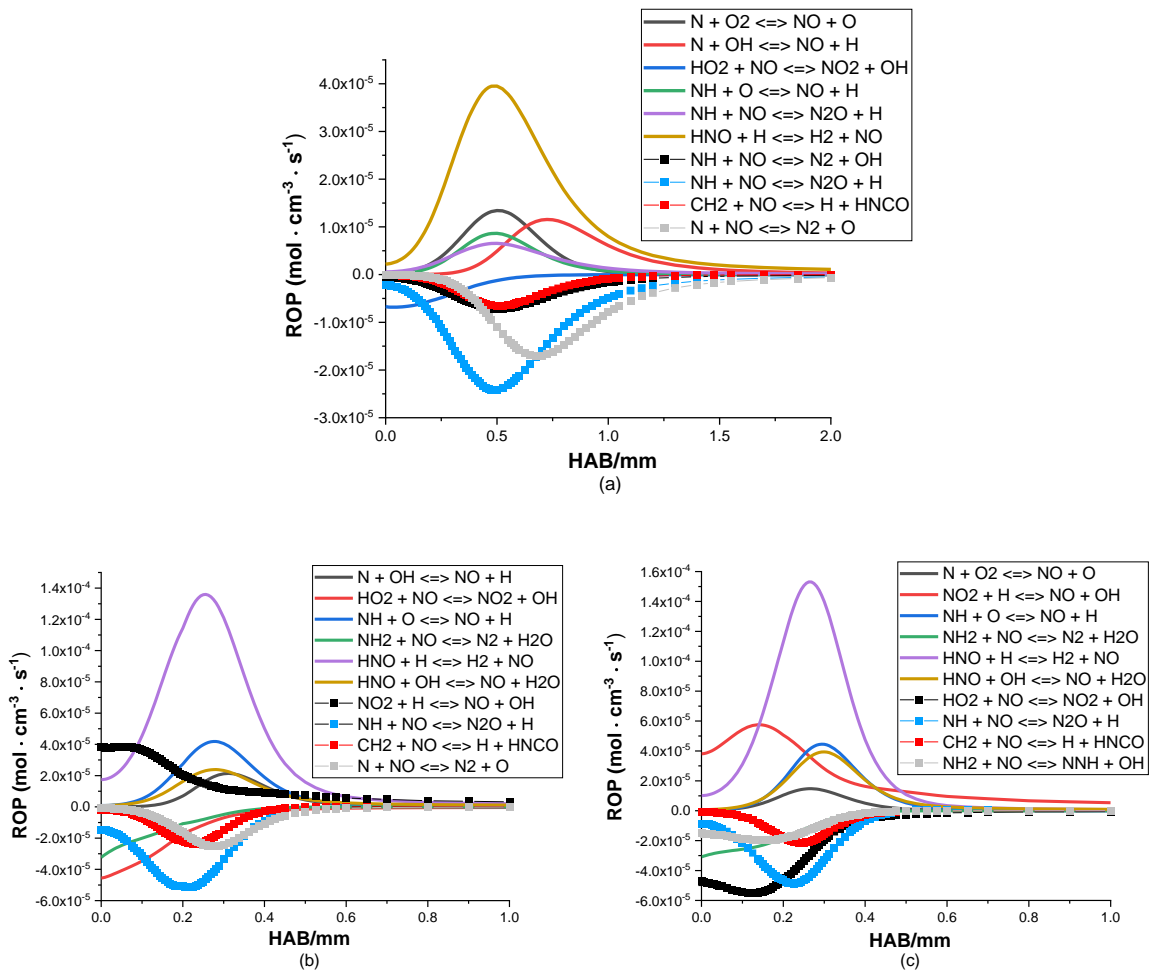


Figure 5.18 Rate of production of the NO: (a) $\varphi = 1.30$; (b) $\varphi = 1.00$; (c) $\varphi = 0.84$.

In conclusion, OH models correspond with the PLIF results quite reasonably, and both the maximum and the end value of the OH from the CH₄/air flames can be employed as reference points for the quantification of the OH for the liquid fuels. For the NO, due to the uncertainty in the simulations, and also because it is difficult to determine the end of the combustion, the maximum values of the NO from the CH₄/NH₃/air flames are utilized as the reference point in the following quantifying NO of the liquid fuels.

5.2.2 OH quantification and validation of the burner-stabilized model

As stated in Section 5.1.4, the temperature data at the lean condition is much less reliable, hence the quantification is only implemented at the rich and stoichiometric condition. The shape of the PLIF graph is essential, and the data with the least discrepancy against the simulations are selected for the subsequent quantifying. Therefore, the quality of the PLIF measurements for the three hydrocarbon mixtures is initially discussed and compared to their

respective model. The criteria are the percentage of the remaining product and the peak position, and details are summarized in Table 5.13.

Table 5.13 Comparison of OH mole fraction between experiments and modelling.

Fuel	Kerosene		Surrogate A		Surrogate B	
	$\varphi = 1.30$	$\varphi = 1.00$	$\varphi = 1.30$	$\varphi = 1.00$	$\varphi = 1.30$	$\varphi = 1.00$
%Remaining product (Model)	12.4	33.1	10.7	25.3	10.1	24.5
%Remaining product (EXP)	25.3	35.9	26.7	39.1	24.0	32.6
Peak position/mm (Model)	0.80	0.80	0.53	0.49	0.49	0.56
Peak position/mm (EXP)	0.81	0.92	1.00	0.86	0.81	0.81
%Peak concentration/ $(\frac{[OH]_{Model}}{[OH]_{EXP}} - 1)$	+7.49	+7.02	+37.0	-1.47	+17.8	-12.9

The OH PLIF results are quite consistent among the three mixtures. The remaining products of the measurements are about 24-26% and 33-39% of the maximum OH at the rich and stoichiometric condition, respectively. The shape of the OH model, as discussed in Section 5.1.3, is largely dependent on the temperature profiles and from the results of the kerosene flame at the stoichiometric condition, there is a noticeable shape difference between the thermocouple (33.1%) and OH LIF thermometry (25.3%). It is observed that for three mixtures at the stoichiometric condition, the simulated shape attained from the OH LIF thermometry is all around 25%. As for the models at the rich condition, the remaining products are consistently about 10-12%. In conclusion, the discrepancy between the two approaches is around 10-15%, which is not considerably large but also exceeds the error limitation. The phenomenon may largely be due to the nature of the flat-flame burner experiments. In practice, the flame is exposed to the open air and further away from the burner surface, more air will enter the flame, which subsequently causes the mixture to be inclined to the fuel lean side and less OH is consumed than in the ideal situation.

In general, the agreements between the model and PLIF are excellent for kerosene flames, while for the two surrogate flames, the simulated peak positions are all around 0.5 mm, resulting in an offset of 0.3-0.5 mm. This is because the temperature profiles are all obtained

by using the OH LIF thermometry, and the innate problems from the R₂(13)/P₁(2) pair were discussed previously. In addition, the maximum values of the PLIF are all reached at the distance 0.8-1 mm above the burner surface.

Initially, both the end and maximum point were utilized to calculate the quantitative OH with the use of equation 5.4. An example is given by using the kerosene/air flames at the rich condition, and the key parameters are shown in Table 5.14. The values of temperature can be traced back to Table 5.2 and Table 5.4, and the simulated OH mole fraction and the PLIF signal of the pure methane flames are from Figure 5.15. The converted OH with the use of two reference points for both the rich and stoichiometric conditions of the kerosene flames are displayed in Figure 5.19. In terms of the absolute value, the result from the peak reference corresponds better with the modelling at the rich condition, and both the end and peak results are quite agreeable with the simulation at the stoichiometric condition. Since the results of the other two mixtures follow the trends, the peak point is consequently utilized. The quantitative OH of surrogate A and surrogate B are displayed in Figure 5.20 and Figure 5.21, respectively.

Table 5.14 Important parameters of two reference points for quantifying OH.

	CH ₄ /air flame		Kerosene/air flame	
	End	Peak	End	Peak
Temperature/K	1914.2	1980.2	1924.2	2027.8
[OH] _{ref}	1.66×10 ⁻⁴	7.30×10 ⁻⁴		
LIF _{ref}	0.26	0.96		

Generally, the measured OH mole fractions at all six flame conditions correspond rather reasonably with the simulated OH of their respective model. However, given the significant uncertainty of the quantitative method, even for the case where the two peak OH values are close, such as the stoichiometric condition of the surrogate A flame, the converted PLIF result can only be considered relatively accurate. Firstly, the predictions show that for each fuel mixture, the amount of OH at the stoichiometric condition is greater than the level of OH at the rich condition by a factor of 3. The observation is sensible as less oxygen is available in the fuel rich environment, which leads to less production of the OH. For the kerosene flames, results show that the predicted data is about 7% greater than the quantitative OH from the measurement in both equivalence ratio cases. This consistent pattern is largely due to the

temperature profiles adopted in these simulations are all measured by thermocouples, which are in good agreement with the thermodynamic theory. Similarly, the inconsistency between the stoichiometric conditions of the two surrogates is a direct reflection of their temperature data.

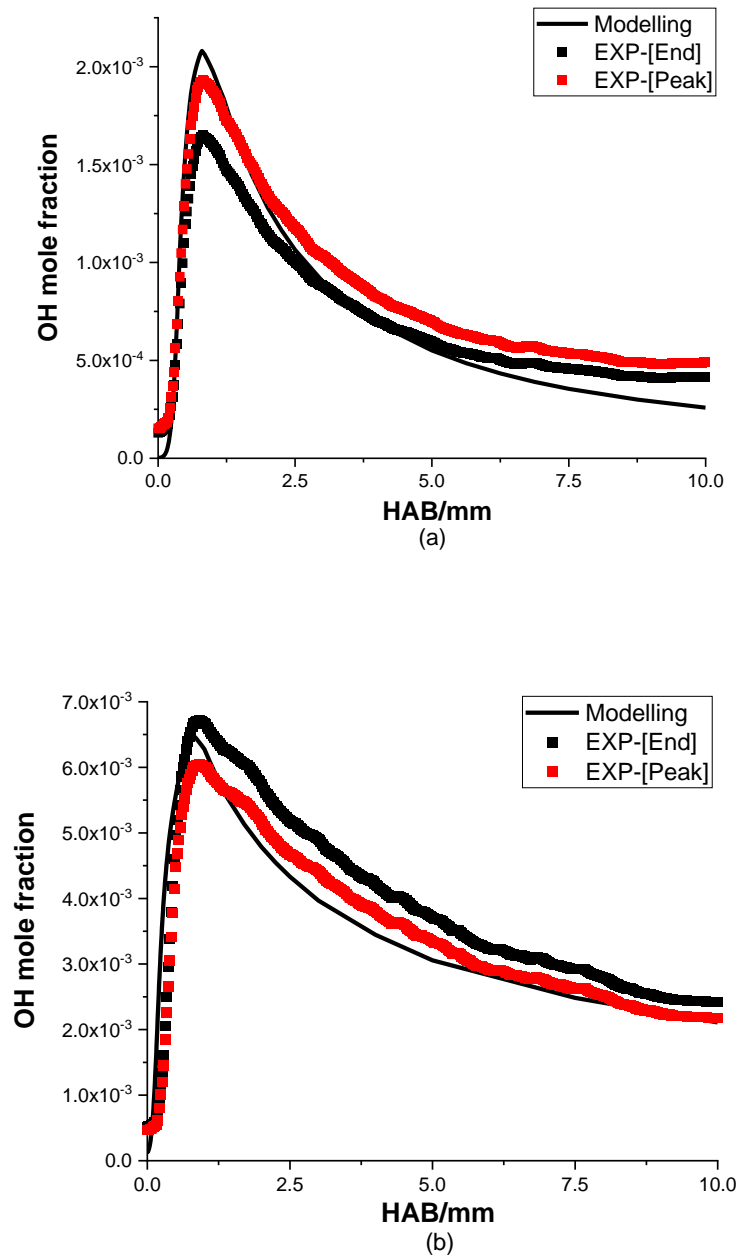


Figure 5.19 The OH profile of the kerosene/air flame: (a) $\varphi = 1.30$; (b) $\varphi = 1.00$.

At the rich condition, the maximum simulated OH of both surrogates, particularly surrogate A, is considerably greater than their respective converted PLIF data, indicating both temperature results may have uncertainty to some extent. Noticeably, the temperature result

of the surrogate B at the stoichiometric condition is derived from the $R_2(2)/R_1(12)$ pair, whose maximum value is around 100 K lower than the peak of the $R_2(13)/P_1(2)$ profiles for the rich condition of the surrogate B and both equivalence ratio condition of the surrogate A. Thus, the maximum quantifying OH being about 13% larger than the predicted result may be due to the deficiency of the temperature profile at this flame condition.

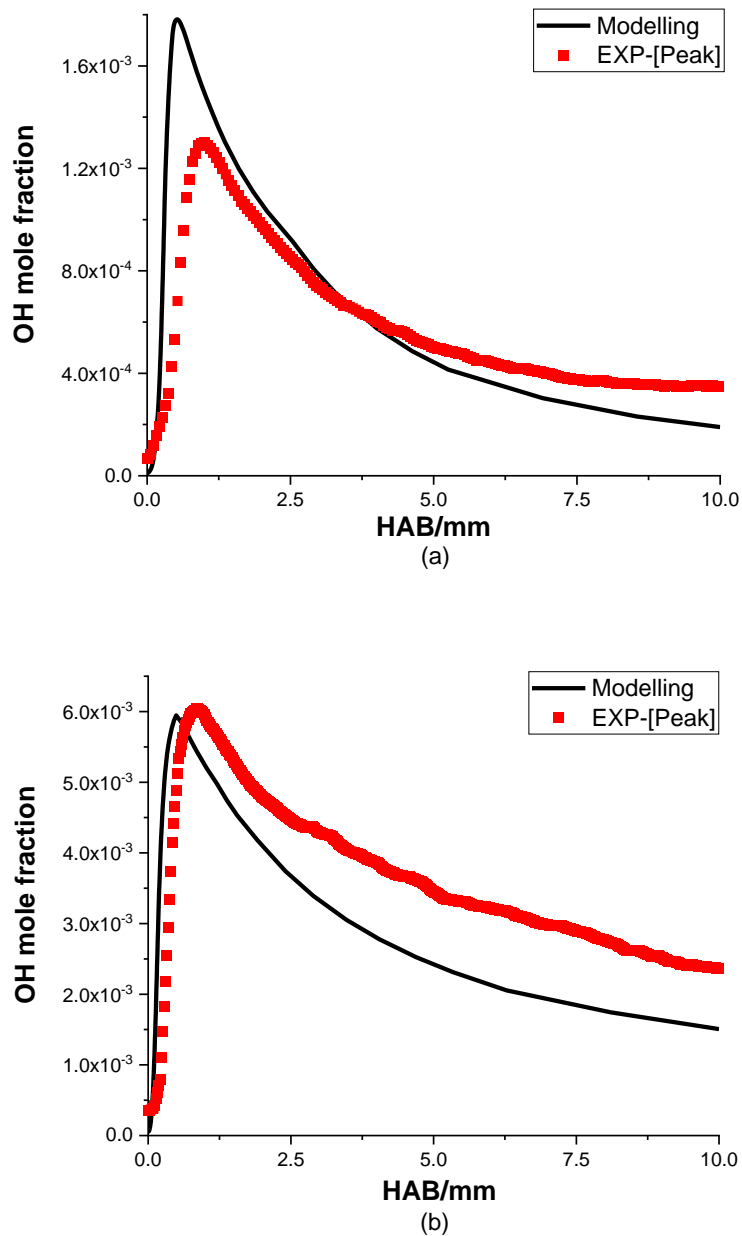


Figure 5.20 The OH profile of the surrogate A/air flame: (a) $\phi = 1.30$; (b) $\phi = 1.00$.

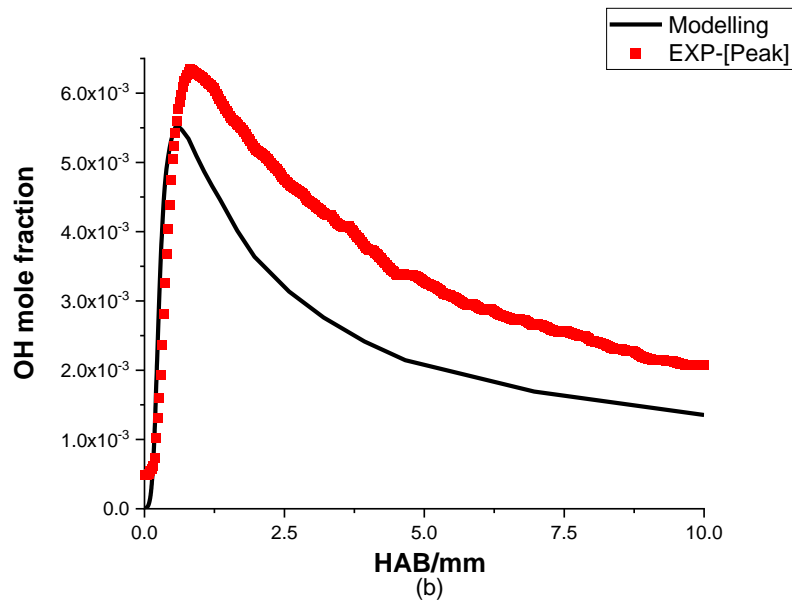
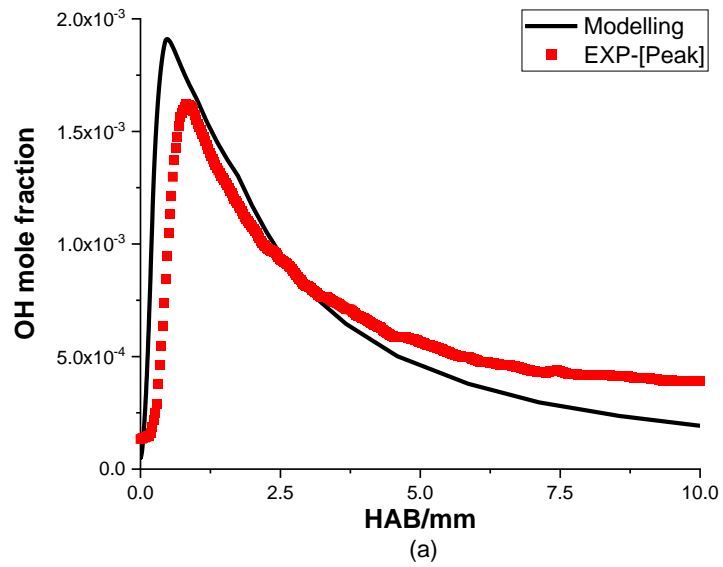


Figure 5.21 The OH profile of the surrogate B/air flame: (a) $\varphi = 1.30$; (b) $\varphi = 1.00$.

Regarding the quality of the proposed surrogates, it is difficult to directly compare the absolute amount of OH in the three mixtures, either by simulations or PLIF measurements. The uncertainty of the former is mainly due to the complexity of the temperature data, and the latter is because of the challenge of directly correcting the PLIF signal. Since the temperature data obtained from the $R_2(13)/P_1(2)$ pair are available for all three mixtures, simulations are carried out and shown in Figure 5.22 (a). Also, discussions over the OH profiles are focused on the region of 0-2 mm where the effect of the open environment is at the minimum. It is first observed that in both model and original PLIF data, the kerosene flame

appears to contain the highest level of OH, followed by surrogate B, and surrogate A has the least amount of OH. Naturally, the maximum temperature should also correspond to this trend. The kerosene data is about 100 K higher than the results of both surrogates, however, the peak temperature of the surrogate A is 6 K higher than the maximum value of the surrogate B, which does not seem to be sensible thermodynamically. Hence, to further determine the impacts of the temperature input, an arbitrary simulation of surrogate A' is calculated with the use of the profile of surrogate B. The model shows that the maximum OH of the surrogate A' is about 8% lower than the original OH result of surrogate A, implying that the current temperature profile of surrogate A has considerable uncertainty and may consequently lead to the overprediction of the OH quantity in the targeted flame. Assuming the initial observation of the OH level among mixtures is accurate to a certain extent, the model of surrogate A' is then a more accurate representation of the surrogate A combustion. Subsequently, by calculating the differences in peak value, the magnitude of the three models seems to correspond quite reasonably to their respective PLIF signals (Figure 5.22 (b)), meaning that for both approaches, the amount of relative OH in a certain flame is consistently greater than the quantity of OH in the flame of its underlying tier by a factor of 1.2. Thus, it can be regarded as relatively sensible to compare the level of OH of the targeted three mixtures at the rich condition.

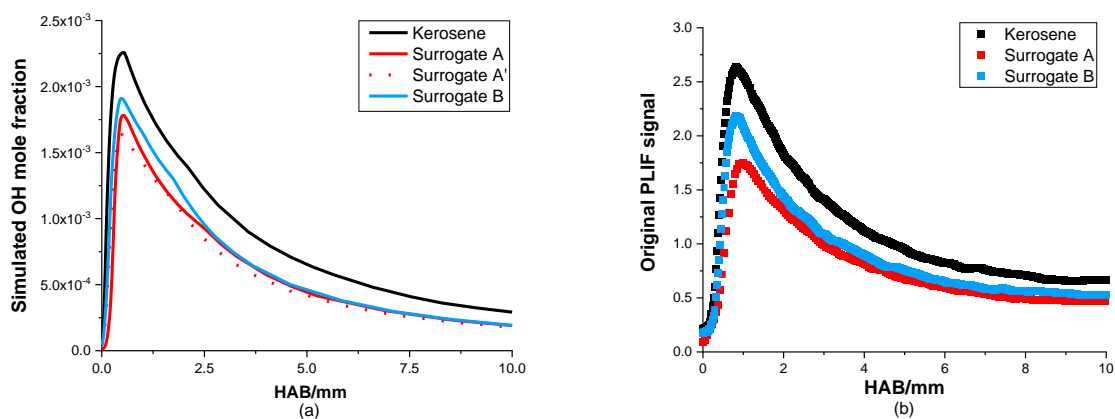


Figure 5.22 Comparison of the relative OH of the three mixtures at $\phi = 1.30$: (a) Model; (b) PLIF.

Since surrogate A is from a previous study of synthetic fuels and the composition of surrogate B is essentially a modified version of surrogate A, it is understandable that both mixtures possess a considerable level of OH, but without additional components, neither alone is ideal to represent the combustion characteristic of the kerosene. Nevertheless, in the

context of the SAF and the blends of Fischer-Tropsch and conventional fuels, these proposed surrogates can be useful applications. From the results of the fuel rich case, surrogate B seems to contain a higher amount of OH than surrogate A, and the only component difference is the representation of the branched alkanes, where A adopts iso-octane and B utilizes 2-methylheptane. As discussed in Section 2.4.3, some authors argue [13, 98] that iso-octane may be too branched, and a less-branched component should be employed to formulate the surrogate. Because no measurements of the S-8 fuel are conducted in this project, it cannot be directly concluded that surrogate B is a more fitting representative of the F-T fuels than surrogate A, but this observation of OH in a way can be regarded as agreeable with the suggestions from the literature.

In addition, the rates of production of the three mixtures are simulated. Since the trends of all cases are identical, the results of kerosene flames are shown in Figure 5.23 as an example. In both equivalence ratio conditions, the reaction $\text{H} + \text{O}_2 \rightleftharpoons \text{O} + \text{OH}$ (R. 2.4) is mainly responsible to produce the OH and the reaction $\text{H}_2 + \text{OH} \rightleftharpoons \text{H} + \text{H}_2\text{O}$ is the primary pathway of the OH consumption. Given the unique lumped way that the CRECK mechanism is formed as mentioned in Section 4.2, it is both not feasible and out of the scale of the current study to perform the optimization of the mechanism. Nevertheless, these reactions can serve as a reference for future work.

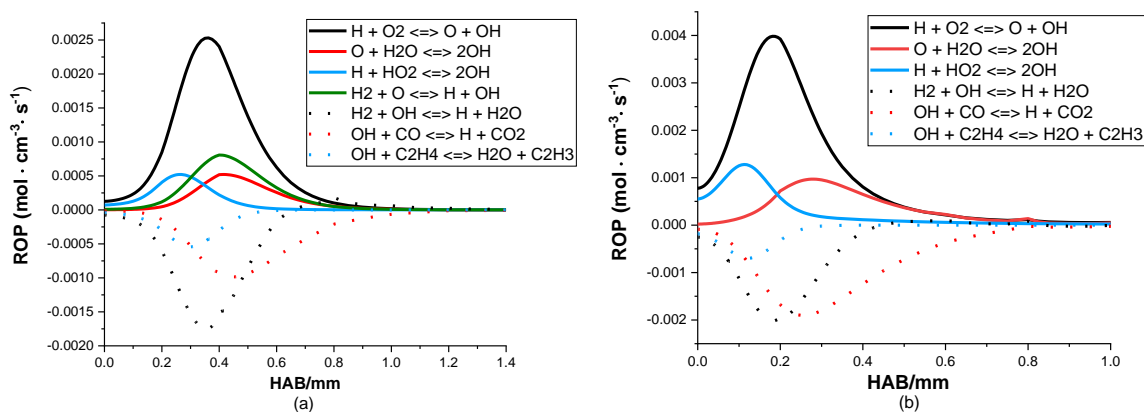


Figure 5.23 Rate of Production of the OH in the kerosene flames: (a) $\phi = 1.30$; (b) $\phi = 1.00$.

5.2.3 NO quantification and validation of the burner-stabilized model

Apart from the considerable uncertainty of the CH_4/NH_3 mechanisms as discussed in Section 5.2.1, another innate problem of the NO quantification is that the amount of NO is considerably less in the targeted flames compared to the OH. Take the kerosene/air flames

for instance, the average resolution of the raw OH image at the stoichiometric and lean condition can be over 3000 (limit = 4096), while for the raw image of NO, the resolution value can barely pass 100 at all three equivalence ratio conditions, even when both the laser power and camera gain is at optimal conditions. This is consequently shown in the PLIF results, the collected NO signals have much more noise and are consequently difficult to determine the general shape. Thus firstly, the model at each equivalence ratio condition is examined.

For the rich condition, the simulated NO profiles of all three mixtures are quite identical regardless of the temperature profiles. Figure 5.24 (a) demonstrates that the amount of NO increases quickly and reaches a higher level at the region of 0-2 mm, then slowly increases further and eventually comes to a stable state around 3 mm above the burner surface. Importantly, as discussed in Section 2.2.5, three channels are responsible for the NO production in the hydrocarbon oxidations. Hence, the NO ROP is simulated to identify the key reactions and an example of the kerosene flame is shown in Figure 5.24 (b). Little activity is observed beyond the distance of 2 mm as the NO approaches equilibrium, and it appears that the thermal NO_x mechanism has a heavy influence on the general production of the NO, as $\text{OH} + \text{N} \rightleftharpoons \text{H} + \text{NO}$ (R. 2.33) has the highest rate to generate NO.

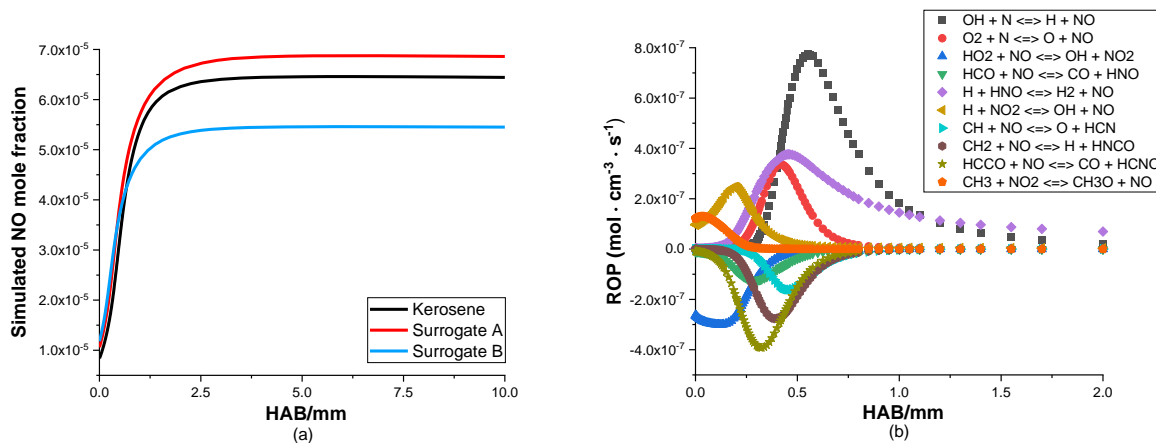


Figure 5.24 Simulated NO profiles at $\varphi = 1.30$: (a) Model of the three mixtures; (b) Example of the NO ROP.

For the stoichiometric condition, the trends of the NO profiles appear to be different dependent on the temperature input. As displayed in Figure 5.25 (a), the predicted results obtained from the OH LIF thermometry all have similar shapes. The amount of NO grows rather quickly at the region of 0-0.5 mm, then the rate of the increase becomes steadier and finally reaches a consistent level around 7-8 mm above the burner surface. As for the

simulation derived from the thermocouple temperature, the increase of the NO seems to be consistent and continues until the end of combustion (HAB = 10 mm). The continuous growth of NO in the region of 5-10 mm is mainly because of the thermal NO_x, as adequate oxygen is presented in the stoichiometric mixtures, and the level of the flame temperature directly leads to the level of the produced NO in the post-combustion zone. Subsequently, two rates of production of the kerosene flames based on the temperature input of thermocouples and LIF thermometry are demonstrated in Figure 5.25 (b) and (c), respectively.

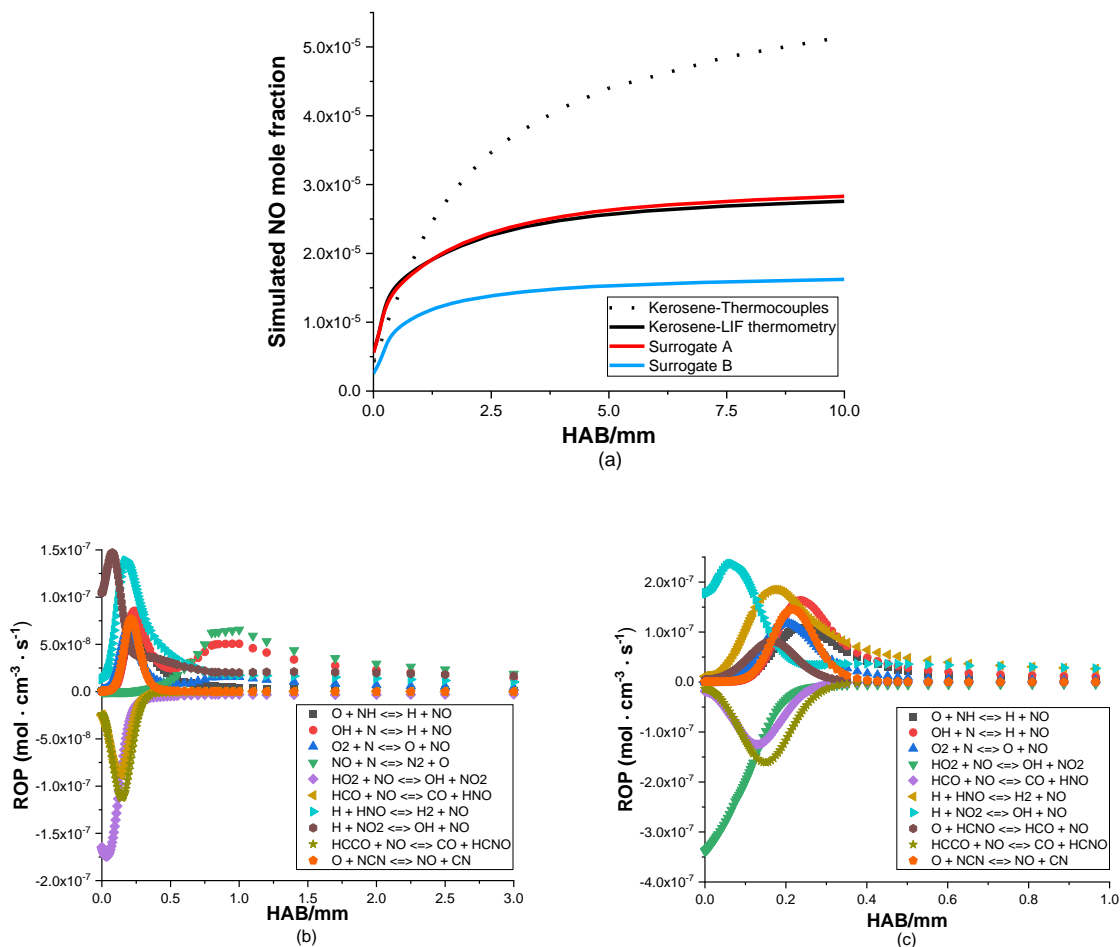


Figure 5.25 NO profiles at $\phi = 1.00$: (a) Model of the three mixtures; (b) Example of the NO ROP (thermocouple temperature); (c) Example of the NO ROP (OH LIF thermometry temperature).

Firstly, it is observed that in both analyses, two reactions, that are $\text{H} + \text{HNO} \rightleftharpoons \text{H}_2 + \text{NO}$ and $\text{H} + \text{NO}_2 \rightleftharpoons \text{OH} + \text{NO}$, are responsible for the main NO production. From the examination of the HNO routes, the reaction between HCO and NO is the primary source of the HNO formation. Therefore, neither reaction is part of either the thermal or prompt NO_x mechanism. Secondly, the reactions of the thermal NO_x are less influential compared to the rich condition,

in terms of the production scale and general contribution. Noticeably, the ROP based on the thermocouple data shows that $\text{OH} + \text{N} \rightleftharpoons \text{H} + \text{NO}$ has a second peak around 1 mm and the effect of $\text{NO} + \text{N} \rightleftharpoons \text{N}_2 + \text{O}$ (the reverse reaction of reaction 2.31) is also emerging rather late, while the result from the OH LIF thermometry indicates that activity generally is generally much reduced after the distance of 0.5 mm. This implies that the thermal influences based on the thermocouple data are greater and last longer. In addition, the chemistry of prompt NO_x , $\text{O} + \text{NH} \rightleftharpoons \text{H} + \text{NO}$ and $\text{O} + \text{NCN} \rightleftharpoons \text{NO} + \text{CN}$, is presented in both analyses.

In conclusion, at the rich condition, the NO mechanism can be regarded as thermal dominating to some extent, while in the stoichiometric case, the involvement of the fuel and nitrogen oxidation appears to be more important. Also, from the discussion in Section 5.1.3 and Section 5.2.2, the measurements from the thermocouples seem to be a more accurate temperature representation than the results from the OH LIF thermometry. Although the trends of the NO at the stoichiometric condition are relatively uncertain, the thermocouple data is utilized for the kerosene flame at both rich and stoichiometric conditions. Given the uncertainty of the measured temperature data and the nitrogen chemistry in the modelling, this insight into the NO production may be inherently limited to a certain degree.

The examples of the NO PLIF at the rich and stoichiometric conditions are displayed in Figure 5.26 (a) and (b), respectively. For the rich case, the data shows that the quantity of NO reaches a higher level at around the distance of 1.5 mm and remains generally consistent, which corresponds with the model profile quite reasonably. Noticeably, an increase of NO at the region of 7-10 mm can be observed and the trend in some PLIF results is more obvious, and this may be due to the extra involvement of the thermal NO_x . Unlike the model which assumes the perfect environment, additional air is likely to enter the flame during the measurements, and the further away from the burner surface, the influence of the open air is more significant. Since the flame temperature is sustained at a high enough level, more thermal NO_x may be produced at the end of the combustion region. And this effect appears to be more obvious for the stoichiometric condition, as the trend of NO growth continues till the end of the oxidation. Apart from this trait, the profiles generally appear to be similar to the results at the rich condition. In short, the collected NO PLIF can be regarded as a decent representative of the NO profiles for the targeted mixtures.

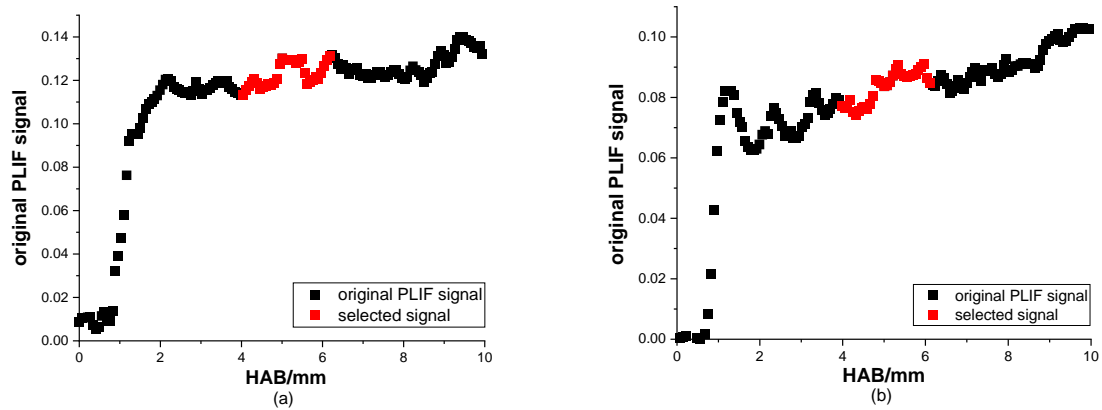


Figure 5.26 PLIF signal with the example of the surrogate A flames: (a) $\phi = 1.30$; (b) $\phi = 1.00$.

Due to the incomplete combustion, theoretically for a certain hydrocarbon fuel, the fuel-rich condition tends to generate more emission of the NO_x than the stoichiometric condition. However, in the current scale of knowledge, to what extent is the produced NO at the equivalence ratio of 1.3 higher than at the equivalence ratio of 1 is unknown. Thus, to properly determine the NO PLIF profiles of each mixture, the level of NO at the rich and stoichiometric conditions are further compared. Given the effects of the additional thermal NO_x in the measurements, the position of 5 mm is utilized as a reference point to calculate the magnitude difference of the NO between the rich and the stoichiometric condition. Importantly, for the PLIF signal that shows a continuous increase, the signal values between 4-6 mm are averaged to represent the relative NO at the reference distance of 5mm, as the highlighted parts demonstrated in Figure 5.26.

A comparison of the NO quantity at the reference point for each flame condition is shown in Table 5.15. It is first observed that the magnitude difference of the PLIF for all three mixtures is consistent, as the NO intensity at the rich condition is greater than the NO intensity at the stoichiometric conditions by a factor of 1.4-1.5. The predicted results, on the other hand, show a larger discrepancy among the different mixtures. For the kerosene flames, the model and the PLIF data correspond quite sensibly regarding the variation of the NO level at the rich and stoichiometric conditions. For the two surrogates, compared to the measurements, the prediction shows a greater level of difference between the rich and the stoichiometric condition, which may be largely due to the deficiency of the temperature profiles particularly at the stoichiometric condition.

Table 5.15 Comparison of the NO magnitude at the rich and the stoichiometric condition at the burner distance of 5 mm.

	$[\text{NO}]_{\text{rich}}/[\text{NO}]_{\text{stoichiometric}}$	
	Model	PLIF
Kerosene	1.47	1.52
Surrogate A	2.59	1.47
Surrogate B	3.46	1.44

For quantifying NO, the maximum point of the CH₄/NH₃/air flame is utilized as the reference, and an example of the crucial parameters is shown in Table 5.16 by using the kerosene/air flames. Importantly, at the stoichiometric condition, due to the disagreement between the ammonia model and the PLIF, also the greater uncertainty of the temperature profiles from the liquid fuels, a larger scale of errors is expected.

Table 5.16 Important parameters of the peak reference point for quantifying NO.

	CH ₄ /NH ₃ /air flame		Kerosene/air flame	
	$\varphi = 1.30$	$\varphi = 1.00$	$\varphi = 1.30$	$\varphi = 1.00$
Temperature/K	2024.8	2063.7	2027.8	2082.2
$[\text{NO}]_{\text{ref}}$	1.29×10^{-3}	4.01×10^{-3}		
LIF _{ref}	1.73	4.66		

The results of the quantitative NO estimation of the kerosene, surrogate A, and surrogate B are displayed in Figure 5.27, Figure 5.28, and Figure 5.29, respectively. Also, Table 5.17 demonstrates the magnitude difference between the two approaches with a reference distance of 5 mm. Generally, at a given flame condition, the observed NO is greater than the simulated NO by at least a factor of 1.3. For the rich condition, the PLIF result of the three mixtures is rather consistent compared to the model, while at the stoichiometric condition, the discrepancy between the two methods is more obvious, particularly for the two surrogates. Apart from the innate credibility issue of the ammonia mechanisms, another potential cause of errors is the measured temperature of the reference fuel. As discussed in Section 5.1.1, the maximum values of the ammonia/methane blend at each condition are higher than their respective peak results of the pure methane flames, which seem to be thermodynamically unrealistic. From the calculation of equation 5.4, the reference

temperature is in proportion to the converted mole fraction of the targeted species. Hence, this factor may also contribute to the overprediction of the quantitative NO in liquid fuels.

Table 5.17 Comparison between the converted NO and the simulated NO at the distance of 5 mm.

	$[\text{NO}]_{\text{EXP}}/[\text{NO}]_{\text{Model}}$		Averaged original PLIF signal at $\varphi = 1.30$	Simulated NO mole fraction at $\varphi = 1.30$
	$\varphi = 1.30$	$\varphi = 1.00$		
Kerosene	1.34	1.50	0.120	6.46×10^{-5}
Surrogate A	1.29	2.55	0.122	6.88×10^{-5}
Surrogate B	1.26	3.43	0.095	5.46×10^{-5}

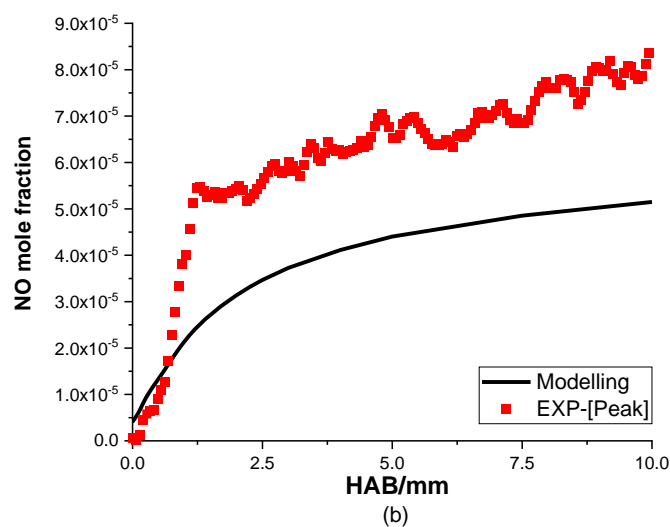
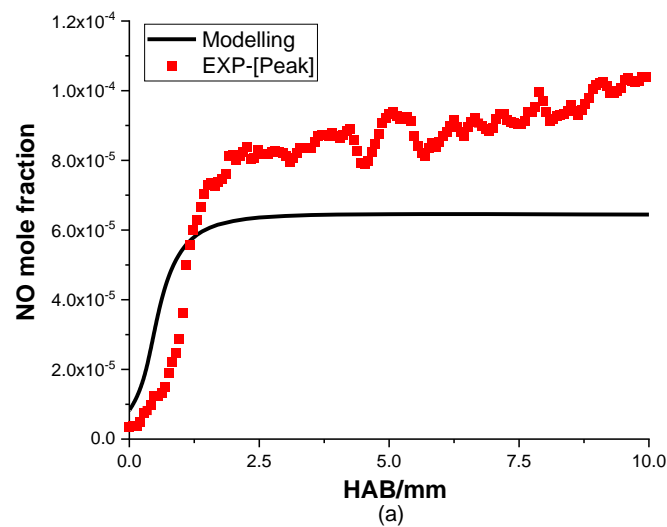


Figure 5.27 The NO profile of the kerosene/air flame: (a) $\varphi = 1.30$; (b) $\varphi = 1.00$.

Like the cases of the OH, directly comparing the absolute amount of NO in the three mixtures is quite challenging, and the uncertainty from either model or PLIF is even greater. Thus, only the results of the rich condition are discussed briefly to offer some perspectives on the NO production in a kerosene-based laminar flame. From the simulated data in Table 5.17, the amount of NO generated from surrogate A appears to be the most substantial, which is about 7% higher than the data from the kerosene, and the surrogate B flame forms the least quantity of NO. On the other hand, the original PLIF results show that the NO level is rather identical between the kerosene and surrogate A, which is about 25% greater than the result of surrogate B.

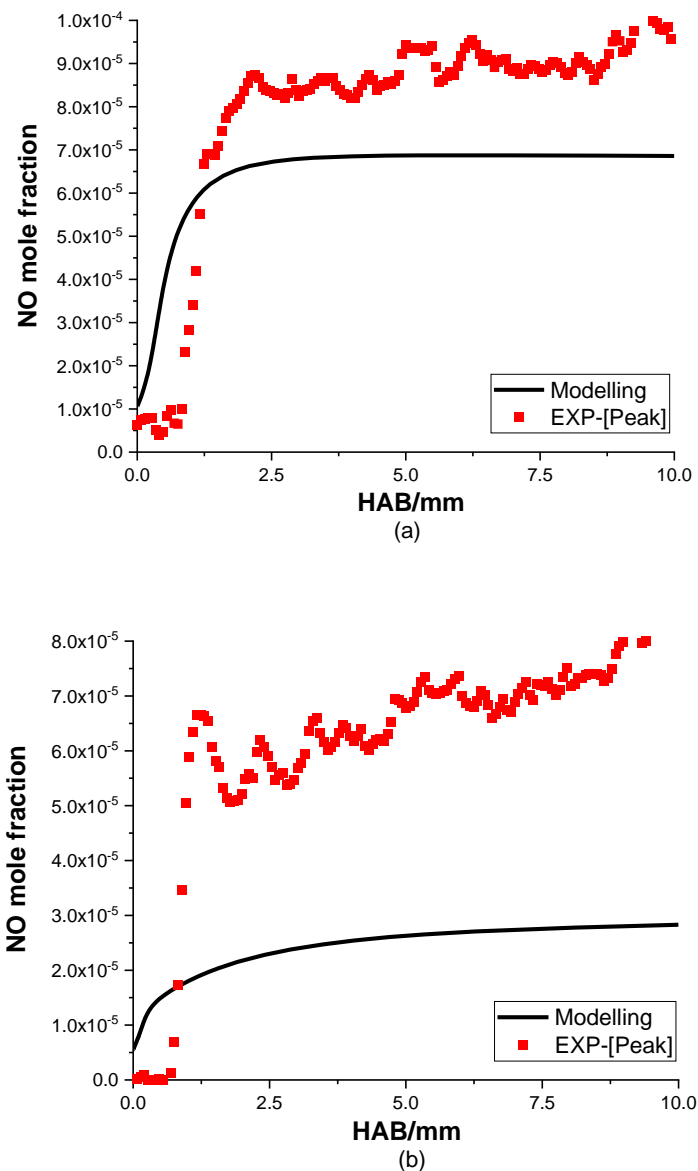


Figure 5.28 The NO profile of the surrogate A/air flame: (a) $\phi = 1.30$; (b) $\phi = 1.00$.

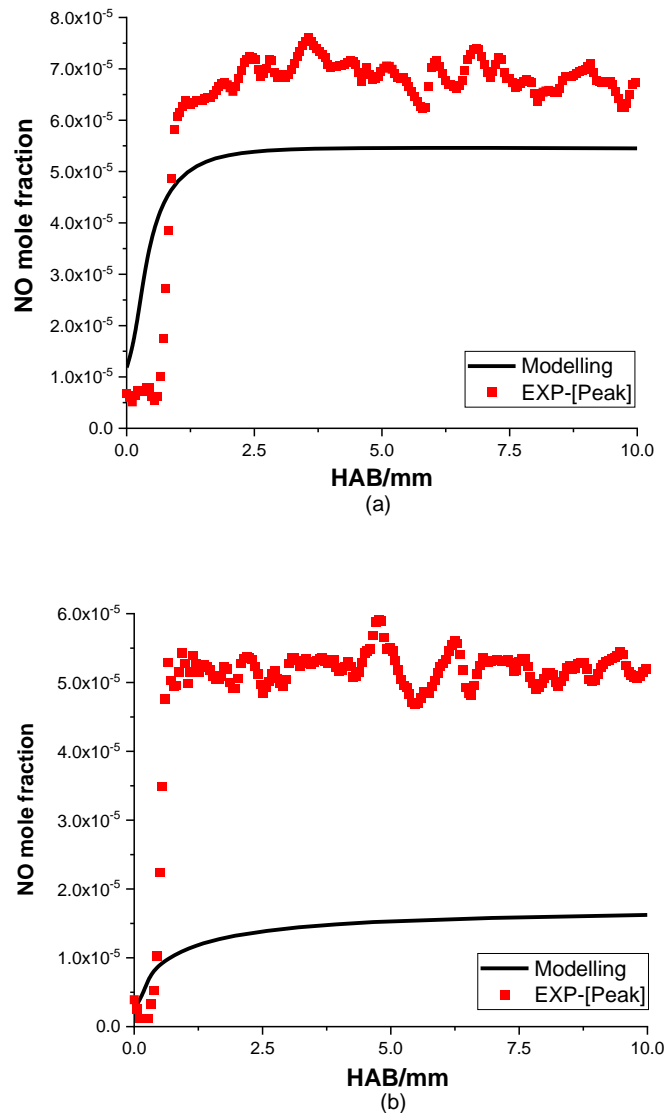


Figure 5.29 The NO profile of the surrogate B/air flame: (a) $\varphi = 1.30$; (b) $\varphi = 1.00$.

As discussed in Section 5.2.2, the measured peak temperature of surrogate A at the rich case seems to be realistically too high. If an arbitrary surrogate A' model is calculated with the use of the temperature profile from surrogate B, similar to the OH case, the new prediction of surrogate A at the reference distance is 5.96×10^{-5} , which is quite close to the surrogate B data. In short, from the general observations and manipulation of the data, it can be deduced that at the rich condition, the formed NO in the three targeted flames is on a similar level, and the surrogate B flame seems to be the cleanest.

5.2.4 Original PLIF signal at the lean condition

Due to the lack of reliable temperature measurements of the liquid mixtures at the equivalence ratio of 0.84, the quantifying of the OH and NO signals is not performed.

Nevertheless, the original PLIF signal is briefly discussed to share some insights for future investigations. The signal examples are provided by using the kerosene flames, and the profiles of OH and NO are demonstrated in Figure 5.30 (a) and (b), respectively.

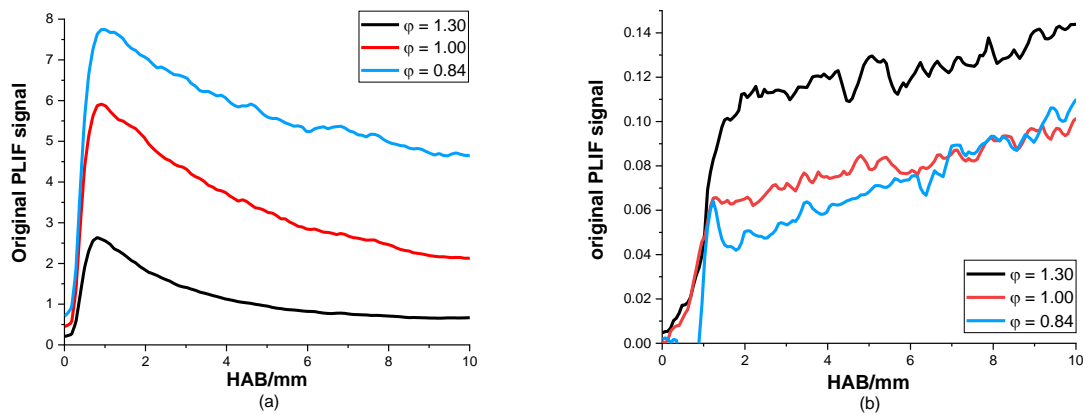


Figure 5.30 Example of the original PLIF signal at three equivalence ratio conditions: (a) OH; (b) NO.

For the collected results of the OH, the remaining product of all three mixtures is around 60-70% and the peak position is around 0.9-1.2 mm. From the shape comparison at the rich and stoichiometric conditions, the PLIF is about 10-15% greater than the simulation. Provided the pattern shall remain consistent and reasonable temperature data at the lean case is available, the remaining OH product from the model is estimated to be around 50-60%. In addition, the peak position at the lean case appears to be corresponding with the rich and stoichiometric conditions. For the collected results of the NO of all three mixtures, the amount of NO at the lean condition appears to be less than the amount of NO at the stoichiometric condition, by approximately a factor of 1-1.5. Also, the trend of continuous NO increase is obvious at the lean case, indicating a strong influence of thermal NO_x .

CHAPTER 6

CONCLUSIONS AND FUTURE SUGGESTIONS

6.1 Introduction

Due to the concern about global warming and the importance of aviation, it is critical to improve the understanding of the elementary combustion characteristics of large hydrocarbon fuels. In this work, kerosene and two proposed surrogates based on a type of Fischer-Tropsch fuel were investigated from both computational and experimental approaches.

From the modelling perspective, the study aims to develop a detailed kinetic model for both large straight-chain alkanes and monomethyl alkanes by using ANSYS Chemkin Pro. Besides the common surrogate components such as n-decane and n-dodecane, 2-methylheptane is used as the representative of the branched alkanes. Initially, available detailed mechanisms for large hydrocarbons are examined and selected. Since the mechanisms of the branched alkanes are often individual packages, the sub-kinetics of the 2-methylheptane is combined with the selected core chemistry. The attempt to improve the model quality is focused on the 2-methylheptane kinetics because the model of branched alkanes is comparatively much less developed than the mechanisms of normal alkanes. Two main approaches, which are rate constants and rate rules, are explored to optimize the original kinetics. The modifications of rate constant focus on the key C0-C4 reactions based on the sensitivity analysis. As for the alternation of rate rules, a total of nine reaction classes that are crucial to the combustion at low and intermediate temperature regions (commonly < 1000 K), are examined sequentially. Besides the updates on the rate rules of a given reaction class, another important aspect of the new adjustment is that the types of the large radicals are differentiated in detail, compared to previous modelling work commonly adopting the same reaction rate constant for analogous situations. Also, new thermodynamic data of the C8 radicals related to the 2-methylheptane oxidation are calculated by using the updated group additivity values. The updated mechanism is compared with the measured ignition delay time at 20 atm and three equivalence ratio conditions ($\varphi = 0.5, 1, \text{ and } 1.5$) from

the literature for validations, and also is employed to simulate the laminar flame conditions in the subsequent quantitative PLIF studies.

From the experimental perspective, a flat-flame burner is utilized to study the fundamental oxidation characteristics of a total of five fuels including two reference mixtures, under the conditions of the equivalence ratio of 1.3, 1, and 0.84. A temperature profile is measured at each flame condition, with the use of either thermocouples or OH LIF thermometry. Also, the planar laser-induced fluorescence is utilized to detect the level of OH and NO in the interested mixtures. Due to the time limitation and the obstacles encountered in the experiments, reasonable temperature data of the three liquid fuels at the lean condition ($\varphi = 0.84$) are unable to be obtained, hence the quantitative OH and NO studies of the targeted flames are not carried out at this equivalence ratio condition. The converted PLIF results are further validated against their respective model.

6.2 Kinetic modelling

Several insights can be drawn from the simulations and stated as follows.

Firstly, the examination of the individual reactions shows that the rate constants from the selected mechanism are generally reasonable and commonly obtained from experimental measurements. Hence, it is advised to keep the rates unchanged. One concern is the fall-off region and the high-pressure limit of the reaction $\text{H}_2\text{O}_2 + \text{M} \rightleftharpoons 2\text{OH} + \text{M}$. The highest-pressure condition of the currently available data is around 10 bar and 15 bar, which is quite near the low-pressure limit. From the observations, the transition behaviours from 1 atm to 10 atm are not visibly obvious and hence may compromise the fitting equation of the intermediate region. Since the high-pressure limit is derived from the extrapolation of the fall-off curve, the precision of the results may consequently be limited. In short, given the importance of the hydrogen peroxide decomposition for the ignition of the large fuel around the intermediate temperature region, measurements at 100 atm or higher are highly recommended to validate the current rate constant expression for high pressure conditions.

Secondly, from the manipulation of the rate rules of the targeted reaction classes, it is first noticed that the suggested rate constant expressions from even the recent studies are mainly obtained from theoretical calculations. Hence, apart from the first group of fuel H abstraction by OH, the chosen rate rules of other reaction classes in general lack validations from direct measurements. For the few reaction classes that possess experimental records, the

measurements are conducted under a quite limited range of conditions, usually at room temperature and low pressure. Another concern is that the studied radicals are usually C3 or C4, thus it is uncertain what degree of impact may be led to by employing the rate rules of these prototypes for larger branched C8 radicals. Due to the above constraints, in this work, the determination of the updated rate rules for each reaction group is primarily based on the balance of the whole chain branching, meaning that the detailed range of the low, intermediate, and high temperature regions should correspond with their respective experimental references. For a given reaction class, if by employing a new rate, the reactivity at low temperatures is considerably increased, the commencement of the NTC region is likely to be increased noticeably, hence it is recommended to not utilize this rate. Also, due to the presence of a tertiary carbon bond, rate rules for a certain type of reaction may not be available. Therefore, the rate constant parameters of their nearest analogy are utilized with additional refinements. Furthermore, based on modelling results, the reaction classes involved in this sequence $R \xrightarrow{+O_2} RO_2 \rightarrow QOOH \xrightarrow{+O_2} OOQOOH \rightarrow RO$ (SEQ. 2.1) may be more impactful for the chemistry in the low temperature combustion.

Thirdly, the discussion regarding the thermochemical properties of the large chemical species related to 2-methylheptane oxidation is summarized as follows. Recent studies show that the group additivity values of OO/C/H, C/C2/H/OO, and ALPEROX change considerably, and these groups are connected to the composition of RO₂, QOOH, and OOQOOH. Also, regarding the additional corrections for either enthalpy or entropy, the radicals are commonly addressed much less compared to the alkanes, and the recommended values from more recent sources vary among different authors. Compared to the simulation of the original thermochemistry, the model from the new thermodynamic data calculated in this work indicates that the reactivity of the combustion reduces mainly at the NTC region, while the kinetics at high and low temperatures remain rather unchanged.

Fourthly, the updated ignition delay time simulations of 2-methylheptane at 20 atm and three equivalence ratio conditions are summarized as follows. In general, substantial improvements are displayed at the temperature condition below 1100 K. At the stoichiometric and rich conditions, the simulated values correspond excellently with the measurements, while the prediction at the lean condition shows relatively less upgrade. Regarding the ranges of the three temperature regions, the results of the stoichiometric and

rich cases are in good agreement with the experiments, however, at the lean condition, the transition of intermediate to high temperature region is decreased by 40 K. In addition, little differences between the original and new models are shown at high temperature regions. The combustion at this region is controlled by the CO-C4 chemistry, and from the examination of the rate constant, the quality of the selected key reactions is quite decent. This indicates the general understanding of these small radical kinetics remains much to be explored.

6.3 Experimental studies

Several insights can be drawn from the experiments and stated as follows.

Firstly, the general shape of all the temperature profiles obtained from either thermocouples or OH LIF thermometry is similar, as the temperature increases and reaches the maximum value at a certain distance above the burner surface, then slowly drops to a lower level. The detailed aspects of the profiles, however, are quite different among methods. For the thermocouple data, the peak position is reached mostly between 1 mm to 1.4 mm, and the maximum temperature of each equivalence ratio condition of a given fuel follows the thermodynamic theory, meaning that the flame at the stoichiometric case has the highest peak temperature. For the results of the OH LIF thermometry from the R₂(13)/P₁(2) pair, the peak position is around 1.8-2.5 mm, while no obvious patterns are observed regarding the peak temperatures of each equivalence ratio condition among the three mixtures. Apart from the concern of the maximum values, another uncommon phenomenon observed from this transition pair is that the propagation around the near burner surface is considerably quick, while the temperature growth at the same region of 0-1 mm from the thermocouples is rather steady.

However, the thermocouple results are not ideal, as the radiation correction brings significant uncertainty, especially for the thicker wires. One uncertainty is that the measured temperatures at position 0 mm at the stoichiometric and lean conditions are relatively high, which may mainly be due to the level of total flow rates. Also, at a given equivalence ratio case, the measured temperature of the CH₄/NH₃ blend is slightly higher than the results of the pure methane flame, which does not align with the theory. In short, certain aspects of the results from both methods exhibit limitations and errors are expected to some extent. In addition, the results of the OH LIF thermometry from the R₂(2)/R₁(12) pair are regarded to be

less sensible compared to the results of the thermocouples and the OH LIF thermometry from the R₂(13)/P₁(2) pair.

Consequently, the model reflects directly from its respective temperature input. It can be concluded that for the OH profiles, the temperature growth rate at the region of 0-1 mm primarily influences where the peak position is, and the peak temperature indicates the maximum level of the OH. Also, the general shape of the OH is an accumulated result of the maximum temperature and particularly the temperature level at the region after the peak. Furthermore, from the comparison of the kerosene flames at the rich and stoichiometric conditions, the simulation produced from the thermocouple data appears to be better quality, although it cannot be concluded that this approach is necessarily more reliable than the OH LIF thermometry for the temperature measurement.

Secondly, planar laser-induced fluorescence is an effective technique to investigate the relative amounts of key species in a targeted flame, while the quantitative study is extremely difficult to carry out and has major uncertainties. Regarding the original PLIF signals from the three liquid fuels, the OH profiles are rather smooth, and the general shape and important features are quite easy to determine and be compared with the model. On the other hand, the NO profiles have much more noise and hence it is difficult to determine the general trend. Also, the scale difference of the NO amount between equivalence ratio conditions is relatively uncertain. For the OH quantification, the methane flame is a quite reliable reference, primarily due to the validated GRI-Mech 3.0 mechanism and the measured temperature data is relatively reasonable. For the NO quantification, the measured temperature of the ammonia/methane flame is significantly uncertain, and the current mechanisms of CH₄ and NH₃ are much less credible and require significant optimizations for the 1D laminar flame.

Thirdly, the quantitative OH of the three liquid fuels is summarized as follows. In general, decent agreement can be found between the measurements and simulations for the six flame conditions. In terms of the difference of the remaining OH product, the measurements are consistently greater than the simulation by 15% and 10%, at the rich and stoichiometric conditions, respectively. This is due to the open air entering into the flame, hence the mixture conditions in practice become more fuel-lean the further away from the burner surface. Importantly, the quality of the converted PLIF is largely dependent on their respective temperature profiles and the results of the reference fuels, and the most agreeable case is

the kerosene flame at the stoichiometric condition, where both the OH shape and the peak position of the experimental data correspond excellently to the simulated results, and the discrepancy of the maximum OH quantity between the two methods is around 7%. Furthermore, at a given equivalence ratio condition, the kerosene flame possesses the most amount of the OH and both surrogates can produce a considerable quantity of OH. Among the two proposed mixtures, more OH seems to be formed in surrogate B than in surrogate A. Since the only component difference between the two surrogates is the representative of the branched alkanes, this implies that compared to iso-octane, 2-methylheptane may be more appropriate to represent kerosene-based fuels.

Fourthly, the quantitative NO of the three liquid fuels is summarized as follows. At the fuel-rich condition, the NO mechanism appears to be thermal NO_x dominant to a certain extent, while at the stoichiometric condition, the main route of the NO production seems to be the chemistry between the fuel and nitrogen. At the rich condition, the converted NO of all three fuels is relatively reasonable compared to the simulation, while larger disagreements are observed at the stoichiometric condition. Particularly for the two surrogates, the model value is greater than the measurement by approximately a factor of 3. Additionally, regarding the relative NO formed among the three mixtures, at the rich condition the kerosene and surrogate A produce a similar level of NO, which is a little higher than the surrogate B.

6.4 Suggestions for future work

Several insights are addressed in the following to extend this work for future studies.

Firstly, the temperature is essential to study the fundamental combustion characteristics. To quantify key species of a targeted laminar flame from the PLIF signal, the precision of the result heavily relies on a reasonable temperature profile. From the experience with the thermocouple, the potential improvement starts with the condition of the flame. Under the circumstance that the current level of flame stability can be maintained and even improved, a more fuel-rich flame ($\varphi > 1.30$), which means the lift-off phenomenon is more obvious, is likely to increase the reliability of the temperature measurements. From the perspective of the thermocouple, this suggestion takes more consideration of the wire thickness when placing the wire and makes the determination of the burner surface easier. However, if the base of the produced flame is too far away from the burner surface, it will cause significant stability issues, while stability is the fundamental requirements of all the measurements.

Hence, the margin of the flame alternation is relatively narrow. Furthermore, regarding the difficulty faced in obtaining temperature results at the fuel-lean condition, with the current burner setup a less lean (e.g., $\phi = 0.90$) flame that emphasizes the lift-off phenomenon may be more suitable to investigate for a similar reason as adopting a more fuel-rich flame.

Secondly, both temperature approaches can be improved in some regards. For the thermocouples, it is assumed that the reason why type S and type R are commonly employed from previous investigations is the experimental conditions, which are usually below 50 torr. As a result, the measured temperature values of hydrocarbon fuels are at a relatively lower level (< 1800 K), hence the application of these thermocouple wires are sufficient. However, under atmospheric conditions, the maximum temperature of the kerosene-based fuels may exceed 2000 K, thus type B appear to be a more suitable tool, particularly in concern of continuous exposure in the flames, as it has a higher gauge limit (1750 °C) compared to the type S (1500 °C) and type R (1600 °C). The potential drawback of this suggestion is that there are few references to using the type B thermocouple wires at atmospheric conditions for large hydrocarbon measurements, and consequently, information such as the coating method and the emissivity of the coated wires is scarce. Also, the correction method for type S or type R considers the bead diameter after coating to be 2.5 times greater than the bare wire diameter. However, the diameter of the thinnest type B bare wires is 0.2 mm, which is much thicker than the usually employed wires (e.g., type P13R-002 = 0.05 mm), hence the current rule may not be suitable to directly apply on these type B wires. In general, these factors all mount up to a greater uncertainty of the temperature correction.

Thirdly, suggestions for OH LIF thermometry are addressed as follows. If laboratory equipment is available, it is suggested to use two laser systems and two ICCD cameras to capture the two-line OH LIF signals of the targeted flames virtually simultaneously. Another uncertainty factor is the determination of the peak wavelength of the selected transitions. The current approach primarily relies on the visual observation of the PLIF image intensity, hence it is only relatively accurate and may lead to significant errors or meaningless results. The application of a photomultiplier (PMT) with appropriate signal collection and averaging will largely help to decide the precise position of the transitions. Theoretically, the placement of the PMT may not be relevant as the fluorescence occurs in every direction, although it may be ideal to mount the device closer to the area of the burner surface. Once the wavelength

range of a certain transition is set in the Sirah control software, the PMT output can be observed with an oscilloscope synchronized to the pulsed laser firing. Also, boxcar averaging is a signal processing technique utilized to reduce signal noise, which could also be useful. The operation begins with the boxcar also being synchronized to the pulsed laser firing, and the boxcar gate also being observed on the oscilloscope. The gate represents the region of time during which the boxcar will integrate the signal it receives from the PMT. The position and width of the gate are then adjusted to coincide with the fluorescence signal from the PMT. The output is then averaged over N periods and subsequently transmitted to a chart recorder, and detailed information about a given transition can be obtained.

Fourthly, experimental studies are essential to investigate fundamental chemical kinetics and develop an accurate model. From the experience of the mechanism optimization, if the equipment is available, it is suggested to use shock tubes or other approaches to directly measure the rate constant of the key reactions, especially the reaction group involved in the chemical chain branching process. Also, for the reaction class with experimental data, such as the first oxygen addition, it is advised to extend the experiments to a wider range of conditions, and if it is applicable, using C6 or C7 for the investigation will be more suitable for the surrogate components of jet fuels.

BIBLIOGRAPHY

- [1] IATA. Air Passenger Market Analysis, <https://www.iata.org/en/iata-repository/publications/economic-reports/air-passenger-market-analysis---december-2022/> (2022, accessed 17 March 2023).
- [2] IATA. Global Outlook for Air Transport, <https://www.iata.org/en/iata-repository/publications/economic-reports/airline-industry-economic-performance---june-2022---report/> (2022, accessed 17 March 2023).
- [3] Ritchie H, Roser M, Rosado P. CO₂ and greenhouse gas emissions. *Our world in data*, https://ourworldindata.org/co2-emissions?utm_source=tri-city-news&utm_campaign=tricity_news%3A_outbound&utm_medium=referral (2020, accessed 17 March 2023).
- [4] IEA. Aviation, <https://www.iea.org/reports/aviation> (2022, accessed 17 March 2023).
- [5] UNFCCC. The Paris Agreement, <https://unfccc.int/process-and-meetings/the-paris-agreement> (accessed 17 March 2023).
- [6] IATA. Net zero 2050: sustainable aviation fuels, <https://www.iata.org/en/iata-repository/pressroom/fact-sheets/fact-sheet---alternative-fuels/> (accessed 16 March 2023).
- [7] Grewe V, Gangoli Rao A, Grönstedt T, Xisto C, Linke F, Melkert J, Middel J, Ohlenforst B, Blakey S, Christie S, Matthes S, Dahlmann K. Evaluating the climate impact of aviation emission scenarios towards the Paris agreement including COVID-19 effects. *Nat Commun* 2021; 12: 1–10.
- [8] Blakey S, Rye L, Wilson CW. Aviation gas turbine alternative fuels: A review. *Proc Combust Inst* 2011; 33: 2863–2885.
- [9] Zhang C, Hui X, Lin Y, Sung CJ. Recent development in studies of alternative jet fuel combustion: Progress, challenges, and opportunities. *Renewable and Sustainable Energy Reviews* 2016; 120–138.
- [10] Holladay J, Abdullah Z, Heyne J. Sustainable aviation fuel: Review of technical pathways, <https://www.osti.gov/biblio/1660415> (2020, accessed 17 March 2023).
- [11] Edwards JT. Reference jet fuels for combustion testing. In: *55th AIAA aerospace sciences meeting*. 2017, p. 0146.

- [12] Catalanotti E. *Theoretical and experimental investigation of alternative aviation fuels*. Doctoral dissertation, University of Leeds, 2011.
- [13] Edwards T, Colket M, Cernansky N, Dryer F, Egolfopoulos F, Friend D, Law E, Lenhart D, Lindstedt P, Pitsch H. Development of an experimental database and kinetic models for surrogate jet fuels. In: *45th AIAA aerospace sciences meeting and exhibit*. 2007, p. 770.
- [14] Suppes GJ, Storvick TS. *Sustainable Power Technologies and Infrastructure: Energy Sustainability and Prosperity in a Time of Climate Change*. Elsevier, Academic Press, 2015.
- [15] ASTM D1655, <https://www.astm.org/d1655-21c.html> (2022, accessed 10 February 2023).
- [16] Naik C V, Puduppakkam K V, Modak A, Meeks E, Wang YL, Feng Q, Tsotsis TT. Detailed chemical kinetic mechanism for surrogates of alternative jet fuels. *Combust Flame* 2011; 158: 434–445.
- [17] Dooley S, Won SH, Chaos M, Heyne J, Ju Y, Dryer FL, Kumar K, Sung CJ, Wang H, Oehlschlaeger MA, Santoro RJ, Litzinger TA. A jet fuel surrogate formulated by real fuel properties. *Combust Flame* 2010; 157: 2333–2339.
- [18] Law CK. *Combustion physics*. Cambridge university press, 2010.
- [19] Glassman I, Yetter RA, Glumac NG. *Combustion*. Academic press, 2014.
- [20] Turányi T, Tomlin AS. *Analysis of Kinetic Reaction Mechanisms*. Springer-Verlag Berlin Heidelberg, 2014.
- [21] Lackner M, Winter F, Agarwal AK. *Handbook of combustion. Volume 1, Fundamentals and Safety*. Wiley-VCH, 2010.
- [22] Gilbert RG, Smith SC. *Theory of unimolecular and recombination reactions*. Blackwell Science Inc, 1990.
- [23] Lindemann FA, Arrhenius S, Langmuir I, Dhar NR, Perrin J, Lewis WCM. Discussion on ‘the radiation theory of chemical action’. *Trans Faraday Soc* 1922; 17: 598–606.
- [24] ANSYS Chemkin Pro Theory Manual, https://personal.ems.psu.edu/~radovic/ChemKin_Theory_PaSR.pdf (2022, accessed 17 March 2022).
- [25] Troe J. Predictive possibilities of unimolecular rate theory. *J Phys Chem* 1979; 83: 114–126.

- [26] Benson SW. *Thermochemical kinetics*. John Wiley & Sons Inc, 1976.
- [27] ANSYS Chemkin Pro, <https://www.ansys.com/products/fluids/ansys-chemkin-pro> (accessed 8 March 2023).
- [28] Cantera, <https://cantera.org/> (accessed 10 March 2023).
- [29] Cosilab, <https://www.rotexo.com/index.php/en/> (accessed 10 March 2023).
- [30] Smith GP, Golden DM, Frenklach M, Moriarty NW, Eiteneer B, Goldenberg M, Bowman CT, Hanson RK, Song S, Gardiner WC, Lissianski V V, Qin ZW. GRI-Mech 3.0, <http://combustion.berkeley.edu/gri-mech/> (2008, accessed 8 March 2023).
- [31] AramcoMech, <https://www.universityofgalway.ie/combustionchemistrycentre/mechanismdownloads/#> (accessed 10 March 2023).
- [32] The San Diego Mechanism, <http://web.eng.ucsd.edu/mae/groups/combustion/mechanism.html> (accessed 10 March 2023).
- [33] Wang H, Dames E, Sirjean B, Sheen DA, Tangko R, Violi A, Lai JYW, Egolfopoulos FN, Davidson DF, Hanson RK. A high-temperature chemical kinetic model of n-alkane (up to n-dodecane), cyclohexane, and methyl-, ethyl-, n-propyl and n-butyl-cyclohexane oxidation at high temperatures. *JetSurF version 2010*; 2: 19.
- [34] ReSpecTh, <http://respecth.elte.hu/index.php> (accessed 10 March 2023).
- [35] Atkinson R, Baulch DL, Cox RA, Crowley JN, Hampson RF, Hynes RG, Jenkin ME, Rossi MJ, Troe J. Evaluated kinetic and photochemical data for atmospheric chemistry: Volume II - Gas phase reactions of organic species. *Atmos Chem Phys* 2006; 6: 3625–4055.
- [36] Atkinson R, Baulch DL, Cox RA, Hampson RF, Kerr Chairman JA, Troe J. Evaluated Kinetic and Photochemical Data for Atmospheric Chemistry: Supplement III. IUPAC Subcommittee on Gas Kinetic Data Evaluation for Atmospheric Chemistry. *J Phys Chem Ref Data* 1989; 18: 881–1097.
- [37] Baulch DL, Cobos Cj, Cox RA, Esser C, Frank P, Just T, Kerr JA, Pilling MJ, Troe J, Walker RW. Evaluated kinetic data for combustion modelling. *J Phys Chem Ref Data* 1992; 21: 411–734.
- [38] Baulch DL, Bowman CT, Cobos CJ, Cox RA, Just T, Kerr JA, Pilling MJ, Stocker D, Troe J,

- Tsang W, Walker RW, Warnatz J. Evaluated kinetic data for combustion modeling: Supplement II. *J Phys Chem Ref Data* 2005; 34: 757–1397.
- [39] NIST Chemical Kinetics Database, Standard reference Database 17, Version 7.1, <https://kinetics.nist.gov/kinetics/index.jsp> (accessed 10 March 2023).
- [40] Curran HJ. Developing detailed chemical kinetic mechanisms for fuel combustion. *Proc Combust Inst* 2019; 37: 57–81.
- [41] Liang W, Law CK. An analysis of the explosion limits of hydrogen/oxygen mixtures with nonlinear chain reactions. *Phys Chem Chem Phys* 2018; 20: 742–751.
- [42] Burke MP, Chaos M, Ju Y, Dryer FL, Klippenstein SJ. Comprehensive H₂/O₂ kinetic model for high-pressure combustion. *Int J Chem Kinet* 2012; 44: 444–474.
- [43] Hashemi H, Christensen JM, Gersen S, Glarborg P. Hydrogen oxidation at high pressure and intermediate temperatures: Experiments and kinetic modeling. *Proc Combust Inst* 2015; 35: 553–560.
- [44] Kéromnès A, Metcalfe WK, Heufer KA, Donohoe N, Das AK, Sung CJ, Herzler J, Naumann C, Griebel P, Mathieu O, Krejci MC, Petersen EL, Pitz WJ, Curran HJ. An experimental and detailed chemical kinetic modeling study of hydrogen and syngas mixture oxidation at elevated pressures. *Combust Flame* 2013; 160: 995–1011.
- [45] Wagner AF, Slagle IR, Sarzynski D, Gutman D. Experimental and theoretical studies of the C₂H₅ + O₂ reaction kinetics. *J Phys Chem* 1990; 94: 1853–1868.
- [46] Carstensen HH, Naik C V, Dean AM. Detailed modeling of the reaction of C₂H₅ + O₂. *J Phys Chem A* 2005; 109: 2264–2281.
- [47] Fernandes RX, Luther K, Marowsky G, Rissanen MP, Timonen R, Troe J. Experimental and Modeling Study of the Temperature and Pressure Dependence of the Reaction C₂H₅ + O₂ (+ M) → C₂H₅O₂ (+ M). *J Phys Chem A* 2015; 119: 7263–7269.
- [48] Miller JA, Klippenstein SJ. The reaction between ethyl and molecular oxygen II: Further analysis. *Int J Chem Kinet* 2001; 33: 654–668.
- [49] Metcalfe WK, Burke SM, Ahmed SS, Curran HJ. A hierarchical and comparative kinetic modeling study of C₁ - C₂ hydrocarbon and oxygenated fuels. *Int J Chem Kinet* 2013; 45: 638–675.
- [50] Slavinskaya N, Mirzayeva A, Whitside R, Starke JH, Abbasi M, Auyelkhanzyzy M, Chernov V. A modelling study of acetylene oxidation and pyrolysis. *Combust Flame*

- 2019; 210: 25–42.
- [51] Curran HJ, Gaffuri P, Pitz WJ, Westbrook CK. A comprehensive modeling study of n-heptane oxidation. *Combust Flame* 1998; 114: 149–177.
- [52] Curran HJ, Gaffuri P, Pitz WJ, Westbrook CK. A comprehensive modeling study of iso-octane oxidation. *Combust Flame* 2002; 129: 253–280.
- [53] Westbrook CK. Chemical kinetics of hydrocarbon ignition in practical combustion systems. *Proc Combust Inst* 2000; 28: 1563–1577.
- [54] Bugler J, Somers KP, Silke EJ, Curran HJ. Revisiting the Kinetics and Thermodynamics of the Low-Temperature Oxidation Pathways of Alkanes: A Case Study of the Three Pentane Isomers. *J Phys Chem A* 2015; 119: 7510–7527.
- [55] Bugler J, Marks B, Mathieu O, Archuleta R, Camou A, Grégoire C, Heufer KA, Petersen EL, Curran HJ. An ignition delay time and chemical kinetic modeling study of the pentane isomers. *Combust Flame* 2016; 163: 138–156.
- [56] Mohamed SY, Cai L, Khaled F, Banyon C, Wang Z, Al Rashidi MJ, Pitsch H, Curran HJ, Farooq A, Sarathy SM. Modeling ignition of a heptane isomer: improved thermodynamics, reaction pathways, kinetics, and rate rule optimizations for 2-methylhexane. *J Phys Chem A* 2016; 120: 2201–2217.
- [57] Wang Z, Mohamed SY, Zhang L, Moshhammer K, Popolan-Vaida DM, Shankar VSB, Lucassen A, Ruwe L, Hansen N, Dagaut P, Sarathy SM. New insights into the low-temperature oxidation of 2-methylhexane. *Proc Combust Inst* 2017; 36: 373–382.
- [58] Glarborg P, Miller JA, Ruscic B, Klippenstein SJ. Modeling nitrogen chemistry in combustion. *Prog Energy Combust Sci* 2018; 67: 31–68.
- [59] Abian M, Alzueta MU, Glarborg P. Formation of NO from N₂/O₂ mixtures in a flow reactor: toward an accurate prediction of thermal NO. *Int J Chem Kinet* 2015; 47: 518–532.
- [60] Roomina MR, Bilger RW. Conditional Moment Closure (CMC) predictions of a turbulent methane-air jet flame. *Combust Flame* 2001; 125: 1176–1195.
- [61] Klippenstein SJ, Harding LB, Glarborg P, Miller JA. The role of NNH in NO formation and control. *Combust Flame* 2011; 158: 774–789.
- [62] Erdemir D, Dincer I. A perspective on the use of ammonia as a clean fuel: Challenges and solutions. *Int J Energy Res* 2021; 45: 4827–4834.

- [63] Tian Z, Li Y, Zhang L, Glarborg P, Qi F. An experimental and kinetic modeling study of premixed NH₃/CH₄/O₂/Ar flames at low pressure. *Combust Flame* 2009; 156: 1413–1426.
- [64] Okafor EC, Naito Y, Colson S, Ichikawa A, Kudo T, Hayakawa A, Kobayashi H. Experimental and numerical study of the laminar burning velocity of CH₄–NH₃–air premixed flames. *Combust Flame* 2018; 187: 185–198.
- [65] Shu B, He X, Ramos CF, Fernandes RX, Costa M. Experimental and modeling study on the auto-ignition properties of ammonia/methane mixtures at elevated pressures. *Proc Combust Inst* 2021; 38: 261–268.
- [66] Kee RJ, Rupley FM, Miller JA. *Chemkin-II: A Fortran chemical kinetics package for the analysis of gas-phase chemical kinetics*. Sandia National Lab.(SNL-CA), Livermore, CA (United States), 1989.
- [67] Kim D, Martz J, Violi A. A surrogate for emulating the physical and chemical properties of conventional jet fuel. *Combust Flame* 2014; 161: 1489–1498.
- [68] Glarborg P, Kee RJ, Grcar JF, Miller JA. *PSR: A FORTRAN program for modeling well-stirred reactors*. Sandia National Laboratories Livermore, CA, 1986.
- [69] Edwards T, Maurice LQ. Surrogate mixtures to represent complex aviation and rocket fuels. *J Propuls Power* 2001; 17: 461–466.
- [70] Violi A, Yan S, Eddings EG, Sarofim AF, Granata S, Faravelli T, Ranzi E. Experimental formulation and kinetic model for JP-8 surrogate mixtures. *Combust Sci Technol* 2002; 174: 399–417.
- [71] Dooley S, Won SH, Heyne J, Farouk TI, Ju Y, Dryer FL, Kumar K, Hui X, Sung CJ, Wang H, Oehlschlaeger MA, Iyer V, Iyer S, Litzinger TA, Santoro RJ, Malewicki T, Brezinsky K. The experimental evaluation of a methodology for surrogate fuel formulation to emulate gas phase combustion kinetic phenomena. *Combust Flame* 2012; 159: 1444–1466.
- [72] Dagaut P, Cathonnet M. The ignition, oxidation, and combustion of kerosene: A review of experimental and kinetic modeling. *Prog Energy Combust Sci* 2006; 32: 48–92.
- [73] Guéret C, Cathonnet M, Boettner JC, Gaillard F. Experimental study and modeling of kerosene oxidation in a jet-stirred flow reactor. *Symp Combust* 1991; 23: 211–216.
- [74] Dagaut P, Reuillon M, Cathonnet M, Voisin D. High pressure oxidation of normal decane and kerosene in dilute conditions from low to high temperature. *J Chim Phys* 1995; 92:

- 47–76.
- [75] Dagaut P, Karsenty F, Dayma G, Diévert P, Hadj-Ali K, Mzé-Ahmed A, Braun-Unkhoff M, Herzler J, Kathrotia T, Kick T, Naumann C, Riedel U, Thomas L. Experimental and detailed kinetic model for the oxidation of a Gas to Liquid (GtL) jet fuel. *Combust Flame* 2014; 161: 835–847.
- [76] Doute C, Delfau J-L, Akrich R, Vovelle C. Chemical structure of atmospheric pressure premixed n-decane and kerosene flames. *Combust Sci Technol* 1995; 106: 327–344.
- [77] Riesmeier E, Honnet S, Peters N. Flamelet modeling of pollutant formation in a gas turbine combustion chamber using detailed chemistry for a kerosene model fuel. *J Eng Gas Turbines Power* 2004; 126: 899–905.
- [78] Patterson PM, Kyne AG, Pourkashanian M, Williams A, Wilson CW. Combustion of kerosene in counterflow diffusion flames. *J Propuls Power* 2001; 17: 453–460.
- [79] Vovelle C, Delfau JL, Reuillon M. *Formation of Aromatic Hydrocarbons in Decane and Kerosene Flames at Reduced Pressure. Soot Formation in Combustion: mechanisms and models*. Springer-Verlag Berlin Heidelberg, 1994.
- [80] Dagaut P. On the kinetics of hydrocarbons oxidation from natural gas to kerosene and diesel fuel. *Phys Chem Chem Phys* 2002; 4: 2079–2094.
- [81] Malewicki T, Brezinsky K. Experimental and modeling study on the pyrolysis and oxidation of n-decane and n-dodecane. *Proc Combust Inst* 2013; 34: 361–368.
- [82] Kim D, Martz J, Abdul-Nour A, Yu X, Jansons M, Violi A. A six-component surrogate for emulating the physical and chemical characteristics of conventional and alternative jet fuels and their blends. *Combust Flame* 2017; 179: 86–94.
- [83] Kim D, Martz J, Violi A. Effects of fuel physical properties on direct injection spray and ignition behavior. *Fuel* 2016; 180: 481–496.
- [84] Kathrotia T, Oßwald P, Naumann C, Richter S, Köhler M. Combustion kinetics of alternative jet fuels, Part-II: Reaction model for fuel surrogate. *Fuel* 2021; 302: 120736.
- [85] Puduppakkam K V, Wang C, Hodgson D, Naik C, Meeks E. Accurate and Dynamic Accounting of Fuel Composition in Flame Propagation during Engine Simulations. In: *SAE Technical Papers*. 2016.
- [86] The Model Fuels Library: Accurate Combustion Chemistry for the Real World, <https://symkom.pl/wp-content/uploads/2019/07/ansys-model-fuel-library->

- brochure.pdf (2016, accessed 10 February 2023).
- [87] Ranzi E, Frassoldati A, Grana R, Cuoci A, Faravelli T, Kelley AP, Law CK. Hierarchical and comparative kinetic modeling of laminar flame speeds of hydrocarbon and oxygenated fuels. *Prog Energy Combust Sci* 2012; 38: 468–501.
- [88] Stagni A, Frassoldati A, Cuoci A, Faravelli T, Ranzi E. Skeletal mechanism reduction through species-targeted sensitivity analysis. *Combust Flame* 2016; 163: 382–393.
- [89] Mawid MA. Development of a detailed chemical kinetic mechanism for JP-8 & Fischer-Tropsch-derived synthetic jet fuels. In: *Collection of Technical Papers - 43rd AIAA/ASME/SAE/ASEE Joint Propulsion Conference*. 2007.
- [90] Mawid MA, Park TW, Sekar B, Grana C. Development and validation of a detailed JP-8 fuel chemistry mechanism. In: *38th AIAA/ASME/SAE/ASEE Joint Propulsion Conference and Exhibit*. 2002.
- [91] Gokulakrishnan P, Klassen MS, Roby RJ. Ignition characteristics of a fischer-tropsch synthetic jet fuel. In: *Turbo Expo: Power for Land, Sea, and Air*. 2008, pp. 921–929.
- [92] Meeks E, Naik C V, Puduppakkam K V, Modak A, Egolfopoulos FN, Tsotsis T, Westbrook CK. *Experimental and Modeling Studies of the Combustion Characteristics of Conventional and Alternative Jet Fuels. Final Report*. 2011.
- [93] Dooley S, Won SH, Jahangirian S, Ju Y, Dryer FL, Wang H, Oehlschlaeger MA. The combustion kinetics of a synthetic paraffinic jet aviation fuel and a fundamentally formulated, experimentally validated surrogate fuel. *Combust Flame* 2012; 159: 3014–3020.
- [94] Mehl M, Pitz WJ, Westbrook CK, Curran HJ. Kinetic modeling of gasoline surrogate components and mixtures under engine conditions. *Proc Combust Inst* 2011; 33: 193–200.
- [95] Dooley S, Won SH, Haas FM, Santner JS, Ju Y, Dryer FL, Farouk T. Development of reduced kinetic models for petroleum-derived and alternative jet fuels. In: *50th AIAA/ASME/SAE/ASEE Joint Propulsion Conference*. 2014, p. 3661.
- [96] Wang H, Oehlschlaeger MA. Autoignition studies of conventional and Fischer-Tropsch jet fuels. *Fuel* 2012; 98: 249–258.
- [97] Hui X, Sung CJ. Laminar flame speeds of transportation-relevant hydrocarbons and jet fuels at elevated temperatures and pressures. *Fuel* 2013; 109: 191–200.

- [98] Mz -Ahmed A, Hadj-Ali K, Di vart P, Dagaut P. Kinetics of oxidation of a synthetic jet fuel in a jet-stirred reactor: experimental and modeling study. *Energy & fuels* 2010; 24: 4904–4911.
- [99] Huber ML, Bruno TJ, Chirico RD, Diky V, Kazakov AF, Lemmon EW, Muzny CD, Frenkel M. Equations of state on demand: Application for surrogate fuel development. *Int J Thermophys* 2011; 32: 596–613.
- [100] Kim D, Violi A. Hydrocarbons for the next generation of jet fuel surrogates. *Fuel* 2018; 228: 438–444.
- [101] Yu W, Zhao F, Yang W, Tay K, Xu H. Development of an optimization methodology for formulating both jet fuel and diesel fuel surrogates and their associated skeletal oxidation mechanisms. *Fuel* 2018; 231: 361–372.
- [102] Fang X, Huang Z, Qiao X, Ju D, Bai X. Skeletal mechanism development for a 3-component jet fuel surrogate using semi-global sub-mechanism construction and mechanism reduction. *Fuel* 2018; 229: 53–59.
- [103] Ogura T, Nagumo Y, Miyoshi A, Koshi M. Chemical kinetic mechanism for high temperature oxidation of butane isomers. *Energy & fuels* 2007; 21: 130–135.
- [104] Westbrook CK, Pitz WJ, Boercker JE, Curran HJ, Griffiths JF, Mohamed C, Ribaucour M. Detailed chemical kinetic reaction mechanisms for autoignition of isomers of heptane under rapid compression. *Proc Combust Inst* 2002; 29: 1311–1318.
- [105] Sarathy SM, Westbrook CK, Mehl M, Pitz WJ, Togbe C, Dagaut P, Wang H, Oehlschlaeger MA, Niemann U, Seshadri K, Veloo PS, Ji C, Egolfopoulos FN, Lu T. Comprehensive chemical kinetic modeling of the oxidation of 2-methylalkanes from C7 to C20. *Combust Flame* 2011; 158: 2338–2357.
- [106] Wang W, Li Z, Oehlschlaeger MA, Healy D, Curran HJ, Sarathy SM, Mehl M, Pitz WJ, Westbrook CK. An experimental and modeling study of the autoignition of 3-methylheptane. *Proc Combust Inst* 2013; 34: 335–343.
- [107] Sarathy SM, Niemann U, Yeung C, Gehmlich R, Westbrook CK, Plomer M, Luo Z, Mehl M, Pitz WJ, Seshadri K, Thomson MJ, Lu T. A counterflow diffusion flame study of branched octane isomers. *Proc Combust Inst* 2013; 34: 1015–1023.
- [108] Liu N, S. Mani Sarathy, Westbrook CK, Egolfopoulos FN. Ignition of non-premixed counterflow flames of octane and decane isomers. *Proc Combust Inst* 2013; 34: 903–

- 910.
- [109] Li S, Campos A, Davidson DF, Hanson RK. Shock tube measurements of branched alkane ignition delay times. *Fuel* 2014; 118: 398–405.
- [110] Ji C, Sarathy SM, Veloo PS, Westbrook CK, Egolfopoulos FN. Effects of fuel branching on the propagation of octane isomers flames. *Combust Flame* 2012; 159: 1426–1436.
- [111] Jahangirian S, Healy D, Sarathy SM, Dooley S, Mehl M, Pitz WJ, Dryer FL, Curran HJ, Westbrook CK. Experimental and modeling study of 2-methylheptane oxidation in a flow reactor, shock tube, and rapid compression machine. In: *Fall Technical Meeting of the Eastern States of the Combustion Institute, Storrs, CT*. 2011.
- [112] Shen HPS, Steinberg J, Vanderover J, Oehlschlaeger MA. A Shock tube study of the ignition of n-heptane, n-decane, n-dodecane, and n-tetradecane at elevated pressures. *Energy and Fuels* 2009; 23: 2482–2489.
- [113] Westbrook CK, Pitz WJ, Herbinet O, Curran HJ, Silke EJ. A comprehensive detailed chemical kinetic reaction mechanism for combustion of n-alkane hydrocarbons from n-octane to n-hexadecane. *Combust Flame* 2009; 156: 181–199.
- [114] Selim H, Mohamed SY, Lucassen A, Hansen N, Sarathy SM. Effect of the methyl substitution on the combustion of two methylheptane isomers: Flame chemistry using vacuum-ultraviolet (VUV) photoionization mass spectrometry. *Energy and Fuels* 2015; 29: 2696–2708.
- [115] Pfahl U, Fieweger K, Adomeit G. Self-ignition of diesel-relevant hydrocarbon-air mixtures under engine conditions. *Symp Combust* 1996; 26: 781–789.
- [116] Zhukov VP, Sechenov VA, Starikovskii AY. Autoignition of n-decane at high pressure. *Combust Flame* 2008; 153: 130–136.
- [117] Ji C, Dames E, Wang YL, Wang H, Egolfopoulos FN. Propagation and extinction of premixed C5-C12 n-alkane flames. *Combust Flame* 2010; 157: 277–287.
- [118] Alekseev VA, Soloviova-Sokolova J V, Matveev SS, Chechet I V, Matveev SG, Konnov AA. Laminar burning velocities of n-decane and binary kerosene surrogate mixture. *Fuel* 2017; 187: 429–434.
- [119] Ranzi E, Cavallotti C, Cuoci A, Frassoldati A, Pelucchi M, Faravelli T. New reaction classes in the kinetic modeling of low temperature oxidation of n-alkanes. *Combust Flame* 2015; 162: 1679–1691.

- [120] Dong S, Wagnon SW, Pratali Maffei L, Kukkadapu G, Nobili A, Mao Q, Pelucchi M, Cai L, Zhang K, Raju M, Chatterjee T, Pitz WJ, Faravelli T, Pitsch H, Senecal PK, Curran HJ. A new detailed kinetic model for surrogate fuels: C3MechV3.3. *Appl Energy Combust Sci* 2022; 9: 100043.
- [121] Auzani AS. *Experimental and Kinetic Modelling Study of Jet A-1/Ethanol Blend Combustion and Oxidation Stability*. Doctoral dissertation, University of Sheffield, 2020.
- [122] Hanson RK, Spearrin RM, Goldenstein CS. *Spectroscopy and optical diagnostics for gases*. Springer International Publishing, 2016.
- [123] Harilal SS, Brumfield BE, Lahaye NL, Hartig KC, Phillips MC. Optical spectroscopy of laser-produced plasmas for standoff isotopic analysis. *Appl Phys Rev* 2018; 5: 021301.
- [124] Eckbreth AC. *Laser diagnostics for combustion temperature and species*. Taylor & Francis Books, 1996.
- [125] Cobra-Stretch Dye Laser Datasheet, <https://www.sirah.com/wp-content/uploads/documents/CobraStretch.pdf> (accessed 7 February 2023).
- [126] LIFBASE, <https://www.sri.com/platform/lifbase-spectroscopy-tool/> (accessed 17 March 2023).
- [127] Bradley D, Matthews KJ. Measurement of High Gas Temperatures with Fine Wire Thermocouples. *J Mech Eng Sci* 1968; 10: 299–305.
- [128] Heitor M V, Moreira ALN. Thermocouples and sample probes for combustion studies. *Prog Energy Combust Sci* 1993; 19: 259–278.
- [129] Kint JH. A noncatalytic coating for platinum-rhodium thermocouples. *Combust Flame* 1970; 14: 279–282.
- [130] Tran LS, Glaude PA, Battin-Leclerc F. Experimental study of the structure of laminar premixed flames of ethanol/methane/oxygen/argon. *Combust Explos Shock Waves* 2013; 49: 11–18.
- [131] Dmitriev AM, Osipova KN, Shmakov AG, Bolshova TA, Knyazkov DA, Glaude PA. Laminar flame structure of ethyl pentanoate at low and atmospheric-pressure: Experimental and kinetic modeling study. *Energy* 2021; 215: 119115.
- [132] Cafiero M, Dias V, Iavarone S, Coussement A, Jeanmart H, Parente A. Investigation of temperature correction methods for fine wire thermocouple losses in low-pressure flat premixed laminar flames. *Combust Flame* 2022; 244: 112248.

- [133] Gerasimov IE, Knyazkov DA, Yakimov SA, Bolshova TA, Shmakov AG, Korobeinichev OP. Structure of atmospheric-pressure fuel-rich premixed ethylene flame with and without ethanol. *Combust Flame* 2012; 159: 1840–1850.
- [134] Kaskan WE. The dependence of flame temperature on mass burning velocity. *Symp Combust* 1957; 6: 134–143.
- [135] Hilsenrath J, Beckett CW, Benedict WS, Fano L, Hoge HJ, Masi JF, Nuttall RL, Touloukian YS, Woolley HW, King C V. Tables of Thermal Properties of Gases. *J Electrochem Soc* 1956; 103: 124C.
- [136] Davisson C, Weeks JR. The Relation between the Total Thermal Emissive Power of a Metal and its Electrical Resistivity. *J Opt Soc Am* 1924; 8: 581–605.
- [137] Bradley D, Entwistle AG. Determination of the emissivity, for total radiation, of small diameter platinum-10% rhodium wires in the temperature range 600-1450°C. *Br J Appl Phys* 1961; 12: 708–711.
- [138] Bradley D, Entwistle AG. The total hemispherical emittance of coated wires. *Br J Appl Phys* 1966; 17: 1155–1164.
- [139] Devillers R, Bruneaux G, Schulz C. Development of a two-line OH-laser-induced fluorescence thermometry diagnostics strategy for gas-phase temperature measurements in engines. *Appl Opt* 2008; 47: 5871–5885.
- [140] Kostka S, Roy S, Lakusta PJ, Meyer TR, Renfro MW, Gord JR, Branam R. Comparison of line-peak and line-scanning excitation in two-color laser-induced-fluorescence thermometry of OH. *Appl Opt* 2009; 48: 6332–6343.
- [141] Fuyuto T, Kronemayer H, Lewerich B, Brübach J, Fujikawa T, Akihama K, Dreier T, Schulz C. Temperature and species measurement in a quenching boundary layer on a flat-flame burner. *Exp Fluids* 2010; 49: 783–795.
- [142] Foo KK, Lamoureux N, Cessou A, Lacour C, Desgroux P. The accuracy and precision of multi-line NO-LIF thermometry in a wide range of pressures and temperatures. *J Quant Spectrosc Radiat Transf* 2020; 255: 107257.
- [143] Stagni A, Cuoci A, Frassoldati A, Faravelli T, Ranzi E. Lumping and reduction of detailed kinetic schemes: An effective coupling. *Ind Eng Chem Res* 2014; 53: 9004–9016.
- [144] Ranzi E, Frassoldati A, Stagni A, Pelucchi M, Cuoci A, Faravelli T. Reduced kinetic schemes of complex reaction systems: Fossil and biomass-derived transportation fuels.

- Int J Chem Kinet* 2014; 46: 512–542.
- [145] Kumar K, Sung CJ. A comparative experimental study of the autoignition characteristics of alternative and conventional jet fuel/oxidizer mixtures. *Fuel* 2010; 89: 2853–2863.
- [146] Kumar K, Sung CJ, Hui X. Laminar flame speeds and extinction limits of conventional and alternative jet fuels. *Fuel* 2011; 90: 1001–1011.
- [147] Benson SW, Golden DM, Haugen GR, Shaw R, Cruickshank FR, Rodgers AS, O’neal HE, Walsh R. Additivity rules for the estimation of thermochemical properties. *Chem Rev* 1969; 69: 279–324.
- [148] Burke SM, Simmie JM, Curran HJ. Critical evaluation of thermochemical properties of C1-C4species: Updated group-contributions to estimate thermochemical properties. *J Phys Chem Ref Data* 2015; 44: 013101.
- [149] Goldsmith CF, Magoon GR, Green WH. Database of small molecule thermochemistry for combustion. *J Phys Chem A* 2012; 116: 9033–9047.
- [150] Ritter ER. THERM: a computer code for estimating thermodynamic properties for species important to combustion and reaction modeling. *J Chem Inf Comput Sci* 1991; 31: 400–408.
- [151] Burcat A, Ruscic B. *Third millenium ideal gas and condensed phase thermochemical database for combustion (with update from active thermochemical tables)*. Argonne National Lab.(ANL), Argonne, IL (United States), 2005.
- [152] Lay TH, Bozzelli JW, Dean AM, Ritter ER. Hydrogen atom bond increments for calculation of thermodynamic properties of hydrocarbon radical species. *J Phys Chem* 1995; 99: 14514–14527.
- [153] Marsi I, Viskolcz B, Seres L. Application of the Group Additivity Method to Alkyl Radicals: An ab Initio Study. *J Phys Chem A* 2000; 104: 4497–4504.
- [154] Sabbe MK, Saeys M, Reyniers M-F, Marin GB, Van Speybroeck V, Waroquier M. Group additive values for the gas phase standard enthalpy of formation of hydrocarbons and hydrocarbon radicals. *J Phys Chem A* 2005; 109: 7466–7480.
- [155] Troe J. Ultraviolettpektrum und Reaktionen des HO₂-Radikals im thermischen Zerfall von H₂O₂. *Berichte der Bunsengesellschaft für Phys Chemie* 1969; 73: 946–952.
- [156] Kijewski H, Troe J. Study of the pyrolysis of H₂O₂ in the presence of H₂ and CO by use of UV absorption of HO₂. *Int J Chem Kinet* 1971; 3: 223–235.

- [157] Hong Z, Cook RD, Davidson DF, Hanson RK. A shock tube study of $\text{OH} + \text{H}_2\text{O}_2 \rightarrow \text{H}_2\text{O} + \text{HO}_2$ and $\text{H}_2\text{O}_2 + \text{M} \rightarrow 2\text{OH} + \text{M}$ using laser absorption of H_2O and OH . *J Phys Chem A* 2010; 114: 5718–5727.
- [158] Hong Z, Davidson DF, Lam K-Y, Hanson RK. A shock tube study of the rate constants of HO_2 and CH_3 reactions. *Combust Flame* 2012; 159: 3007–3013.
- [159] Hong Z, Lam K-Y, Sur R, Wang S, Davidson DF, Hanson RK. On the rate constants of $\text{OH} + \text{HO}_2$ and $\text{HO}_2 + \text{HO}_2$: A comprehensive study of H_2O_2 thermal decomposition using multi-species laser absorption. *Proc Combust Inst* 2013; 34: 565–571.
- [160] Kappel C, Luther K, Troe J. Shock wave study of the unimolecular dissociation of H_2O_2 in its falloff range and of its secondary reactions. *Phys Chem Chem Phys* 2002; 4: 4392–4398.
- [161] Sajid MB, Es-sebbar E, Javed T, Fittschen C, Farooq A. Measurement of the rate of hydrogen peroxide thermal decomposition in a shock tube using quantum cascade laser absorption near $7.7 \mu\text{m}$. *Int J Chem Kinet* 2014; 46: 275–284.
- [162] Patrick R, Pilling MJ. The temperature dependence of the $\text{HO}_2 + \text{HO}_2$ reaction. *Chem Phys Lett* 1982; 91: 343–347.
- [163] Dobis O, Benson SW. Reaction of the Ethyl Radical with Oxygen at Millitorr Pressures at 243–368 K and a Study of the $\text{Cl} + \text{HO}_2$, Ethyl + HO_2 , and $\text{HO}_2 + \text{HO}_2$ Reactions. *J Am Chem Soc* 1993; 115: 8798–8809.
- [164] Stone D, Rowley DM. Kinetics of the gas phase HO_2 self-reaction: Effects of temperature, pressure, water and methanol vapours. *Phys Chem Chem Phys* 2005; 7: 2156–2163.
- [165] Lightfoot PD, Lesclaux R, Veyret B. Flash photolysis study of the methylperoxy+methylperoxy reaction: rate constants and branching ratios from 248 to 573 K. *J Phys Chem* 1990; 94: 700–707.
- [166] Hong Z, Davidson DF, Barbour EA, Hanson RK. A new shock tube study of the $\text{H} + \text{O}_2 \rightarrow \text{OH} + \text{O}$ reaction rate using tunable diode laser absorption of H_2O near $2.5 \mu\text{m}$. *Proc Combust Inst* 2011; 33: 309–316.
- [167] Pirraglia AN, Michael J V, Sutherland JW, Klemm RB. A flash photolysis-shock tube kinetic study of the H atom reaction with O_2 : $\text{H} + \text{O}_2 \rightleftharpoons \text{OH} + \text{O}$ ($962 \text{ K} \leq T \leq 1705 \text{ K}$) and $\text{H} + \text{O}_2 + \text{Ar} \rightarrow \text{HO}_2 + \text{Ar}$ ($746 \text{ K} \leq T \leq 987 \text{ K}$). *J Phys Chem* 1989; 93: 282–291.

- [168] Yang H, Gardiner WC, Shin KS, Fujii N. Shock tube study of the rate coefficient of $H + O_2 \rightarrow OH + O$. *Chem Phys Lett* 1994; 231: 449–453.
- [169] Wang S, Davidson DF, Hanson RK. Shock Tube and Laser Absorption Study of CH_2O Oxidation via Simultaneous Measurements of OH and CO. *J Phys Chem A* 2017; 121: 8561–8568.
- [170] Martinez S, Baigmohammadi M, Patel V, Panigrahy S, Sahu AB, Nagaraja S, Ramalingam A, Heufer KA, Pekalski A, Curran HJ. A comprehensive experimental and modeling study of the ignition delay time characteristics of ternary and quaternary blends of methane, ethane, ethylene, and propane over a wide range of temperature, pressure, equivalence ratio, and dilution. *Combust Flame* 2021; 234: 111626.
- [171] Jasper AW, Klippenstein SJ, Harding LB. Theoretical rate coefficients for the reaction of methyl radical with hydroperoxyl radical and for methylhydroperoxide decomposition. *Proc Combust Inst* 2009; 32: 279–286.
- [172] Zhu R, Lin MC. The $CH_3 + HO_2$ reaction: First-principles prediction of its rate constant and product branching probabilities. *J Phys Chem A* 2001; 105: 6243–6248.
- [173] Droege AT, Tully FP. Hydrogen-atom abstraction from alkanes by OH. 5. n-butane. *J Phys Chem* 1986; 90: 5937–5941.
- [174] Cohen N. Are reaction rate coefficients additive? Revised transition state theory calculations for OH + alkane reactions. *Int J Chem Kinet* 1991; 23: 397–417.
- [175] Sivaramakrishnan R, Michael J V. Rate constants for OH with selected large alkanes: Shock-tube measurements and an improved group scheme. *J Phys Chem A* 2009; 113: 5047–5060.
- [176] Badra J, Elwardany A, Farooq A. Shock tube measurements of the rate constants for seven large alkanes + OH. *Proc Combust Inst* 2015; 35: 189–196.
- [177] Sivaramakrishnan R, Srinivasan NK, Su MC, Michael J V. High temperature rate constants for OH+ alkanes. *Proc Combust Inst* 2009; 32 I: 107–114.
- [178] Lenhardt TM, McDade CE, Bayes KD. Rates of reaction of butyl radicals with molecular oxygen. *J Chem Phys* 1980; 72: 304–310.
- [179] Slagle IR, Park JY, Gutman D. Experimental investigation of the kinetics and mechanism of the reaction of n-propyl radicals with molecular oxygen from 297 to 635 K. *Symp Combust* 1985; 20: 733–741.

- [180] Ruiz RP, Bayes KD. Rates of reaction of propyl radicals with molecular oxygen. *J Phys Chem* 1984; 88: 2592–2595.
- [181] Atkinson R, Baulch DL, Cox RA, Hampson RF, Kerr JA, Troe J. Evaluated Kinetic and Photochemical Data for Atmospheric Chemistry: Supplement IV. IUPAC Subcommittee on Gas Kinetic Data Evaluation for Atmospheric Chemistry. *J Phys Chem Ref Data* 1992; 21: 1125–1568.
- [182] Goldsmith CF, Green WH, Klippenstein SJ. Role of O₂ + QOOH in low-temperature ignition of propane. 1. temperature and pressure dependent rate coefficients. *J Phys Chem A* 2012; 116: 3325–3346.
- [183] Huang H, Merthe DJ, Zádor J, Jusinski LE, Taatjes CA. New experiments and validated master-equation modeling for OH production in propyl + O₂ reactions. *Proc Combust Inst* 2011; 33: 293–299.
- [184] Dilger H, Stelmár M, Tregenna-Piggott PLW, Roduner E, Reid ID. Gas phase addition kinetics of the tert-butyl radical to oxygen. *Berichte der Bunsengesellschaft/Physical Chem Chem Phys* 1997; 101: 956–960.
- [185] Xi Z, Han WJ, Bayes KD. Temperature dependence of the rate constant for the reaction of neopentyl radicals with oxygen. *J Phys Chem* 1988; 92: 3450–3453.
- [186] Eskola AJ, Pekkanen TT, Joshi SP, Timonen RS, Klippenstein SJ. Kinetics of 1-butyl and 2-butyl radical reactions with molecular oxygen: Experiment and theory. *Proc Combust Inst* 2019; 37: 291–298.
- [187] Gilbert RG, Luther K, Troe J. Theory of thermal unimolecular reactions in the fall-off range. II. Weak collision rate constants. *Berichte der Bunsengesellschaft für Phys Chemie* 1983; 87: 169–177.
- [188] Miyoshi A. Systematic computational study on the unimolecular reactions of alkylperoxy (RO₂), hydroperoxyalkyl (QOOH), and hydroperoxyalkylperoxy (O₂QOOH) radicals. *J Phys Chem A* 2011; 115: 3301–3325.
- [189] Villano SM, Huynh LK, Carstensen HH, Dean AM. High-pressure rate rules for Alkyl + O₂ reactions. 1. the dissociation, concerted elimination, and isomerization channels of the alkyl peroxy radical. *J Phys Chem A* 2011; 115: 13425–13442.
- [190] Auzmendi-Murua I, Bozzelli JW. Thermochemistry, reaction paths, and kinetics on the secondary isooctane radical reaction with 3O₂. *Int J Chem Kinet* 2014; 46: 71–103.

- [191] Snitsiriwat S, Bozzelli JW. Thermochemistry, reaction paths, and kinetics on the tert-isooctane radical reaction with O₂. *J Phys Chem A* 2014; 118: 4631–4646.
- [192] Sun H, Bozzelli JW. Thermochemical and Kinetic Analysis on the Reactions of Neopentyl and Hydroperoxy-Neopentyl Radicals with Oxygen: Part I. OH and Initial Stable HC Product Formation. *J Phys Chem A* 2004; 108: 1694–1711.
- [193] Zádor J, Huang H, Welz O, Zetterberg J, Osborn DL, Taatjes CA. Directly measuring reaction kinetics of QOOH—a crucial but elusive intermediate in hydrocarbon autoignition. *Phys Chem Chem Phys* 2013; 15: 10753–10760.
- [194] Baldwin RR, Hisham MWM, Walker RW. Arrhenius parameters of elementary reactions involved in the oxidation of neopentane. *J Chem Soc Faraday Trans 1 Phys Chem Condens Phases* 1982; 78: 1615–1627.
- [195] Hughes KJ, Lightfoot PD, Pilling MJ. Direct measurements of the peroxy—hydroperoxy radical isomerisation, a key step in hydrocarbon combustion. *Chem Phys Lett* 1992; 191: 581–586.
- [196] Hughes KJ, Halford-Maw PA, Lightfoot PD, Turányi T, Pilling MJ. Direct measurements of the neopentyl peroxy-hydroperoxy radical isomerisation over the temperature range 660–750 K. *Symp Combust* 1992; 24: 645–652.
- [197] Baldwin RR, Hisham MWM, Walker RW. Arrhenius parameters of elementary reactions involved in the oxidation of neopentane. *J Chem Soc Faraday Trans 1 Phys Chem Condens Phases* 1982; 78: 1615–1627.
- [198] Nozière B, Vereecken L. Direct Observation of Aliphatic Peroxy Radical Autoxidation and Water Effects: An Experimental and Theoretical Study. *Angew Chemie - Int Ed* 2019; 58: 13976–13982.
- [199] Bozzelli JW, Pitz WJ. The reaction of hydroperoxy-propyl radicals with molecular oxygen. *Symp Combust* 1994; 25: 783–791.
- [200] Evans MG, Polanyi M. Inertia and driving force of chemical reactions. *Trans Faraday Soc* 1938; 34: 11–24.
- [201] Kruse TM, Wong H-W, Broadbelt LJ. Mechanistic modeling of polymer pyrolysis: polypropylene. *Macromolecules* 2003; 36: 9594–9607.
- [202] Pfaendtner J, Yu X, Broadbelt LJ. Quantum chemical investigation of low-temperature intramolecular hydrogen transfer reactions of hydrocarbons. *J Phys Chem A* 2006; 110:

- 10863–10871.
- [203] Blowers P, Masel R. Engineering approximations for activation energies in hydrogen transfer reactions. *AIChE J* 2000; 46: 2041–2052.
- [204] Hughes KJ. Personal communications.
- [205] Sharma S, Ramans S, Green WH. Intramolecular hydrogen migration in alkylperoxy and hydroperoxyalkylperoxy radicals: Accurate treatment of hindered rotors. *J Phys Chem A* 2010; 114: 5689–5701.
- [206] Zhang K, Banyon C, Togbé C, Dagaut P, Bugler J, Curran HJ. An experimental and kinetic modeling study of n-hexane oxidation. *Combust Flame* 2015; 162: 4194–4207.
- [207] Villano SM, Huynh LK, Carstensen HH, Dean AM. High-pressure rate rules for alkyl + O₂ reactions. 2. the isomerization, cyclic ether formation, and β -scission reactions of hydroperoxy alkyl radicals. *J Phys Chem A* 2012; 116: 5068–5089.
- [208] Mohamed SY, Davis AC, Al Rashidi MJ, Sarathy SM. Computational Kinetics of Hydroperoxybutylperoxy Isomerizations and Decompositions: A Study of the Effect of Hydrogen Bonding. *J Phys Chem A* 2018; 122: 6277–6291.
- [209] Jalan A, Alecu IM, Meana-Pañeda R, Aguilera-Iparraguirre J, Yang KR, Merchant SS, Truhlar DG, Green WH. New pathways for formation of acids and carbonyl products in low-temperature oxidation: The Korcek decomposition of γ -keto hydroperoxides. *J Am Chem Soc* 2013; 135: 11100–11114.
- [210] Bagheri G, Ranzi E, Pelucchi M, Parente A, Frassoldati A, Faravelli T. Comprehensive kinetic study of combustion technologies for low environmental impact: MILD and OXY-fuel combustion of methane. *Combust Flame* 2020; 212: 142–155.
- [211] Hughes KJ, Pourkashanian M, Wilson CW. OH concentration measurements in a jet engine exhaust. *Int J Energy a Clean Environ* 2007; 8: 305–320.
- [212] Tamura M, Berg PA, Harrington JE, Luque J, Jeffries JB, Smith GP, Crosley DR. Collisional quenching of CH(A), OH(A), and NO(A) in low pressure hydrocarbon flames. *Combust Flame* 1998; 114: 502–514.
- [213] Smith GP, Crosley DR. Quenching of OH (A $2\Sigma^+$, $v'=0$) by H₂, N₂O, and hydrocarbons at elevated temperatures. *J Chem Phys* 1986; 85: 3896–3901.
- [214] Lamoureux N, El Merhubi H, Pillier L, De Persis S, Desgroux P. Modeling of NO formation in low pressure premixed flames. *Combust Flame* 2016; 163: 557–575.

APPENDIX A: NEW GROUP ADDITIVITY VALUE OF STABLE SPECIES

AND RADICALS

T/K	H°	S°	C_p					
	(kcal · mol ⁻¹)	(cal · mol ⁻¹ · K ⁻¹)	300	400	500	600	800	1000
C/C/H3	-10.01	30.29	6.22	7.74	9.24	10.62	12.84	14.59
C/C2/H2	-5.00	9.65	5.59	7.08	8.43	9.53	11.23	12.48
C/C3/H	-2.14	-11.43	4.90	6.73	8.01	8.81	9.87	10.43
C/C2/H/OO	-8.02	6.62	3.85	4.84	6.52	7.45	9.28	10.60
C/C/H2/OO	-7.03	-15.46	4.43	5.32	6.63	7.23	7.94	8.47
C/C3/OO	-6.20	-34.64	3.53	4.61	5.83	5.96	6.70	6.53
OO/C/H	-20.60	38.64	9.52	11.05	11.56	12.53	13.40	14.05
CO/C2	-31.50	15.14	5.59	6.09	6.81	7.48	8.54	9.14
CO/C/H	-29.34	34.45	6.72	7.71	8.77	9.90	11.45	12.63
P	101.15	2.51	-1.14	-1.64	-2.14	-2.60	-3.32	-3.89
S	98.07	4.26	-1.78	-2.98	-3.49	-3.81	-4.40	-4.78
T	96.14	5.14	-2.81	-4.19	-4.84	-5.10	-5.33	-5.36
ALPEROX	85.27	-0.48	-1.17	-1.78	-2.28	-2.74	-3.25	-3.68

APPENDIX B: UPDATED THERMODYNAMIC DATA OF SPECIES

RELATED TO 2-METHYLHEPTANE COMBUSTION

C8H18-2	5/ 8/ 5	THERMC	8H	18	0	OG	300.000	5000.000	1000.000	71
2.23510898E+01	4.52823431E-02	-1.75714464E-05	3.01647224E-09	-1.90956444E-13						2
-3.69992537E+04	-9.06028227E+01	-6.10805451E-01	8.93201040E-02	-2.80719788E-05						3
-2.46887913E-08	1.64871751E-11	-2.93519112E+04	3.44304720E+01							4
C8H17-2A	5/ 8/ 5	THERMC	8H	17	0	OG	300.000	5000.000	1000.000	71
2.19996000E+01	4.30340167E-02	-1.68526459E-05	2.92459599E-09	-1.87704722E-13						2
-1.23696575E+04	-8.52658261E+01	-8.68364589E-01	9.04897900E-02	-3.89289241E-05						3
-1.17268841E-08	1.15110499E-11	-4.97161588E+03	3.82513188E+01							4
C8H17-2G	5/ 8/ 5	THERMC	8H	17	0	OG	300.000	5000.000	1000.000	71
2.19996000E+01	4.30340167E-02	-1.68526459E-05	2.92459599E-09	-1.87704722E-13						2
-1.23696575E+04	-8.59589823E+01	-8.68364589E-01	9.04897900E-02	-3.89289241E-05						3
-1.17268841E-08	1.15110499E-11	-4.97161588E+03	3.75581633E+01							4
C8H17-2C	5/ 8/ 5	THERMC	8H	17	0	OG	300.000	5000.000	1000.000	71
2.04330909E+01	4.44554724E-02	-1.70697367E-05	2.90885675E-09	-1.83205015E-13						2
-1.31796049E+04	-7.66271355E+01	4.61952764E+00	5.09809948E-02	5.21990082E-05						3
-1.01297228E-07	4.35261525E-11	-6.82867410E+03	1.52619224E+01							4
C8H17-2D	5/ 8/ 5	THERMC	8H	17	0	OG	300.000	5000.000	1000.000	71
2.04330909E+01	4.44554724E-02	-1.70697367E-05	2.90885675E-09	-1.83205015E-13						2
-1.31796049E+04	-7.66271355E+01	4.61952764E+00	5.09809948E-02	5.21990082E-05						3
-1.01297228E-07	4.35261525E-11	-6.82867410E+03	1.52619224E+01							4
C8H17-2E	5/ 8/ 5	THERMC	8H	17	0	OG	300.000	5000.000	1000.000	71
2.04330909E+01	4.44554724E-02	-1.70697367E-05	2.90885675E-09	-1.83205015E-13						2
-1.31796049E+04	-7.66271355E+01	4.61952764E+00	5.09809948E-02	5.21990082E-05						3
-1.01297228E-07	4.35261525E-11	-6.82867410E+03	1.52619224E+01							4
C8H17-2F	5/ 8/ 5	THERMC	8H	17	0	OG	300.000	5000.000	1000.000	71
2.04330909E+01	4.44554724E-02	-1.70697367E-05	2.90885675E-09	-1.83205015E-13						2
-1.31796049E+04	-7.66271355E+01	4.61952764E+00	5.09809948E-02	5.21990082E-05						3
-1.01297228E-07	4.35261525E-11	-6.82867410E+03	1.52619224E+01							4
C8H17-2B	5/ 8/ 5	THERMC	8H	17	0	OG	300.000	5000.000	1000.000	71
1.79458361E+01	4.72492704E-02	-1.77486225E-05	2.97857255E-09	-1.85615609E-13						2
-1.30153243E+04	-6.21599053E+01	5.11666087E+00	4.57821990E-02	5.85990274E-05						3
-1.02148561E-07	4.23870365E-11	-7.77146109E+03	1.41479658E+01							4
C8H16-1-2	5/ 8/ 5	thermH	16C	8	0	Og	300.000	5000.000	1391.000	61
2.42942390E+01	3.55409247E-02	-1.21060032E-05	1.87427516E-09	-1.08530718E-13						2
-2.41421368E+04	-1.01024824E+02	-1.08321803E+00	9.24399869E-02	-6.06179940E-05						3
2.06787399E-08	-2.91728752E-12	-1.50410212E+04	3.61960465E+01							4
C8H16-2-2	5/9/ 5	thermH	16C	8	0	Og	300.000	5000.000	1390.000	61
2.38193041E+01	3.59772998E-02	-1.22634136E-05	1.89952994E-09	-1.10027885E-13						2
-2.54871418E+04	-9.88136938E+01	-6.41567800E-01	8.93020246E-02	-5.59544372E-05						3
1.79652327E-08	-2.35791972E-12	-1.65489479E+04	3.40131577E+01							4
C8H16-3-2	5/10/5	thermH	16C	8	0	Og	300.000	5000.000	1394.000	61
2.38767788E+01	3.61765064E-02	-1.23847165E-05	1.92376372E-09	-1.11647873E-13						2
-2.47852141E+04	-9.97101266E+01	-2.93094454E+00	9.77846785E-02	-6.69422779E-05						3
2.41823763E-08	-3.64732395E-12	-1.53024373E+04	4.47425556E+01							4
C8H16-4-2	5/10/5	thermH	16C	8	0	Og	300.000	5000.000	1392.000	61
2.39175593E+01	3.61853901E-02	-1.23978686E-05	1.92690358E-09	-1.11875817E-13						2
-2.49544972E+04	-1.00001110E+02	-2.85430581E+00	9.72921010E-02	-6.60680343E-05						3
2.36327956E-08	-3.53172870E-12	-1.54359038E+04	4.44185307E+01							4
C8H16-5-2	5/10/5	thermH	16C	8	0	Og	300.000	5000.000	1391.000	61
2.38013945E+01	3.61907786E-02	-1.23796975E-05	1.92202845E-09	-1.11510927E-13						2
-2.49569821E+04	-9.94195299E+01	-1.84180635E+00	9.30484963E-02	-6.02063894E-05						3
2.01810906E-08	-2.79595615E-12	-1.56800350E+04	3.94922145E+01							4
C8H16-6-2	5/11/5	thermH	16C	8	0	Og	300.000	5000.000	1393.000	61
2.42774208E+01	3.57623689E-02	-1.22267721E-05	1.89763691E-09	-1.10070078E-13						2
-2.36141529E+04	-1.01643888E+02	-2.36563988E+00	9.65215499E-02	-6.53224689E-05						3
2.31537549E-08	-3.40888793E-12	-1.41589879E+04	4.20613726E+01							4
C8H17O-1-2	5/24/5	thermC	8H	17O	1	Og	300.000	5000.000	1390.000	81
2.74811848E+01	3.75744020E-02	-1.29161783E-05	2.01202962E-09	-1.17007752E-13						2
-3.20795559E+04	-1.15742919E+02	-1.32517927E+00	1.02067227E-01	-6.78362870E-05						3
2.32912073E-08	-3.29828280E-12	-2.17345686E+04	4.00606608E+01							4

C8H17O-2-2	5/24/5	thermC	8H	17O	1	0g	300.000	5000.000	1391.000	81
2.81549772e+01	3.70804138e-02	-1.27622778e-05	1.98966012e-09	-1.15770090e-13						2
-3.56420078e+04	-1.20909218e+02	-1.40755987e+00	1.05669541e-01	-7.43774728e-05						3
2.76076622e-08	-4.27631781e-12	-2.52426405e+04	3.81705249e+01							4
C8H17O-3-2	5/24/5	thermC	8H	17O	1	0g	300.000	5000.000	1392.000	81
2.81162098e+01	3.72856173e-02	-1.28708561e-05	2.01051889e-09	-1.17142050e-13						2
-3.45081038e+04	-1.20396348e+02	-2.16653642e+00	1.07739651e-01	-7.64424806e-05						3
2.85978776e-08	-4.46409575e-12	-2.38690364e+04	4.24995699e+01							4
C8H17O-4-2	5/24/5	thermC	8H	17O	1	0g	300.000	5000.000	1392.000	81
2.81162098e+01	3.72856173e-02	-1.28708561e-05	2.01051889e-09	-1.17142050e-13						2
-3.45081038e+04	-1.20396348e+02	-2.16653642e+00	1.07739651e-01	-7.64424806e-05						3
2.85978776e-08	-4.46409575e-12	-2.38690364e+04	4.24995699e+01							4
C8H17O-5-2	5/24/5	thermC	8H	17O	1	0g	300.000	5000.000	1392.000	81
2.81162098e+01	3.72856173e-02	-1.28708561e-05	2.01051889e-09	-1.17142050e-13						2
-3.45081038e+04	-1.20396348e+02	-2.16653642e+00	1.07739651e-01	-7.64424806e-05						3
2.85978776e-08	-4.46409575e-12	-2.38690364e+04	4.24995699e+01							4
C8H17O-6-2	5/24/5	thermC	8H	17O	1	0g	300.000	5000.000	1392.000	81
2.81162098e+01	3.72856173e-02	-1.28708561e-05	2.01051889e-09	-1.17142050e-13						2
-3.45081038e+04	-1.20396348e+02	-2.16653642e+00	1.07739651e-01	-7.64424806e-05						3
2.85978776e-08	-4.46409575e-12	-2.38690364e+04	4.24995699e+01							4
C8H17O-7-2	5/24/5	thermC	8H	17O	1	0g	300.000	5000.000	1390.000	81
2.74811848e+01	3.75744020e-02	-1.29161783e-05	2.01202962e-09	-1.17007752e-13						2
-3.20795559e+04	-1.15742919e+02	-1.32517927e+00	1.02067227e-01	-6.78362870e-05						3
2.32912073e-08	-3.29828280e-12	-2.17345686e+04	4.00606608e+01							4
C8H17OOH-1-2	5/5	THERMC	8H	18O	2	0G	300.000	5000.000	1000.000	81
2.93145063E+01	4.08721880E-02	-1.43972726E-05	2.37257600E-09	-1.47448109E-13						2
-4.90982652E+04	-1.20859995E+02	1.23384042E+00	9.49746640E-02	-2.41018587E-05						3
-3.76866917E-08	2.30820499E-11	-3.99342183E+04	3.14480056E+01							4
C8H17OO-1-2		000000H	17O	2C	8	0G	300.000	5000.000	1000.00	1
2.70940088E+01	4.34288275E-02	-1.70931978E-05	2.96363344E-09	-1.88911463E-13						2
-3.17039958E+04	-1.08699166E+02	4.05492696E-01	1.01282264E-01	-5.15643374E-05						3
-3.91832379E-09	9.40637869E-12	-2.30917386E+04	3.49947215E+01							4
C8H17OOH-2-2	5/5	THERMC	8H	18O	2	0G	300.000	5000.000	1000.000	81
2.80693889E+01	4.49665375E-02	-1.76720724E-05	3.06080884E-09	-1.94964195E-13						2
-5.18799712E+04	-1.16215609E+02	-8.35430133E-01	1.16983726E-01	-8.90035192E-05						3
3.79130976E-08	-7.54906726E-12	-4.29018264E+04	3.73929074E+01							4
C8H17OO-2-2	5/5	THERMC	8H	17O	2	0G	300.000	5000.000	1000.000	81
2.66563074E+01	4.40328267E-02	-1.71986037E-05	2.96597717E-09	-1.88356997E-13						2
-3.40101798E+04	-1.07467992E+02	-1.66295194E+00	1.23354901E-01	-1.16482131E-04						3
7.16562390E-08	-2.12092879E-11	-2.56596165E+04	4.09168721E+01							4
C8H17OOH-3-2	5/5	THERMC	8H	18O	2	0G	300.000	5000.000	1000.000	81
3.01763987E+01	4.16677262E-02	-1.66497134E-05	2.91741316E-09	-1.87341280E-13						2
-5.16272262E+04	-1.28084301E+02	5.79624699E+00	6.53641531E-02	5.33719165E-05						3
-1.24236105E-07	5.71572360E-11	-4.21284644E+04	9.71215644E+00							4
C8H17OO-3-2		000000H	17O	2C	8	0G	300.000	5000.000	1000.00	1
2.92337516E+01	4.03886008E-02	-1.60969805E-05	2.81546952E-09	-1.80567010E-13						2
-3.40390050E+04	-1.22244977E+02	4.96872519E+00	7.17353280E-02	2.58933044E-05						3
-9.04929638E-08	4.34970154E-11	-2.52888715E+04	1.32785693E+01							4
C8H17OOH-4-2	5/5	THERMC	8H	18O	2	0G	300.000	5000.000	1000.000	81
3.01763987E+01	4.16677262E-02	-1.66497134E-05	2.91741316E-09	-1.87341280E-13						2
-5.15768086E+04	-1.28084301E+02	5.79624699E+00	6.53641531E-02	5.33719165E-05						3
-1.24236105E-07	5.71572360E-11	-4.25310814E+04	9.71215644E+00							4
C8H17OO-4-2		000000H	17O	2C	8	0G	300.000	5000.000	1000.00	1
2.92337516E+01	4.03886008E-02	-1.60969805E-05	2.81546952E-09	-1.80567010E-13						2
-3.44416220E+04	-1.22244977E+02	4.96872519E+00	7.17353280E-02	2.58933044E-05						3
-9.04929638E-08	4.34970154E-11	-2.56914885E+04	1.32785693E+01							4
C8H17OOH-5-2	5/5	THERMC	8H	18O	2	0G	300.000	5000.000	1000.000	81
3.01763987E+01	4.16677262E-02	-1.66497134E-05	2.91741316E-09	-1.87341280E-13						2
-5.15768086E+04	-1.28084301E+02	5.79624699E+00	6.53641531E-02	5.33719165E-05						3
-1.24236105E-07	5.71572360E-11	-4.25310814E+04	9.71215644E+00							4
C8H17OO-5-2		000000H	17O	2C	8	0G	300.000	5000.000	1000.00	1
2.92337516E+01	4.03886008E-02	-1.60969805E-05	2.81546952E-09	-1.80567010E-13						2
-3.44416220E+04	-1.22244977E+02	4.96872519E+00	7.17353280E-02	2.58933044E-05						3
-9.04929638E-08	4.34970154E-11	-2.56914885E+04	1.32785693E+01							4
C8H17OOH-6-2	5/5	THERMC	8H	18O	2	0G	300.000	5000.000	1000.000	81
3.01763987E+01	4.16677262E-02	-1.66497134E-05	2.91741316E-09	-1.87341280E-13						2
-5.15768086E+04	-1.28084301E+02	5.79624699E+00	6.53641531E-02	5.33719165E-05						3

-1.24236105E-07	5.71572360E-11	-4.25310814E+04	9.71215644E+00	4	
C8H17OO-6-2	000000H	17O 2C 8 OG	300.000 5000.000 1000.00	1	
2.92337516E+01	4.03886008E-02	-1.60969805E-05	2.81546952E-09	-1.80567010E-13	2
-3.44416220E+04	-1.22244977E+02	4.96872519E+00	7.17353280E-02	2.58933044E-05	3
-9.04929638E-08	4.34970154E-11	-2.56914885E+04	1.32785693E+01		4
C8H17OOH-7-2	5/5 THERMC	8H 18O 2 OG	300.000 5000.000 1000.000	81	
2.93145063E+01	4.08721880E-02	-1.43972726E-05	2.37257600E-09	-1.47448109E-13	2
-4.90982652E+04	-1.21553142E+02	1.23384042E+00	9.49746640E-02	-2.41018587E-05	3
-3.76866917E-08	2.30820499E-11	-3.99342183E+04	3.07548585E+01		4
C8H17OO-7-2	000000H	17O 2C 8 OG	300.000 5000.000 1000.00	1	
2.70940088E+01	4.34288275E-02	-1.70931978E-05	2.96363344E-09	-1.88911463E-13	2
-3.17039958E+04	-1.09392312E+02	4.05492696E-01	1.01282264E-01	-5.15643374E-05	3
-3.91832379E-09	9.40637869E-12	-2.30917386E+04	3.43015743E+01		4
C8OOH1-2A	5/25/ 5 THERMC	8H 17O 2 OG	300.000 5000.000 1000.000	81	
2.88188264E+01	3.86542728E-02	-1.35822607E-05	2.23573839E-09	-1.38861917E-13	2
-2.40158665E+04	-1.14693628E+02	9.76281223E-01	9.61443507E-02	-3.49588066E-05	3
-2.47247811E-08	1.81059231E-11	-1.51513060E+04	3.53064289E+01		4
C8OOH1-2B	5/25/ 5 THERMC	8H 17O 2 OG	300.000 5000.000 1000.000	81	
2.70082462E+01	4.06837003E-02	-1.46740200E-05	2.44647690E-09	-1.53024884E-13	2
-2.62246374E+04	-1.05586155E+02	6.96130686E+00	5.14367583E-02	6.25691489E-05	3
-1.15146463E-07	4.89819118E-11	-1.81765721E+04	1.04706189E+01		4
C8OOH1-2C	5/25/ 5 THERMC	8H 17O 2 OG	300.000 5000.000 1000.000	81	
2.87284112E+01	3.86668797E-02	-1.40017922E-05	2.34042927E-09	-1.46642191E-13	2
-2.55548766E+04	-1.14815197E+02	6.46417345E+00	5.66355555E-02	5.61691257E-05	3
-1.14295125E-07	5.01210257E-11	-1.70083642E+04	1.22780202E+01		4
C8OOH1-2D	5/25/ 5 THERMC	8H 17O 2 OG	300.000 5000.000 1000.000	81	
2.87284112E+01	3.86668797E-02	-1.40017922E-05	2.34042927E-09	-1.46642191E-13	2
-2.55548766E+04	-1.14815197E+02	6.46417345E+00	5.66355555E-02	5.61691257E-05	3
-1.14295125E-07	5.01210257E-11	-1.70083642E+04	1.22780202E+01		4
C8OOH1-2E	5/25/ 5 THERMC	8H 17O 2 OG	300.000 5000.000 1000.000	81	
2.87284112E+01	3.86668797E-02	-1.40017922E-05	2.34042927E-09	-1.46642191E-13	2
-2.55548766E+04	-1.14815197E+02	6.46417345E+00	5.66355555E-02	5.61691257E-05	3
-1.14295125E-07	5.01210257E-11	-1.70083642E+04	1.22780202E+01		4
C8OOH2-2A	000000H	17O 2C 8 OG	300.000 5000.000 1000.00	1	
2.78013679E+01	4.24269175E-02	-1.67234137E-05	2.90250075E-09	-1.85147175E-13	2
-2.69038440E+04	-1.11359795E+02	-1.09281795E+00	1.18152638E-01	-9.98532190E-05	3
5.08663524E-08	-1.25218710E-11	-1.81189792E+04	4.12503331E+01		4
C8OOH2-2C	000000H	17O 2C 8 OG	300.000 5000.000 1000.00	1	
2.56722256E+01	4.45109027E-02	-1.73009455E-05	2.97350029E-09	-1.88388752E-13	2
-2.73738096E+04	-9.93746950E+01	4.39140113E+00	7.86702863E-02	-8.78627944E-06	3
-3.86440415E-08	1.94718042E-11	-1.99756871E+04	1.82371919E+01		4
C8OOH2-2D	000000H	17O 2C 8 OG	300.000 5000.000 1000.00	1	
2.56722256E+01	4.45109027E-02	-1.73009455E-05	2.97350029E-09	-1.88388752E-13	2
-2.73738096E+04	-9.93746950E+01	4.39140113E+00	7.86702863E-02	-8.78627944E-06	3
-3.86440415E-08	1.94718042E-11	-1.99756871E+04	1.82371919E+01		4
C8OOH2-2E	000000H	17O 2C 8 OG	300.000 5000.000 1000.00	1	
2.56722256E+01	4.45109027E-02	-1.73009455E-05	2.97350029E-09	-1.88388752E-13	2
-2.73738096E+04	-9.93746950E+01	4.39140113E+00	7.86702863E-02	-8.78627944E-06	3
-3.86440415E-08	1.94718042E-11	-1.99756871E+04	1.82371919E+01		4
C8OOH2-2F	000000H	17O 2C 8 OG	300.000 5000.000 1000.00	1	
2.56722256E+01	4.45109027E-02	-1.73009455E-05	2.97350029E-09	-1.88388752E-13	2
-2.73738096E+04	-9.93746950E+01	4.39140113E+00	7.86702863E-02	-8.78627944E-06	3
-3.86440415E-08	1.94718042E-11	-1.99756871E+04	1.82371919E+01		4
C8OOH3-2A	5/25/ 5 THERMC	8H 17O 2 OG	300.000 5000.000 1000.000	81	
3.09304261E+01	3.59358707E-02	-1.29404780E-05	2.15818424E-09	-1.35084694E-13	2
-2.57155976E+04	-1.27569419E+02	5.54256975E+00	6.65776270E-02	4.25507088E-05	3
-1.11357402E-07	5.22193912E-11	-1.66824007E+04	1.42276248E+01		4
C8OOH3-2B	5/25/ 5 THERMC	8H 17O 2 OG	300.000 5000.000 1000.000	81	
2.91769766E+01	3.77135179E-02	-1.38527230E-05	2.33324313E-09	-1.46850681E-13	2
-2.76718591E+04	-1.18673310E+02	1.15275958E+01	2.18700313E-02	1.40078672E-04	3
-2.01779092E-07	8.30953829E-11	-1.94742869E+04	-1.06081870E+01		4
C8OOH3-2D	5/25/ 5 THERMC	8H 17O 2 OG	300.000 5000.000 1000.000	81	
3.09002727E+01	3.56793537E-02	-1.31675687E-05	2.22435670E-09	-1.40263575E-13	2
-2.72250389E+04	-1.28604638E+02	1.10304625E+01	2.70688283E-02	1.33678650E-04	3
-2.00927754E-07	8.42344971E-11	-1.85314998E+04	-9.49393308E+00		4
C8OOH3-2E	5/25/ 5 THERMC	8H 17O 2 OG	300.000 5000.000 1000.000	81	
3.09002727E+01	3.56793537E-02	-1.31675687E-05	2.22435670E-09	-1.40263575E-13	2

-2.72250389E+04-1.28604638E+02 1.10304625E+01 2.70688283E-02 1.33678650E-04 3
-2.00927754E-07 8.42344971E-11-1.85314998E+04-9.49393308E+00 4
C80OH3-2F 5/25/ 5 THERMC 8H 170 2 OG 300.000 5000.000 1000.000 81
3.09002727E+01 3.56793537E-02-1.31675687E-05 2.22435670E-09-1.40263575E-13 2
-2.72250389E+04-1.28604638E+02 1.10304625E+01 2.70688283E-02 1.33678650E-04 3
-2.00927754E-07 8.42344971E-11-1.85314998E+04-9.49393308E+00 4
C80OH3-2G 5/25/ 5 THERMC 8H 170 2 OG 300.000 5000.000 1000.000 81
3.09304261E+01 3.59358707E-02-1.29404780E-05 2.15818424E-09-1.35084694E-13 2
-2.57155976E+04-1.28254054E+02 5.54256975E+00 6.65776270E-02 4.25507088E-05 3
-1.11357402E-07 5.22193912E-11-1.66824007E+04 1.35344776E+01 4
C80OH4-2A 5/25/ 5 THERMC 8H 170 2 OG 300.000 5000.000 1000.000 81
3.09304261E+01 3.59358707E-02-1.29404780E-05 2.15818424E-09-1.35084694E-13 2
-2.57155976E+04-1.27569419E+02 5.54256975E+00 6.65776270E-02 4.25507088E-05 3
-1.11357402E-07 5.22193912E-11-1.66824007E+04 1.42276248E+01 4
C80OH4-2B 5/25/ 5 THERMC 8H 170 2 OG 300.000 5000.000 1000.000 81
2.91769766E+01 3.77135179E-02-1.38527230E-05 2.33324313E-09-1.46850681E-13 2
-2.78882658E+04-1.18673310E+02 1.15275958E+01 2.18700313E-02 1.40078672E-04 3
-2.01779092E-07 8.30953829E-11-1.96906935E+04-1.06081870E+01 4
C80OH4-2C 5/25/ 5 THERMC 8H 170 2 OG 300.000 5000.000 1000.000 81
3.09002727E+01 3.56793537E-02-1.31675687E-05 2.22435670E-09-1.40263575E-13 2
-2.74414455E+04-1.28604638E+02 1.10304625E+01 2.70688283E-02 1.33678650E-04 3
-2.00927754E-07 8.42344971E-11-1.87479065E+04-9.49393308E+00 4
C80OH4-2E 5/25/ 5 THERMC 8H 170 2 OG 300.000 5000.000 1000.000 81
3.09002727E+01 3.56793537E-02-1.31675687E-05 2.22435670E-09-1.40263575E-13 2
-2.74414455E+04-1.28604638E+02 1.10304625E+01 2.70688283E-02 1.33678650E-04 3
-2.00927754E-07 8.42344971E-11-1.87479065E+04-9.49393308E+00 4
C80OH4-2F 5/25/ 5 THERMC 8H 170 2 OG 300.000 5000.000 1000.000 81
3.09002727E+01 3.56793537E-02-1.31675687E-05 2.22435670E-09-1.40263575E-13 2
-2.74414455E+04-1.28604638E+02 1.10304625E+01 2.70688283E-02 1.33678650E-04 3
-2.00927754E-07 8.42344971E-11-1.87479065E+04-9.49393308E+00 4
C80OH4-2G 5/25/ 5 THERMC 8H 170 2 OG 300.000 5000.000 1000.000 81
3.09304261E+01 3.59358707E-02-1.29404780E-05 2.15818424E-09-1.35084694E-13 2
-2.57155976E+04-1.28254054E+02 5.54256975E+00 6.65776270E-02 4.25507088E-05 3
-1.11357402E-07 5.22193912E-11-1.66824007E+04 1.35344776E+01 4
C80OH5-2A 5/25/ 5 THERMC 8H 170 2 OG 300.000 5000.000 1000.000 81
3.09304261E+01 3.59358707E-02-1.29404780E-05 2.15818424E-09-1.35084694E-13 2
-2.57155976E+04-1.27569419E+02 5.54256975E+00 6.65776270E-02 4.25507088E-05 3
-1.11357402E-07 5.22193912E-11-1.66824007E+04 1.42276248E+01 4
C80OH5-2B 5/25/ 5 THERMC 8H 170 2 OG 300.000 5000.000 1000.000 81
2.91769766E+01 3.77135179E-02-1.38527230E-05 2.33324313E-09-1.46850681E-13 2
-2.78882658E+04-1.18673310E+02 1.15275958E+01 2.18700313E-02 1.40078672E-04 3
-2.01779092E-07 8.30953829E-11-1.96906935E+04-1.06081870E+01 4
C80OH5-2C 5/25/ 5 THERMC 8H 170 2 OG 300.000 5000.000 1000.000 81
3.09002727E+01 3.56793537E-02-1.31675687E-05 2.22435670E-09-1.40263575E-13 2
-2.74414455E+04-1.28604638E+02 1.10304625E+01 2.70688283E-02 1.33678650E-04 3
-2.00927754E-07 8.42344971E-11-1.87479065E+04-9.49393308E+00 4
C80OH5-2D 5/25/ 5 THERMC 8H 170 2 OG 300.000 5000.000 1000.000 81
3.09002727E+01 3.56793537E-02-1.31675687E-05 2.22435670E-09-1.40263575E-13 2
-2.74414455E+04-1.28604638E+02 1.10304625E+01 2.70688283E-02 1.33678650E-04 3
-2.00927754E-07 8.42344971E-11-1.87479065E+04-9.49393308E+00 4
C80OH5-2F 5/25/ 5 THERMC 8H 170 2 OG 300.000 5000.000 1000.000 81
3.09002727E+01 3.56793537E-02-1.31675687E-05 2.22435670E-09-1.40263575E-13 2
-2.74414455E+04-1.28604638E+02 1.10304625E+01 2.70688283E-02 1.33678650E-04 3
-2.00927754E-07 8.42344971E-11-1.87479065E+04-9.49393308E+00 4
C80OH5-2G 5/25/ 5 THERMC 8H 170 2 OG 300.000 5000.000 1000.000 81
3.09304261E+01 3.59358707E-02-1.29404780E-05 2.15818424E-09-1.35084694E-13 2
-2.57155976E+04-1.28254054E+02 5.54256975E+00 6.65776270E-02 4.25507088E-05 3
-1.11357402E-07 5.22193912E-11-1.66824007E+04 1.35344776E+01 4
C80OH6-2B 5/25/ 5 THERMC 8H 170 2 OG 300.000 5000.000 1000.000 81
2.91769766E+01 3.77135179E-02-1.38527230E-05 2.33324313E-09-1.46850681E-13 2
-2.78882658E+04-1.18673310E+02 1.15275958E+01 2.18700313E-02 1.40078672E-04 3
-2.01779092E-07 8.30953829E-11-1.96906935E+04-1.06081870E+01 4
C80OH6-2C 5/25/ 5 THERMC 8H 170 2 OG 300.000 5000.000 1000.000 81
3.09002727E+01 3.56793537E-02-1.31675687E-05 2.22435670E-09-1.40263575E-13 2
-2.74414455E+04-1.28604638E+02 1.10304625E+01 2.70688283E-02 1.33678650E-04 3
-2.00927754E-07 8.42344971E-11-1.87479065E+04-9.49393308E+00 4
C80OH6-2D 5/25/ 5 THERMC 8H 170 2 OG 300.000 5000.000 1000.000 81

3.09002727E+01 3.56793537E-02-1.31675687E-05 2.22435670E-09-1.40263575E-13 2
-2.74414455E+04-1.28604638E+02 1.10304625E+01 2.70688283E-02 1.33678650E-04 3
-2.00927754E-07 8.42344971E-11-1.87479065E+04-9.49393308E+00 4
C800H6-2E 5/25/ 5 THERMC 8H 170 2 0G 300.000 5000.000 1000.000 81
3.09002727E+01 3.56793537E-02-1.31675687E-05 2.22435670E-09-1.40263575E-13 2
-2.74414455E+04-1.28604638E+02 1.10304625E+01 2.70688283E-02 1.33678650E-04 3
-2.00927754E-07 8.42344971E-11-1.87479065E+04-9.49393308E+00 4
C800H6-2G 5/25/ 5 THERMC 8H 170 2 0G 300.000 5000.000 1000.000 81
3.09304261E+01 3.59358707E-02-1.29404780E-05 2.15818424E-09-1.35084694E-13 2
-2.57155976E+04-1.28254054E+02 5.54256975E+00 6.65776270E-02 4.25507088E-05 3
-1.11357402E-07 5.22193912E-11-1.66824007E+04 1.35344776E+01 4
!
C800H7-2C 5/25/ 5 THERMC 8H 170 2 0G 300.000 5000.000 1000.000 81
2.87284112E+01 3.86668797E-02-1.40017922E-05 2.34042927E-09-1.46642191E-13 2
-2.55548766E+04-1.15508345E+02 6.46417345E+00 5.66355555E-02 5.61691257E-05 3
-1.14295125E-07 5.01210257E-11-1.70083642E+04 1.15848730E+01 4
C800H7-2D 5/25/ 5 THERMC 8H 170 2 0G 300.000 5000.000 1000.000 81
2.87284112E+01 3.86668797E-02-1.40017922E-05 2.34042927E-09-1.46642191E-13 2
-2.55548766E+04-1.15508345E+02 6.46417345E+00 5.66355555E-02 5.61691257E-05 3
-1.14295125E-07 5.01210257E-11-1.70083642E+04 1.15848730E+01 4
C800H7-2E 5/25/ 5 THERMC 8H 170 2 0G 300.000 5000.000 1000.000 81
2.87284112E+01 3.86668797E-02-1.40017922E-05 2.34042927E-09-1.46642191E-13 2
-2.55548766E+04-1.15508345E+02 6.46417345E+00 5.66355555E-02 5.61691257E-05 3
-1.14295125E-07 5.01210257E-11-1.70083642E+04 1.15848730E+01 4
C800H7-2F 5/25/ 5 THERMC 8H 170 2 0G 300.000 5000.000 1000.000 81
2.87284112E+01 3.86668797E-02-1.40017922E-05 2.34042927E-09-1.46642191E-13 2
-2.55548766E+04-1.15508345E+02 6.46417345E+00 5.66355555E-02 5.61691257E-05 3
-1.14295125E-07 5.01210257E-11-1.70083642E+04 1.15848730E+01 4
C800H1-001-2 5/5 THERMC 8H 170 4 0G 300.000 5000.000 1000.000 91
3.28101930E+01 4.28052776E-02-1.71042595E-05 2.99706010E-09-1.92455797E-13 2
-4.32585422E+04-1.33729879E+02 2.24890356E+00 1.06933041E-01-4.75968801E-05 3
-1.69075175E-08 1.59968364E-11-3.33257332E+04 3.11815108E+01 4
C800H1-002-2 5/5 THERMC 8H 170 4 0G 300.000 5000.000 1000.000 91
3.25979584E+01 4.32668330E-02-1.71984291E-05 3.00254267E-09-1.92315465E-13 2
-4.61315628E+04-1.33234432E+02 1.80458566E-01 1.29005681E-01-1.12514681E-04 3
5.86670529E-08-1.46188330E-11-3.62971587E+04 3.77936984E+01 4
C800H2-001-2 5/5 THERMC 8H 170 4 0G 300.000 5000.000 1000.000 91
3.25979584E+01 4.32668330E-02-1.71984291E-05 3.00254267E-09-1.92315465E-13 2
-4.61315628E+04-1.33234432E+02 1.80458566E-01 1.29005681E-01-1.12514681E-04 3
5.86670529E-08-1.46188330E-11-3.62971587E+04 3.77936984E+01 4
C800H1-003-2 5/5 THERMC 8H 170 4 0G 300.000 5000.000 1000.000 91
3.46582619E+01 3.99800875E-02-1.61305824E-05 2.84565038E-09-1.83599832E-13 2
-4.57993786E+04-1.44810959E+02 6.81213557E+00 7.73861083E-02 2.98607529E-05 3
-1.03482148E-07 5.00874698E-11-3.59266144E+04 1.01122768E+01 4
C800H3-001-2 5/5 THERMC 8H 170 4 0G 300.000 5000.000 1000.000 91
3.46582619E+01 3.99800875E-02-1.61305824E-05 2.84565038E-09-1.83599832E-13 2
-4.57993786E+04-1.44810959E+02 6.81213557E+00 7.73861083E-02 2.98607529E-05 3
-1.03482148E-07 5.00874698E-11-3.59266144E+04 1.01122768E+01 4
C800H1-004-2 5/5 THERMC 8H 170 4 0G 300.000 5000.000 1000.000 91
3.46582619E+01 3.99800875E-02-1.61305824E-05 2.84565038E-09-1.83599832E-13 2
-4.57993786E+04-1.44810959E+02 6.81213557E+00 7.73861083E-02 2.98607529E-05 3
-1.03482148E-07 5.00874698E-11-3.59266144E+04 1.01122768E+01 4
C800H4-001-2 5/5 THERMC 8H 170 4 0G 300.000 5000.000 1000.000 91
3.46582619E+01 3.99800875E-02-1.61305824E-05 2.84565038E-09-1.83599832E-13 2
-4.57993786E+04-1.44810959E+02 6.81213557E+00 7.73861083E-02 2.98607529E-05 3
-1.03482148E-07 5.00874698E-11-3.59266144E+04 1.01122768E+01 4
C800H1-005-2 5/5 THERMC 8H 170 4 0G 300.000 5000.000 1000.000 91
3.46582619E+01 3.99800875E-02-1.61305824E-05 2.84565038E-09-1.83599832E-13 2
-4.57993786E+04-1.44810959E+02 6.81213557E+00 7.73861083E-02 2.98607529E-05 3
-1.03482148E-07 5.00874698E-11-3.59266144E+04 1.01122768E+01 4
C800H5-001-2 5/5 THERMC 8H 170 4 0G 300.000 5000.000 1000.000 91
3.46582619E+01 3.99800875E-02-1.61305824E-05 2.84565038E-09-1.83599832E-13 2
-4.57993786E+04-1.44810959E+02 6.81213557E+00 7.73861083E-02 2.98607529E-05 3
-1.03482148E-07 5.00874698E-11-3.59266144E+04 1.01122768E+01 4
C800H3-007-2 5/5 THERMC 8H 170 4 0G 300.000 5000.000 1000.000 91
3.46582619E+01 3.99800875E-02-1.61305824E-05 2.84565038E-09-1.83599832E-13 2
-4.57993786E+04-1.45504105E+02 6.81213557E+00 7.73861083E-02 2.98607529E-05 3

-1.03482148E-07	5.00874698E-11	-3.59266144E+04	9.41912965E+00	4	
C80OH7-003-2	5/5 THERMC	8H 170 4 OG	300.000 5000.000 1000.000	91	
3.46582619E+01	3.99800875E-02	-1.61305824E-05	2.84565038E-09	-1.83599832E-13	2
-4.57993786E+04	-1.45504105E+02	6.81213557E+00	7.73861083E-02	2.98607529E-05	3
-1.03482148E-07	5.00874698E-11	-3.59266144E+04	9.41912965E+00	4	
C80OH4-007-2	5/5 THERMC	8H 170 4 OG	300.000 5000.000 1000.000	91	
3.46582619E+01	3.99800875E-02	-1.61305824E-05	2.84565038E-09	-1.83599832E-13	2
-4.57993786E+04	-1.45504105E+02	6.81213557E+00	7.73861083E-02	2.98607529E-05	3
-1.03482148E-07	5.00874698E-11	-3.59266144E+04	9.41912965E+00	4	
C80OH7-004-2	5/5 THERMC	8H 170 4 OG	300.000 5000.000 1000.000	91	
3.46582619E+01	3.99800875E-02	-1.61305824E-05	2.84565038E-09	-1.83599832E-13	2
-4.57993786E+04	-1.45504105E+02	6.81213557E+00	7.73861083E-02	2.98607529E-05	3
-1.03482148E-07	5.00874698E-11	-3.59266144E+04	9.41912965E+00	4	
C80OH5-007-2	5/5 THERMC	8H 170 4 OG	300.000 5000.000 1000.000	91	
3.46582619E+01	3.99800875E-02	-1.61305824E-05	2.84565038E-09	-1.83599832E-13	2
-4.57993786E+04	-1.45504105E+02	6.81213557E+00	7.73861083E-02	2.98607529E-05	3
-1.03482148E-07	5.00874698E-11	-3.59266144E+04	9.41912965E+00	4	
C80OH7-005-2	5/5 THERMC	8H 170 4 OG	300.000 5000.000 1000.000	91	
3.46582619E+01	3.99800875E-02	-1.61305824E-05	2.84565038E-09	-1.83599832E-13	2
-4.57993786E+04	-1.45504105E+02	6.81213557E+00	7.73861083E-02	2.98607529E-05	3
-1.03482148E-07	5.00874698E-11	-3.59266144E+04	9.41912965E+00	4	
C80OH6-007-2	5/5 THERMC	8H 170 4 OG	300.000 5000.000 1000.000	91	
3.46582619E+01	3.99800875E-02	-1.61305824E-05	2.84565038E-09	-1.83599832E-13	2
-4.57993786E+04	-1.45504105E+02	6.81213557E+00	7.73861083E-02	2.98607529E-05	3
-1.03482148E-07	5.00874698E-11	-3.59266144E+04	9.41912965E+00	4	
C80OH7-006-2	5/5 THERMC	8H 170 4 OG	300.000 5000.000 1000.000	91	
3.46582619E+01	3.99800875E-02	-1.61305824E-05	2.84565038E-09	-1.83599832E-13	2
-4.57993786E+04	-1.45504105E+02	6.81213557E+00	7.73861083E-02	2.98607529E-05	3
-1.03482148E-07	5.00874698E-11	-3.59266144E+04	9.41912965E+00	4	
C80OH2-003-2	5/5 THERMC	8H 170 4 OG	300.000 5000.000 1000.000	91	
3.44587452E+01	4.04352624E-02	-1.62376140E-05	2.85510432E-09	-1.83785639E-13	2
-4.84618422E+04	-1.45084534E+02	4.74369107E+00	9.94587442E-02	-3.50570383E-05	3
-2.79075890E-08	1.94718045E-11	-3.86816333E+04	1.60313152E+01	4	
C80OH3-002-2	5/5 THERMC	8H 170 4 OG	300.000 5000.000 1000.000	91	
3.44587452E+01	4.04352624E-02	-1.62376140E-05	2.85510432E-09	-1.83785639E-13	2
-4.84618422E+04	-1.45084534E+02	4.74369107E+00	9.94587442E-02	-3.50570383E-05	3
-2.79075890E-08	1.94718045E-11	-3.86816333E+04	1.60313152E+01	4	
C80OH2-004-2	5/5 THERMC	8H 170 4 OG	300.000 5000.000 1000.000	91	
3.44587452E+01	4.04352624E-02	-1.62376140E-05	2.85510432E-09	-1.83785639E-13	2
-4.86782489E+04	-1.45084534E+02	4.74369107E+00	9.94587442E-02	-3.50570383E-05	3
-2.79075890E-08	1.94718045E-11	-3.88980399E+04	1.60313152E+01	4	
C80OH4-002-2	5/5 THERMC	8H 170 4 OG	300.000 5000.000 1000.000	91	
3.44587452E+01	4.04352624E-02	-1.62376140E-05	2.85510432E-09	-1.83785639E-13	2
-4.86782489E+04	-1.45084534E+02	4.74369107E+00	9.94587442E-02	-3.50570383E-05	3
-2.79075890E-08	1.94718045E-11	-3.88980399E+04	1.60313152E+01	4	
C80OH2-005-2	5/5 THERMC	8H 170 4 OG	300.000 5000.000 1000.000	91	
3.44587452E+01	4.04352624E-02	-1.62376140E-05	2.85510432E-09	-1.83785639E-13	2
-4.86782489E+04	-1.45084534E+02	4.74369107E+00	9.94587442E-02	-3.50570383E-05	3
-2.79075890E-08	1.94718045E-11	-3.88980399E+04	1.60313152E+01	4	
C80OH5-002-2	5/5 THERMC	8H 170 4 OG	300.000 5000.000 1000.000	91	
3.44587452E+01	4.04352624E-02	-1.62376140E-05	2.85510432E-09	-1.83785639E-13	2
-4.86782489E+04	-1.45084534E+02	4.74369107E+00	9.94587442E-02	-3.50570383E-05	3
-2.79075890E-08	1.94718045E-11	-3.88980399E+04	1.60313152E+01	4	
C80OH2-006-2	5/5 THERMC	8H 170 4 OG	300.000 5000.000 1000.000	91	
3.44587452E+01	4.04352624E-02	-1.62376140E-05	2.85510432E-09	-1.83785639E-13	2
-4.86782489E+04	-1.45084534E+02	4.74369107E+00	9.94587442E-02	-3.50570383E-05	3
-2.79075890E-08	1.94718045E-11	-3.88980399E+04	1.60313152E+01	4	
C80OH6-002-2	5/5 THERMC	8H 170 4 OG	300.000 5000.000 1000.000	91	
3.44587452E+01	4.04352624E-02	-1.62376140E-05	2.85510432E-09	-1.83785639E-13	2
-4.86782489E+04	-1.45084534E+02	4.74369107E+00	9.94587442E-02	-3.50570383E-05	3
-2.79075890E-08	1.94718045E-11	-3.88980399E+04	1.60313152E+01	4	
C80OH3-004-2	5/5 THERMC	8H 170 4 OG	300.000 5000.000 1000.000	91	
3.66587544E+01	3.70169165E-02	-1.50812571E-05	2.67876126E-09	-1.73660298E-13	2
-4.84485502E+04	-1.57536162E+02	1.13753682E+01	4.78391710E-02	1.07318397E-04	3
-1.90056792E-07	8.41781077E-11	-3.85274957E+04	-1.16501069E+01	4	
C80OH4-003-2	5/5 THERMC	8H 170 4 OG	300.000 5000.000 1000.000	91	
3.66587544E+01	3.70169165E-02	-1.50812571E-05	2.67876126E-09	-1.73660298E-13	2

-4.84485502E+04-1.57536162E+02 1.13753682E+01 4.78391710E-02 1.07318397E-04	3
-1.90056792E-07 8.41781077E-11-3.85274957E+04-1.16501069E+01	4
C80OH3-005-2 5/5 THERMC 8H 170 4 OG 300.000 5000.000 1000.000	91
3.66587544E+01 3.70169165E-02-1.50812571E-05 2.67876126E-09-1.73660298E-13	2
-4.84485502E+04-1.57536162E+02 1.13753682E+01 4.78391710E-02 1.07318397E-04	3
-1.90056792E-07 8.41781077E-11-3.85274957E+04-1.16501069E+01	4
C80OH5-003-2 5/5 THERMC 8H 170 4 OG 300.000 5000.000 1000.000	91
3.66587544E+01 3.70169165E-02-1.50812571E-05 2.67876126E-09-1.73660298E-13	2
-4.84485502E+04-1.57536162E+02 1.13753682E+01 4.78391710E-02 1.07318397E-04	3
-1.90056792E-07 8.41781077E-11-3.85274957E+04-1.16501069E+01	4
C80OH3-006-2 5/5 THERMC 8H 170 4 OG 300.000 5000.000 1000.000	91
3.66587544E+01 3.70169165E-02-1.50812571E-05 2.67876126E-09-1.73660298E-13	2
-4.84485502E+04-1.57536162E+02 1.13753682E+01 4.78391710E-02 1.07318397E-04	3
-1.90056792E-07 8.41781077E-11-3.85274957E+04-1.16501069E+01	4
C80OH6-003-2 5/5 THERMC 8H 170 4 OG 300.000 5000.000 1000.000	91
3.66587544E+01 3.70169165E-02-1.50812571E-05 2.67876126E-09-1.73660298E-13	2
-4.84485502E+04-1.57536162E+02 1.13753682E+01 4.78391710E-02 1.07318397E-04	3
-1.90056792E-07 8.41781077E-11-3.85274957E+04-1.16501069E+01	4
C80OH4-005-2 5/5 THERMC 8H 170 4 OG 300.000 5000.000 1000.000	91
3.66587544E+01 3.70169165E-02-1.50812571E-05 2.67876126E-09-1.73660298E-13	2
-4.84485502E+04-1.57536162E+02 1.13753682E+01 4.78391710E-02 1.07318397E-04	3
-1.90056792E-07 8.41781077E-11-3.85274957E+04-1.16501069E+01	4
C80OH5-004-2 5/5 THERMC 8H 170 4 OG 300.000 5000.000 1000.000	91
3.66587544E+01 3.70169165E-02-1.50812571E-05 2.67876126E-09-1.73660298E-13	2
-4.84485502E+04-1.57536162E+02 1.13753682E+01 4.78391710E-02 1.07318397E-04	3
-1.90056792E-07 8.41781077E-11-3.85274957E+04-1.16501069E+01	4
C80OH4-006-2 5/5 THERMC 8H 170 4 OG 300.000 5000.000 1000.000	91
3.66587544E+01 3.70169165E-02-1.50812571E-05 2.67876126E-09-1.73660298E-13	2
-4.84485502E+04-1.57536162E+02 1.13753682E+01 4.78391710E-02 1.07318397E-04	3
-1.90056792E-07 8.41781077E-11-3.85274957E+04-1.16501069E+01	4
C80OH6-004-2 5/5 THERMC 8H 170 4 OG 300.000 5000.000 1000.000	91
3.66587544E+01 3.70169165E-02-1.50812571E-05 2.67876126E-09-1.73660298E-13	2
-4.84485502E+04-1.57536162E+02 1.13753682E+01 4.78391710E-02 1.07318397E-04	3
-1.90056792E-07 8.41781077E-11-3.85274957E+04-1.16501069E+01	4
C80OH5-006-2 5/5 THERMC 8H 170 4 OG 300.000 5000.000 1000.000	91
3.66587544E+01 3.70169165E-02-1.50812571E-05 2.67876126E-09-1.73660298E-13	2
-4.84485502E+04-1.57536162E+02 1.13753682E+01 4.78391710E-02 1.07318397E-04	3
-1.90056792E-07 8.41781077E-11-3.85274957E+04-1.16501069E+01	4
C80OH6-005-2 5/5 THERMC 8H 170 4 OG 300.000 5000.000 1000.000	91
3.66587544E+01 3.70169165E-02-1.50812571E-05 2.67876126E-09-1.73660298E-13	2
-4.84485502E+04-1.57536162E+02 1.13753682E+01 4.78391710E-02 1.07318397E-04	3
-1.90056792E-07 8.41781077E-11-3.85274957E+04-1.16501069E+01	4
C8H1601-1-2 5/5 thermC 8H 160 1 Og 300.000 5000.000 1395.000	51
2.56118327e+01 3.76233253e-02-1.28765778e-05 2.00013283e-09-1.16089001e-13	2
-3.67189319e+04-1.09860085e+02-5.40482169e+00 1.08749262e-01-7.48467625e-05	3
2.64504076e-08-3.80853915e-12-2.58272257e+04 5.71684727e+01	4
C8H1601-2-2 5/5 thermC 8H 160 1 Og 300.000 5000.000 1395.000	61
2.69350619e+01 3.62269057e-02-1.24260983e-05 1.93287404e-09-1.12290408e-13	2
-3.93911683e+04-1.16145863e+02-3.60205585e+00 1.08934139e-01-7.95107222e-05	3
3.04988477e-08-4.83611359e-12-2.88857998e+04 4.74331957e+01	4
C8H1601-3-2 5/5 thermC 8H 160 1 Og 300.000 5000.000 1397.000	51
2.60151372e+01 3.74487135e-02-1.28509995e-05 1.99955302e-09-1.16187204e-13	2
-3.90029246e+04-1.11685802e+02-5.63382516e+00 1.11874905e-01-8.01070539e-05	3
2.98231614e-08-4.55998166e-12-2.80570050e+04 5.81192431e+01	4
C8H1601-4-2 5/5 C 8H 160 1 Og 300.000 5000.000 1398.000	41
2.54163303e+01 3.83718019e-02-1.31677133e-05 2.04885623e-09-1.19053970e-13	2
-4.90984507e+04-1.09889889e+02-7.47935138e+00 1.15710852e-01-8.28958633e-05	3
3.07606645e-08-4.67317263e-12-3.77349410e+04 6.65848734e+01	4
C8H1601-5-2 5/5 C 8H 160 1 Og 300.000 5000.000 1395.000	31
2.61275633e+01 3.85346767e-02-1.33009532e-05 2.07778557e-09-1.21070821e-13	2
-5.17314278e+04-1.19235520e+02-8.07012812e+00 1.17636558e-01-8.31088723e-05	3
3.00991594e-08-4.44404140e-12-3.97852471e+04 6.46910371e+01	4
C8H1602-3-2 5/5 thermC 8H 160 1 Og 300.000 5000.000 1396.000	61
2.75398866e+01 3.58905331e-02-1.23480065e-05 1.92453349e-09-1.11957295e-13	2
-4.17812642e+04-1.20567305e+02-4.70421124e+00 1.15885624e-01-9.01941669e-05	3
3.71106240e-08-6.28561974e-12-3.09834538e+04 5.10580331e+01	4
C8H1602-4-2 5/5 C 8H 160 1 Og 300.000 5000.000 1397.000	51

2.67410850e+01	3.69665215e-02	-1.27136485e-05	1.98107195e-09	-1.15228929e-13	2
-4.26147924e+04	-1.17914935e+02	-6.49812756e+00	1.18835287e-01	-9.15381092e-05	3
3.71546118e-08	-6.20476358e-12	-3.14436443e+04	5.91855120e+01		4
C8H16O2-5-2	5/5	C 8H 16O	1 0g	300.000 5000.000 1398.000	41
2.61186562e+01	3.78120585e-02	-1.29822920e-05	2.02067355e-09	-1.17442557e-13	2
-5.26672221e+04	-1.15895531e+02	-7.62783622e+00	1.19565939e-01	-8.97587613e-05	3
3.52306529e-08	-5.67588923e-12	-4.12319883e+04	6.43195183e+01		4
C8H16O2-6-2	5/5	C 8H 16O	1 0g	300.000 5000.000 1395.000	31
2.68371811e+01	3.79614615e-02	-1.31093898e-05	2.04849744e-09	-1.19389383e-13	2
-5.53021053e+04	-1.25280066e+02	-8.21618329e+00	1.21481256e-01	-8.99496124e-05	3
3.45487099e-08	-5.44090850e-12	-4.32827153e+04	6.24141201e+01		4
C8H16O3-4-2	5/5	thermC 8H 16O	1 0g	300.000 5000.000 1397.000	61
2.78393315e+01	3.56650608e-02	-1.22781984e-05	1.91459366e-09	-1.11421258e-13	2
-4.08011101e+04	-1.21339070e+02	-5.26842413e+00	1.16291693e-01	-8.85194547e-05	3
3.51609027e-08	-5.72406157e-12	-2.96215411e+04	5.53212833e+01		4
C8H16O3-5-2	5/5	C 8H 16O	1 0g	300.000 5000.000 1396.000	51
2.69513102e+01	3.69638661e-02	-1.27520898e-05	1.99120631e-09	-1.15987389e-13	2
-4.15778076e+04	-1.18142927e+02	-7.70075528e+00	1.23350248e-01	-9.72719471e-05	3
4.03972394e-08	-6.88677171e-12	-3.00182356e+04	6.61469966e+01		4
C8H16O3-6-2	5/5	C 8H 16O	1 0g	300.000 5000.000 1396.000	41
2.63344777e+01	3.79036786e-02	-1.30748454e-05	2.04147799e-09	-1.18911483e-13	2
-5.16725470e+04	-1.16257789e+02	-9.60383939e+00	1.27303831e-01	-1.00158943e-04	3
4.13707441e-08	-7.00453646e-12	-3.96834408e+04	7.49095505e+01		4
C8H16O3-7-2	6/5	C 8H 16O	1 0g	300.000 5000.000 1395.000	31
2.61275633e+01	3.85346767e-02	-1.33009532e-05	2.07778557e-09	-1.21070821e-13	2
-5.17314278e+04	-1.19925002e+02	-8.07012812e+00	1.17636558e-01	-8.31088723e-05	3
3.00991594e-08	-4.44404140e-12	-3.97852471e+04	6.40015554e+01		4
C8H16O4-5-2	5/5	thermC 8H 16O	1 0g	300.000 5000.000 1397.000	61
2.78393315e+01	3.56650608e-02	-1.22781984e-05	1.91459366e-09	-1.11421258e-13	2
-4.08011101e+04	-1.21339070e+02	-5.26842413e+00	1.16291693e-01	-8.85194547e-05	3
3.51609027e-08	-5.72406157e-12	-2.96215411e+04	5.53212833e+01		4
C8H16O4-6-2	5/5	C 8H 16O	1 0g	300.000 5000.000 1396.000	51
2.69513102e+01	3.69638661e-02	-1.27520898e-05	1.99120631e-09	-1.15987389e-13	2
-4.15778076e+04	-1.18142927e+02	-7.70075528e+00	1.23350248e-01	-9.72719471e-05	3
4.03972394e-08	-6.88677171e-12	-3.00182356e+04	6.61469966e+01		4
C8H16O4-7-2	6/5	C 8H 16O	1 0g	300.000 5000.000 1398.000	41
2.54163303e+01	3.83718019e-02	-1.31677133e-05	2.04885623e-09	-1.19053970e-13	2
-4.90984507e+04	-1.10579371e+02	-7.47935138e+00	1.15710852e-01	-8.28958633e-05	3
3.07606645e-08	-4.67317263e-12	-3.77349410e+04	6.58953918e+01		4
C8H16O5-6-2	5/5	thermC 8H 16O	1 0g	300.000 5000.000 1397.000	61
2.78393315e+01	3.56650608e-02	-1.22781984e-05	1.91459366e-09	-1.11421258e-13	2
-4.08011101e+04	-1.21339070e+02	-5.26842413e+00	1.16291693e-01	-8.85194547e-05	3
3.51609027e-08	-5.72406157e-12	-2.96215411e+04	5.53212833e+01		4
C8H16O5-7-2	6/5	C 8H 16O	1 0g	300.000 5000.000 1397.000	51
2.60151372e+01	3.74487135e-02	-1.28509995e-05	1.99955302e-09	-1.16187204e-13	2
-3.90029246e+04	-1.12375284e+02	-5.63382516e+00	1.11874905e-01	-8.01070539e-05	3
2.98231614e-08	-4.55998166e-12	-2.80570050e+04	5.74297614e+01		4
C8H16O6-7-2	6/5	thermC 8H 16O	1 0g	300.000 5000.000 1396.000	61
2.67852989e+01	3.64563118e-02	-1.25270973e-05	1.95085791e-09	-1.13425497e-13	2
-3.81888136e+04	-1.14937683e+02	-4.25973270e+00	1.10497178e-01	-8.09484014e-05	3
3.11174030e-08	-4.93839217e-12	-2.75247088e+04	5.13114909e+01		4
C8KET1-1-2	5/5	THERMC 8H 16O	3 0G	300.000 5000.000 1000.000	81
2.90624988E+01	4.18807391E-02	-1.66474612E-05	2.90635338E-09	-1.86154458E-13	2
-5.88563170E+04	-1.16191653E+02	5.30160337E+00	6.99541058E-02	3.20038602E-05	3
-9.50583574E-08	4.42758893E-11	-5.02052489E+04	1.71339879E+01		4
C8KET1-2-2	5/5	THERMC 8H 16O	3 0G	300.000 5000.000 1000.000	81
2.89107735E+01	4.22851843E-02	-1.67155997E-05	2.90699078E-09	-1.85693965E-13	2
-6.17194086E+04	-1.16306007E+02	3.23315823E+00	9.20267463E-02	-3.29139431E-05	3
-1.94837849E-08	1.36602190E-11	-5.31259842E+04	2.35102010E+01		4
C8KET1-3-2	5/5	THERMC 8H 16O	3 0G	300.000 5000.000 1000.000	81
3.11409043E+01	3.88752551E-02	-1.56299063E-05	2.75055976E-09	-1.77160049E-13	2
-6.15556212E+04	-1.29114402E+02	9.86483535E+00	4.04071732E-02	1.09461493E-04	3
-1.81632988E-07	7.83665223E-11	-5.28061302E+04	-4.34071110E+00		4
C8KET1-4-2	5/5	THERMC 8H 16O	3 0G	300.000 5000.000 1000.000	81
3.11409043E+01	3.88752551E-02	-1.56299063E-05	2.75055976E-09	-1.77160049E-13	2
-6.15556212E+04	-1.29114402E+02	9.86483535E+00	4.04071732E-02	1.09461493E-04	3
-1.81632988E-07	7.83665223E-11	-5.28061302E+04	-4.34071110E+00		4

C8KET1-5-2	5/5	THERMC	8H	160	3	OG	300.000	5000.000	1000.000	81
3.11409043E+01	3.88752551E-02	-1.56299063E-05	2.75055976E-09	-1.77160049E-13						2
-6.15556212E+04	-1.29114402E+02	9.86483535E+00	4.04071732E-02	1.09461493E-04						3
-1.81632988E-07	7.83665223E-11	-5.28061302E+04	-4.34071110E+00							4
C8KET7-3-2	5/5	THERMC	8H	160	3	OG	300.000	5000.000	1000.000	81
3.11409043E+01	3.88752551E-02	-1.56299063E-05	2.75055976E-09	-1.77160049E-13						2
-6.15556212E+04	-1.29807549E+02	9.86483535E+00	4.04071732E-02	1.09461493E-04						3
-1.81632988E-07	7.83665223E-11	-5.28061302E+04	-5.03385828E+00							4
C8KET7-4-2	5/5	THERMC	8H	160	3	OG	300.000	5000.000	1000.000	81
3.11409043E+01	3.88752551E-02	-1.56299063E-05	2.75055976E-09	-1.77160049E-13						2
-6.15556212E+04	-1.29807549E+02	9.86483535E+00	4.04071732E-02	1.09461493E-04						3
-1.81632988E-07	7.83665223E-11	-5.28061302E+04	-5.03385828E+00							4
C8KET7-5-2	5/5	THERMC	8H	160	3	OG	300.000	5000.000	1000.000	81
3.11409043E+01	3.88752551E-02	-1.56299063E-05	2.75055976E-09	-1.77160049E-13						2
-6.15556212E+04	-1.29807549E+02	9.86483535E+00	4.04071732E-02	1.09461493E-04						3
-1.81632988E-07	7.83665223E-11	-5.28061302E+04	-5.03385828E+00							4
C8KET7-6-2	5/5	THERMC	8H	160	3	OG	300.000	5000.000	1000.000	81
3.11409043E+01	3.88752551E-02	-1.56299063E-05	2.75055976E-09	-1.77160049E-13						2
-6.15556212E+04	-1.29807549E+02	9.86483535E+00	4.04071732E-02	1.09461493E-04						3
-1.81632988E-07	7.83665223E-11	-5.28061302E+04	-5.03385828E+00							4
C8KET3-1-2	5/5	THERMC	8H	160	3	OG	300.000	5000.000	1000.000	81
2.75745605E+01	4.29807707E-02	-1.69168467E-05	2.93305753E-09	-1.86962457E-13						2
-6.18687319E+04	-1.08385385E+02	4.76669775E+00	7.55791220E-02	8.07750233E-06						3
-6.31964899E-08	3.05557546E-11	-5.37488730E+04	1.84804543E+01							4
C8KET3-7-2	5/5	THERMC	8H	160	3	OG	300.000	5000.000	1000.000	81
2.75745605E+01	4.29807707E-02	-1.69168467E-05	2.93305753E-09	-1.86962457E-13						2
-6.18687319E+04	-1.08385385E+02	4.76669775E+00	7.55791220E-02	8.07750233E-06						3
-6.31964899E-08	3.05557546E-11	-5.37488730E+04	1.84804543E+01							4
C8KET4-1-2	5/5	THERMC	8H	160	3	OG	300.000	5000.000	1000.000	81
2.75745605E+01	4.29807707E-02	-1.69168467E-05	2.93305753E-09	-1.86962457E-13						2
-6.18687319E+04	-1.08385385E+02	4.76669775E+00	7.55791220E-02	8.07750233E-06						3
-6.31964899E-08	3.05557546E-11	-5.37488730E+04	1.84804543E+01							4
C8KET4-7-2	5/5	THERMC	8H	160	3	OG	300.000	5000.000	1000.000	81
2.75745605E+01	4.29807707E-02	-1.69168467E-05	2.93305753E-09	-1.86962457E-13						2
-6.18687319E+04	-1.08385385E+02	4.76669775E+00	7.55791220E-02	8.07750233E-06						3
-6.31964899E-08	3.05557546E-11	-5.37488730E+04	1.84804543E+01							4
C8KET5-1-2	5/5	THERMC	8H	160	3	OG	300.000	5000.000	1000.000	81
2.75745605E+01	4.29807707E-02	-1.69168467E-05	2.93305753E-09	-1.86962457E-13						2
-6.18687319E+04	-1.08385385E+02	4.76669775E+00	7.55791220E-02	8.07750233E-06						3
-6.31964899E-08	3.05557546E-11	-5.37488730E+04	1.84804543E+01							4
C8KET5-7-2	5/5	THERMC	8H	160	3	OG	300.000	5000.000	1000.000	81
2.75745605E+01	4.29807707E-02	-1.69168467E-05	2.93305753E-09	-1.86962457E-13						2
-6.18687319E+04	-1.08385385E+02	4.76669775E+00	7.55791220E-02	8.07750233E-06						3
-6.31964899E-08	3.05557546E-11	-5.37488730E+04	1.84804543E+01							4
C8KET6-7-2	5/5	THERMC	8H	160	3	OG	300.000	5000.000	1000.000	81
2.75745605E+01	4.29807707E-02	-1.69168467E-05	2.93305753E-09	-1.86962457E-13						2
-6.18687319E+04	-1.08385385E+02	4.76669775E+00	7.55791220E-02	8.07750233E-06						3
-6.31964899E-08	3.05557546E-11	-5.37488730E+04	1.84804543E+01							4
C8KET3-4-2	5/5	THERMC	8H	160	3	OG	300.000	5000.000	1000.000	81
2.96932418E+01	3.99636615E-02	-1.59276198E-05	2.78584721E-09	-1.78667216E-13						2
-6.45955078E+04	-1.21864682E+02	9.32993039E+00	4.60321845E-02	8.55351474E-05						3
-1.49771134E-07	6.46463930E-11	-5.63497543E+04	-3.28192954E+00							4
C8KET4-3-2	5/5	THERMC	8H	160	3	OG	300.000	5000.000	1000.000	81
2.96932418E+01	3.99636615E-02	-1.59276198E-05	2.78584721E-09	-1.78667216E-13						2
-6.45955078E+04	-1.21864682E+02	9.32993039E+00	4.60321845E-02	8.55351474E-05						3
-1.49771134E-07	6.46463930E-11	-5.63497543E+04	-3.28192954E+00							4
C8KET3-5-2	5/5	THERMC	8H	160	3	OG	300.000	5000.000	1000.000	81
2.96932418E+01	3.99636615E-02	-1.59276198E-05	2.78584721E-09	-1.78667216E-13						2
-6.45955078E+04	-1.21864682E+02	9.32993039E+00	4.60321845E-02	8.55351474E-05						3
-1.49771134E-07	6.46463930E-11	-5.63497543E+04	-3.28192954E+00							4
C8KET5-3-2	5/5	THERMC	8H	160	3	OG	300.000	5000.000	1000.000	81
2.96932418E+01	3.99636615E-02	-1.59276198E-05	2.78584721E-09	-1.78667216E-13						2
-6.45955078E+04	-1.21864682E+02	9.32993039E+00	4.60321845E-02	8.55351474E-05						3
-1.49771134E-07	6.46463930E-11	-5.63497543E+04	-3.28192954E+00							4
C8KET3-6-2	5/5	THERMC	8H	160	3	OG	300.000	5000.000	1000.000	81
2.96932418E+01	3.99636615E-02	-1.59276198E-05	2.78584721E-09	-1.78667216E-13						2
-6.45955078E+04	-1.21864682E+02	9.32993039E+00	4.60321845E-02	8.55351474E-05						3

-1.49771134E-07	6.46463930E-11	-5.63497543E+04	-3.28192954E+00							4
C8KET6-3-2	5/5 THERMC	8H 160	3 OG	300.000	5000.000	1000.000				81
2.96932418E+01	3.99636615E-02	-1.59276198E-05	2.78584721E-09	-1.78667216E-13						2
-6.45955078E+04	-1.21864682E+02	9.32993039E+00	4.60321845E-02	8.55351474E-05						3
-1.49771134E-07	6.46463930E-11	-5.63497543E+04	-3.28192954E+00							4
C8KET4-5-2	5/5 THERMC	8H 160	3 OG	300.000	5000.000	1000.000				81
2.96932418E+01	3.99636615E-02	-1.59276198E-05	2.78584721E-09	-1.78667216E-13						2
-6.45955078E+04	-1.21864682E+02	9.32993039E+00	4.60321845E-02	8.55351474E-05						3
-1.49771134E-07	6.46463930E-11	-5.63497543E+04	-3.28192954E+00							4
C8KET5-4-2	5/5 THERMC	8H 160	3 OG	300.000	5000.000	1000.000				81
2.96932418E+01	3.99636615E-02	-1.59276198E-05	2.78584721E-09	-1.78667216E-13						2
-6.45955078E+04	-1.21864682E+02	9.32993039E+00	4.60321845E-02	8.55351474E-05						3
-1.49771134E-07	6.46463930E-11	-5.63497543E+04	-3.28192954E+00							4
C8KET4-6-2	5/5 THERMC	8H 160	3 OG	300.000	5000.000	1000.000				81
2.96932418E+01	3.99636615E-02	-1.59276198E-05	2.78584721E-09	-1.78667216E-13						2
-6.45955078E+04	-1.21864682E+02	9.32993039E+00	4.60321845E-02	8.55351474E-05						3
-1.49771134E-07	6.46463930E-11	-5.63497543E+04	-3.28192954E+00							4
C8KET6-4-2	5/5 THERMC	8H 160	3 OG	300.000	5000.000	1000.000				81
2.96932418E+01	3.99636615E-02	-1.59276198E-05	2.78584721E-09	-1.78667216E-13						2
-6.45955078E+04	-1.21864682E+02	9.32993039E+00	4.60321845E-02	8.55351474E-05						3
-1.49771134E-07	6.46463930E-11	-5.63497543E+04	-3.28192954E+00							4
C8KET5-6-2	5/5 THERMC	8H 160	3 OG	300.000	5000.000	1000.000				81
2.96932418E+01	3.99636615E-02	-1.59276198E-05	2.78584721E-09	-1.78667216E-13						2
-6.45955078E+04	-1.21864682E+02	9.32993039E+00	4.60321845E-02	8.55351474E-05						3
-1.49771134E-07	6.46463930E-11	-5.63497543E+04	-3.28192954E+00							4
C8KET6-5-2	5/5 THERMC	8H 160	3 OG	300.000	5000.000	1000.000				81
2.96932418E+01	3.99636615E-02	-1.59276198E-05	2.78584721E-09	-1.78667216E-13						2
-6.45955078E+04	-1.21864682E+02	9.32993039E+00	4.60321845E-02	8.55351474E-05						3
-1.49771134E-07	6.46463930E-11	-5.63497543E+04	-3.28192954E+00							4
C8KET3-2-2	5/5 THERMC	8H 160	3 OG	300.000	5000.000	1000.000				81
2.71491461E+01	4.35724338E-02	-1.70187807E-05	2.93496588E-09	-1.86387597E-13						2
-6.45354811E+04	-1.07076829E+02	2.69825327E+00	9.76517576E-02	-5.68402883E-05						3
1.23780689E-08	-5.99102381E-14	-5.66700712E+04	2.45674352E+01							4
C8KET4-2-2	5/5 THERMC	8H 160	3 OG	300.000	5000.000	1000.000				81
2.71491461E+01	4.35724338E-02	-1.70187807E-05	2.93496588E-09	-1.86387597E-13						2
-6.45354811E+04	-1.07076829E+02	2.69825327E+00	9.76517576E-02	-5.68402883E-05						3
1.23780689E-08	-5.99102381E-14	-5.66700712E+04	2.45674352E+01							4
C8KET5-2-2	5/5 THERMC	8H 160	3 OG	300.000	5000.000	1000.000				81
2.71491461E+01	4.35724338E-02	-1.70187807E-05	2.93496588E-09	-1.86387597E-13						2
-6.45354811E+04	-1.07076829E+02	2.69825327E+00	9.76517576E-02	-5.68402883E-05						3
1.23780689E-08	-5.99102381E-14	-5.66700712E+04	2.45674352E+01							4
C8KET6-2-2	5/5 THERMC	8H 160	3 OG	300.000	5000.000	1000.000				81
2.71491461E+01	4.35724338E-02	-1.70187807E-05	2.93496588E-09	-1.86387597E-13						2
-6.45354811E+04	-1.07076829E+02	2.69825327E+00	9.76517576E-02	-5.68402883E-05						3
1.23780689E-08	-5.99102381E-14	-5.66700712E+04	2.45674352E+01							4

APPENDIX C: UPDATED RATE RULES OF THE REACTION CLASS

RELATED TO 2-METHYLHEPTANE COMBUSTION AT LOW AND

INTERMEDIATE REGIONS

Reaction	A ($\text{cm}^3 \cdot \text{mol}^{-1} \cdot \text{s}^{-1}$)	n	E_a ($\text{cal} \cdot \text{mol}^{-1}$)
$\text{C8H18-2} + \text{OH} = \text{C8H17-2A} + \text{H2O}$	3.35×10^6	2.08	375.5
$\text{C8H18-2} + \text{OH} = \text{C8H17-2B} + \text{H2O}$	1.72×10^{13}	0	2261
$\text{C8H18-2} + \text{OH} = \text{C8H17-2C} + \text{H2O}$	5.42×10^{12}	0	1578
$\text{C8H18-2} + \text{OH} = \text{C8H17-2D} + \text{H2O}$	5.62×10^{11}	0.32	846.5
$\text{C8H18-2} + \text{OH} = \text{C8H17-2E} + \text{H2O}$	5.72×10^6	1.81	-1015
$\text{C8H18-2} + \text{OH} = \text{C8H17-2F} + \text{H2O}$	7.05×10^9	0.935	504.7
$\text{C8H18-2} + \text{OH} = \text{C8H17-2G} + \text{H2O}$	1.37×10^7	1.81	868.3
$\text{C8H18-2} + \text{HO2} = \text{C8H17-2A} + \text{H2O2}$	1.63×10^2	3.59	17160
$\text{C8H18-2} + \text{HO2} = \text{C8H17-2B} + \text{H2O2}$	2.60×10^3	3.01	12090
$\text{C8H18-2} + \text{HO2} = \text{C8H17-2C} + \text{H2O2}$	2.53×10^2	3.37	13720
$\text{C8H18-2} + \text{HO2} = \text{C8H17-2D} + \text{H2O2}$	2.53×10^2	3.37	13720
$\text{C8H18-2} + \text{HO2} = \text{C8H17-2E} + \text{H2O2}$	2.53×10^2	3.37	13720
$\text{C8H18-2} + \text{HO2} = \text{C8H17-2F} + \text{H2O2}$	2.53×10^2	3.37	13720
$\text{C8H18-2} + \text{HO2} = \text{C8H17-2G} + \text{H2O2}$	8.16×10^1	3.59	17160
$\text{C8H17-2A} + \text{O2} = \text{C8H17OO-1-2}$	6.87×10^{16}	-1.63	199
$\text{C8H17-2B} + \text{O2} = \text{C8H17OO-2-2}$	9.76×10^{11}	0.325	-417
$\text{C8H17-2C} + \text{O2} = \text{C8H17OO-3-2}$	3.49×10^{14}	-0.82	-536
$\text{C8H17-2D} + \text{O2} = \text{C8H17OO-4-2}$	3.49×10^{14}	-0.82	-536
$\text{C8H17-2E} + \text{O2} = \text{C8H17OO-5-2}$	3.49×10^{14}	-0.82	-536
$\text{C8H17-2F} + \text{O2} = \text{C8H17OO-6-2}$	3.49×10^{14}	-0.82	-536
$\text{C8H17-2G} + \text{O2} = \text{C8H17OO-7-2}$	6.87×10^{16}	-1.63	199
$\text{C8H17OO-1-2} = \text{C8OOH1-2A}$	3.57×10^6	1.6	21000
$\text{C8H17OO-1-2} = \text{C8OOH1-2B}$	2.31×10^9	0.8	27100
$\text{C8H17OO-1-2} = \text{C8OOH1-2C}$	1.36×10^7	1.3	18200
$\text{C8H17OO-1-2} = \text{C8OOH1-2D}$	3.72×10^6	1.2	16600
$\text{C8H17OO-1-2} = \text{C8OOH1-2E}$	2.60×10^6	1	18200
$\text{C8H17OO-2-2} = \text{C8OOH2-2A}$	3.01×10^9	1.2	33500
$\text{C8H17OO-2-2} = \text{C8OOH2-2C}$	6.51×10^9	0.7	30100

C8H1700-2-2 = C800H2-2D	3.52×10^{10}	0.2	18500
C8H1700-2-2 = C800H2-2E	1.86×10^6	1.2	16600
C8H1700-2-2 = C800H2-2F	1.30×10^6	1	18200
C8H1700-3-2 = C800H3-2A	2.88×10^7	1.4	20800
C8H1700-3-2 = C800H3-2B	7.45×10^9	0.6	27300
C8H1700-3-2 = C800H3-2D	1.72×10^9	0.9	29500
C8H1700-3-2 = C800H3-2E	7.03×10^{10}	0.2	18500
C8H1700-3-2 = C800H3-2F	1.86×10^6	1.2	16600
C8H1700-3-2 = C800H3-2G	1.47×10^5	1.5	19900
C8H1700-4-2 = C800H4-2A	1.23×10^6	1.5	20000
C8H1700-4-2 = C800H4-2B	6.15×10^6	1.2	15400
C8H1700-4-2 = C800H4-2C	1.72×10^9	0.9	29500
C8H1700-4-2 = C800H4-2E	1.72×10^9	0.9	29500
C8H1700-4-2 = C800H4-2F	7.03×10^{10}	0.2	18500
C8H1700-4-2 = C800H4-2G	6.17×10^5	1.5	20000
C8H1700-5-2 = C800H5-2A	2.94×10^5	1.5	19900
C8H1700-5-2 = C800H5-2B	8.54×10^5	1.2	13800
C8H1700-5-2 = C800H5-2C	7.03×10^{10}	0.2	18500
C8H1700-5-2 = C800H5-2D	1.72×10^9	0.9	29500
C8H1700-5-2 = C800H5-2F	1.72×10^9	0.9	29500
C8H1700-5-2 = C800H5-2G	1.44×10^7	1.4	20800
C8H1700-6-2 = C800H6-2B	2.76×10^5	1.1	14300
C8H1700-6-2 = C800H6-2C	1.86×10^6	1.2	16600
C8H1700-6-2 = C800H6-2D	7.03×10^{10}	0.2	18500
C8H1700-6-2 = C800H6-2E	1.72×10^9	0.9	29500
C8H1700-6-2 = C800H6-2G	1.46×10^9	1.1	33500
C8H1700-7-2 = C800H7-2C	2.60×10^6	1	18200
C8H1700-7-2 = C800H7-2D	3.72×10^6	1.2	16600
C8H1700-7-2 = C800H7-2E	1.36×10^7	1.3	18200
C8H1700-7-2 = C800H7-2F	4.01×10^8	1.1	30100
<hr/>			
C8H1700-1-2 = C8H16-1-2 + HO2	2.89×10^9	0.93	29800
C8H1700-2-2 = C8H16-1-2 + HO2	1.73×10^{10}	0.93	29800
C8H1700-2-2 = C8H16-2-2 + HO2	5.77×10^9	0.93	29800
C8H1700-3-2 = C8H16-2-2 + HO2	2.89×10^9	0.93	29800
C8H1700-3-2 = C8H16-3-2 + HO2	5.77×10^9	0.93	29800

C8H1700-4-2 = C8H16-3-2 + HO2	5.77×10^9	0.93	29800
C8H1700-4-2 = C8H16-4-2 + HO2	5.77×10^9	0.93	29800
C8H1700-5-2 = C8H16-4-2 + HO2	5.77×10^9	0.93	29800
C8H1700-5-2 = C8H16-5-2 + HO2	5.77×10^9	0.93	29800
C8H1700-6-2 = C8H16-5-2 + HO2	5.77×10^9	0.93	29800
C8H1700-6-2 = C8H16-6-2 + HO2	8.66×10^9	0.93	29800
C8H1700-7-2 = C8H16-6-2 + HO2	5.77×10^9	0.93	29800
<hr/>			
C8OOH1-2B = C8H16O1-2-2 + OH	1.78×10^{12}	0	13800
C8OOH2-2A = C8H16O1-2-2 + OH	1.78×10^{12}	0	15100
C8OOH2-2C = C8H16O2-3-2 + OH	1.78×10^{12}	0	13000
C8OOH3-2B = C8H16O2-3-2 + OH	1.78×10^{12}	0	10300
C8OOH3-2D = C8H16O3-4-2 + OH	1.78×10^{12}	0	10900
C8OOH4-2C = C8H16O3-4-2 + OH	1.78×10^{12}	0	11400
C8OOH4-2E = C8H16O4-5-2 + OH	1.78×10^{12}	0	11400
C8OOH5-2D = C8H16O4-5-2 + OH	1.78×10^{12}	0	11400
C8OOH5-2F = C8H16O5-6-2 + OH	1.78×10^{12}	0	11400
C8OOH6-2E = C8H16O5-6-2 + OH	1.78×10^{12}	0	11400
C8OOH6-2G = C8H16O6-7-2 + OH	1.78×10^{12}	0	13000
C8OOH7-2F = C8H16O6-7-2 + OH	1.78×10^{12}	0	13900
C8OOH1-2A = C8H16O1-1-2 + OH	3.17×10^{11}	0	19600
C8OOH1-2C = C8H16O1-3-2 + OH	3.17×10^{11}	0	18300
C8OOH2-2D = C8H16O2-4-2 + OH	3.17×10^{11}	0	17800
C8OOH3-2A = C8H16O1-3-2 + OH	3.17×10^{11}	0	17800
C8OOH3-2E = C8H16O3-5-2 + OH	3.17×10^{11}	0	16400
C8OOH4-2B = C8H16O2-4-2 + OH	3.17×10^{11}	0	16100
C8OOH4-2F = C8H16O4-6-2 + OH	3.17×10^{11}	0	16800
C8OOH5-2C = C8H16O3-5-2 + OH	3.17×10^{11}	0	16800
C8OOH5-2G = C8H16O5-7-2 + OH	3.17×10^{11}	0	17800
C8OOH6-2D = C8H16O4-6-2 + OH	3.17×10^{11}	0	16800
C8OOH7-2E = C8H16O5-7-2 + OH	3.17×10^{11}	0	18300
C8OOH1-2D = C8H16O1-4-2 + OH	2.77×10^{10}	0	10600
C8OOH2-2E = C8H16O2-5-2 + OH	2.77×10^{10}	0	9720
C8OOH3-2F = C8H16O3-6-2 + OH	2.77×10^{10}	0	7740
C8OOH4-2G = C8H16O4-7-2 + OH	2.77×10^{10}	0	9720
C8OOH4-2A = C8H16O1-4-2 + OH	2.77×10^{10}	0	9720

C8OOH5-2B = C8H16O2-5-2 + OH	2.77×10^{10}	0	7170
C8OOH6-2C = C8H16O3-6-2 + OH	2.77×10^{10}	0	8230
C8OOH7-2D = C8H16O4-7-2 + OH	2.77×10^{10}	0	10600
C8OOH1-2E = C8H16O1-5-2 + OH	5.20×10^9	0	11200
C8OOH2-2F = C8H16O2-6-2 + OH	5.20×10^9	0	10600
C8OOH3-2G = C8H16O3-7-2 + OH	5.20×10^9	0	10600
C8OOH5-2A = C8H16O1-5-2 + OH	5.20×10^9	0	10600
C8OOH6-2B = C8H16O2-6-2 + OH	5.20×10^9	0	8740
C8OOH7-2C = C8H16O3-7-2 + OH	5.20×10^9	0	11200
<hr/>			
C8OOH1-2B = C8H16-1-2 + HO2	1.83×10^{10}	0.79	15100
C8OOH2-2A = C8H16-1-2 + HO2	1.83×10^{10}	0.79	15100
C8OOH2-2C = C8H16-2-2 + HO2	1.83×10^{10}	0.79	15100
C8OOH3-2B = C8H16-2-2 + HO2	1.83×10^{10}	0.79	15100
C8OOH3-2D = C8H16-3-2 + HO2	1.83×10^{10}	0.79	15100
C8OOH4-2C = C8H16-3-2 + HO2	1.83×10^{10}	0.79	15100
C8OOH4-2E = C8H16-4-2 + HO2	1.83×10^{10}	0.79	15100
C8OOH5-2D = C8H16-4-2 + HO2	1.83×10^{10}	0.79	15100
C8OOH5-2F = C8H16-5-2 + HO2	1.83×10^{10}	0.79	15100
C8OOH6-2E = C8H16-5-2 + HO2	1.83×10^{10}	0.79	15100
C8OOH6-2G = C8H16-6-2 + HO2	1.83×10^{10}	0.79	15100
C8OOH7-2F = C8H16-6-2 + HO2	1.83×10^{10}	0.79	15100
<hr/>			
C8OOH1-2A + O2 = C8OOH1-OO1-2	3.44×10^{16}	-1.63	199
C8OOH1-2B + O2 = C8OOH1-OO2-2	4.88×10^{11}	0.325	-417
C8OOH1-2C + O2 = C8OOH1-OO3-2	1.75×10^{14}	-0.816	-537
C8OOH1-2D + O2 = C8OOH1-OO4-2	1.75×10^{14}	-0.816	-537
C8OOH1-2E + O2 = C8OOH1-OO5-2	1.75×10^{14}	-0.816	-537
C8OOH2-2A + O2 = C8OOH2-OO1-2	3.44×10^{16}	-1.63	199
C8OOH2-2C + O2 = C8OOH2-OO3-2	1.75×10^{14}	-0.816	-537
C8OOH2-2D + O2 = C8OOH2-OO4-2	1.75×10^{14}	-0.816	-537
C8OOH2-2E + O2 = C8OOH2-OO5-2	1.75×10^{14}	-0.816	-537
C8OOH2-2F + O2 = C8OOH2-OO6-2	1.75×10^{14}	-0.816	-537
C8OOH3-2A + O2 = C8OOH3-OO1-2	3.44×10^{16}	-1.63	199
C8OOH3-2B + O2 = C8OOH3-OO2-2	4.88×10^{11}	0.325	-417
C8OOH3-2D + O2 = C8OOH3-OO4-2	1.75×10^{14}	-0.816	-537
C8OOH3-2E + O2 = C8OOH3-OO5-2	1.75×10^{14}	-0.816	-537

C800H3-2F + O2 = C800H3-006-2	1.75×10^{14}	-0.816	-537
C800H3-2G + O2 = C800H3-007-2	3.44×10^{16}	-1.63	199
C800H4-2A + O2 = C800H4-001-2	3.44×10^{16}	-1.63	199
C800H4-2B + O2 = C800H4-002-2	4.88×10^{11}	0.325	-417
C800H4-2C + O2 = C800H4-003-2	1.75×10^{14}	-0.816	-537
C800H4-2E + O2 = C800H4-005-2	1.75×10^{14}	-0.816	-537
C800H4-2F + O2 = C800H4-006-2	1.75×10^{14}	-0.816	-537
C800H4-2G + O2 = C800H4-007-2	3.44×10^{16}	-1.63	199
C800H5-2A + O2 = C800H5-001-2	3.44×10^{16}	-1.63	199
C800H5-2B + O2 = C800H5-002-2	4.88×10^{11}	0.325	-417
C800H5-2C + O2 = C800H5-003-2	1.75×10^{14}	-0.816	-537
C800H5-2D + O2 = C800H5-004-2	1.75×10^{14}	-0.816	-537
C800H5-2F + O2 = C800H5-006-2	1.75×10^{14}	-0.816	-537
C800H5-2G + O2 = C800H5-007-2	3.44×10^{16}	-1.63	199
C800H6-2B + O2 = C800H6-002-2	4.88×10^{11}	0.325	-417
C800H6-2C + O2 = C800H6-003-2	1.75×10^{14}	-0.816	-537
C800H6-2D + O2 = C800H6-004-2	1.75×10^{14}	-0.816	-537
C800H6-2E + O2 = C800H6-005-2	1.75×10^{14}	-0.816	-537
C800H6-2G + O2 = C800H6-007-2	3.44×10^{16}	-1.63	199
C800H7-2C + O2 = C800H7-003-2	1.75×10^{14}	-0.816	-537
C800H7-2D + O2 = C800H7-004-2	1.75×10^{14}	-0.816	-537
C800H7-2E + O2 = C800H7-005-2	1.75×10^{14}	-0.816	-537
C800H7-2F + O2 = C800H7-006-2	1.75×10^{14}	-0.816	-537
<hr/>			
C800H1-001-2 = C8KET1-1-2 + OH	1.87×10^{11}	0	21900
C800H1-002-2 = C8KET1-2-2 + OH	2.42×10^{12}	0	31000
C800H1-003-2 = C8KET1-3-2 + OH	3.34×10^{11}	0	21300
C800H1-004-2 = C8KET1-4-2 + OH	4.96×10^{10}	0	20700
C800H1-005-2 = C8KET1-5-2 + OH	5.54×10^{10}	0	23500
C800H3-001-2 = C8KET3-1-2 + OH	1.07×10^{11}	0	19700
C800H3-002-2 = C8KET3-2-2 + OH	1.30×10^{12}	0	27700
C800H3-004-2 = C8KET3-4-2 + OH	2.16×10^{12}	0	28500
C800H3-005-2 = C8KET3-5-2 + OH	1.64×10^{11}	0	19300
C800H3-006-2 = C8KET3-6-2 + OH	2.14×10^{10}	0	18800
C800H3-007-2 = C8KET3-7-2 + OH	5.73×10^9	0	19600
C800H4-001-2 = C8KET4-1-2 + OH	1.47×10^{10}	0	17900

C8OOH4-OO2-2 = C8KET4-2-2 + OH	1.78×10^{11}	0	19700
C8OOH4-OO3-2 = C8KET4-3-2 + OH	2.16×10^{12}	0	28500
C8OOH4-OO5-2 = C8KET4-5-2 + OH	2.16×10^{12}	0	28500
C8OOH4-OO6-2 = C8KET4-6-2 + OH	1.64×10^{11}	0	19300
C8OOH4-OO7-2 = C8KET4-7-2 + OH	1.47×10^{10}	0	17900
C8OOH5-OO1-2 = C8KET5-1-2 + OH	5.73×10^9	0	19600
C8OOH5-OO2-2 = C8KET5-2-2 + OH	2.10×10^{10}	0	18700
C8OOH5-OO3-2 = C8KET5-3-2 + OH	1.64×10^{11}	0	19300
C8OOH5-OO4-2 = C8KET5-4-2 + OH	2.16×10^{12}	0	28500
C8OOH5-OO6-2 = C8KET5-6-2 + OH	2.16×10^{12}	0	28500
C8OOH5-OO7-2 = C8KET5-7-2 + OH	1.07×10^{11}	0	19700
C8OOH6-OO2-2 = C8KET6-2-2 + OH	1.02×10^{10}	0	21200
C8OOH6-OO3-2 = C8KET6-3-2 + OH	2.14×10^{10}	0	18800
C8OOH6-OO4-2 = C8KET6-4-2 + OH	1.64×10^{11}	0	19300
C8OOH6-OO5-2 = C8KET6-5-2 + OH	2.16×10^{12}	0	28500
C8OOH6-OO7-2 = C8KET6-7-2 + OH	3.49×10^{11}	0	27000
C8OOH7-OO3-2 = C8KET7-3-2 + OH	5.54×10^{10}	0	23500
C8OOH7-OO4-2 = C8KET7-4-2 + OH	4.96×10^{10}	0	20700
C8OOH7-OO5-2 = C8KET7-5-2 + OH	3.34×10^{11}	0	21300
C8OOH7-OO6-2 = C8KET7-6-2 + OH	1.79×10^{12}	0	32800
<hr/>			
C8OOH2-OO4-2 = C3H6 + OH + IC5KETDB	7.03×10^{10}	0.2	18500
C8OOH2-OO5-2 = C2H4 + OH + IC6KETEB	1.44×10^7	1.4	20800
C8OOH2-OO3-2 = C4H8-1 + OH + IC4KETIT	7.03×10^{10}	0.2	18500
<hr/>			